CELAL MOHAN ÖGÜN

SURFACE WAVE DRIVEN MOLECULAR LOW PRESSURE PLASMAS FOR GENERAL LIGHTING

KIT Scientific Publishing

Celal Mohan Ögün

**Surface wave driven molecular low
pressure plasmas for general lighting**

Surface wave driven molecular low pressure plasmas for general lighting

by
Celal Mohan Ögün

Impressum

SKIT Scientific
Publishing

Surface wave driven molecular low pressure plasmas for general lighting

Zur Erlangung des akademischen Grades eines
DOKTOR-INGENIEURS

von der Fakultät für
Elektrotechnik und Informationstechnik
des Karlsruher Instituts für Technologie (KIT)
genehmigte

DISSERTATION

von
Dipl.-Ing. Celal Mohan Ögün
geb. in Istanbul, Türkei

Tag der mündlichen Prüfung: 24. 11. 2015

Hauptreferent: Prof. Dr.-Ing. Wolfgang Heering
Korreferent: Prof. Dr. rer. nat. Dr. h.c. Manfred Thumm

Kurzfassung

Kompaktleuchtstofflampen (CFL) sind heute insbesondere in der Allgemeinbeleuchtung weit verbreitet. Dennoch kämpfen sie wegen des gesundheitsschädlichen Quecksilbers, das als Leuchtkomponente in der Lampe dient, gegen Akzeptanzprobleme. Das Entfernen des Quecksilbers aus diesen Niederdruckplasmastrahlungsquellen ist noch eine weitgehend ungelöste Herausforderung. Die Herausforderung liegt hier in der Auswahl der Ersatzmaterialien. Sie müssen das Quecksilber sowohl radiometrisch als auch elektrotechnisch ersetzen. Eine weitere Kritik an der CFL ist die geringere Lebensdauer im Vergleich zu LED, die meist auf elektrodenbedingte Ausfallskriterien zurückzuführen ist.

Die vorliegende Arbeit befasst sich mit der Entwicklung einer quecksilberfreien, elektrodenlosen, mit Mikrowellen angeregten Niederdrucklampe mit molekularer Füllung, die die konventionellen Kompaktleuchtstofflampen ersetzen soll.

Der elektrodenlose Betrieb verhindert, dass die Füllmaterialien im Betrieb mit den metallischen Elektroden chemische Reaktionen eingehen und dadurch zur Korrosion der Elektroden führen. Dies ermöglicht somit eine Vielzahl neuer Leuchtkomponenten und Lampengeometrien.

Im Rahmen dieser Arbeit wurde die Leistung in die Lampe ohne Elektroden mittels Oberflächenwellen mit einer Frequenz von 2,45 GHz eingespeist. Ein geeigneter Mikrowellenkoppler für die Anregung und die Einkopplung der Oberflächenwellen in die Lampe wurde mit Hilfe von computergestützten Multiphysik-Simulationen entwickelt.

Die Auswahl einer umweltverträglichen und nicht gesundheitsschädlichen Leuchtkomponente als Ersatz für Quecksilber bildet die Basis dieser Arbeit. Im Hinblick auf spektrale, themodynamische und physikalische Eigenschaften des Quecksilber konnten Auswahlkriterien für Ersatzmaterialien aufgestellt werden. Indium(I)iodid hat sich als vielversprechendster Kandidat erwiesen.

Der Fokus dieser Arbeit liegt auf der Charakterisierung der Beziehung sowohl zwischen den Betriebsparametern der Lampe und der Plasmaeffizienz als auch zwischen den Plasmaparametern und der Plasmaeffizienz.

Zu diesem Zweck wurde ein Diagnoseverfahren entwickelt, das sowohl die räumlich aufgelöste Bestimmung der Linienemissionskoeffizienten der Lampe als auch die absolute Bestimmung der Plasmaeffizienz ohne goniometrische Messaufbauten ermöglicht.

Erstmals wurde in dieser Arbeit ein Modell für das Indium(I)iodid-Argon Niederdruckplasma entworfen, das sowohl atomare als auch molekulare Prozesse im Plasma berücksichtigt. Dabei liegt ein besonderes Augenmerk darauf, dass das Plasmamodell Linienemissionskoeffizienten für die relevanten Linien von Indium für ausgewählte Puffergasdruck-Coldspot Temperatur Paare vorkalkuliert. Dadurch bietet das Modell die Möglichkeit, die Messwerte zu interpretieren und dadurch die Plasmaparameter zu bestimmen.

Die im Rahmen dieser Arbeit erzielte Plasmaeffizienz ist kleiner als die von quecksilberhaltigen Plasmen. Dennoch gleichen kleinere Konversionsverluste in der Leuchtstoffbeschichtung und die lange Lebensdauer des elektrodenlosen Betriebs diesen Nachteil aus.

Zusammengefasst zeigt die vorliegende Dissertation das Potential von elektrodenlosen, quecksilberfreien Niederdruckplasmen sowohl für Allgemeinbeleuchtungs- als auch für Spezialbeleuchtungszwecke. Die

Forschungsergebnisse dieser Arbeit zeigen, dass ein effizienter Lampenbetrieb ohne Quecksilber und ohne Elektroden möglich ist, und eröffnen damit neue Wege für den Einsatz von Plasmastrahlungsquellen.

Abstract

Nowadays, compact fluorescent lamps (CFL) are widely-used in general lighting applications. However, they still struggle with acceptance problems due to the hazardous mercury, which serves as the radiant component inside the lamp. The removal of the mercury from the lamp presents a challenge, which still remains unsolved. The challenge lies in the selection of a suitable substitute for mercury, which has to fulfill certain radiometric and electrical requirements. Furthermore, most CFLs come under increased criticism due to their relatively short lifetime compared to LEDs, which can be mainly attributed to the failure of the electrodes.

The presented work deals with the development of a mercury-free, electrodeless, low pressure plasma based on a molecular filling and driven by microwaves, which may replace the conventional CFLs.

The electrodeless operation of the lamp prevents that the molecular filling reacts with the metallic electrodes during the operation, which may lead to the corrosion of the electrodes. Hence, the electrodeless operation offers a variety of new lamp geometries and allows the utilization of numerous new radiant components.

Within the framework of this work, the electrical power is applied to the lamp without electrodes via surface waves at the frequency of 2.45 GHz. An adequate microwave coupler, which is responsible for the excitation and coupling of the surface waves, was developed with the help of computer aided multi-physics simulations.

The selection of an environmentally friendly and nonhazardous radiant component as substitute of mercury forms the basis of this work. With regard to spectral, thermodynamic and physical properties of mercury, a set of selection criteria could be established. Indium(I)iodide proved itself as the most promising candidate.

The focus of this report is centered on the characterization of the relations between operating parameters of the lamp and plasma efficiency as well as between plasma parameters and plasma efficiency.

For this purpose, a novel diagnostic method was established, which allows the determination of spatially resolved line emission coefficients of the lamp as well as of the absolute plasma efficiency without any goniometric measurement setup.

For the first time, a plasma model, which considers both the atomic and the molecular processes inside the indium(I)iodide-argon plasma, was developed and presented. Special emphasis is placed on the estimation of the line emission coefficients of the relevant emission lines of the indium by the plasma model for given pairs of buffer gas pressure and cold spot temperature. Hence, the model allows the interpretation of the measurement data and subsequently the determination of the plasma parameters.

The highest plasma efficiency achieved in the presented work is lower than that of a common mercury-argon low pressure plasma. Nevertheless, this disadvantage may be partially counterbalanced by lower Stokes' losses in the fluorescent coating and the longer lifetime by electrodeless operation.

In summary, the presented dissertation demonstrates the potential of electrodeless, mercury-free low pressure plasmas both for general lighting and special lighting applications. The research findings of this work show that plasmas can be operated efficiently also without mercury and electrodes, and open up new paths for the utilization of discharge lamps.

Contents

Chapter 1

Introduction

Light sources are an inseparable part of modern world. Everyday life depends now on light sources, not only at home or in office for general lighting purposes, but also for special lighting applications in hospitals, industrial facilities, automotive headlights, displays etc. Thus, lighting represents about 19 % of global electric consumption (as of 2011) [1]. The biggest share belongs to the general lighting, which accounts for about 75 % of the global lighting market with its total revenue of € 52 billion (as of 2011) and is forecast to reach € 83 billion in 2020 [2]. In the last years, a decrease by 5 % can be observed in electric consumption for lighting in industrialized world, e.g., in the EU [3]. This can be explained with the rapid adoption of energy efficient light sources. The technology transition was surely fueled by the ban on inefficient incandescent lamps within EU [4].

Energy efficient light sources can be divided in two categories: Compact fluorescent lamps (CFL), linear fluorescent lamps (LFL) and high intensity discharges (HID) can be classified as traditional energy efficient light sources based on gas discharges, while light emitting diodes (LED) are based on solid-state technology [3]. As of 2011, the market share of traditional energy efficient light sources is > 50 % [2]. The market reports predict a fast increase of the market share of LED in the next decade due to its unexpectedly fast price erosion. Nonetheless, the CFL will have a

market volume of about 1.5 billion pieces annually due to new installation or replacements by 2020 [2].

Although CFLs were commercialized in the early 1980s [5], they are still suffering from acceptance problems [6]: The relatively low color rendering index compared to incandescent lamp and long warm-up time before achieving maximum luminous flux are important barriers for market penetration. However, the most important factor is undoubtedly the hazardous mercury, serving as the radiant component inside the LFLs and CFLs. The European commission already issued a directive about "Restriction of certain Hazardous Substances (RoHS)" to regulate the use of mercury in all electronic devices, whereas the amount of mercury inside CFLs is restricted with a gradually decreasing limit [7]. All CFLs have to be collected and disposed as special waste in the EU, which increases the indirect economic costs and carbon footprint. Therefore, a novel mercury-free low pressure discharge lamp can help to reduce the indirect costs and to overcome the association of CFLs with environmental and health problems.

The search for an environmentally friendly substitute for mercury has been continuing for the last decades. Numerous papers were published about suitable candidates [8–13] and also about the selection rules adopted in the search efforts [14]. The replacement of mercury has to feature certain radiometric and thermodynamic characteristics to meet requirements, which are essential for lighting and electronic technologies. The requirements comprise the following two aspects amongst others: First, the candidate species has to exhibit an emission spectrum with strong emission lines in UV and VIS. It is beneficial that the emission lines are located in the longer wavelength part of the UV, thus reducing the Stokes' losses in the phosphor coating. Secondly, temperature-vapor pressure characteristic of the candidate species should be similar to that of mercury to prevent excessive heat losses.

Molecular species are believed to be the most promising candidates and their investigation as mercury substitutes has been continuing for more than three decades [9]. However, the use of molecular components is a big technological transition, since all commercial low pressure lamps for general lighting employ atomic species as radiant component. Thus, a commercial product is not yet marketed.

Depending on the molecular species, the gas discharge may exhibit a pure molecular emission spectrum, atomic line emission spectrum or a composition of both. In this work, indium monoiodide (indium(I)iodide) is chosen and investigated as mercury substitute, which features strong atomic line emission as well as weak molecular radiation. Certainly, strong emission lines of atomic indium indicate a high dissociation rate of indium(I)iodide. However, in a gas discharge lamp with electrodes, halogen atoms react with the hot metallic electrodes, which results in their rapid corrosion [15]. Thus, the lamps should be operated without internal electrodes.

The electrodeless operation of light sources was first introduced by Tesla in 1891 [16], but it took 100 years to commercialize the electrodeless fluorescent lamp technology [17]. The inefficient, unreliable and expensive electronics were the limiting factor. With high-frequency, high-efficiency electronics based on solid-state technology, e.g., gallium nitride (GaN) power transistors, this limitation is widely removed.

The electrodeless operation offers several advantages: The failure mechanisms associated with electrodes, e.g., gas contamination and blackening of the lamp body due to electrode erosion are eliminated, which increases the lifetime of the lamp system significantly [15]. Additionally, the power loss associated with anode and cathode falls is eliminated.

In this work, the power coupling into the lamp is realized by means of guided microwaves, the so-called surface waves. In compliance with

regulations on RF-frequency and RF power emission, the excitation frequency of 2.45 GHz is chosen due to its worldwide availability as an industrial, scientific and medical (ISM) frequency band. The surface waves offer several advantages [18, 19]: Plasma columns produced by mono-mode surface waves are very stable and reproducible. No waveguide or resonant cavity is required, since the plasma column itself serves as the propagating medium for the surface waves. Thus, the generated radiation is not blocked by a resonant structure. Furthermore, the dimensions of the plasma are not limited by the wavelength of the chosen excitation frequency, as is the case with cavity-based microwave driven plasmas. Additionally, the electric field components outside of the discharge vessel are evanescent, which reduces electromagnetic interference (EMI). Finally, the structure responsible for the power coupling into the plasma, the so-called surface wave launcher "surfatron", is easy to manufacture and operates efficiently for a broad range of parameters, e.g., excitation frequency, gas pressure, lamp dimensions and input power.

The present work describes the research activities to develop an electrodeless, surface wave driven, mercury-free low pressure lamp filled with indium(I)iodide as radiant component and argon as buffer gas. Two important technological transitions, i.e., the use of a molecular filling in a low pressure lamp and the surface wave operation for lighting purposes, are realized at once. Thus, this work comprises every development step from designing an adequate wave launcher to characterization of mercury-free plasmas with regard to plasma efficiency. Individual steps are presented and discussed in detail.

This scientific research work is based on the selection of a promising candidate to replace mercury as radiant component in fluorescent lamp. Therefore, a set of selection criteria is established and applied to all elements on the periodic table. Indium(I)iodide proves to be the most-promising candidate and hence is chosen for further investigation.

A surfatron wave launcher, which allows mechanical impedance and frequency matching without an additional matching network, is designed for an optimum operation at 2.45 GHz and for cylindrical lamps with a diameter of 16 mm. With the new design, relatively high electric field strengths can be achieved inside of the coupling gap of the surfatron, thus allowing the ignition of the discharge inside the lamp without external support, e.g., a Tesla coil.

A diagnostic method based on spatially resolved optical emission spectroscopy (SROES) is developed for the characterization of plasma. The radiance of the lamp can be measured spatially and line emission coefficients can be derived from the measured data by means of inverse Abel transform [20]. The applicability of the developed method for surface wave driven plasmas is validated optically and electrically. The optical thinness of the plasma is verified by means of the escape factor concept.

However, the measurement results, as well as the data derived therefrom, do not deliver the desired plasma parameters, e.g., electron temperature and density, directly and must be interpreted. Thus, a collisional-radiative model (CRM) is developed for indium(I)iodide-argon plasma. Since low pressure plasmas do not exhibit thermal equilibrium, cross sections are required to describe the plasma processes. Therefore, cross sections are calculated for relevant processes including molecular processes, e.g., dissociation of neutral indium(I)iodide or direct-dissociative recombination of indium(I)iodide ion. Lifetimes of individual species due to free and ambipolar diffusions are also determined. Rate equations for each plasma process are set up and solved. The important plasma parameters, e.g., electron density, ion density and line emission coefficients are calculated as a function of electron temperature for different operating parameters, e.g., input power, buffer gas pressure and cold spot temperature.

By combining the diagnostic method and plasma model, or more precisely, by comparing the experimentally and theoretically obtained emission coefficients, plasma parameters can be determined for a broad range of operating configurations. Since the diagnostic method delivers the line emission coefficients spatially resolved, radiant flux of the lamp can be obtained without any goniometric setup. By evaluating the results, the dependency of plasma efficiency on plasma parameters and operating configurations can be identified.

Finally, the application of an adequate phosphor coating, as well as of necessary measures for heat management, is modeled to compile the overall energy balance of the investigated technology. In this way, the feasibility of electrodeless, surface wave driven, mercury-free low pressure plasmas based on indium(I)iodide-argon filling as a CFL is validated and opportunities for further improvements are discussed.

Chapter 2

Fundamentals
of plasma physics

In this chapter, the theoretical foundation of this work is given. Section 2.1 serves as an introduction into the plasma physics. After an overview about the high frequency discharges in section 2.2, the main focus will be extended to the surface waves and surface wave driven plasmas in section 2.3.

2.1 Ionized gases and plasmas

The main difference between an undisturbed gas at room temperature and an ionized gas is that the latter has the ability to interact with electric and magnetic fields. By increasing the temperature of the gas or by applying an electric field of sufficient strength to the gas, the kinetic energy of particles rises and heavy particles, e.g., atoms and molecules, may be ionized, creating free charge carriers. The same process can be realized with a strong irradiation of the gas. Thus, the ionized gas features electrical conductivity. Additionally, the Coulomb force allows long range interactions between the charged particles, which result in a

collective behavior resembling a fluid with a higher density than that of a neutral gas [21].

In this section, the physical basics of ionized gases on a microscopic and macroscopic level are explained. First, the individual particles in an ionized gas and the different types of interaction between these particles are explained. Secondly, the relation between microscopic and macroscopic processes is described with the help of equilibrium laws, which are valid if a thermodynamic equilibrium prevails between the particles. Furthermore, the deviation from thermodynamic equilibrium and its consequences are discussed. Thirdly, the transport processes inside an ionized gas and the associated terms such as collision frequency, mean free path and diffusion are presented. Finally, the plasma characteristics and the boundaries separating plasmas from other types of ionized gases are defined by introducing the most fundamental property of a plasma: *quasi-neutrality*, which is the tendency of the plasma to remain electrically neutral.

2.1.1 Particles

Before describing the interaction processes between the particles, the types of particles must be explained.

Photons and electrons

The first two kind of particles to be described here are photons and free electrons. Since they have no internal structure, they possess only kinetic

energy without limitations or quantification. The energy of a photon at a given wavelength λ can be calculated as

$$E_{\text{Photon}} = h\frac{c}{\lambda} = h\nu, \tag{2.1}$$

while the non-relativistic kinetic energy of an electron is given by

$$E_{\text{e}} = \frac{1}{2}m_{\text{e}}v^2, \tag{2.2}$$

where h is the Planck constant, c is the speed of light, ν is the frequency, v is the translational velocity and m_{e} is the electron mass.

Atoms

In contrast to electrons and photons, the heavy particles, e.g., the atoms exhibit an internal structure. They can exist in any of their energy states given by their internal structure in addition to their kinetic energy, with the exception of ions that are fully stripped of their electrons [22]. The internal structure of atoms was first explained by Bohr in 1913. According to Bohr [23], electrons move in a circular path of radius a around the nucleus of electric charge Ze, where Z is the number of charged particles and e is the elementary charge. For the stability of the structure, electrostatic attraction force must balance the centrifugal force.

$$\frac{Ze^2}{4\pi\varepsilon_0 a^2} = \frac{m_e v^2}{a}, \tag{2.3}$$

where ε_0 is the permittivity of vacuum. Since the angular momentum of electrons is quantized as a multiple of $\hbar = \frac{h}{2\pi}$, the quantized radii are $a_{n_{\text{p}}} = n_{\text{p}}^2 a_0$, where n_{p} is the principal quantum number and $a_0 = \frac{4\pi\varepsilon_0\hbar^2}{e^2 m_e} = 0.529 \cdot 10^{-10}$ m is the Bohr radius, which corresponds to

the lowest level $n_\mathrm{p} = 1$. The total energy of the bound electron consists of kinetic and potential energy:

$$E_{n_\mathrm{p}} = \frac{m_e v^2}{a} - \frac{Ze^2}{4\pi\varepsilon_0 a^2} = -\left(\frac{Z^2 e^2}{8\pi\varepsilon_0 a_0}\right)\frac{1}{n_\mathrm{p}^2}. \tag{2.4}$$

The lowest energy state $n_\mathrm{p} = 1$ corresponds to the ionization energy of hydrogen and is defined as the Rydberg constant $R_\mathrm{H} = 13.605$ eV.

The observed line spectra in absorption and emission of radiation by atoms can be explained with the quantized energy states. Thus, the frequency of the radiation due to the transition between two energy states n_p1 and n_p2 is calculated as

$$v_{n_\mathrm{p1} n_\mathrm{p2}} = \frac{Z^2 e^2}{8\pi\varepsilon_0 a_0 h}\left(\frac{1}{n_\mathrm{p1}^2} - \frac{1}{n_\mathrm{p2}^2}\right). \tag{2.5}$$

The Bohr model, which is adequate only for the hydrogen atom and hydrogen-like ions (from which all electrons have been stripped except one), can be extended by considering the quantum mechanics of energy states. They can be characterized in terms of four quantum numbers, i.e., participial quantum number n_p, orbital angular momentum number l, its component for a particular direction m_l and projection of electron spin m_s [23]. Every energy state can be addressed by the notation $n_\mathrm{p}^{2n_S+1} X_{n_J}$ [22, 23], where S, L and $J = L + S$ are the total spin angular momentum, the total orbital angular momentum and the total angular momentum with their corresponding numbers n_S, n_L and n_J, respectively. The capital letter X stands for different values of n_L, e.g., S for $n_L = 0$, P for $n_L = 1$ and D for $n_L = 2$. The superscript on the left hand side of X is the multiplicity. Thus, the ground energy state of indium with its electron configuration $[\mathrm{Kr}]4\mathrm{d}^{10}5\mathrm{s}^2 5\mathrm{p}^1$ can be addressed as $5^2 P_{1/2}$ and its first metastable state as $5^2 P_{3/2}$. The energy state diagram of indium is displayed in figure 2.1 with the energy states and radiative transitions, which are relevant for this work.
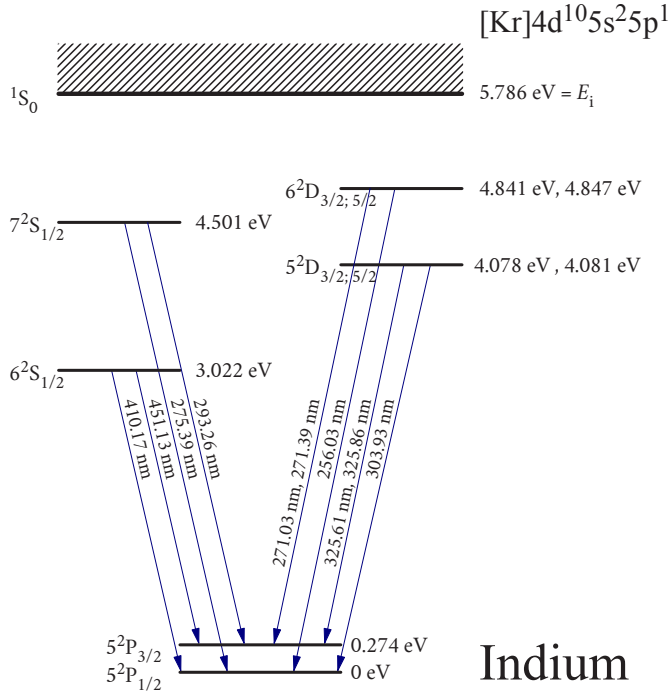
Figure 2.1: Energy state diagram of indium with the energy states relevant for this work. Needed data was taken from [24]. The hatched zone denotes the state of ionization, while the arrows correspond to spontaneous emission at the specified wavelength.

The statistical weight $g_{n_p l}$ of an energy state $n_p l$ is calculated with the total angular quantum number j_{taq} as $2j_{\text{taq}} + 1$, which gives the number of possible quantum states. Electrons have a statistical weight of $g_e = 2$, since they have two possible spin states.

For convenience, the following notation is adopted to describe the transition between energy states and to address their energies: The lowest energy state is called the ground state with the label g, while the excited states are labeled as k = 1, 2, 3 . . .. The label k is used to address a higher

state, while a lower state is identified with j. The transition energy between a neutral particle and an ion is called ionization energy E_i with the label i for the ionic state.

Molecules

In addition to their electron energy states, molecules have vibrational and rotational degrees of freedom due to the motion of the nuclei. Thus, the internal structure of a molecule is more complicated to describe than an atomic one. Since a diatomic molecule, viz., indium(I)iodide is an essential component of this work, the standardized notation of diatomic molecules is followed [25]. For a more detailed treatment of molecules and molecular physics, further reading of [23, 26–28] is recommended.

In analogy to atoms, the energy states of a molecule can be characterized by quantum numbers with the notation $^{2n_S+1}\Lambda^{(+,-)}_{\Omega_{\mathrm{mol}},(g/u)}$ [23]. The total orbital angular momentum Λ along the internuclear axis is identified with the symbol Σ, Π, Δ and Φ for total orbital angular momentum numbers $n_\Lambda = 0, \pm 1, \pm 2$ and ± 3, respectively. Prefixed superscript $2n_S + 1$ describes the multiplicity, while the superscript on the right hand side of Λ denotes whether the wave function is symmetric or antisymmetric along an arbitrary plane through the internuclear axis. Finally, the subscript Ω_{mol} is the projection of the total angular momentum along the internuclear axis and (g/u) gives the parity. Historically, the molecular ground state is labeled as X, the next excited state that is optically accessible from ground state, is labeled as A and then B etc. Thus, the electronic ground state of indium(I)iodide molecule is addressed as $X^1\Sigma_0^+$ and the next optically accessible excited state as $A^3\Pi_0$.

The most realistic model to describe a diatomic molecule is a rotating oscillator (or vibrating rotator), in which the rotation of a non-rigid ro-

tor and the vibration of an anharmonic oscillator take place simultaneously [26]. To increase the accuracy of the model, the interaction between rotor and oscillator must be also considered. Thus, the term value for the total energy of a molecule T^{mol} consists not only of the term value T^{el} of the electron state energy, but also of term values $G(v)$ and $F_v(J)$ for vibrational and rotational state energies, respectively:

$$T^{\text{mol}}(v, J) = \left(T^{\text{el}} + G(v) + F_v(J)\right) = \frac{E_{\text{el}} + E_{\text{vib}}(v) + E_{\text{rot}}(v, J)}{hc}, \quad (2.6)$$

where v is the vibrational and J is the rotational quantum number, E_{el}, $E_{\text{vib}}(v)$ and $E_{\text{rot}}(v, J)$ are the electrical, vibrational and rotational state energies, respectively.

According to Herzberg [25] and Haken [29], the rotational and vibrational term values can be calculated as

$$
\begin{aligned}
G(v) &= \omega_e \left(v + \frac{1}{2}\right) - \omega_e x_e \left(v + \frac{1}{2}\right)^2 + \ldots \\
F_v(J) &= B_v J(J + 1) - D_v J^2(J + 1)^2 + \ldots \\
B_v &= B_{\text{rc}} - \alpha_e \left(v + \frac{1}{2}\right) + \ldots \\
D_v &= D_{\text{dc}} + \beta_e \left(v + \frac{1}{2}\right) + \ldots
\end{aligned}
\quad (2.7)
$$

where B_{rc} and B_v are the rotational constant and its average over the vibrational motion, D_{dc} and D_v are the centrifugal distortion constant and its average over vibrational motion, ω_e is the harmonic wavenumber and x_e is the anharmonicity constant [23, 25]. α_e and β_e are correction factors for the interaction between rotor and oscillator [29]. B_{rc}, D_{dc}, ω_e, $\omega_e x_e$, α_e and β_e can be determined spectroscopically.

The potential of a molecular state depends on the instantaneous configuration of the nuclei, which can be given solely with the internuclear distance r in case of a diatomic molecule [22]. In order that a molecule is

stable, a potential minimum must exist at the so-called equilibrium inter-nuclear distance r_{eq}. For an internuclear distance $r < r_{eq}$, the molecular atoms experience a repulsive force due to the Coulomb potential, which results in a steeper rise of the potential [28]. In case of internuclear distances $r > r_{eq}$, the molecular atoms experience an attraction force, which diminishes with increasing distance and finally the molecule dissociates. At the distance $r \to \infty$, molecule potential approximates to the dissociation energy $E_{diss.}$. The potential of a molecule can be expressed with the well-known Morse approximation as

$$U\left(T^{el}, v, J, r\right) = hc \left[T^{el} + G(v) + \left(\frac{E_{diss.}}{hc} - G(v)\right) \left(1 - e^{-\beta_0(r - r_{eq})}\right)^2 \right.$$
$$\left. + \frac{h}{8\pi^2 c \mu_{12}} \frac{J(J+1)}{r^2} \right], \tag{2.8}$$

where $\beta_0 = \omega_{vib}\sqrt{\frac{\mu_{12}}{2E_{diss.}}}$ is a molecule specific quantity [30, 31], ω_{vib} is the vibrational angular frequency of the oscillator and $\mu_{12} = \frac{m_1 m_2}{m_1 + m_2}$ is the reduced mass of the molecule with atoms of types 1 and 2 [26, 30]. Figure 2.2 shows the potential curve of indium in neutral ground state and at first two ionic states calculated with equation (2.8).

2.1.2 Collisions in ionized gases

It is well known from the kinetic gas theory that gas particles collide with each other, resulting in a repartition of kinetic energy between different constitutive elements [32]. In contrast to a neutral gas, a number of collisions take place in an ionized gas, where the total kinetic energy of collision partners is not conserved. Furthermore, long range interactions due to the Coulomb force between charge carriers play an important role beside short range interactions due to van der Waals force between neutral particles. Thus, the term collision must be used in a broader sense than

an impact between rigid spheres resulting in the exchange of kinetic energy. A collision takes place if the momentum, velocity, path or internal state of a particle have been altered by the presence of one or many other particles in its vicinity [33]. For describing interactions between two particles, the notion of an *incident particle* as moving relative to a fixed *field particle* is used [34].
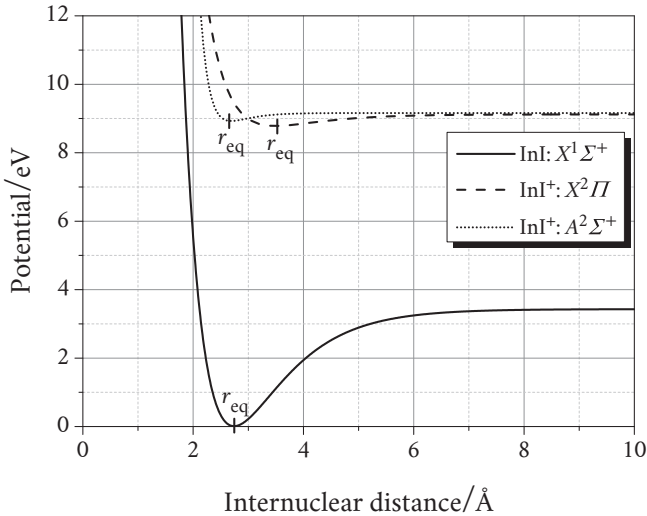
Figure 2.2: Potential curves of indium(I)iodide molecule in neutral ground state and the first two ionic states $A^2\Sigma^+$ and $X^2\Pi$ as a function of internuclear distance.

The collisions can be divided into two subcategories, i.e., elastic and inelastic collisions. A distinction must also be made for collisions between charge carriers, since the interaction between those is governed by the Coulomb force. Especially in highly or fully ionized gases, Coulomb collisions control the gas characteristics. The scattering of electrons by ions tune the resistivity of the gas, while collisions between electrons

are partially responsible for the electron diffusion rate [35]. Since this work deals with low pressure plasmas, where the electron-neutral particle collisions govern, the Coulomb collisions will not be explained here in detail.

Elastic collisions

Elastic collisions represent the classical meaning of collisions, where interaction results in a redistribution of kinetic energy and change of direction of motion, while the total kinetic energy and total initial momentum of collision partners are conserved [34]. The internal energies of collision partners do not change. Elastic collision is a reversible process, since the probability of losing or gaining energy due to a collision is equal for any given particle [33]. Elastic collisions occur, when the kinetic energy of the incident particle is lower than the threshold energy of its collision partner for excitation, ionization as well as dissociation in case of molecules. In low pressure ionized gases, most of the electron collisions are elastic [35].

The collisions between charge carriers. e.g., electron-electron, electron-ion and ion-ion collision, belong also to this group, if the energy of collision partners is too low for the emission and absorption of electromagnetic (EM) radiation [33].

Inelastic and super-elastic collisions

Inelastic collisions are characterized by the loss of total kinetic energy, while the internal energy or identities of the collision partners are altered. Additionally, super-elastic collisions, e.g., de-excitation of an

excited atoms, may occur, where the total kinetic energy of collision partners increases [22]. Some sources employ the term inelastic collisions more generally, when the sum of kinetic energy is not conserved after the collision. The absorption and emission of radiation may also be regarded as inelastic collision, since a photon can be described as a particle-like entity [34]. In order that an inelastic collision occurs, the kinetic energy of the incident particle must be higher than the threshold energy of its collision partner for this particular inelastic interaction. In case of an excitation or ionization, the amount of energy transferred from the incident particle to its collision partner is quantified [33].

A detailed list of inelastic processes can be found in [34]. The relevant inelastic collisions for this work are listed and explained below, where "$\underline{e}$" denotes a high energy electron, "A^*" denotes an excited atom, "A^+" an ion and "AB" a molecule:

- Excitation of a neutral atom
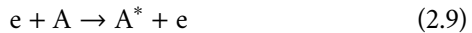
$$\underline{e} + A \rightarrow A^* + e \qquad (2.9)$$

- Collisional de-excitation

$$e + A^* \rightarrow A + \underline{e} \qquad (2.10)$$

- Ionization of a neutral atom

$$\underline{e} + A \rightarrow A^+ + 2e \qquad (2.11)$$

- Three-body recombination

$$e + A + A^+ \rightarrow 2A \qquad (2.12)$$
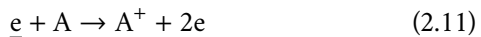
As can be seen in equation (2.12), a third body is needed for the recombination of an atomic ion to ensure the energy and momentum conservation [33]. For high electron densities, ionization can also take place step-wise, using already excited atoms as stepping stone. The step-wise

ionization is advantageous, since the necessary kinetic energy for each step is lower than for the direct ionization, allowing the electrons with low energies to participate in inelastic collisions. Step-wise ionization is also possible, if molecular species are present in the plasma. After dissociation of the molecule, the individual atoms of the former molecule can be excited or ionized, which may be more energy efficient than the direct ionization of the molecule.

- Dissociation of a neutral molecule

$$\underline{e} + AB \rightarrow A + B + e \qquad (2.13)$$

- Ionization of a neutral molecule

$$\underline{e} + AB \rightarrow AB^+ + 2e \qquad (2.14)$$
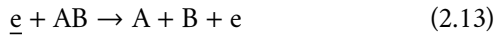
The recombination of an electron with a molecular ion may result in the dissociation of the molecule if the recombination energy is high enough to overcome the dissociation energy. This process is called the dissociative recombination.

- Dissociative recombination

$$e + AB^+ \rightarrow A + B \qquad (2.15)$$

- Photoexcitation or absorbtion

$$A + h\nu \rightarrow A^* \qquad (2.16)$$
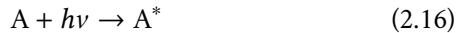
The absorption process given in equation (2.16) results in the removal of the incident photon and the energy of the photon is transferred to the field particle. It can be considered similar to the collisional excitation.

Thus, three body recombination can then be related to the induced emission, where a photon stimulates the excited field particle to emit a photon in the same direction with the same frequency [34]. However, an excited field particle can also emit a photon without external stimulation. It is called spontaneous emission, which cannot be related to any collisional process.

- Spontaneous emission

$$A^* \rightarrow A + h\nu \qquad (2.17)$$

An excited atom can return to a lower energy state or directly to its stable ground state by emitting a photon as electric dipole radiation, if the transition from the excited state into the lower state is allowed. Such a radiative transition is permitted, if the following rules are satisfied:

$$\Delta l = \pm 1,$$
$$\Delta n_S = 0, \pm 1 \quad \text{(if } n_S = 0 \rightarrow n_S = 0 \text{ forbidden);}$$

where l and n_S are the orbital angular and total angular momentum number, respectively [22].

In some cases, the selection rules are not satisfied and an optical transition between two states is not allowed for electrical dipole radiation. However, other means of radiative transitions, e.g., electric quadrupole or magnetic dipole radiation, or non-radiative transitions, e.g., collisional de-excitation may still be possible. But the probability of such transitions are small compared to electric dipole radiation and the lifetime of these excited states is some orders of magnitude longer than the lifetimes of the states that fulfill the selection rules. The energy states with long lifetimes are called metastable and the atoms in these excited states are called metastable atoms [22].

Cross sections

The probability of a microscopic process, e.g., elastic or inelastic collision in an ionized gas, can be given by a geometrical quantity, the cross section. The term cross section comes from the classical gas theory, where atoms are approximated as hard spheres to describe collisions between them [36]. Hence, the collision between two hard spheres with radii r_1 and r_2 can be described with their collective cross section $Q = \pi(r_1 + r_2)^2$ [36], which gives the effective geometrical blocking area of field particle to the incident particle [34]. In reality, a more complex system should be used to define the cross section, since this basic interpretation does not distinct between the different kinds of collisions and interaction forces. A general description of methods and formulas used to calculate the cross sections for different collision processes can be found in [34, 37]. Section 5.2 is dedicated to the presentation of the *Gryziński method*, which is employed for this work.

The radiative processes, e.g., absorption and emission, arising from transitions between two discrete energy states of an atom, can also be described with the corresponding cross section. The absorption cross section corresponding to an atomic transition from a lower energy state j into a higher excited state k is calculated as

$$Q_{j \to k} = \frac{e^2}{4\varepsilon_0 m_e c} f_{jk} \Psi(\nu), \tag{2.18}$$

where f_{jk} is the absorption oscillator strength for the transition from the state j into k, e is the elementary charge and Ψ is the absorption line profile as a function of frequency ν. The line profile defines the shape and the width of an absorption or emission line and is determined by the properties of the gas environment, which makes the line profile a macroscopic parameter [34]. However, an atomic quantity is needed to describe a microscopic process independent from macroscopic state of

the gas. Thus, the Einstein coefficient for absorption is introduced in equation (2.19) [34].

$$B_{jk} = \frac{e^2}{4\varepsilon_0 m_e c h \nu_{jk}} f_{jk}.$$

(2.19)

The Einstein coefficient for spontaneous emission is given by

$$A_{kj} = \frac{8\nu_{kj}^2 \pi^2 e^2}{m_e c^3} \frac{g_j}{g_k} f_{jk}.$$

(2.20)

Rate coefficient

While the cross section describes the microscopic properties of a process triggered by a mono-energetic incident particle colliding with a field particle, the rate of the collision is given by the rate coefficient K, which is a macroscopic quantity depending on the thermodynamic properties such as temperature and pressure [34]. Thus, the kinetics of particles in an ionized gas must be known to calculate the rate coefficients. The corresponding formula can be found in the next section together with the Maxwell velocity distribution, which relates microscopic processes with macroscopic properties.

2.1.3 Concept of thermodynamic equilibrium

Thermodynamic equilibrium (TE) denotes that each process is balanced with its reciprocal process [35]. Such processes are called inverse, since the initial state of the given process is the final state of its reciprocal process and vice versa. In the list of the collision processes given above, equations (2.9), (2.11), (2.14) and (2.16) denote generation processes,

while equations (2.10), (2.12), (2.15) and (2.17) are their respective counterpart loss processes, also known as secondary processes.

In TE, an ionized gas can be characterized by two important parameters, i.e., gas temperature T and particle density n [33]. The state of thermodynamic equilibrium is achieved, if the following four equilibrium laws are satisfied simultaneously.

The Maxwell-Boltzmann velocity distribution

The fundamental kinetics of a particle species in a partially ionized gas is given by its velocity distribution, which is essential to relate the underlying microscopic processes to the macroscopic properties of an ionized gas. The Maxwell-Boltzmann distribution determines the velocity distribution of free particles in thermodynamic equilibrium, which reads as

$$f(v) = 4\pi v^2 n \left(\frac{m}{2\pi k_\mathrm{B} T} \right)^{3/2} \exp\left(-\frac{mv^2}{2 k_\mathrm{B} T} \right), \tag{2.21}$$

where k_B is the Boltzmann constant and m is the mass of the particle [35]. The Maxwell distribution has its maximum at $v_{T\mathrm{max}} = \left(\frac{2 k_\mathrm{B} T}{m} \right)^{1/2}$, which is the most probable speed of the particles. The term $4\pi v^2$ in equation (2.21) describes the surface area of a sphere in three dimensional velocity space. Since the exponential part decreases more rapidly than the growth of the sphere surface area for $v > v_{T\mathrm{max}}$, the Maxwell distribution decays after $v_{T\mathrm{max}}$. The mean speed of Maxwellian particles can be calculated by the first moment of Maxwell velocity distribution as $\overline{v}_T = \left(\frac{8 k_\mathrm{B} T}{\pi m} \right)^{1/2}$, while the second moment gives the mean kinetic energy of particles as $\overline{E}_\mathrm{kin} = \frac{3}{2} k_\mathrm{B} T$ [35].

Most of the calculations in plasma physics are carried out with respect to the energy of the particles instead of their velocity. Thus, the Maxwell

distribution can be transformed with the help of the kinetic energy formula $E = \frac{1}{2}mv^2$ into energy scale [35]

$$f(E) = \frac{2}{\sqrt{\pi}} \frac{1}{(k_B T)^{3/2}} \sqrt{E} \exp\left(-\frac{E}{k_B T}\right). \qquad (2.22)$$

The characteristic temperature T of the Maxwell distribution can be converted into energy by $E = k_B T$. Hence, $T = 11604.5\,\text{K}$ corresponds to an equivalent temperature of $T_{eV} = \frac{k_B T}{e} = 1\,\text{eV}$. However, it should be kept in mind, that a gas with the equivalent temperature $T_{eV} = 1\,\text{eV}$ has a mean energy of 1.5 eV.

Finally, the rate coefficient K of a particular collision in an ionized gas, where the collision partners are following a Maxwell distribution with a characteristic temperature T, can be calculated by

$$K(T) = \int_0^\infty Q(E) \sqrt{\frac{2E}{m}} f(E, T)\, \mathrm{d}E. \qquad (2.23)$$

For an inelastic collision, the lower bound of the integral can be chosen as the threshold energy of the corresponding collision process, since the cross section of the inelastic collision below the threshold energy is zero.

The Boltzmann distribution

The population of heavy particles in a given higher excited energy state k can be calculated with respect to the particle density in a lower state n_j with the Boltzmann distribution by

$$\frac{n_k}{n_j} = \frac{g_k}{g_j} \exp\left(-\frac{E_k - E_j}{k_B T}\right). \qquad (2.24)$$

The exponential part of equation (2.24) is called as the Boltzmann factor and relates the portion of atoms that have overcome the energy difference of $E_k - E_j$ [33].

The Saha's equation

The Saha's equation describes the equilibrium between ionization as generation process and volume recombination as loss process, and allows the calculation of singly ionized ion density n_i respectively to the ground state density n_g as a function of temperature T with the assumption that all ions and atoms are in their corresponding ground states [33].

$$\frac{n_e n_i}{n_g} = \frac{2g_i}{g_g} \frac{(2\pi m_e k_B T)^{3/2}}{h^3} \exp\left(-\frac{E_i - E_g}{k_B T}\right). \tag{2.25}$$

The factor 2 is according to the spin states of electrons [35]. The Saha's equation applies to each particle species in the ionized gas independently [34].

The Planck's law

The three equilibrium laws explained above pertains only to matter. Likewise, the photons can also be in a thermodynamic equilibrium with matter. The Planck's law, also known as the law of black body radiation describes the spectral radiance $L_{\Omega,\lambda}$ of the electromagnetic radiation at the wavelength λ assuming a balance between absorption and emission [33].

$$L_{\Omega,\lambda} = \frac{2hc^2}{\lambda^5} \left[\exp\left(\frac{hc}{\lambda k_B T}\right) - 1\right]^{-1}. \tag{2.26}$$

2.1.4 Departure from thermodynamic equilibrium

In practical applications, the ionized gas deviates from a total thermo-dynamic equilibrium, since the balance between reciprocal processes is not perfect [33]. Thus, the number of parameters to describe all processes increases with the increasing number of non-reversible processes.

Local thermal equilibrium

If the ionized gas is inhomogeneous due to a density or temperature gra-dient, or if the gas is homogeneous but radiation is escaping the gas for certain wavelengths, then the ionized gas is not in a total thermodynamic equilibrium [33]. The radiation escape or the mentioned gradients cause a net energy flux, which indicates an incomplete equilibrium between reciprocal processes. However, as long as the energy change at a given point in gas is small with respect to the total energy at this point, the behavior of the ionized gas can be approximated with a local thermal equilibrium (LTE) [33]. In this system, the gas does not follow the Planck's law, but other equilibrium laws are locally valid. In other words, the matter particles are in equilibrium with themselves, but the radi-ation is not in equilibrium with matter [34]. In LTE, the collisional rates of population and depopulation processes of excited states must exceed the corresponding radiative rates [34]. In this case, the ionized gas can be characterized as a function of spatially resolved gas temper-ature $T(x, y, z)$ and density $n(x, y, z)$, where x, y and z are the spatial coordinates of the gas.

Non thermodynamic equilibrium

If the ionized gas is so thin, that the number of collisions between the electrons and heavy particles does not suffice to bring the ionized gas to an equilibrium, then the behavior of the gas cannot be described with equilibrium laws. The kinetic energy transfer from an electron to a heavy particle is very inefficient with the maximum factor of $4m_e/m_H$, where m_H is the mass of the heavy particle [33]. Without sufficient collisions, the temperatures of electrons and heavy particles differ significantly. Furthermore, the insufficient energy transfer between particles of same type causes a deviation from Maxwell distribution. In this case, the behavior of the particles cannot be predicted with a single characteristic temperature [33]. Additionally, the collision time between electrons and atoms for excitation and de-excitation processes exceeds the radiative lifetimes of the excited states. Thus, the radiative population and depopulation processes govern the density of excited states of atoms and ions, and the Boltzmann equation becomes invalid [33]. The case of an ionized gas, where not a single equilibrium law prevails, is defined to be in *non thermodynamic equilibrium* (NTE).

Two temperature plasma

The two temperature equilibrium is a special case between NTE and LTE. In this case, the electrons and heavy particles have different temperatures. However, the collision rate between particles of same type is sufficiently high that a thermal equilibrium is reached among same type particles. The Maxwell distribution can be applied to electrons with the characteristic electron temperature T_e, to atoms with the atom temperature T_g and to ions with the ion temperature T_i. The insufficient energy transfer from

electrons to heavy particles results in very high electron temperatures $T_e \gg T_g \approx T_i$ [33].

The principle of detailed balancing

The principle of detailed balancing is derived from thermodynamic equilibrium. It states that the differential reaction rates of each microscopic process and its inverse process are equal [34]. An example is presented in equation (2.27) for transitions between two atomic energy states j and k due to collisional excitation and de-excitation processes [37].

$$Q_{k \to j}(E + \Delta E) = \frac{g_j}{g_k} \frac{E}{E + \Delta E} Q_{j \to k}(E), \qquad (2.27)$$

where ΔE corresponds to the energy difference between the energy states j and k, and $g_{j,k}$ is the statistical weight of the corresponding state. Equation (2.27) shows that the principle of detailed balancing takes into account only microscopic quantities describing the changes between quantum states and the macroscopic characteristics of the gas are not included. Thus, thermodynamic equilibrium is not necessary to validate the principle of detailed balancing [34]. However, the electrons must follow a Maxwellian energy distribution [37].

The principle of detailed balancing also prevails for radiative processes. The Einstein coefficient B_{jk} for absorption of a photon by an atom resulting in a transition from the energy state j into k is already explained in section 2.1.2. The induced emission as well as the spontaneous emission contributes to the inverse process, i.e., de-excitation from the state k into j, with their corresponding Einstein coefficients B_{kj} and A_{kj}, respectively. Thus, the detailed balancing results in

$$g_k B_{kj} = g_j B_{jk}, \qquad (2.28)$$

and

$$\frac{A_{kj}}{B_{kj}} = \frac{8\pi h v_{kj}^3}{c^2}. \tag{2.29}$$

Also for radiative processes, the principle of detailed balancing is independent of thermodynamic conditions of the gas [34].

In contrast to the principle of detailed balancing, the *method* of detailed balancing describes the equilibrium between macroscopic rates, but with limited applicability, since the conditions of thermodynamic equilibrium must prevail for its validity [34]. The rates of three-body recombination process are calculated by applying the method of detailed balancing in section 5.4.

2.1.5 Transport processes

In a gas with a low degree of ionization, the motion of neutral particles is governed by density gradients, while the motion of charge carriers is determined by electric field forces. Both mechanisms are balanced by a friction force due to the elastic collisions, resulting in momentum transfer.

According to the Chapman-Enskog approximation [34], the average momentum transfer collision frequency, at which an incident particle of type 1 collides with a collision partner of type 2, can be given by equation (2.30).

$$\overline{v}_{12} = n_2 \overline{v}_{12} \overline{Q}_{12} = \int_0^\infty \left(\frac{\mu_{12} v^2/2}{3k_B T/2} \right) v_{12}(v) f_{12}(v) 4\pi v^2 dv, \tag{2.30}$$

where n_2 is the density of field particles, $\overline{Q}_{12}$ is the average momentum transfer cross section between particles of types 1 and 2, f_{12} is the

Maxwellian velocity distribution of a hypothetical particle with the reduced mass μ_{12} [34]. The collision partner is assumed motionless and the incident particle of type 1 has the the mean relative speed v_{12} with regard to the collision partner of type 2, assuming a Maxwellian velocity distribution for all particles. The motionless collision partners are called field particles [34].

If the gas consists of more than one species, then equation (2.30) should be extended for all types of field particles

$$\overline{v}_1 = \sum_s \overline{v}_{1s} = \sum_s n_s \overline{v}_{1s} \overline{Q}_{1s}, \tag{2.31}$$

which is called the total collision frequency for momentum transfer for particles of type 1.

The *mean free path* is the covered distance by the incident particle of type 1 between successive collisions and is calculated by equation (2.32) [34].

$$\lambda_{mfp} = \frac{\overline{C}_1}{\overline{v}_1} = \frac{1}{\sum_s (m_1/m_s)^{1/2} n_s \overline{Q}_{1s}}, \tag{2.32}$$

where $\overline{C}_1$ is the mean speed of incident particles with Maxwellian velocity distribution relative to the local mean mass velocity of the gas.

Mobility and electron heating

The mobility describes the response of charge carriers to an electric field E. They experience an acceleration due to the electric field, while elastic collisions inhibit their motion. Thus, the velocity of charged particles $v_{e,i}$ increases until the electric field force is balanced by the friction force due to the collisions.

$$m_{e,i} \frac{dv_{e,i}}{dt} = -eE - m_{e,i} \overline{v}_{e,i} v_{e,i}. \tag{2.33}$$

The velocity along the field in equilibrium state is called the drift velocity v_d and is given for electrons and ions by

$$v_{d,e,i} = -\frac{e}{m_{e,i}\overline{v}_{e,i}}\mathbf{E} = -\mu_{e,i}\mathbf{E}, \qquad (2.34)$$

with the mobility of electrons μ_e and mobility of ions μ_i

$$\mu_e = -\frac{e}{m_e\overline{v}_e} \quad ; \quad \mu_i = -\frac{e}{m_i\overline{v}_i}, \qquad (2.35)$$

where $\overline{v}_{e,i}$ is the total collision frequency for momentum transfer for electrons and ions, respectively.

The gain of kinetic energy per time by the electrons in an electric field between two consecutive collisions can be calculated as

$$\left.\frac{dE_{kin}}{dt}\right|_{gain} = -ev_{d,e}\mathbf{E} = \frac{e^2}{m_e\overline{v}_e}\mathbf{E}^2. \qquad (2.36)$$

The drastically unequal masses of electrons and heavy particles lead to a very small momentum transfer in the collision, but a redirection of electrons momentum. Assuming that the elastic collisions are isotropic, the ratio of average energy loss per collision to kinetic energy of electron is $\Delta E/E_{kin} = 2m_e/m_H$ [34, 35]. Thus, the loss of kinetic energy per time is given by equation (2.37).

$$\left.\frac{dE_{kin}}{dt}\right|_{loss} = \Delta E\,\overline{v}_e. \qquad (2.37)$$

By neglecting the less frequent inelastic collisions as an energy loss mechanism, the mean electron collision frequency can be approximated as $\overline{v}_e \approx \overline{v}_T/\lambda_{mfp}$. The electron temperature can then be calculated by balancing the gain and loss rates by

$$k_B T_e = e\lambda_{mfp}\left(\frac{M}{6m_e}\right)^{1/2}\mathbf{E}, \qquad (2.38)$$

with $\overline{E}_{kin} = \frac{3}{2}k_B T_e = \frac{1}{2}m_e \overline{v}_T^2$ [35]. Equation (2.38) shows that the electron thermal energy cannot be described as the energy gained in the electric field between two consecutive collisions. The collisions are only responsible for the loss of a small fraction of the electrons kinetic energy. Thus, the kinetic energy of the electron rises until an equilibrium is established between gain and loss rate. Thereby, the high electron temperatures in low pressure plasmas can be explained by the weak energy coupling between the electrons and heavy particles, or, in other words by the inefficient cooling mechanism [35].

Electrical conductivity

The drift velocity of charged particles results in an electric current, whose density can be calculated by equation (2.39) for electrons as well as ions.

$$j_e = -e n_e v_{d,e},$$
$$j_i = e n_i v_{d,i},$$
(2.39)

with the assumption that the ions are singly positive charged. The total current density is then given by

$$j = -j_e + j_i = e\left(n_i \mu_i + n_e \mu_e\right) E$$
$$= \left(\frac{n_e e^2}{m_e \overline{v}_e} + \frac{n_i e^2}{m_e \overline{v}_i}\right) E$$
$$= \left(\sigma_e + \sigma_i\right) E.$$
(2.40)

The relation between the current density and the electric field is called the total conductivity $\sigma = \sigma_e + \sigma_i$, where σ_e and σ_i are the electrical conductivity of electrons and ions, respectively.

Free diffusion

Diffusion stems either from a gradient in particle density or a gradient of the particles kinetic energy, which is also known as heat transfer [33]. In a low pressure ionized gas, the energy is transferred from an electric field directly to the electrons. Due to the inefficient momentum exchange between electrons and heavy particles, the temperature of the latter remains low. Thus, a strong gradient of kinetic energy inside the ionized gas does not occur for heavy particles. Hence, the temperature gradient can be neglected and free diffusion results from a gradient of particle density. Collisions between particles are random and isotropic, which result in an equal probability for scattering in all directions [33]. If the density of particles is higher at one point than at a second point, then the flux of scattered particles from the first point to the second point is higher than vice versa due to equipartition of collisions at each point [33]. The net flux from first point to the second can be calculated by

$$\Gamma_{\mathrm{H}} = -D_{\mathrm{free}}\nabla n_{\mathrm{H}}, \tag{2.41}$$

where n_{H} is the density of heavy particles and D_{free} is the free diffusion coefficient, which describes the combination of thermal motion with the friction force due to the elastic collisions with neutral particles.

Ambipolar diffusion

The charge carriers, i.e., electrons and ions are also driven by their thermal motion in the direction of density gradient but blocked by collisions with the background gas atoms. Since the electrons are smaller, they feature a higher mobility. Thus, the diffusion of electrons and ions results in different particle fluxes, which cause unequal densities of positive and

negative charges. This inequality leads to the formation of a space charge electric field E, which decelerates the electrons, while accelerating the ions until the particle fluxes of electrons and ions reach an equilibrium. The equilibrium flux of diffusion of electrons and ions is called the ambipolar diffusion.

The particle fluxes for the diffusion of electrons Γ_e and ions Γ_i are given by

$$\Gamma_{e,i} = \pm n_{e,i}\mu_{e,i}E - D_{e,i}\nabla n_{e,i}, \tag{2.42}$$

where $D_{e,i}$ are the diffusion coefficient and $n_{e,i}$ are the density of electrons and ions, respectively [35].

Assuming that $n \equiv n_e \approx n_i$, and the electron and ion fluxes are balanced to the ambipolar diffusion $\Gamma_a = -D_a\frac{dn}{dx}$ [35], the ambipolar diffusion coefficient can be determined as

$$D_a = \frac{D_e\mu_i + D_i\mu_e}{\mu_e + \mu_i}. \tag{2.43}$$

Einstein introduced a relation to illuminate the dependency of the diffusion coefficient and the mobility from the kinetic energy of the charge carrier [35], which is given by

$$\frac{D_{e,i}}{\mu_{e,i}} = \frac{k_B T_{e,i}}{e}. \tag{2.44}$$

2.1.6 Plasma characteristics

In the sections above, the individual behavior of particles in an ionized gas is explained in detail. In this section, the macroscopic behavior of charged and neutral particles as an ensemble is discussed, since the plasma is characterized by its collective behavior. In a neutral gas, the

particles interact only in the case of near field collisions, since the van der Waals force between neutral particles weakens with the 6. order of inter-atomic distance as $1/r^6$. In contrast to a neutral gas, the Coulomb force should be considered to describe the electrostatic interaction of charged particles in a plasma, which weakens with the square of the interatomic distance as $1/r^2$ [35]. Thereby, the interaction between the particles is stronger, which results in a collective response to external interferences. This response can be described with two important parameters: the Debye length and the plasma frequency.

Debye shielding and Debye length

A partially ionized gas has the strong tendency to electrical neutrality. This behavior can be explained with very large electrostatic forces, which would arise even in case of small spatial non-uniformities of positive and negative charges in a macroscopic volume. Since such large potentials could not be sustained without external support, the charged particles arrange themselves to reduce the potential differences [34].

Following an electrical perturbation in the plasma, the electrons and ions move themselves in such a way that the electric potential around the charge Ze of the perturbator weakens. Thus, its influence is limited. The attenuation of the electrical potential is given by

$$\phi_{\mathrm{D}}(r) = \frac{Ze}{4\pi\varepsilon_r\varepsilon_0 r}\exp\left(-\frac{r}{\lambda_{\mathrm{D}}}\right), \qquad (2.45)$$

where ϕ_{D} is the Debye-Hückel potential and ε_r is the relative permittivity of medium.

Debye shielding is characterized by its length $\lambda_D = \left(\frac{1}{\lambda_{De}^2} + \frac{1}{\lambda_{Di}^2} \right)^{-1/2}$, combining the contribution of electrons

$$\lambda_{De} = \left(\frac{\varepsilon_0 k_B T_e}{n_e e^2} \right)^{1/2}, \tag{2.46}$$

and ions

$$\lambda_{Di} = \left(\frac{\varepsilon_0 k_B T_i}{n_i e^2} \right)^{1/2}. \tag{2.47}$$

Equations (2.46) and (2.47) show that the shielding length is determined by the equilibrium between thermal and electrostatic energy [36]. Shielding is more efficient with increasing density of charge carriers, while the increased temperature scales the perturbed volume up. In NTE plasmas, T_e is much larger than T_i, thus the shielding effect can be approximated by λ_{Di}. Since the Debye potential decreases faster than the Coulomb potential, the Debye length sets the limits for electrons and ions acting as a plasma. Plasmas with dimensions larger than the Debye length tends to become quasi-neutral, if any deviation from equal densities between electrons and ions arises.

Response time and plasma frequency

The collective response of electrons and ions to an electrical perturbation is already explained above. Since the ions are more massive than the electrons, it takes less time for electrons to reach their new positions to establish an electrostatic equilibrium at a typical distance of λ_{De}. If the perturbating potential ϕ is small as $|e\phi| \ll k_B T$, the electrons do not gain much kinetic energy in the potential well and their velocity v_e remains nearly the same.

The needed time for electrons to reach λ_{De} is called as the response time and is calculated by

$$\tau_{pe} = \frac{\lambda_{De}}{v_e}. \tag{2.48}$$

However, the electrons cannot stop instantly at their equilibrium positions but continue their motion with v_e. This inertia results in a new departure from electrostatic neutrality in the opposite direction to the initial perturbation field, assuming that their motion is not disrupted by collisions [33]. Therefore, the electrons oscillate with an angular frequency given by

$$\omega_{pe} = \frac{1}{\tau_{pe}} = \left(\frac{n_e e^2}{\varepsilon_0 m_e} \right)^{1/2}, \tag{2.49}$$

where ω_{pe} is the angular electron plasma frequency [35]. The electron plasma frequency is easily calculated by $f_{pe} = \frac{\omega_{pe}}{2\pi}$. During the collective oscillatory motion of electrons, the ions can be assumed as immobile, as their response to fast changing electric fields is very slow.

Quasi-neutrality

A plasma is not a neutral ensemble of ions and electrons, since deviations from neutrality can occur microscopically. The Debye length sets the boundary between the microscopic and macroscopic scales. In a plasma, the variation of electric potential along the distance l can be approximated by means of Poisson's equation as

$$\nabla^2 \phi \sim \frac{\phi}{l^2} \sim \left| \frac{e}{\varepsilon_0} \left(Z n_i - n_e \right) \right|. \tag{2.50}$$

With the assumption that $\phi \leq T_e$ and deriving from the definition of Debye length $T_e = \frac{en_e\lambda_{De}^2}{\varepsilon_0}$, equation (2.50) becomes

$$\frac{|Zn_i - n_e|}{n_e} \leq \frac{\lambda_{De}^2}{l^2}. \tag{2.51}$$

As mentioned above, the plasma length must be much longer than λ_{De}. Thus, equation (2.51) can be simplified with $\lambda_{De}^2/l^2 \ll 1$ to

$$|Zn_i - n_e| \ll n_e,$$
$$\text{or} \tag{2.52}$$
$$Zn_i \approx n_e.$$

Equation (2.52) states that the density of electrons is approximately equal to the density of positive ions for plasma dimensions larger than λ_{De} and defines a fundamental property of the plasma: the quasi-neutrality. Equation (2.52) can be extended also for the negative ions without violating the quasi-neutrality.

Conditions for the plasma state

The boundary between an ionized gas and the special case of plasma is defined by the conditions, which can be summarized as follows:

- The smallest dimension of the plasma volume should be much larger than λ_D (Langmuir condition).

- The number of charge carriers in a Debye sphere ($\frac{4}{3}\pi\lambda_D^3$) should be much larger than 1.

- Quasi-neutrality can only be violated within the Debye sphere.

- The lifetime of the plasma must be longer than $1/\omega_{pe}$.

2.2 High frequency discharges

If a harmonic electromagnetic field, whose components are sinusoidal functions of time t, is applied to a plasma, its electric properties also become sinusoidal functions. The electric field component can be described as $\mathbf{E} = \mathbf{E}_0 \exp(j\omega t)$, while the magnetic one is given as $\mathbf{H} = \mathbf{H}_0 \exp(j\omega t)$, where $\mathbf{E}_0$ and $\mathbf{H}_0$ are the maximum amplitudes of the electric and magnetic fields in the course of a period of oscillation, respectively, and ω is the angular excitation frequency. The nomenclature used for plasma parameters does not differ for a high frequency or DC excitation. The plasma permeability is assumed as equal to the vacuum permeability μ_0.

2.2.1 Influence of the frequency on plasma properties

In this section, the influence of an alternating electric field on the plasma properties is explained with the help of the *free charges in space description* [38]. Since the ions have a large mass, they remain unaffected for frequencies $f > 1\,\mathrm{MHz}$ [33]. Thus, the plasma response to the electric field is governed by the drift velocity of electrons [38].

The steady state solution of the differential equation (2.33) becomes a sinusoidal function of time

$$v_{d,e} = -\frac{e\mathbf{E}}{m_e} \frac{1}{\overline{v}_e + j\omega}.\tag{2.53}$$

Consequently, all plasma properties related to drift velocity feature both a real and an imaginary part.

Mean power

The mean power θ_A, transferred from the electric field to the electron, can be calculated by equation (2.54).

$$\theta_A = -e\overline{\mathbf{E}(t) \cdot v_e(t)} = \frac{e^2}{m_e} \cdot \frac{\overline{v}_e}{\overline{v}_e^2 + \omega^2} \mathbf{E}_{\text{rms}}^2, \qquad (2.54)$$

where $v_e(t)$ is the time dependent electron velocity and $\mathbf{E}_{\text{rms}} = \sqrt{\mathbf{E}_0^2/2}$ is the root mean square of the total electric field strength. In the high frequency electric field, the electrons are accelerated for the first half period in a given direction and in the second half period in the reverse direction. Thus, the mean effective work, undertaken by an electron is zero [33]. As a result, there is no average power transfer from electric field to the electrons in case of a collisionless plasma. However, if collisions take place in plasma, the periodic motions of electrons are interrupted. The random energy of electrons increases until the gained energy is dissipated in collisions. Thus, the energy is transferred from field to electron and subsequently from electrons to heavy particles.

In accordance with equation (2.54), the amplitude of the electric field must be increased with increasing excitation frequency to maintain a constant power transfer to electrons. For constant input power and electron density, the gained energy per electron decreases with increasing operating frequency [36]. Furthermore, for low pressures plasmas with small $\overline{v}_e$, electric field intensity must be increased with frequency to maintain the discharge, otherwise the discharge extinguishes. Hence, at frequencies in microwave range, the pressure should exceed 1 mbar for practical applications [36].

Electrical conductivity

The complex electrical conductivity is given by

$$\sigma = \frac{n_e e^2}{m_e \left(\overline{v}_e + j\omega\right)} = \sigma_0 \frac{\left(\frac{\overline{v}_e}{\omega}\right)^2 - j\frac{\overline{v}_e}{\omega}}{1 + \left(\frac{\overline{v}_e}{\omega}\right)^2}, \qquad (2.55)$$

where σ_0 is the DC electrical conductivity [39]. At one extreme with $\overline{v}_e \gg \omega$, the electrical conductivity approximates the DC value. The electric current density j_e is in phase with the electric field $\mathbf{E}$. However, at the other extreme with $\overline{v}_e \ll \omega$, there is a phase displacement of 90 between j_e and $\mathbf{E}$. Thus, the conductivity becomes imaginary and the displacement corresponds to that of an inductor, resulting in an inductive plasma behavior. Figure 2.3 displays the normalized real and imaginary parts of the electrical conductivity as well as the phase angle of a plasma excited with a high frequency field as a function of the ratio between $\overline{v}_e$ and ω.

Plasma permittivity and plasma impedance

The permittivity of an unmagnetized plasma can be calculated by equation (2.56) [39]. The real part of the complex permittivity describes the reactive behavior of plasma, while the imaginary part gives the resistive behavior.

Thus, the storage and dissipation of energy inside the plasma can be expressed with the help of the permittivity [38].

$$\varepsilon_p = 1 - \frac{\left(\frac{\omega_{pe}}{\omega}\right)^2}{1 + \left(\frac{\overline{v}_e}{\omega}\right)^2} - j\frac{\overline{v}_e}{\omega} \frac{\left(\frac{\omega_{pe}}{\omega}\right)^2}{1 + \left(\frac{\overline{v}_e}{\omega}\right)^2}. \qquad (2.56)$$

In the absence of collisions with $\bar{\nu}_e \approx 0$, the plasma permittivity is real and the plasma behaves like a lossless medium [38]. With increasing electron density n_e, which subsequently results in an increase of plasma electron frequency ω_{pe}, the capacitive component of vacuum and the inductive component of plasma approach each other. For $\omega_{pe} = \omega$ and $\bar{\nu}_e \ll \omega$, the plasma permittivity becomes zero.
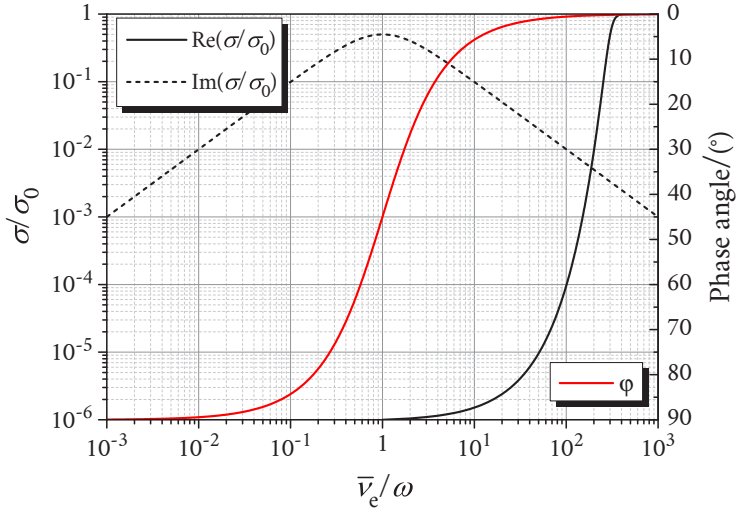
Figure 2.3: Real and imaginary parts of the electrical conductivity, and the phase shift of a plasma excited with a high frequency electric field as a function of the ratio between $\bar{\nu}_e$ and ω.

This configuration is called the *plasma cutoff*, at which the waves are unable to propagate. It can be related to the total reflection in the high frequency engineering [39]. The electron density, at which the plasma cutoff is reached, is called the critical electron density $n_{ec} = \frac{\varepsilon_0 m_e \omega^2}{e^2}$. For electron densities $n > n_{ec}$, ω_{pe} exceeds the angular excitation frequency, which results in a negative permittivity and causes an aperiodic attenu-

ation of waves in plasma. In presence of collision, there are no sharp boundaries for plasma cutoff, but it still exists.

The complex plasma impedance Z_p is given by the ratio of the electric field to the magnetic field at a transversal wave.

$$Z_p = \frac{E}{H} = \sqrt{\frac{\mu_0}{\varepsilon_p \varepsilon_0}} \approx \frac{377\,\Omega}{\sqrt{\varepsilon_p}}, \tag{2.57}$$

where $377\,\Omega$ is the vacuum impedance. Z_p is important to achieve the best possible impedance matching when launching the high frequency power into the plasma. At the plasma cutoff, Z_p becomes infinity, while Z_p is within $0 < Z_p < 377\,\Omega$ for $\omega_{pe} > \omega$ [39].

Propagation constant and penetration depth

The propagation of an electromagnetic wave in a given direction z may be described with the propagation coefficient $\gamma = \alpha + j\beta$, where the phase factor of the the wave is given by $\exp(j\omega t - \gamma z)$. α and β are the attenuation and phase coefficients, respectively [39]. γ can be calculated by

$$\gamma = j\frac{\omega}{c}\sqrt{\varepsilon_p}, \tag{2.58}$$

while the wavelength of electromagnetic waves in plasma is given by $\lambda = \frac{2\pi}{\beta}$.

In a high frequency plasma, the radial distribution of the electric field strength is not constant, as it is for DC operation. It decreases from the surface of the discharge vessel to the axis. This decrease can be explained analogously with the skin effect in high frequency engineering. The characteristic penetration depth $\delta_c = \frac{(c/\omega)}{\mathrm{Re}(-\sqrt{\varepsilon_p})} = \frac{1}{\alpha}$ of a high frequency field inside a plasma is the radial distance from the surface of the discharge

vessel, at which the field strength reduces to $1/e_{\text{Eu}}$ of its initial value [33], where e_{Eu} is the Euler's number. The power transfer from the field to the electrons takes place in the so-called skin sheath with a thickness equal to the penetration depth [40].

Electron energy distribution function

As mentioned above, in low pressure high frequency plasmas, the electrons are primarily responsible for generation and loss processes. Thus, particle densities inside the plasma depend strongly on the form of the electron energy distribution function (EEDF), which can be controlled by means of the excitation frequency. The application of a high frequency field to the plasma may result in a stationary or non-stationary EEDF [33]. The latter occurs, if the frequency of elastic and inelastic collisions is that high, that the energy transfer from the electric field to the electrons and subsequently to the heavy particles takes place at each instant of the HF period. Therefore, the EEDF varies with the momentary value of the field strength as a function of time. By increasing excitation frequency, the EEDF becomes more stationary. For low pressure plasmas, the boundary for the stationary EEDF can be set as $\omega > 100\,\text{MHz}$ [33].

The collision frequency in equation (2.54) is calculated by equations (2.30) and (2.31) assuming a Maxwellian EEDF. If the electron-electron collision rate is too small to bring electrons to a thermal equilibrium, the excitation frequency shapes the non-Maxwellian EEDF. Two limiting cases are the microwave (MW) regime with $\overline{\nu}_{\text{e}}/\omega \approx 0$ and the DC regime with $\overline{\nu}_{\text{e}}/\omega \approx \infty$. At constant electron density, the plasma in DC regime exhibits a higher excited particle density as well as a higher average electron energy than both in Maxwellian and in MW regime [33]. However, from a more practical perspective, the regimes should be compared at

constant absorbed power $P_A = n_e \theta_A$. The smallest θ_A, thereby the highest n_e is achieved with a Maxwellian distribution for high pR, where p and R are the gas pressure and radius of the plasma, respectively. For low pR, the MW regime is beneficial [33]. The threshold for low and high pR depends on the type of the ionized gas and corresponds to $pR = 0.13 \, \text{Pa·m}$ for argon [33]. With increasing electron density, both regimes approach Maxwellian distribution and EEDF becomes independent of ω for $n_e/n_H > 10^{-4}$ [33], where n_H is the heavy particle density. Nevertheless, the microwave operation presents a superior possibility than any other operation mode to reach high electron densities in a low pressure plasma, where the thermal equilibrium is in most cases not complete.

In summary, the EEDF of the discharge is a function of the so-called operating conditions, i.e., dimensions of discharge vessel, pressure and type of the ionized gas, as well as the excitation frequency. The input power density has an indirect effect on the EEDF. The increase of electron density at higher powers leads to a higher electron-electron collision rate, which results in a more Maxwellian distribution. Furthermore, the stepwise processes become more common, resulting in a higher ionization rate and in a reduced average energy of electrons [33].

2.2.2 Types of HF-discharges

The HF-discharges can be categorized depending on their discharge configurations, e.g., mechanical structure of the employed field applicator, electromagnetic field distribution, geometrical dimensions, temporal behavior or thermal and pressure attributes [41]. In this work, the classification proposed by Moisan [38] is adopted, which considers, how the electromagnetic field is applied to the plasma. In this way, all RF

and microwave discharges can be sorted into two categories: *discharges with a localized active zone* and *traveling-wave discharges*. The discharges sustained within HF circuits, where the phase difference of the field oscillation between any two points in the plasma is negligible, belong to the first category. The term "localized" is used, since the discharge occurs within the corresponding field applicator. The second category consists of discharges, where the electromagnetic waves propagate along the plasma, which they sustain at the same time. This dualism results in a spatially extended plasma, whose dimensions are larger than the wavelength of the excitation field, with a non-negligible phase difference between two points inside the discharge. There are two groups of traveling wave discharges: For the first group, a wave guiding structure along the plasma column is necessary for the wave propagation. In the second group, the waves are excited at the so-called wave launcher, which encloses only a small part of the discharge vessel. The waves propagate on the interface between the plasma and the dielectric discharge vessel. Such discharges are called "surface wave discharges". The main advantage of plasma sources driven by surface waves is that the length of the plasma column is limited only by practical applicability, e.g., power handling capability of the wave launcher [38].

The most widely used types of discharges of the first category are summarized below shortly. Since the surface wave plasmas are an essential part of this work, they are described in section 2.3 in detail.

Capacitively Coupled Plasma (CCP)

The simplest method to realize a CCP is to generate the plasma between two conductive plates, building a capacitor. The plasma may be separated from the plates with a dielectric discharge vessel and the CCP is then

considered as electrodeless. There are two modes of CCP: the α-mode with lower currents and positive voltage-current characteristic, and the γ-mode with higher currents and partially negative voltage-current characteristic [40]. The notation α and γ originates from the Townsend's ionization coefficients [40], which describe the volume electron impact ionization rate and secondary ionization rate from the electrodes [41].

Inductively Coupled Plasma (ICP)

If an alternating magnetic field is applied to the ionized gas with the help of a current carrying coil, the induced electric field accelerates the free charge carriers, thus sustaining the discharge. ICP features two modes of operation: **E-** and **H-**mode. In the starting phase or at low operating powers, a capacitively coupled **E-**mode occurs between the adjacent turns of the coil, until the induced azimuthal electric field is sufficiently strong to sustain a steady state discharge and the discharge enters into the **H-**mode [41, 42]. Higher particle densities and stronger radiation are reached with the latter. The ICP can simply be modeled as a transformer, where the inductive coupling is given by an N-turn primary winding, while a single loop secondary winding and in series connected plasma impedance Z_p correspond to the plasma with its resistive and inductive components [42, 43].

ICPs can be divided into three geometric categories [44]: re-entrant cavity, external coil and toroidal geometry. The first one is realized by inserting an insulated coil wound around a ferrite core inside the re-entrant cavity of the discharge vessel. The ferrite core magnifies the magnetic flux, which results in a more efficient coupling [44]. In the second method, coils are wound directly around the discharge vessel. Although this method is easier to realize, the external coils block a part

of the generated radiation. The final method is based on the so-called ring discharge, where the ring shaped discharge vessel penetrates a coil wound ferrite core, resulting in a closed magnetic path.

Plasmas with crossed electric and magnetic fields

It is also possible to apply crossed magnetic and electric fields to an ionized gas to enhance the particle densities in the plasma [41]. Most important types of crossed field discharges are electron cyclotron resonance plasmas (ECR), helicon sources and helical resonator sources [41]: The ECR is based on the superimposition of an electric field at microwave frequencies with a DC magnetic field, where the electrons rotate in the magnetic field with the electron cyclotron frequency. When the cyclotron motion is in resonance with the microwave field, then the power absorption is maximized [40]. For a microwave excitation frequency of $\omega = 2.45\,\text{GHz}$, a magnetic field of $B = \frac{\omega m_e}{e} = 0.0875\,\text{T}$ is necessary [40, 41]. A helicon source consists of an RF-powered antenna surrounded by a magnet coil. A lower magnetic field (between 0.002 and 0.02 T [41]) and an RF-generator working at lower frequencies, e.g., 13.56 MHz, are needed, which make the helicon source a cheaper alternative to ECR. A current carrying coil, wound around the discharge vessel and enclosed by a grounded conducting cylinder forms the helical resonator source, which uses an AC magnetic field in the frequency range between 3 and 30 MHz [41].

Microwave discharges

HF-discharges, excited in the frequency range between 300 MHz and 10 GHz are described as microwave discharges. The greatest disadvantage of the microwave discharges is that the wavelength of the electromagnetic field should be in the same order of magnitude as the exciting structure and discharge vessel [41]. The excitation frequency of $f = 2.45$ GHz corresponds to a wavelength of 12.24 cm. Yet, high electric field strengths can be achieved with microwave reactors. According to equation (2.54), a high pressure plasma with high collision frequency can only be maintained with a strong electric field, what makes microwave discharges suitable for high pressure applications [40]. Different mechanisms, e.g., resonant cavity plasma (RCP) and antenna excited microwave discharge (AEMD), can be adopted for the coupling of the field [41]. The RCP is a closed structure, where a standing wave inside a cavity drives the discharge. The cavity length defines the corresponding resonant frequency. The AEMD consists of a coaxial feed connected to a monopole antenna, which is enclosed by a hollow glass body filled with high pressure gas [45]. A small gap between the two separated parts of the antenna excites strong electric fields, which may serve as a spot light source.

2.3 Surface wave driven plasmas

Electromagnetic waves can be divided into two categories, i.e., bulk waves and surface waves. The bulk waves propagate in all directions, while surface waves propagate bound to the interface between two media, even when the interface is not straightforward [46]. Barlow and Brown [47] defined the surface waves as:

"A surface wave is one that propagates along an interface between two different media without radiation; such radiation being construed to mean energy, converted from the surface wave field to some other form."

Thus, the major part of energy is carried within a small interval around the interface, which is why this type of waves are called the surface waves [46].

The surface waves may appear in three different forms [48]: The first form is the Zenneck wave, which is an inhomogeneous plane wave supported by a flat surface. Second form is the radial version of the Zenneck wave, which is an inhomogeneous radial cylindrical wave supported by a flat surface. The third form is the Sommerfeld-Goubau wave, which is an axial cylindrical wave with a supporting surface of circular profile in the transverse plane. The latter one is the most important type from the point of view of applications, e.g., dielectric coated wires and gas discharges inside a cylindrical glass body. It was presented by Sommerfeld [49] that the electromagnetic waves can propagate as surface waves in azimuthally symmetric mode along a conductive wire surrounded by a dielectric environment, which can be theoretically described with three field components, i.e., E_r, E_z and H_θ, where r, θ and z stand for cylindrical coordinates radial distance, azimuth and axial coordinate in the direction of propagation, respectively. Later, Goubau [50] demonstrated the practical applicability of the surface waves. Since the field component may extend a significant distance outside of conductive medium, it is not practical to adopt surface waves for excitation frequencies $f < 3\,\text{GHz}$ [50]. A method to confine the field components as much as possible to the conductive medium is the encasement of the conductor with a thin layer of dielectric, which has a higher permittivity than the surrounding environment [51]. The surface waves with evanescent fields on both sides of the interface are called pure surface waves of the electron type, which is excited without an external magnetic field [46]. Since both axial compo-

nents **E** and **H** are present, the surface waves are hybrid, thus pure surface waves allow only one propagation mode for a given azimuthal mode [46].

It should be kept in mind that the excitation of surface waves is inevitably associated with the co-excitation of bulk waves by the source. The source can be designed in such a way that the energy of bulk waves is negligible small compared to the energy of the surface waves. But it is still required in order to fulfill the continuity of the total field around the source [52].

2.3.1 Field components of surface waves

In this section, cylindrical surface waves in a TM mode supported by a circular surface are discussed. The axial and radial profile of field components are illustrated in figure 2.4 for three different media, where med = 1 is air or vacuum as the surrounding environment, med = 2 is a dielectric material to confine the surface waves to the conductor and med = 3 is the conductor, i.e., the plasma.
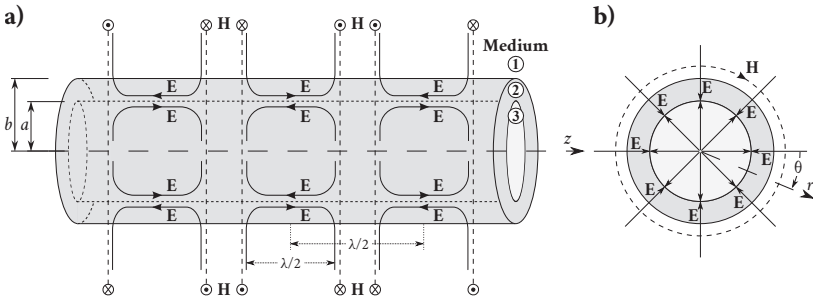
Figure 2.4: Axial field components on the central plane and radial field components on the cross section of a plasma driven with axial cylindrical surface waves supported with a dielectric coating and surrounded with a dielectric environment are presented in **a)** and **b)**, respectively. The schematic is not true to scale.

Each medium has its own permeability μ_{med}, permittivity ε_{med} and conductivity σ_{med}. This plasma structure is called the open plasma guide, since it is not enclosed within a conductive medium such as a metal cylinder [46].

For angle depended waves, both TM and TE modes exist in combination and all six field components must be considered [51]. However, as long as the azimuthal symmetry prevails, a pure TM mode exists, which can be described with three field components mentioned above.

Thus, the Maxwell's equations are reduced to

$$\frac{\partial E_r}{\partial z} - \frac{\partial E_r}{\partial r} = -\mu \frac{\partial H_\theta}{\partial t},$$

$$-\frac{\partial H_\theta}{\partial z} = \sigma E_r + \varepsilon \frac{\partial E_r}{\partial t}, \tag{2.59}$$

$$\frac{1}{r} H_\theta + \frac{\partial H_\theta}{\partial r} = \sigma E_z + \varepsilon \frac{\partial E_z}{\partial t},$$

with the azimuthal symmetry conditions $\frac{\partial E_z}{\partial \theta} = 0$ and $\frac{\partial E_r}{\partial \theta} = 0$.

With the assumption of a harmonic electromagnetic field, whose components are sinusoidal functions $e^{j\omega t}$ of time t [38], equation (2.59) becomes

$$\frac{\partial E_r}{\partial z} - \frac{\partial E_r}{\partial r} = -j\omega\mu H_\theta,$$

$$-\frac{\partial H_\theta}{\partial z} = (\sigma + j\omega\varepsilon) E_r, \tag{2.60}$$

$$\frac{1}{r} H_\theta + \frac{\partial H_\theta}{\partial r} = (\sigma + j\omega\varepsilon) E_z.$$

Harms [53] and Frank [54] solved the set of equations (2.60) by introducing the approach $E_r(r, z) = F_1(r) \cdot F_2(z)$ with a radial $F_1(r)$ and an axial

function $F_2(z) = e^{-\gamma z}$, where $\gamma = \alpha + j\beta$ is the propagation coefficient of surface waves, as explained in section 2.2.1. $F_1(r)$ must fulfill the second order differential equation (2.61).

$$\frac{\partial^2 F_1(r)}{\partial r^2} + \frac{1}{r}\frac{\partial F_1(r)}{\partial r} - u^2 F_1(r) = 0, \tag{2.61}$$

where $u^2_{med} = -(k^2_{med} + \gamma^2_{med})$ with the intrinsic propagation coefficient of the given medium $k^2_{med} = -j\omega\mu_{med}(\sigma_{med} + j\omega\varepsilon_{med})$ [47].

By substituting $p = ju_{med}r$, equation (2.61) can be converted into a Bessel's equation

$$\frac{\partial^2 F_1(p)}{\partial p^2} + \frac{1}{p}\frac{\partial F_1(p)}{\partial p} - F_1(p) = 0. \tag{2.62}$$

The field components can be described for different media by

$$\mathbf{E}_{z,med} = F^{(o)}_{1,med}(r)F_{2,med}(z)e^{j\omega t},$$

$$\mathbf{E}_{r,med} = -\frac{j\gamma}{u}F^{(o)}_{1,med}(r)F_{2,med}(z)e^{j\omega t}, \tag{2.63}$$

$$\mathbf{H}_{\theta,med} = \frac{\sigma + j\omega\varepsilon}{u}F^{(o)}_{1,med}(r)F_{2,med}(z)e^{j\omega t}.$$

The solution of equation (2.62) is an appropriate linear combination of modified Bessel's functions I_o and K_o of first and second kind, respectively [51, 53, 55, 56]. The order of the corresponding function is given by o. $F^{(o)}_{1,med}(r)$ becomes

$$F^{(o)}_{1,med}(r) = \begin{cases} B_1 K_o(ju_1 r) & r > b \\ A_2 I_o(ju_2 r) + B_2 K_o(ju_2 r) & a < r < b \\ A_1 I_o(ju_3 r) & r < a \end{cases}, \tag{2.64}$$

where A_{med} and B_{med} are coefficients set by boundary conditions between different media [47], as given by the set of equations

$$
\begin{aligned}
\mathbf{E}_{z,1}(b) &= \mathbf{E}_{z,2}(b), & \mathbf{H}_{\theta,1}(b) &= \mathbf{H}_{\theta,2}(b), \\
\mathbf{E}_{z,2}(a) &= \mathbf{E}_{z,3}(a), & \mathbf{H}_{\theta,2}(a) &= \mathbf{H}_{\theta,3}(a),
\end{aligned}
\tag{2.65}
$$

since the axial and azimuthal field components must be continuous at the boundaries [57]. F_1 has the order $o = 0$ for $\mathbf{E}_z$, while $o = 1$ for $\mathbf{E}_r$ and $\mathbf{H}_\theta$ [47, 50].

The radial distribution of electric field components $\mathbf{E}_z$ and $\mathbf{E}_r$ for a plasma column inside a glass cylinder, made of fused silica with a relative permittivity of $\varepsilon_a = 3.8$, surrounded by air is calculated by adopting the following assumptions to simplify the calculations: The excitation frequency is chosen as 2.45 GHz, while the electron density is assumed as spatially constant and equal to $1 \cdot 10^{18}\,\mathrm{m}^{-3}$. This assumption is eligible, as long as the product of plasma radius a and phase coefficient of the surface waves $\beta = \frac{2\pi}{\lambda}$ is < 1 [58]. Additionally, a weak collisional plasma approximation is adopted, where the plasma permittivity is assumed as purely real and can be calculated by $\varepsilon_p = 1 - \omega_{\mathrm{pe}}^2/\omega^2$, since $\overline{\nu}_e \ll \omega$. Thus, the attenuation coefficient α can be neglected and the propagation coefficient of surface waves is approximated as $\gamma \approx j\beta$ [59], which results in an unattenuated wave along z [57]. Finally, the relative magnetic permeability of all three media is assumed as $\mu_{\mathrm{med}} = 1$.

According to Zhelyazkov [55, 56], the local dispersion relation for plasma columns contained in a dielectric tube and surrounded by vacuum, as given in equation (2.66), can be solved to determine the phase coefficient β of the surface waves. The relative permittivity of air ε_a is approximated as 1.

$$
\frac{\varepsilon_3}{u_3}\frac{I_1(u_3)}{I_0(u_3)} + \frac{\varepsilon_2}{u_2}\frac{\mathcal{A}_1 + (u_2/\varepsilon_2)(1/u_2)[K_1(ju_1b)/K_0(ju_1b)]\mathcal{A}_2}{\mathcal{A}_3 + (u_2/\varepsilon_2)(1/u_2)[K_1(ju_1b)/K_0(ju_1b)]\mathcal{A}_4} = 0,
\tag{2.66}
$$

where

$$\mathcal{A}_1 = I_1(u_2)K_1(u_2 b) - I_1(u_2 b)K_1(u_2),$$
$$\mathcal{A}_2 = I_1(u_2)K_0(u_2 b) - I_0(u_2 b)K_1(u_2),$$
$$\mathcal{A}_3 = I_1(u_2 b)K_0(u_2) - I_0(u_2)K_1(u_2 b),$$
$$\mathcal{A}_4 = I_0(u_2 b)K_0(u_2) - I_0(u_2)K_0(u_2 b).$$

(2.67)

After the determination of β, A_{med} and B_{med}, equation (2.63) is solved to calculate the strength of the electric field components $|E_z|$ and $|E_r|$, which are plotted in figure 2.5 normalized to $|E_z(0)|$ as a function of radial distance r from central axis together with the permittivity of plasma ε_p, of the glass ε_g and air ε_a.

For high plasma densities, at which the plasma frequency is higher than the excitation frequency, the plasma permittivity becomes negative. The plasmas are the only dielectric media featuring a negative permittivity [46]. For $|\varepsilon_p| > |\varepsilon_g|$, the surface waves can propagate along the interfaces [60], whereas the negative permittivity results in an increasing strength of both field components in the plasma and in a decreasing strength in the glass and air with increasing radial distance r, although the radial component E_r exhibits discontinuities at both interfaces, i.e., plasma-glass and glass-air. Since neither glass nor air exhibit a negative permittivity, an evanescent field profile can only be observed on one side of the glass-air interface. Nonetheless, the evanescent field profile outside the plasma helps to reduce electromagnetic interference (EMI) [46].

With increasing excitation frequency ω, the steepness of field strength variation rises towards the dielectric tube walls, since u is a function of excitation frequency [46, 61]. Thus, the field strength concentrates near the tube walls and subsequently the magnitude of the confined energy at the interface increases [61]. Hence, the waves are called the surface waves. As a result, a higher electron temperature T_e is achieved at the plasma-wall interface.

Additionally, the penetration depth of the field components into the plasma decreases with increasing plasma frequency, since ε_p is a function of ω_{pe} [46]. It can be concluded that in contrast to T_e, n_e is higher in the central axis of the plasma than near the dielectric walls due to the dependency of ω_{pe} on n_e. The expected profiles of n_e and T_e are verified experimentally in section 7.2.
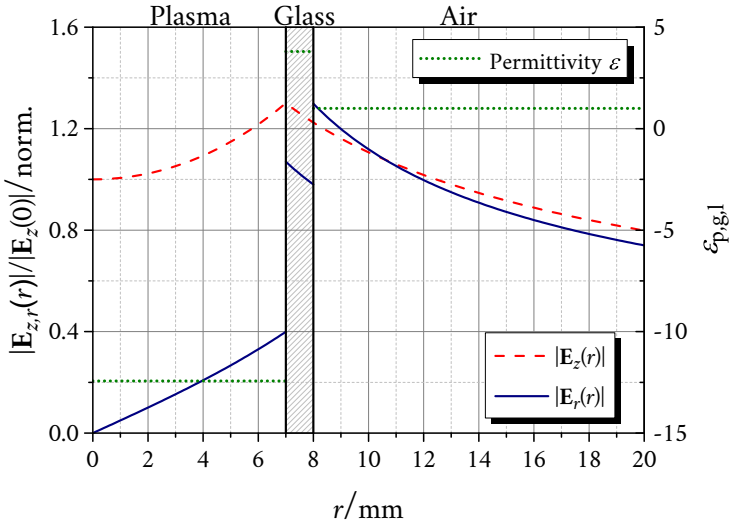
Figure 2.5: Radial distribution of the strength of the field components $|E_z|$ and $|E_r|$ normalized to $|E_z(0)|$, as well as of the permittivity, for a plasma column inside a fused silica cylinder with a permittivity of 3.8 surrounded by air. Excitation frequency is chosen as 2.45 GHz, while the electron density is assumed as spatially constant and equal to $1 \cdot 10^{18} \text{ m}^{-3}$. Weak collisional plasma approximation is adopted to calculate the plasma permittivity.

In contrast to ω_{pe}, the permittivity of glass and air is independent of the plasma frequency. Thus, for high electron densities and consequently for high plasma frequencies, most of the wave power is carried in the air [46].

It should be also noted that the axial field component $\mathbf{E}_z$ is dominant in the plasma and thus responsible for the heating of the electrons as long as the attenuation coefficint α is negligible small. With increasing collision frequency, power flux perpendicular to the boundaries intensifies [57].

2.3.2 Surface wave launcher

A surface wave launcher can be divided into two main parts [38]: the field applicator and impedance matching network. The former is responsible for the electromagnetic field shaping, which is needed to excite surface waves in the desired mode, while the latter adjusts the launchers impedance in order to optimize the power transfer from the feed line into the plasma. The most basic field shaping structure to generate azimuthally symmetric surface waves consists of a cylindrical metallic tube and a thin metallic plate. They are positioned perpendicular to each other in a short distance, thus forming a gap in between. A cylindrical discharge vessel, made from a dielectric material, may be positioned axially inside the metallic cylinder and extends through a hole in the metallic plate. Figure 2.6 **a)** and **b)** display the schematic of the wave launcher and the equivalent circuit, respectively.

When HF-power is applied, the electric field in the gap excites surface waves, which propagate in both axial directions along the discharge vessel. It should be noted that the excitation of backward surface waves, whose phase and group velocities have different signs, depends on some conditions [57]: Without a dielectric medium between surrounding medium and plasma, azimuthally symmetric waves cannot be excited backwards. Even with an adequate discharge vessel, conditions concerning the radius, permittivity and thickness of the discharge vessel as well as excitation frequency must be fulfilled.
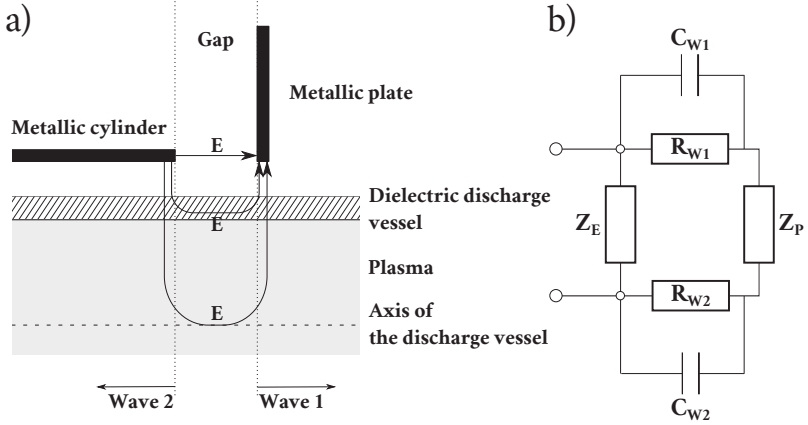
Figure 2.6: a) Components of a basic field shaping structure; **b)** The equivalent circuit of a basic field shaping structure.

Nevertheless, propagating surface waves carry a large part of the applied power, which is represented by R_{W1} and R_{W2} in the equivalent circuit. The stored energy during the wave excitation is given by the capacities C_{W1} and C_{W2}. The rest of the power is either absorbed inside or outside of the plasma in the gap or stored in the field, which are presented by Z_P and Z_E, respectively. The equivalent circuit can be summarized as the gap impedance Z_{gap}.

Four different surface wave launchers were developed by Moisan [62], which allow to sustain surface wave driven plasmas in a broad frequency range between 1 MHz and 10 GHz [55]: The first launcher "Ro-box" is designed for low frequencies between 1 and 300 MHz range. The so-called "surfatron" consists of coaxial transmission line elements and is employed in the frequency range between 200 MHz and 10 GHz. The third launcher "surfaguide" can be described as the waveguide version of the surfatron. Thus, a higher power handling capability is achieved in the frequency range between 1.5 and 10 GHz. The final launcher is the "waveguide surfatron", which includes both waveguide and coaxial line

elements. It is a high power substitute of the surfatron at frequencies of about 2.45 GHz. The schematic representation of all four surface wave launchers is shown in figure 2.7.
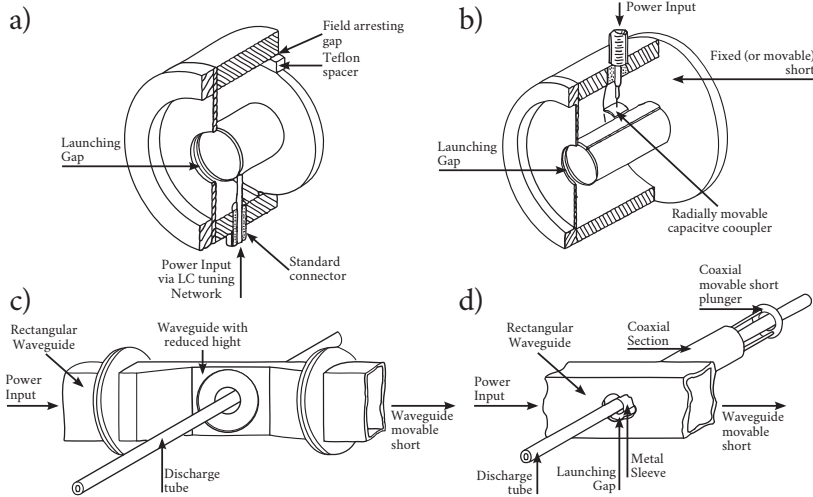
Figure 2.7: Schematic presentation of surface wave launchers: **a)** Ro-box field applicator; **b)** Surfatron; **c)** Surfaguide field applicator and **d)** Waveguide-surfatron. The schematics were taken from [62] and are restored for higher quality.

In due consideration of the desired power range and the chosen excitation frequency of 2.45 GHz, a surfatron is employed for this work. The design and electomagnetic properties of the employed surfatron can be found in section 6.2.

2.3.3 Plasma breakdown and ionization front

Assuming a weak collisional plasma, whose permittivity can be calculated as $\varepsilon_p = 1 - \omega_p^2/\omega^2$, two important electron densities should be considered to describe the wave-plasma interaction: the critical and the resonance electron density. At the critical electron density n_{ec}, also known as the cutoff density, the plasma permittivity becomes zero. As explained in section 2.2.1, the waves experience a total reflection and cannot penetrate into the plasma. The resonance electron density is given by $n_{res} = (1 + \varepsilon_g)n_{ec}$, where ε_g is the permittivity of glass. It describes the density, at which the absolute value of the plasma permittivity exceeds the glass permittivity, which is the necessary condition for surface wave propagation at the interface between the plasma and the glass wall [38].

Since the wave launcher forms an extremity of electric field strength, the breakdown of the discharge takes place in the section of the discharge vessel, enclosed by the wave launcher. The field component $\mathbf{E}_z$ decreases with increasing distance z from the wave launcher. This field gradient causes the electrons to move from the wave launcher into the direction of wave propagation z due to the ponderomotive force [35, 38]. When the electron density in the enclosed section of the discharge vessel exceeds n_{res}, the surface waves begin to propagate along the discharge vessel, until they are reflected at the position, where $n_e = n_{res}$.

Even with the propagation of surface waves, the field gradient remains, which pushes more electrons into the same direction. Thus, the motion of electrons forms a so-called ionization front. The surface waves propagate gradually farther from the wave launcher, until the wave power flux drops below the necessary level to sustain the minimum electron density n_{res}. For a collisional plasma, the critical density and subsequently the resonance density is not defined exactly, as mentioned in section 2.2.1.

2.3.4 Steady-state operation

In this section, a simplified mathematical description of the plasma behavior in steady-state operation is given. The radial distribution of plasma parameters is neglected as a first approximation. Thus, each plasma cross section with the length Δz is assumed uniform and is described with average plasma parameters, e.g., cross section average electron density $\overline{n}_e$. It is also assumed that each cross section can be analyzed individually, as if there is no energy exchange between consecutive cross sections [38]. Figure 2.8 illustrates the schematic of a plasma cross section with the relevant power transfer processes in steady-state operation.
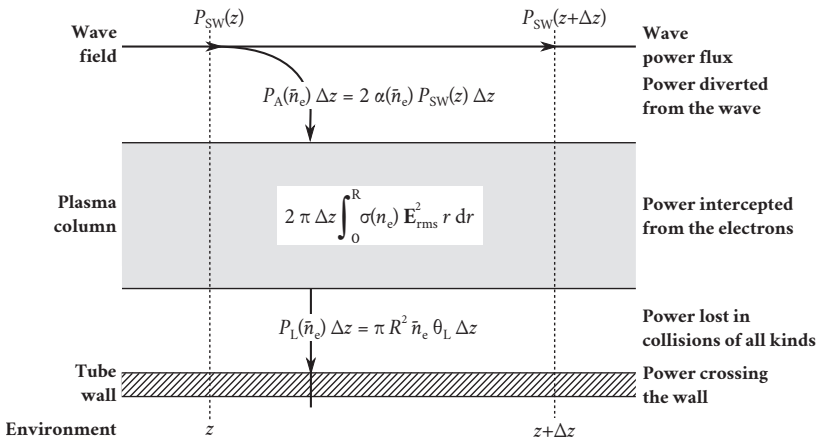
Figure 2.8: Schematic of a plasma cross section with the relevant power transfer processes.

The power flux of surface waves $P_{SW}(z)$ is a decaying function of the axial position z, since the waves sustain the plasma as they propagate along it. The amount of power P_A diverted per unit length from surface wave power flux P_{SW} is a function of amplitude attenuation coefficient α,

which depends on the corresponding plasma permittivity, as shown in equation (2.58). Furthermore, the plasma permittivity is via ω_{pe} a function of electron density $\overline{n}_{\mathrm{e}}$, as presented in equation (2.56). Since $\overline{n}_{\mathrm{e}}$ varies with axial position z, so does the absorbed power per unit length. Hence, P_{A} can be given by equation (2.68) [38].

$$P_{\mathrm{A}}(\overline{n}_{\mathrm{e}}) = \frac{\mathrm{d}P_{\mathrm{SW}}(z)}{\mathrm{d}z} = 2\alpha(\overline{n}_{\mathrm{e}})P_{\mathrm{SW}}(z), \tag{2.68}$$

As mentioned in section 2.2.1, inside an HF-plasma at an excitation frequency of $f > 1\,\mathrm{MHz}$, nearly all power is absorbed by the electrons [62]. Therefore, the absorbed power from the wave field has to balance the absorbed power by the electrons. The mean absorbed power per electron θ_{A} can be calculated by equation (2.54), whose radial integration delivers the total absorbed power by the plasma cross section, as given in the enumerator of the last term in equation (2.69). Thus, the attenuation constant can be calculated by

$$\alpha(\overline{n}_{\mathrm{e}}) = -\frac{1}{2}\frac{1}{P_{\mathrm{SW}}(z)}\frac{\mathrm{d}P_{\mathrm{SW}}(z)}{\mathrm{d}z} = \frac{\pi \int_{0}^{R} \sigma(n_{\mathrm{e}})\mathbf{E}_{\mathrm{rms}}^{2}r\,\mathrm{d}r}{P_{\mathrm{SW}}(z)}, \tag{2.69}$$

where $\mathbf{E}_{\mathrm{rms}}$ is the root mean square of the total field intensity and $\sigma(n_{\mathrm{e}})$ is the complex electrical conductivity of the plasma section with average electron density $\overline{n}_{\mathrm{e}}$.

The power absorbed by the electrons is afterward lost by the collisional processes in the plasma and leaves the plasma in form of radiation or heat. Furthermore, for steady-state operation, the mean absorbed power per electron θ_{A} must be equal to the mean power lost per electron θ_{L} [38]. Hence, the power lost per unit length can be calculated by

$$P_{\mathrm{L}}(\overline{n}_{\mathrm{e}}) = \pi R^{2}\overline{n}_{\mathrm{e}}\theta_{\mathrm{L}} = 2\alpha(\overline{n}_{\mathrm{e}})P_{\mathrm{SW}}(z). \tag{2.70}$$

With the assumption that the EEDF is independent of the electron density and the secondary processes, as well as the step-wise processes, do

not contribute consequentially to the plasma dynamics, the power lost per electron θ_L can be assumed axially constant and independent from z as well as from $\overline{n}_e$ [62, 63]. This assumption results in a linearly decreasing axial electron density profile [55], which is a good approximation for low pressure noble gas plasmas [64].

However, for discharges with molecular gases, such as indium(I)iodide, equation (2.54) contradicts this assumption, since θ_A is a function of plasma frequency, as well as total electron collision frequency for momentum transfer. In addition to that, the contribution of secondary and step-wise processes grows with increasing electron density. Thus, Ferreira [65] proposed the analytical expression for the axial plasma density gradient as

$$\frac{d\overline{n}_e}{dz} = -2\alpha(z)\overline{n}_e \left(1 - \frac{\overline{n}_e}{\alpha(\overline{n}_e)}\frac{d\alpha(\overline{n}_e)}{d\overline{n}_e} + \frac{\overline{n}_e}{\theta_L}\frac{d\theta_L}{d\overline{n}_e}\right)^{-1}. \tag{2.71}$$

Zakrzewski [66] stated that a steady state is achieved, when two conditions are fulfilled: First, P_A has to balance P_L. Secondly, this power balance has to be stable. A decrease in the electron density should lead to a shift of the balance in favor of the absorbed power over the lost power as shown by

$$\frac{dP_A(\overline{n}_e)}{d\overline{n}_e} < \frac{dP_L(\overline{n}_e)}{d\overline{n}_e}, \tag{2.72}$$

or in terms of $\alpha(\overline{n}_e)$ by equation (2.73) [64].

$$\frac{d\alpha(\overline{n}_e)}{\alpha(\overline{n}_e)} < \frac{d\overline{n}_e}{\overline{n}_e}\left(1 + \frac{\overline{n}_e}{\theta_L}\frac{d\theta_L}{d\overline{n}_e}\right). \tag{2.73}$$

Finally, in due consideration of equations (2.68) and (2.70), a minimum surface wave power $P_{min} = \pi R^2 \overline{n}_{res}\theta_A(2\alpha(\overline{n}_{res}))^{-1}$ should be provided by the wave launcher to sustain the plasma with surface waves [38].

Chapter 3

Selection of substitutes for mercury in light technologies

In this work, the plasma efficiency is defined as the ratio of the generated radiation power to the electrical power accepted by the surfatron from the feed line, while the ratio of the generated light flux in lumen to the accepted electrical power by the surfatron gives the plasma efficacy. In conventional fluorescent lamps, a two step process is responsible for the generation of light [67]: In the first step, the energy, which is absorbed by the plasma from the applied electric field, is converted to UV radiation at 184.95 nm and 253.65 nm by mercury, i.e., the radiant component in the lamp, by means of inelastic collisions and spontaneous emission. In the second step, the emitted photons travel to the walls of the discharge vessel, which is coated with a fluorescent powder, also known as phosphor coating. There, the UV-photons are converted to light by means of fluorescence. Furthermore, the loss processes inside the plasma are controlled by the buffer component, in most cases a noble gas such as argon.

The efficiency of each step and consequently the luminous efficacy of the lamp depends on the physical and chemical properties of the radiant and buffer components of the lamp as well as the efficiency of the phosphor coating. In section 3.1, the selection criteria to find a suitable substi-

tute for mercury are presented. The selection rules are applied to all elements in the periodic table and the results are discussed. Section 3.2 is dedicated to a short description of the function and the right utilization of buffer component. The structural and radiometric attributes of fluorescent powders are beyond the scope of this work and are not further discussed.

3.1 Criteria for radiant component

A high efficiency can be achieved in the above-mentioned steps, if the following requirements are met by the radiant component of the lamp:

- Vaporization of the radiant component at low temperatures to prevent excessive heat losses from the lamp body.

- Efficient ionization and excitation of the radiant component due to a low ionization and excitation potential as well as large collision cross sections.

- High transition probabilities for spontaneous emission from excited states.

- Transport of the generated radiation to the walls of the discharge vessel with minimum self-absorption and without repartition of the radiated energy in collisional processes.

- Conversion of the generated radiation into visible light by the phosphor coating with minimum Stokes' losses by exciting it with a radiation at the limit between UV and VIS.

A set of criteria is developed to simplify the selection of suitable materials in accordance with the above-listed requirements.

3.1.1 Emission lines

The noble gases fulfill the first requirement from the list without difficulty. However, the Stokes' losses in the phosphor coating makes the use of the noble gases as emitting material unfavorable, since their resonance emission lines are located dominantly in the vacuum UV region (< 200 nm) similar to their excimer radiation [24, 68]. To avoid high Stokes' losses, the first selection criterion states that the emission lines of the substitute should be located in the spectral region between 360 nm and 460 nm.

The noble gases can be mixed with halogens to shift the excimer radiation to longer wavelengths, reducing the Stokes' losses. However, these mixtures deliver considerably lower plasma efficiencies compared to the pure noble gases [68], thus their use is not widespread.

In contrast to the noble gases, several metals meet the first selection criterion. However, metals with toxic or radioactive nature, e.g., cadmium and lead should be excluded from the selection together with the alkali metals due to their high diffusion rate into glass, which leads to a very short lamp life time. The remaining metals with strong resonance emission lines in the chosen spectral region are listed in table 3.1. The wavelengths of emission lines are taken from [24].

3.1.2 Characteristics of temperature vs. vapor pressure

Partial vapor pressure of the radiant component inside the lamp is adjusted by the so-called cold spot temperature T_{CS}, which is the coldest point of the discharge vessel. At low vapor pressures, the probability of

inelastic collisions resulting in excitation and ionization of atoms is insufficient, while high vapor pressures lead to an excessive self-absorption of the generated radiation. The optimum partial vapor pressure of pure mercury inside a fluorescent lamp with a diameter of 30~40 mm is about $p_{Hg} = 0.93$ Pa [44, 67], which corresponds to a cold spot temperature of $T_{CS} = 314.92$ K [69, p. 177]. To reach the optimum vapor pressure at higher temperatures, mercury amalgams are adopted [44].

Table 3.1: List of selected metals featuring strong resonance emission lines in the spectral region between 360 nm and 460 nm. The wavelengths of emission lines are taken from [24] and temperature-vapor pressure characteristics from [69].

Metal	Wavelength / nm	Diatomic metal-halogen composition	T_{CS} for 0.93 Pa / K
Fe	364.93, 367.99, 382.44, 421.61, 437.59	-	-
Ru	372.80	-	-
Tl	377.57, 535.05	TlBr	579.38
		TlI	582.13
Yb	398.79	-	
Er	400.79	-	
Mn	403.07, 403.30, 403.44	-	-
Dy	404.59, 418.68, 421.17	-	-
Tm	409.41	-	
In	410.17, 451.13	InBr	484.52
		InI	535.42
Eu	459.40	-	-

The second selection criterion states that the radiant component should reach a partial vapor pressure of 0.93 Pa at a cold spot temperature below 533.15 K, since higher temperatures would lead to excessive heat losses from the lamp body. The upper temperature limit is chosen as 533.15 K, since it is the optimum cold spot temperature of conventional sodium low pressure lamp, for which measures against excessive heat losses are already investigated and optimized.

However, the vapor pressure of the listed metals in table 3.1 is small compared to mercury. Thus, the use of metal halogen compounds comes into consideration. Yet, fluorine and chlorine are volatile and aggressive. They may leave the lamp by diffusing into the glass walls or degrade the glass by reacting with it chemically. For this reason, their chemical compositions should be avoided. The remaining halogens, bromine and iodine can form either diatomic or polyatomic molecules according to the chemical structure of their metallic partners. In principle, the polyatomic molecules feature a higher vapor pressure than the diatomic ones [69]. However, polyatomic molecules are disadvantageous as feedstock of the radiant component, since the energy dissipation by the excitation of rotational-vibrational states is high due to their complex molecular structure [70]. Furthermore, the energy cost of the multi-step dissociation to form metal atoms is relatively high. Therefore, the third criterion states that only diatomic metal halogen compounds should be considered in the selection, which is fulfilled only by indium and thallium.

As the fourth and final criterion, the stoichiometrically driven condensation should be avoided [14]. If the utilized metal-halide is not chemically stable, changes in its chemical composition may occur during operation, which results in a fast condensation of the vaporized portion, since the final chemical composition features a lower vapor pressure than that of its initial state or in the formation of polyatomic molecules, which contradicts with the third selection criterion. These changes reduce the plasma

efficiency as well as the life time of the lamp. The diatomic halogen compounds of both indium and thallium prove to be chemically stable [14].

In due consideration of all four criteria, only indium-monohalides, i.e., indium(I)bromide (InBr) and indium(I)iodide (InI) qualify as promising substitutes. According to Hansen [69, p. 181], a cold spot temperature of $T_{CS} = 1179\,\text{K}$ is needed to achieve a vapor pressure of 0.93 Pa with indium, while cold spot temperatures of $T_{CS} = 485\,\text{K}$ and $T_{CS} = 535\,\text{K}$ suffice for the same vapor pressure with InBr and InI, respectively [69, p. 127, p. 129]. Although, InBr features a higher vapor pressure, InI is chosen for the further investigation due to its more than 0.5 eV lower dissociation and ionization energy compared to InBr [71], which result in a higher electron and indium atom density.

3.1.3 Ionization and excitation

The first excited resonance state of mercury 6^3P_1, which fulfills the selection rules for a radiative transition into the ground state 6^1S_0, has an excitation energy of 4.88 eV, which corresponds to a wavelength of 253.65 nm [24]. Furthermore, two metastable energy states 6^3P_0 and 6^3P_2 are located closely to 6^3P_1 with excitation energies of 4.67 eV and 5.46 eV, respectively. The excitation energies of metastable states are about half of the ionization energy $E_i = 10.44$ eV. Thus, the metastable states promote an increased electron density due to step-wise ionization as well as an increased density of 6^3P_1 due to excitation and de-excitation from metastable states [44]. Figure 3.1 depicts the ionization cross sections of mercury from ground and metastable states.

The excitation cross sections from ground and 6^3P_0-states into 6^3P_1-state as well as the de-excitation cross section from 6^3P_2- into 6^3P_1-state are shown in figure 3.2.

The electron-impact cross sections for ionization, excitation and de-excitation are calculated by means of simplified Gryziński method and Klein-Rosseland formula, described in sections 5.2.2 and 5.4.1, respectively. Measurement data on cross sections are available in the literature for mercury unlike for indium. Yet, theoretical cross sections are presented here for the sake of consistency to allow a direct comparison between mercury and indium.
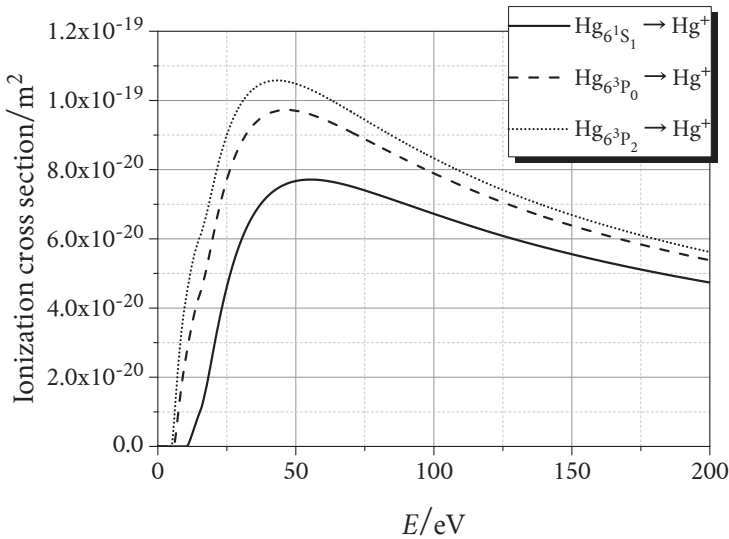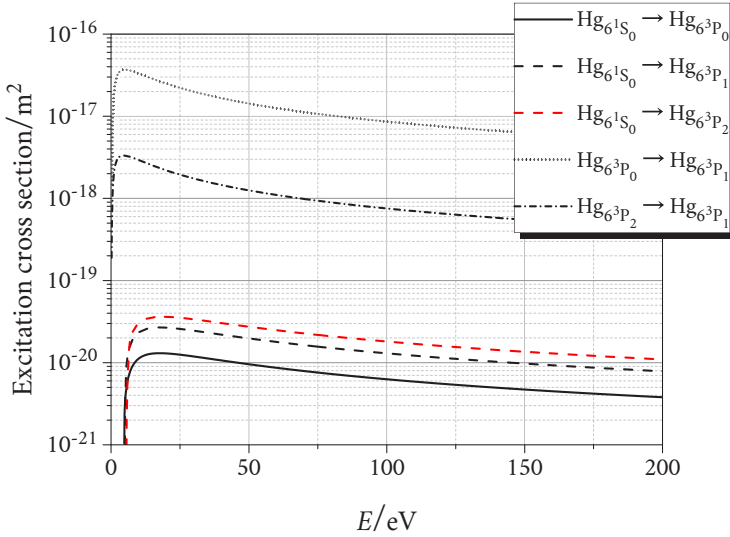

Figure 3.1: Electron impact ionization cross sections of mercury from energy states 6^1S_0, 6^3P_0 and 6^3P_2.

Indium features two strong emission lines at the wavelengths 410.17 nm and 451.13 nm due to the spontaneous emission from the excited state $6^2S_{1/2}$ into the ground state $5^2P_{1/2}$ and metastable state $5^2P_{3/2}$, respectively. The metastable state is located very closely to the ground state with an excitation energy of 0.27 eV and forming almost a second ground state. The calculated Einstein coefficients for spontaneous emission of

the resonance lines of mercury and indium are given in table 3.3. The spontaneous emission rates of indium are an order of magnitude higher than that of mercury. The electron-impact cross sections of indium for ionization and excitation are given in figures 5.5 and 5.6, respectively.

Figure 3.2: Electron impact excitation cross sections of mercury from energy state 6^1S_0 into $6^3P_{0,1,2}$ and from 6^3P_0 into 6^3P_1 as well as the electron impact de-excitation cross sections from energy state 6^3P_2 into 6^3P_1.

Compared to that of mercury, the maximum of direct ionization cross section from ground state is smaller for indium. Furthermore, the contribution of metastable states to the ionization is stronger by mercury. Yet, the tail of the Maxwellian EEDF is responsible for the inelastic collisions. The lower ionization energy of 5.79 eV of indium may result in a higher electron density even with a lower ionization cross section maximum. Therefore, the rate coefficients of relevant generation processes

are calculated and displayed in figure 3.3 for mercury, and in figures 5.9 and 5.10 for indium.
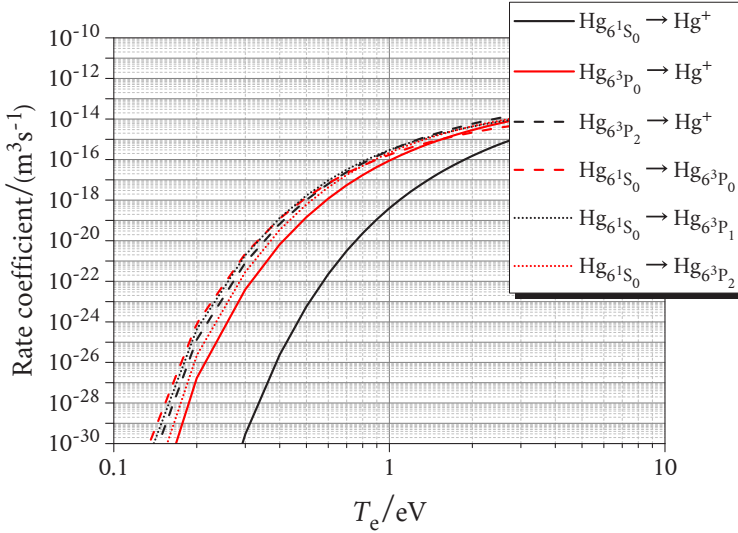
Figure 3.3: Rate coefficients of mercury for electron impact ionization from energy states 6^1S_0, 6^3P_0 and 6^3P_2 as well as for electron impact excitation from energy state 6^1S_0 to $6^3P_{0,1,2}$.

The electron temperature in a low pressure plasma is typically ≈ 1 eV [44]. At this temperature, the ionization rate coefficient of ground state indium atoms is more than three orders of magnitude higher than that of mercury atoms.

However, it should be kept in mind that mercury atoms are formed in the plasma by vaporizing the pure mercury filling, while for the formation of atomic indium, an additional step of dissociation is needed. Thus, a direct comparison of ionization rate coefficients is not definitive. The total kinetic energy needed to dissociate an indium(I)iodide molecule and then to ionize the indium atom is $E_{\text{total}} = E_{\text{diss.}} + E_i = 3.43 \, \text{eV} + 5.79 \, \text{eV} =$

9.22 eV. It is 1.22 eV lower than the ionization energy of mercury, which means that the step-wise dissociation and ionization process for indium is more energy efficient than the ionization of mercury. Nevertheless, the amount of energy needed for a collision process does not provide information about the probability of the collision process. Therefore, the effective ionization rates are considered as follows: It is assumed that the free and ambipolar diffusions are the only loss mechanisms, and the ionization from excited energy states can be neglected. Subsequently, the mercury ion density is calculated by the balance of the loss and the generation rates in partial equilibrium as

$$n_{\mathrm{Hg}^+} = n_{\mathrm{e}}\, n_{\mathrm{Hg}}\, {}^{\mathrm{Hg}}_{\ \mathrm{e}}K^{\mathrm{Hg}^+}_{2\mathrm{e}}\, \tau_{\mathrm{Hg}^+}. \tag{3.1}$$

The indium ion density is given analogously by

$$n_{\mathrm{In}^+} = n_{\mathrm{e}}\, n_{\mathrm{In}}\, {}^{\mathrm{In}}_{\ \mathrm{e}}K^{\mathrm{In}^+}_{2\mathrm{e}}\, \tau_{\mathrm{In}^+}$$

$$= n_{\mathrm{e}}^2\, n_{\mathrm{InI}}\, {}^{\mathrm{InI}}_{\ \mathrm{e}}K^{\mathrm{diss.}}\, {}^{\mathrm{In}}_{\ \mathrm{e}}K^{\mathrm{In}^+}_{2\mathrm{e}}\, \tau_{\mathrm{In}}\, \tau_{\mathrm{In}^+}, \tag{3.2}$$

with

$$n_{\mathrm{In}} = n_{\mathrm{e}}\, n_{\mathrm{InI}}\, {}^{\mathrm{InI}}_{\ \mathrm{e}}K^{\mathrm{diss.}}\, \tau_{\mathrm{In}}, \tag{3.3}$$

where n_{e}, n_{InI}, n_{In} and n_{Hg} are the densities of electrons, indium(I)iodide molecules, indium atoms and mercury atoms, respectively. ${}^{\mathrm{Hg}}_{\ \mathrm{e}}K^{\mathrm{Hg}^+}_{2\mathrm{e}}$, ${}^{\mathrm{In}}_{\ \mathrm{e}}K^{\mathrm{In}^+}_{2\mathrm{e}}$ and ${}^{\mathrm{InI}}_{\ \mathrm{e}}K^{\mathrm{diss.}}$ give the rate coefficients of electron impact ionization of mercury and indium, and of electron impact dissociation of indium(I)iodide, respectively. Finally, τ_{Hg^+}, τ_{In^+} and τ_{In} denote the life times of mercury and indium ions due to the ambipolar diffusion, and of indium atoms due to free diffusion, respectively.

For $T_{\mathrm{e}} = 1\,\mathrm{eV}$ and $p_{\mathrm{Hg}} = p_{\mathrm{InI}} = 0.93\,\mathrm{Pa}$, the calculated ion densities are shown in figure 3.4 as a function of electron density. The needed diffusion coefficients and subsequently the lifetimes are calculated according to sections 5.5.1 and 5.5.2. With indium, a higher ion density is achieved

for $n_e > 2.51 \cdot 10^{15} \text{ m}^{-3}$, which is generally the case in low pressure plasmas for light technologies.
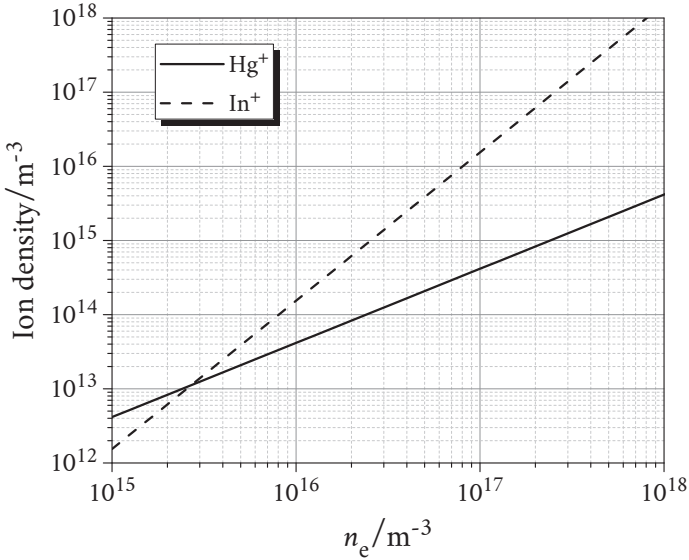

Figure 3.4: Mercury and indium ion densities as a function of electron density, calculated with the assumptions that the free and ambipolar diffusions are the only loss mechanisms, and ionization from excited states can be neglected.

The excitation cross section from the ground state into the first excited state of indium, which is optically accessible from ground state, is one order of magnitude larger than that of mercury, while the corresponding excitation rate coefficient of indium is more than two orders of magnitude higher. Furthermore, in mercury or pure noble gas plasmas, the resonance states experience a density saturation, since the energy sum of resonance and metastable states is higher than the ionization energy [44]. Thus, the collisions between excited states lead to ionization. However,

the energy sum of the first resonance and metastable states of indium does not exceed the ionization threshold. Although, the collisions between resonance states can result in ionization, their lifetimes are negligibly short compared to that of metastable states, which reduces the probability of an ionizing collision. Therefore, only at very high particle densities, their contribution to ionization becomes significant and the resonance state densities saturate.

Table 3.1 comprises thallium(I)iodide and thallium(I)bromide in addition to indium halides. Neither thallium(I)bromide nor thallium(I)iodide can fulfill the second selection criterion on the temperature-vapor pressure characteristic. Therefore, they are excluded from the selection as mercury substitute. However, thallium belongs to the same main group as indium and exhibits a similar orbital structure with a metastable state, located at 0.96 eV. Its ionization energy of 5.99 eV is also higher than that of indium. Higher ionization energy with similar orbital structure, such as one bound electron on the utmost $P_{1/2}$-orbital, results in a smaller ionization rate and consequently in lower electron densities. Thallium has two strong emission lines at 377.57 nm and 535.05 nm due to the transition from the first optically accessible excited state into the ground and first metastable state, respectively [24]. The latter cannot be employed as main stimulator of the phosphor coating to generate white light and the former causes higher Stokes' losses in phosphor than the lines of indium. However, thallium(I)iodide can be adopted in an indium(I)iodide plasma as an additive to populate the resonance state with the emission at 535.05 nm, which is located very closely to the maximum of the spectral sensitivity of the human eye at 555 nm.

3.1.4 Radiation trapping

The emitted photons are re-absorbed and re-emitted many times before reaching the walls of the discharge vessel [72]. This process results in an effective decrease of the Einstein coefficient of the spontaneous emission A_λ, or in other words, the vacuum decay rate of the radiative transition at the wavelength λ. Consequently, the effective lifetime of the corresponding excited energy state increases. The increase is strongest, when dealing with resonance emission lines, whose final energy state is the ground state of the corresponding atom. Thus, the probability of the spontaneous emission approaches that of the non-radiative transitions, such as collisional excitation, de-excitation and ionization from the excited state. The repartition of the radiative energy in collisional processes leads to a lower plasma efficiency. Therefore, it is of utmost importance that the radiant component has a high effective decay rate. In most plasma models, the vacuum decay rate of the spontaneous emission is replaced with the fundamental mode decay rate for the trapped radiation A_λ^{tr} [73].

The radiation trapping can be modeled as a diffusion of radiative energy for low opacity plasmas. However, in low pressure plasmas, the opacity of the plasma is high and the radiation transport is non-local in coordinate space [74, 75]. Thus, an integral transport equation was introduced by Holstein [76], whose solutions for different lamp geometries are available in the literature [75]. In chapter 4, a detailed description of radiation trapping as well as of line broadening mechanisms can be found. Furthermore, the escape factor concept is presented for cylindrical lamp geometry and discussed. However, at this point, only a simple comparison between mercury and indium without complex calculations is needed.

A highly realistic Monte Carlo simulation was developed to analyze the trapping of the atomic resonance radiation in a cylindrical geometry with a line shape arising from natural, Doppler, radiative and resonance

collisional broadening [77]. The simulation uses the so-called partial frequency redistribution approximation (PFR), which assumes that the frequency of the re-emitted photon may be in correlation with the frequency of the absorbed photon. PFR delivers realistic results at lower gas densities, while the complete frequency redistribution approximation (CFR), which rejects any correlation between the frequencies of the absorbed and re-emitted photons and randomly chooses a frequency from the emission line shape, is suitable for high gas densities, where collision broadening is dominant [77]. The results of Monte Carlo simulations are used to develop analytical expressions, which can simply be applied to calculate the ratio $\beta_{tr} = A_\lambda^{tr}/A_\lambda$ of fundamental mode decay rate to the vacuum decay rate for a broad range of gas densities [74]. However, neither isotopic nor hyperfine structures of emission lines are considered [73].

For the determination of β_{tr}, four dimensionless parameters are needed: First, the reduced number of the absorbing atoms N_{red} in a volume equal to cubic wavelength is given by

$$N_{red} = n_{Ab}\lambda^3, \tag{3.4}$$

where n_{Ab} is the absorber density.

Secondly, the Voigt parameter a_{v0} at the limit of low gas density is calculated by

$$a_{v0} = \left[4\pi v_0 \tau_k \left(\frac{2k_B T_g}{m_{Ab}c^2}\right)^{1/2}\right]^{-1}, \tag{3.5}$$

where v_0 is the center frequency of the emission line, τ_k is the vacuum lifetime of the excited state k and m_{Ab} is the mass of the absorber.

At the limit of low gas density, only radiative and Doppler broadening should be considered for the profile of the emission line and the pressure broadening can be neglected.

Thirdly, the probability of a dephasing resonance collision during a radiative lifetime is given by

$$P_{\text{drc}} = \left(1 + \frac{g_{\text{k}}}{g_{\text{j}}} \frac{65.71}{N_{\text{red}}}\right). \tag{3.6}$$

Finally, the reduced radius is calculated by normalizing the radius of the cylindrical discharge vessel to the wavelength by

$$R_{\text{red}} = \frac{R}{\lambda}. \tag{3.7}$$

Van Tright [78] proposed analytical solutions to Holstein-Bibermann equation with CFR for cylindrical geometry at the limit of low absorbing gas density, where Doppler broadening dominates, and at the limit of high absorbing gas density, where resonance collisional broadening dominates. Lawler [73] modified analytical solutions of van Tright according to the results of Monte Carlo simulations. The contribution of the Doppler broadening β_{Dtr} to the ratio β_{tr} can be calculated by

$$\begin{aligned}
\beta_{\text{Dtr}} = {} & \left[1.575 + \frac{\sqrt{a_{v0}}}{2.75} + \frac{0.18\left(\ln 1 + 2.75 a_{v0}^{1.5}\lambda_{\text{mfpp}}\right)^{1.3}}{\left(0.35 + \sqrt{a_{v0}}\right)}\right] \\
& \times \left[1.575 + \frac{\sqrt{a_{v0}}}{2.75} + \lambda_{\text{mfpp}}\sqrt{\ln 1.57 + 0.37\lambda_{\text{mfpp}}}\right]^{-1},
\end{aligned} \tag{3.8}$$

while the contribution of resonance collision broadening β_{Rtr} is given by

$$\beta_{\text{Rtr}} = \frac{0.196 P_{\text{drc}}}{\sqrt{R_{\text{red}}}}, \tag{3.9}$$

with the mean free path of the photons between re-emission and re-absorption

$$\lambda_{\text{mfpp}} = N_{\text{red}} a_{v0} R_{\text{red}} \frac{g_{\text{k}}}{2g_{\text{j}}}. \tag{3.10}$$

Finally, the contributions of both broadening mechanisms are combined by

$$\beta_{tr} = \sqrt{\frac{\beta_{Dtr}^2 + \beta_{Rtr}^2}{1 - 0.2\beta_{Rtr} + \beta_{Rtr}^2}}$$

$$\times \left[1 + \frac{4P_{drc}}{\left(\frac{2.7\beta_{Dtr}}{\beta_{Rtr}} + \frac{\beta_{Rtr}}{2.7\beta_{Dtr}} + \sqrt{\frac{1900}{R_{red}}}\right)^2}\right]^{-1} . \tag{3.11}$$

The calculated β_{tr} as well as the effective lifetimes $\tau_{k \to j}^{eff}$ of excited states of both mercury and indium are listed in table 3.2 for a lamp radius of $R = 0.007$ m. $T_{CS} = 313.15$ K and 493.15 K are chosen for mercury and indium(I)iodide, respectively. Furthermore, it is assumed that the dissociation rate in plasma is high enough to achieve an indium density equal to the indium(I)iodide density. The validity of this assumption is verified in section 5.7.2, at least for low electron temperatures at the chosen cold spot temperature.

Table 3.2: Calculated β_{tr}-values and effective lifetimes $\tau_{k \to j}^{eff}$ for the radiative transition $6^3P_1 \to 6^1S_0$ of mercury as well as for the radiative transitions $6^2S_{1/2} \to 5^2P_{1/2}$ and $6^2S_{1/2} \to 5^2P_{3/2}$ of indium.

	Mercury	Indium	
$k \to j$	$6^3P_1 \to 6^1S_0$	$6^2S_{1/2} \to 5^2P_{1/2}$	$6^2S_{1/2} \to 5^2P_{3/2}$
β_{tr}	0.07085	0.01569	0.00339
$\tau_{k \to j}^{eff} / \mu s$	1.764	1.275	3.308

The necessary data to calculate β_{tr} can be found in table 3.3. The calculated $\tau_{k \to j}^{eff}$ for the indium resonance line at 410.17 nm agrees well with the data, published by Bicchi [79]. The effective lifetimes of mercury and indium are in the same order of magnitude, although the vacuum decay rate of indium is higher than that of mercury.

Table 3.3: Necessary data to calculate β_{tr}-values and effective lifetimes for the radiative transition $6^3P_1 \rightarrow 6^1S_0$ of mercury as well as for the radiative transitions $6^2S_{1/2} \rightarrow 5^2P_{1/2}$ and $6^2S_{1/2} \rightarrow 5^2P_{3/2}$ of indium [24, 80].

	$k \rightarrow j$	m_{Ab} / u	$g_k - g_j$	$\lambda_{k \rightarrow j}$ / nm	$A_{k \rightarrow j}$ / s^{-1}
Mercury	$6^3P_1 \rightarrow 6^1S_0$	200.59	3 - 1	253.65	$8 \cdot 10^6$
Indium	$6^2S_{1/2} \rightarrow 5^2P_{1/2}$	114.82	2 - 2	410.17	$5 \cdot 10^7$
	$6^2S_{1/2} \rightarrow 5^2P_{3/2}$		2 - 4	451.13	$8.9 \cdot 10^7$

It indicates that a stronger self absorption occurs within the indium(I)-iodide plasma.

3.1.5 Natural abundance

The adopted method to calculate the β_{tr}-values in the last section is only applicable for gases, which exhibit negligible isotopic and hyperfine structures on their resonance lines [72]. However, mercury has seven naturally occurring isotopes, whereas ^{200}Hg and ^{202}Hg constitute more than 50 % of the isotopic composition [81]. The emission lines of heavier isotopes are shifted to longer wavelengths, since the nuclear field shift is larger than the mass shift [75]. Furthermore, according to Walsh [82], the 254 nm resonance line feature a hyperfine structure with 5 lines of equal amplitude and separation. The isotopic and hyperfine characteristics of mercury as emitting material in the lamp lead to a reduced radiation trapping by a factor of 5 compared to the case of a single isotope [44, 75]. Therefore, studies are conducted to increase the plasma efficiency by changing the mixing ratio of individual isotopes in the natural composi-

tion. Lawler [83] presented simulation results, where 20 % improvement of plasma efficiency in a T5 lamp can be achieved by optimizing the ^{196}Hg amount of the natural composition.

Indium exhibits two naturally occurring isotopes, i.e., ^{113}In and ^{115}In with a mixing ratio of 5 % and 95 %, respectively [81]. The emission line at 410.17 nm exhibits 4 hyperfine transitions, while the line at 451.13 nm has 6 transitions for each isotope, since the energy states $6^2S_{1/2}$, $5^2P_{3/2}$ and $5^2P_{1/2}$ feature 2, 4 and 2 hyperfine components, respectively [84]. Each hyperfine line experiences a redshift of about 0.15 pm at 410.17 nm and 0.18 pm at 451.13 nm for the heavier isotope, ^{115}In [85]. At low pressures, no overlap occurs among the hyperfine lines. Thus, they can be resolved as individual lines [86, 87], which reduces the self-absorption. All calculations in this work are based on the physical and chemical properties of the dominant ^{115}In isotope and ^{113}In is neglected. However, the same approach of mixing ratio optimization can also be adopted for indium to achieve higher plasma efficiencies.

In due consideration of wavelengths of the essential emission lines, temperature-vapor pressure characteristic, effective rate coefficients for ionization and excitation, effective decay rates due to self-absorption, and isotopic and hyperfine structures, indium proves itself as a promising substitute for mercury in low pressure fluorescent lamps.

3.2 Criteria for buffer gas

At the vapor pressure of 0.93 Pa, the mean free path of electrons is larger than the lamp dimensions. Thus, the electrons most probably travel directly to the walls of the discharge vessel and recombine at the wall than to collide with the mercury atoms. Furthermore, the electrons gain ki-

netic energy in the alternating electric field, if only collisions take place within the plasma, as explained in section 2.2.1. To reduce the wall losses of electrons and to increase the probability of collisions in the plasma, a noble gas is filled into the lamp at higher pressures than that of mercury.

However, the buffer gas pressure has to be chosen adequately [67]: At low pressures, the effect of the buffer gas on the wall losses is negligible. With increasing buffer gas pressure, the number of elastic collisions between electrons and buffer gas atoms also increases. As shown in section 2.1.5, the momentum transfer at each elastic collision between an electron and an atom is small. However, with increasing collision frequency, the total amount of kinetic energy dissipated in gas heating rises. Therefore, an optimum buffer gas pressure exists, at which the total energy loss due to the wall losses and gas heating is minimum. Since the lifetime of electrons due to the ambipolar diffusion depends on the lamp dimensions, a lower gas pressure is needed for larger diameters. Furthermore, the electron temperature depends on the equilibrium between ambipolar diffusion and elastic collision losses. The EEDF can be adjusted by the buffer gas pressure in order to favor the excitation of $6^2S_{1/2}$-state of indium over other energy states to prevent line emission at shorter wavelengths and consequently stronger Stokes' losses.

The heavier the atom, the smaller is the momentum transfer from the electron to the atom by the elastic collision. Thus, with heavier atoms, the mean free path and consequently diffusion losses of the electrons can be reduced, while the energy dissipation in gas heating decreases, as long as the lamp parameters and operating configurations, e.g., lamp dimensions and applied electric field remain constant. The noble gases can be listed with ascending atom mass as helium, neon, argon, krypton and xenon [67], whereas their breakdown voltage increases in the same order. Xenon delivers the highest plasma efficiency, yet its use is unfavorable due to its high cost. The increase of the efficiency achieved

by using krypton instead of argon is small [67]. Additionally, the breakdown of the mercury plasma with krypton as buffer gas requires a higher voltage [67, 88]. The achieved plasma efficiency with neon and helium is lower than that with argon due to their smaller atom mass. Furthermore, helium easily escapes the lamp by diffusing through the glass walls [89]. Thus, argon is employed as buffer gas in the majority of cases as well as in this work.

Chapter 4

Diagnostic methods

The spectroscopic diagnostic methods can be divided into categories based on the interactions between the plasma and the electromagnetic radiation, e.g., emission, absorption, scattering and fluorescence. The optical emission spectroscopy is the natural choice for the characterization of a light source. However, some complimentary methods, e.g., absorption spectroscopy, laser-induced fluorescence, microwave interferometry and Thomson scattering may be employed to gain information about the fundamental plasma parameters, e.g, the electron density and temperature, density of heavy particles in the ground state or excited states as well as the energy distribution functions of the investigated particles [44]. A detailed description of every technique of plasma spectroscopy is beyond the scope of this work. For further reading, the following books by Huddlestone [90], Lochte-Holtgreven [20] and Griem [91] are recommended.

In this work, spatially resolved optical emission spectroscopy (SROES) complemented with a collisional-radiative model (CRM) is employed to characterize the mercury-free surface wave driven low pressure lamps. The concept of SROES is explained in section 4.1. Furthermore, spectral irradiance measurements, a straightforward and swift emission spectroscopy technique, are used to determine the efficiency of the lamps by deriving the relation between irradiance data and radiant flux of the

lamps via a transfer standard. Section 4.2 is dedicated to the description of this method.

4.1 Concept of spatially resolved optical emission spectroscopy

Optical emission spectroscopy is the most powerful tool for the diagnostic of plasma light sources, since a broad range of plasma properties can be determined solely by its means [20, 44]: The radiant components and the unwanted impurities of a gas composition can be identified by the emission spectrum of the gas composition. Furthermore, the spectral profile of the emission lines provides information about the temperature and the density of neutral particles and charge carriers, while the continuum radiation can be used to determine the electron density. Additionally, the temporal evaluation of the plasma can be monitored and the optical thickness of the plasma can be investigated. The emission spectroscopy is non-intrusive, so the plasma remains undisturbed during the measurement, while the measurement process is not affected by the electric and magnetic fields driving the plasma at a given frequency.

However, the measured data does not deliver the plasma parameters directly, but it has to be be interpreted. Therefore, it requires a general conception of the plasma state [20]. For plasmas in thermal equilibrium, the plasma state is easy to describe. Yet, for a plasma without thermodynamic equilibrium, optical emission spectroscopy must be complemented with a suitable plasma model to derive the plasma parameters. If the plasma density exceeds the given limit for coronal equilibrium, a complicated collisional-radiative model (CRM) should be employed [90]. The CRM, developed and used for this work, is presented in chapter 5.

Additionally, the spatial distribution of the aforementioned plasma properties can be identified by scanning the discharge vessel spatially. And most importantly, the plasma efficiency can be determined without a goniometric setup. The experimental setup, assembled and used for this work, is presented in chapter 6.

The SROEM is valid under some conditions, e.g., an optically thin plasma and a radial profile suitable for inverse Abel transformation. These conditions are explained in the following section, while the validity check on the basis of theoretical calculations and experimental data can be found in section 7.1.

4.1.1 Spatially resolved determination of radiance

The line integral of the spectral emission coefficients $\epsilon(\lambda, r)$ [$\mathrm{W \cdot m^{-3} \cdot nm^{-1} \cdot sr^{-1}}$] along a straight observation line through the cross section of the lamp can be measured as spectral radiance $L_\lambda(\lambda, y)$ [$\mathrm{W \cdot m^{-2} \cdot nm^{-1} \cdot sr^{-1}}$] at the perpendicular distance y from the lamp axis for a given wavelength λ.

$$L_\lambda(\lambda, y) = \int_y^R \epsilon(\lambda, r) \exp\left(-\int_r^R \alpha(\lambda, r')\, dr'\right) dr, \qquad (4.1)$$

where r is the radial distance from the central axis of the lamp, R is the radius of the discharge vessel and Ω is the solid angle. As the radiation crosses through the plasma, the emitted photons undergo absorption, which can be described by the spectral absorption coefficient $\alpha(\lambda, r)$. The spectral emission and absorption coefficients as a function of radial distance r as well as the spectral radiance as a function of perpendicular distance y from the lamp axis are illustrated in figure 4.1.
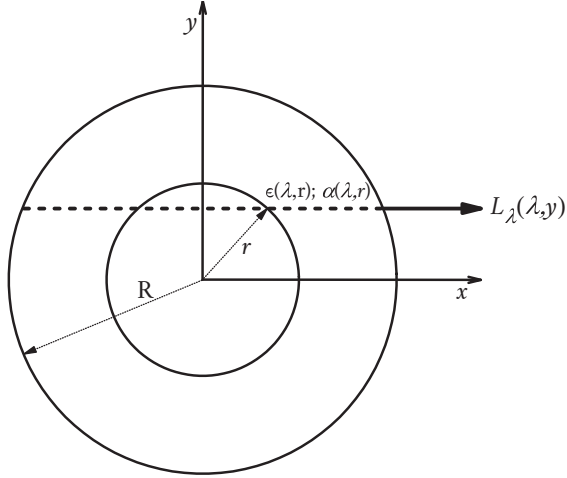
Figure 4.1: Illustration of the spectral emission and absorption coefficients as a function of radial distance, and the spectral radiance as a function of perpendicular distance to the lamp axis.

According to Summers [92], $\epsilon(\lambda, r)$ can be assumed as $\epsilon(\lambda, r) = \epsilon_\lambda \, \Psi_\epsilon(\lambda) \, f_\epsilon(r)$, where $\epsilon_\lambda \, [\text{W·m}^{-3}\text{·sr}^{-1}]$ is the line emission coefficient, $f_\epsilon(r)$ is the radial variation of ϵ_λ inside the discharge vessel and $\Psi_\epsilon(\lambda)$ is the spectral line emission profile, which is normalized to $\int_{-\infty}^{\infty} \Psi_\epsilon(\lambda) \, d\lambda = 1$.

Analogously, $\alpha(\lambda, r)$ can be replaced by $\alpha(\lambda, r) = \alpha_\lambda \, \Psi_\alpha(\lambda) \, f_\alpha(r)$, where $f_\alpha(r)$ is the radial distribution of the spectral absorption coefficient and α_λ is the absorption coefficient integrated over the spectral line with the profile $\Psi_\alpha(\lambda)$, where $\int_{-\infty}^{\infty} \Psi_\alpha(\lambda) \, d\lambda = 1$.

With the assumption of cylindrical symmetry, optically thin plasma and that $\epsilon(r)$ vanishes for $r > R$, the exponential part of equation (4.1) can be neglected, and $\epsilon(r)$ can be reconstructed from the measured $L_\lambda(y)$ by means of Abel's inversion as given in equation (4.2) [20].

$$\epsilon(r) = -\frac{1}{\pi} \int_r^R \frac{\mathrm{d}L_\lambda(y)}{\mathrm{d}y} \frac{\mathrm{d}y}{\sqrt{y^2 - r^2}}. \tag{4.2}$$

For an m = 0-mode surface-wave driven low pressure plasma in a cylindrical geometry, cylindrical symmetry is a safe assumption. However, the validity of optically thin plasma should be theoretically proved.

4.1.2 Self absorption and "Escape factor" concept

An easy way to determine the opacity of a low pressure plasma for a given wavelength λ is the calculation of the escape factor Θ_λ, which gives the mean probability that a photon emitted in the plasma travels to the discharge vessel wall in any direction and leaves the plasma in a single flight without absorption or scattering [76, 93].

Summers [92] introduced equation (4.3) to calculate the escape factor for a line of sight perpendicular to the central axis of the lamp as the ratio of the radiance with and without absorption.

$$\Theta_\lambda = \frac{\int_{-R}^R \int_{\lambda-\Delta\lambda}^{\lambda+\Delta\lambda} \epsilon_\lambda \Psi_\epsilon(\lambda) f_\epsilon(r) \exp\big((r-R)\alpha_\lambda \Psi_\alpha(\lambda) f_\alpha(r)\big)\, \mathrm{d}\lambda\, \mathrm{d}r}{\int_{-R}^R \int_{\lambda-\Delta\lambda}^{\lambda+\Delta\lambda} \epsilon_\lambda \Psi_\epsilon(\lambda) f_\epsilon(r)\, \mathrm{d}\lambda\, \mathrm{d}r}. \tag{4.3}$$

Nonetheless, the opacity of the plasma depends on the probability that an emitted photon eventually leaves the discharge vessel regardless of the number of re-absorptions and re-emissions until it reaches the wall of the discharge vessel. Therefore, an effective escape factor $\Theta_\lambda^{\mathrm{eff}}$ should be considered as given by equation (4.4) [94].

$$\Theta_\lambda^{\text{eff}} = \frac{\Theta_\lambda}{1 - (1 - \epsilon_{\text{rem}})(1 - \Theta_\lambda)}, \tag{4.4}$$

where ϵ_{rem} is the so-called removal factor, which gives the probability that a photon is completely removed from the plasma in the re-absorption or scattering event due to a non-radiative process, e.g., collisional de-excitation of the absorber to a lower energy state [94]. For $\epsilon_{\text{rem}} = 1$, $\Theta_\lambda^{\text{eff}}$ is equal to Θ_λ, while every photon ultimately escapes the plasma for $\epsilon_{\text{rem}} = 0$.

Thus, for the calculation of the effective escape factor, line absorption coefficients, spectral line absorption profile and the rate coefficients of non-radiative plasma processes concerning the radiating particles are required.

4.1.3 Determination of absorption coefficient and line profile

The line absorption coefficient α_λ is a dimensionless quantity and can be calculated via the Ladenburg relation [95], as given in equation (4.5).

$$\alpha_\lambda = n_j \frac{g_k}{g_j} \frac{\lambda^4}{c} \frac{A_{kj}}{8\pi}, \tag{4.5}$$

where g_k and g_j are the statistical weights of the higher k and lower j states of the optical transition, respectively, n_j is the absorber density in the lower state j, c is the speed of light, A_{kj} is the corresponding Einstein coefficient of spontaneous emission.

The recorded spectra of the emission lines feature a line profile, which results from the convolution of the source line profile and instrument profile. The instrumental broadening arises from the spectral resolution

of the measurement system and has no influence on the self-absorption of radiation in plasma. Thus, only the source line profile $\Psi_\lambda(\lambda)$ should be considered, which results from line broadening mechanisms in the plasma, e.g., natural, Doppler and pressure broadening. The latter can be divided into three subgroups, viz., Stark broadening, van der Waals broadening and resonance broadening. The Stark effect describes the perturbation of the radiating particle in the Coulomb field of a charge carrier [96]. Similarly, a dipole induced interaction can be observed in the vicinity of neutral particles due to the van der Waals force [96]. Finally, if the initial or the final energy state of the transition resulting in the emission line is connected to the ground state of the emitting particle via dipole radiation and if the emitting particle is surrounded with particles of the same kind in the ground state, then the resonance broadening arises due to the dipole-dipole interaction [97].

According to Thorne [96], the Doppler and natural broadening have the strongest contributions to the line profile in low pressure plasmas and pressure broadening can be neglected. Furthermore, the absorption and re-emission cycle of photons may lead to the spectral redistribution of energy [96]. However, this effect is neglected for this work and only the intrinsic line profiles are considered. If the particles in excited and ground state follow different kinetic energy distributions, then differing line profiles should be used for emission and absorption. In low pressure plasmas, this effect can also be neglected.

Natural broadening

Natural broadening is caused by the finite lifetime of the excited energy states of the radiating particle. According to the energy-time uncertainty principle, the line width cannot be infinitely narrow, since the lifetimes

and the energies of the higher and lower energy states of the optical transition can be determined simultaneously only with the uncertainty of $\Delta E \Delta t = \hbar$ [96, 98]. Thus, the FWHM of natural broadening $\Delta\lambda_{\text{Natural}}$ is calculated by considering the mean lifetimes of relevant energy states as given in

$$\Delta\lambda_{\text{Natural}} = \frac{\lambda_0{}^2}{2\pi c} \left(\frac{1}{\tau_k} + \frac{1}{\tau_j} \right), \tag{4.6}$$

where λ_0 is the central wavelength of the emission line, and τ_k and τ_j are the lifetimes of the higher and lower energy states of the spontaneous emission, respectively. The natural lifetime of an energy state is calculated as the inverse sum of the decay rates to lower states as given in equation (4.7) [98].

$$\tau_k = \frac{1}{\sum_j A_{kj}}. \tag{4.7}$$

The broadening profile $\Psi_{\text{Natural}}(\lambda)$ has a Lorentzian shape and is calculated by

$$\Psi_{\text{Natural}}(\lambda) = \frac{1}{\pi} \frac{\Delta\lambda_{\text{Natural}}/2}{(\lambda - \lambda_0)^2 + (\Delta\lambda_{\text{Natural}}/2)^2}. \tag{4.8}$$

According to equations (2.20) and (4.7), the FWHM of natural broadening decreases with decreasing frequency very rapidly. Thus, the contribution of the natural broadening in UV-region is significant, while it presents the lower limit for broadening in VIS-region [96].

Doppler broadening

Doppler broadening is the wavelength shift due to the thermal motion of radiating particles with regard to the observer [96]. Doppler broadening

features the same profile as the energy distribution function of the radiating species. With the assumption that the gas particles in plasma exhibit a Maxwellian energy distribution, the broadening profile $\Psi_{\text{Doppler}}(\lambda)$ has a Gaussian line shape as given by

$$\Psi_{\text{Doppler}}(\lambda) = \frac{2}{\Delta\lambda_{\text{Doppler}}}\sqrt{\frac{\ln 2}{\pi}}\exp\left(-4\ln 2\frac{(\lambda - \lambda_0)^2}{\Delta\lambda_{\text{Doppler}}^2}\right), \qquad (4.9)$$

with the FWHM

$$\Delta\lambda_{\text{Doppler}} = 2\lambda_0\sqrt{\frac{2k_{\text{B}}T_{\text{g}}\ln 2}{mc^2}}, \qquad (4.10)$$

where T_{g} is the temperature of excited neutral particles, k_{B} is the Boltzmann constant and m is the mass of the radiating particle [98].

Combination as Voigt profile

The combined contribution of both broadening mechanisms can be taken into account by the convolution of Gaussian and Lorentzian line shapes, resulting in the so-called Voigt profile [20, eq. 51] as given in equation (4.11), which cannot be solved analytically.

$$\Psi_{\text{Voigt}}(\lambda) = \int_{-\infty}^{\infty} \Psi_{\text{Natural}}(\lambda)\Psi_{\text{Doppler}}(\lambda - \lambda')\,d\lambda'. \qquad (4.11)$$

Figure 4.2 displays a comparison of Lorentzian, Gaussian and Voigt line profiles. The Lorentzian and the Gaussian profiles are calculated with a FWHM of $\Delta\lambda_{\text{Natural}} = 1$ nm and $\Delta\lambda_{\text{Doppler}} = 2$ nm, respectively. All profiles are area-normalized. It should be noted that the FWHMs are chosen for a good illustration and are not realistic for low pressure plasmas. The Gaussian profile features an exponential decay on the wings with

$\exp(-\Delta\lambda^2)$, while Lorentzian profile has a decay with $\Delta\lambda^{-2}$ [20]. Thus, the wings of the resulting Voigt profile follows that of the Lorentzian [96], while the FWHM of the Voigt profile is determined by the Gaussian [96].
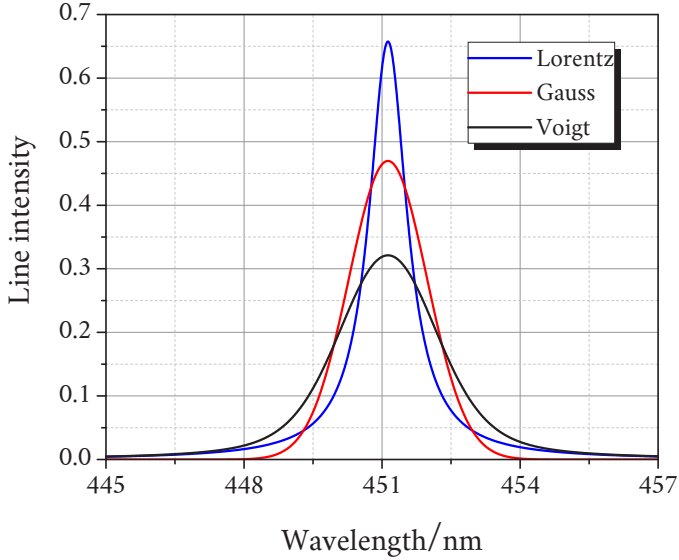
Figure 4.2: Comparison of Lorentzian, Gaussian and Voigt line profiles. The Lorentzian and Gaussian profiles feature a FWHM of $\Delta\lambda_{\text{Natural}} = 1\,\text{nm}$ and $\Delta\lambda_{\text{Doppler}} = 2\,\text{nm}$, respectively. All profiles are area-normalized. It should be noted that the FWHMs are chosen for a good illustration and are not realistic for low pressure plasmas.

4.1.4 Abel inversion and determination of emission coefficients

If the optical thinness of the plasma can be validated, one can solve equation (4.2) to determine the line emission coefficients from measured radiance data. However, for optically thick plasmas, more complex solutions, such as introduced by Young [99] and Ding [100] should be employed.

In any case, $L_\lambda(\lambda, y)$ is not obtained experimentally as an analytical formula, but a set of discretized measurement values, which rule out the analytical differentiation and integration in equation (4.2). Therefore, a number of numerical methods were proposed in the last decades to solve the Abel's integral equation, e.g., by means of iterative, integral transform and curve fitting techniques. Since the radiance at the edge of the plasma is hard to measure accurately, iterative techniques cause an accumulation of errors and lead to larger errors on the axis of the plasma [20, 101]. Furthermore, the surface wave driven plasmas tend to feature off-axis peaks near the discharge vessel wall, which can complicate the reconstruction of the radial profile of the emission coefficients. Curve fitting can be performed by employing orthogonal polynomials, by assuming a Gaussian profile or by using polynomial as well as spline fitting methods. Integral transformation technique is based on the expansion of the unknown radial profile in a series of basis functions, such as Fourier series.

Buie [101] compared these techniques using test functions and experimental data with regard to their stability and accuracy for optical emission spectroscopy. To fit the whole set of measurement data with a 6th or 8th order polynomial function, which contains only the even powers of y, and then to integrate the function analytically proves to be the most effective technique. This method provides three advantages [101]: First, with data fitting, the missing data at the edge of the plasma can be extrapolated. Secondly, the set of measurement data is smoothed against noise dur-

ing the curve fitting and lastly, the analytical calculation of the inversion is easy to perform. Considering that the measurement setup presented in section 6.4 have a high spatial resolution, a large number of measurement points and thereby an accurate curve fitting can be achieved. Also, the processing capacity of today's computers allows a very fast curve fitting with higher order polynomials by means of least square method.

However, smoothing can sometimes filter the real information along with the statistical noise [101]. According to Pretzler [102], even the order of the magnitude of the resulting error due to the incorrect smoothing cannot be estimated correctly. Thus, smoothing must be avoided. He compared five numerical methods for Abel inversion including his own method based on the expansion of the unknown radial profile of ϵ_λ in a series of cosine-functions [103]. His method is derivative free and smoothing can be avoided, since it acts as a low pass filter. In this work, both the curve fitting and cosine-expansion methods are used to validate the applicability of the Abel inversion.

After solving inverse Abel's equation, the characteristic plasma parameters, e.g., T_e and n_e can be determined by comparing the experimentally obtained line emission coefficients with the simulated ones from the model.

4.2 Determination of total radiant flux and plasma efficiency

The radiant flux of a lamp can be measured either in a spatially integrated or spatially resolved manner. The former is performed by means of an Ulbricht-sphere, while for the latter, a goniometric setup is needed,

where the radiant intensity distribution is measured on a virtual surface around the lamp and integrated numerically.

The microwave radiation from the surface wave launcher into the surrounding prevents the use of the Ulbricht-sphere, which has a metal chassis. A goniometer on the other hand is a complex and unpractical setup. Therefore, the following method is introduced to determine the radiant flux of the investigated lamps: The derived line emission coefficients are integrated over the whole discharge vessel volume V_{Lamp} and whole solid angle Ω to calculate the radiant flux Φ_λ for the given wavelength λ, as given by equation (4.12), assuming that the emission is isotropic.

$$
\begin{aligned}
\Phi_\lambda &= \int_\Omega \int_V \epsilon_L(r, l) \, dV \, d\Omega \\
&= \int_\Omega \int_0^{2\pi} \int_0^L \int_0^R \epsilon_L(r, l) r \, dr \, dl \, d\phi \, d\Omega \quad\quad (4.12) \\
&= 8\pi^2 \int_0^L \int_0^R \epsilon_L(r, l) r \, dr \, dl.
\end{aligned}
$$

Yet, the spatially resolved measurement of L_λ is a very time-consuming method as explained in section 6.4. Thus, it is unsuitable for a systematic investigation of lamp parameters and operating configurations, e.g., buffer gas pressure, electrical input power and cold spot temperature. Furthermore, as mentioned in section 6.4, the telescopic optical probe, which is responsible for the measurement of the radiance, is only sensitive down to 368 nm. Hence, only the two emission lines of indium at 410.17 nm and 451.13 nm can be observed. Yet, for the determination of total radiant flux Φ_{total}, the emission lines of indium at lower wavelengths down to 250 nm must also be considered. Therefore, the following method is adopted: Spectral irradiance measurements are carried out between the wavelengths 200 nm and 800 nm and subsequently irradiance E_{451} of the emission line at 451.13 nm is calculated. A conversion

factor ξ_{con} between radiant flux and irradiance is determined by equation (4.13) for a single emission line.

$$\xi_{con} = \frac{\Phi_{451}}{E_{451}}. \tag{4.13}$$

The conversion factor is then multiplied with the total irradiance for all emission lines of indium, assuming all emission lines are optically thin. The total radiant flux Φ_{total} is calculated by equation (4.14).

$$\Phi_{total} = \xi_{con} \sum_{\lambda} E_{\lambda}. \tag{4.14}$$

Finally, the plasma efficiency is calculated by dividing the total radiant flux by the microwave power accepted by the microwave coupler P_{acc}, as given by equation (4.15).

$$\eta_{Pl} = \frac{\Phi_{total}}{P_{acc}}. \tag{4.15}$$

A detailed description of the power balance of the microwave coupler can be found in section 6.2.

Chapter 5

Collisional-radiative model (CRM) for indium(I)iodide-argon plasma

The development of a theoretical model for indium(I)iodide-argon plasmas is important for a deeper understanding of generation and loss processes and allows the accurate interpretation of experimentally obtained data. Hence, it supports the investigations to find the optimum discharge conditions and increase the plasma efficiency.

In this chapter, a collisional-radiative model (CRM) of a low pressure plasma based on indium(I)iodide-argon system is introduced. The objective of this model is to determine the fundamental plasma parameters, e.g., electron, ion and excited particle densities as a function of electron temperature at varied lamp parameters, i.e., argon buffer gas pressure p_{Ar} and cold spot temperature T_{CS}, which is the coldest point of the discharge vessel. The presented model can also predict the line emission coefficients of essential emission lines of indium for given electron temperatures and densities, thus allowing to characterize lamps with indium(I)iodide and argon filling by means of non-intrusive spectroscopic measurements. The diagnostic method is described in chapter 4 in detail.

The fundamentals of the CRM and the methods to calculate the needed cross sections for generation processes are explained in section 5.1 and section 5.2, respectively. The calculated cross sections and rate coefficients for generation processes are presented in section 5.3, while that of secondary processes can be found in section 5.4. Section 5.5 details the lifetimes of relevant particles due to free and ambipolar diffusion. Section 5.6 is devoted to the presentation of the rate balance equations. Finally, in section 5.7 the calculated results are presented and analyzed in detail.

5.1 Theoretical basis of the model

The law of equipartition among the energy states does not prevail in low pressure plasmas in general lighting applications due to the absence of thermal equilibrium. Thus, the distribution of population densities in different energy states cannot be calculated without knowledge of atomic cross sections [90, p. 203]. Every relevant process should be described with its corresponding rate coefficient and rate balance equations should be formed to calculate the population densities. The selection of relevant processes relies on the particle densities in the plasma. For extremely small electron and atom densities, a corona state can be assumed for the plasma, where collisional ionization and excitation are balanced by the radiative recombination and spontaneous emission, respectively [20, 90]. However, higher particle densities than the given limits for coronal equilibrium $n_e, n_H \geq 1 \cdot 10^{17}$ m^{-3} are achieved in general lighting plasmas [104]. Thus, a more complex model based on collisional and radiative processes inside the plasma is adopted: The electron impact excitation and ionization processes from ground and metastable states are considered. Since molecular indium(I)iodide with a density of

$n_{\mathrm{InI}} \geq 1 \cdot 10^{18} \mathrm{~m}^{-3}$ is present in the modeled plasma, the dissociation and ionization of molecular particles are also considered. However, the vibrational and rotational excitation of molecules are neglected. Secondary processes, i.e., collisional de-excitation of excited particles, three-body recombination of atomic ions and direct-dissociative recombination of molecular ions are also included in the model. Generation and loss processes concerning negative ions, e.g., electron detachment and associative detachment are yet neglected.

According to Sobel'man [37], equation (2.23) can be adapted to calculate the rate coefficient $K(T_{\mathrm{e}})$ of a particular electron impact process with the threshold energy E_{th} as

$$K(T_{\mathrm{e}}) = \int\limits_{E_{\mathrm{th}}}^{\infty} Q(E)\sqrt{\frac{2E}{m_{\mathrm{e}}}} f_{\mathrm{M}}\,(E, T_{\mathrm{e}})\,\mathrm{d}E, \qquad (5.1)$$

where $Q(E)$ is the cross section, $f_{\mathrm{M}}\,(E, T_{\mathrm{e}})$ is the Maxwellian electron energy distribution function (EEDF) and E is the energy of the incident electrons.

For low electron densities, the rate of Coulomb electron-electron collisions is usually small in order to bring the low and high energy electrons to an equilibrium. It results in a departure from Maxwellian EEDF. The absence of balance between generation and loss processes, e.g., electron impact ionization of an atom and three-body recombination of the corresponding ion, leads to a further departure from Maxwellian EEDF, since the strongest loss mechanism in low pressure plasmas is the wall losses due to the ambipolar diffusion. Godyak [105] discussed different non-equilibrium EEDFs, e.g., Druyvesteyn or bi-Maxwellian, depending on the discharge conditions.

However, Godyak [105] stated that the EEDF approaches to Maxwellian with increasing operating frequency, buffer gas pressure and electron

density for low electron temperatures, where the electron-electron collision frequency $\nu_{ee} \sim n_e T_e^{-3/2}$. Although the highest operating frequency investigated by Godyak was 13.56 MHz at a maximum pressure of 1.3 Pa and with an electron density of about $1 \cdot 10^{17}\,\mathrm{m}^{-3}$, the measured EEDF became nearly Maxwellian.

The buffer gas pressures investigated in this work lie in a range between 100 Pa and 800 Pa. These relatively high buffer gas pressures reduce the ambipolar diffusion inside the lamp significantly and result in electron densities $> 1 \cdot 10^{17}\,\mathrm{m}^{-3}$. Furthermore, the relatively high frequency of elastic collisions between electrons and buffer gas atoms results in a stronger kinetic energy transfer and in the normalization of the energy distribution of the electrons. Electron temperatures about of 1 eV are achieved, as will be shown in section 7.2. Additionally, the mercury-free lamps are driven in this work at an operating frequency of 2.45 GHz. Therefore, for the plasma modeling, a Maxwellian EEDF is assumed.

For the excited states of indium that are optically accessible from ground and metastable states, a coronal balance between the electron impact excitation and the relaxation of the excited atoms by spontaneous emission is assumed due to the short lifetimes of these states. Such a kinetic model with collisional-radiative and coronal equilibrium parts was already adopted by Cotrino [106] to determine the electron temperature of a microwave driven argon plasma by means of emission spectroscopy with good accuracy.

However, even with the coronal balance, the contribution of metastable states to the radiation generation should be considered, since the electron density may lie between the given limits for the extended corona model, as $1 \cdot 10^{17}\,\mathrm{m}^{-3} \leq n_e \leq 1 \cdot 10^{19}\,\mathrm{m}^{-3}$ [104], in the investigated plasmas for high power densities.

Thus, the rate equation for spontaneous emission can be written as

$$n_e n_g{}_e^g K^k \left(T_e\right) + n_e n_m{}_e^m K^k \left(T_e\right) = n_k \sum_{j=1}^{k-1} A_{kj}, \tag{5.2}$$

where n_g, n_m and n_k are the atom densities in the ground state g, metastable state m and excited state k, respectively, ${}_e^{g,m} K^k \left(T_e\right)$, is the electron impact excitation rate coefficient from the ground or metastable state into the excited state k, T_e is the electron temperature and A_{kj} is the Einstein coefficient of the spontaneous emission from the excited state k into a lower energy state j.

Nomenclature of the model

For a simple description of a broad range of processes, a nomenclature according to Gryziński [107] is adopted for the cross section Q, as illustrated in figure 5.1.
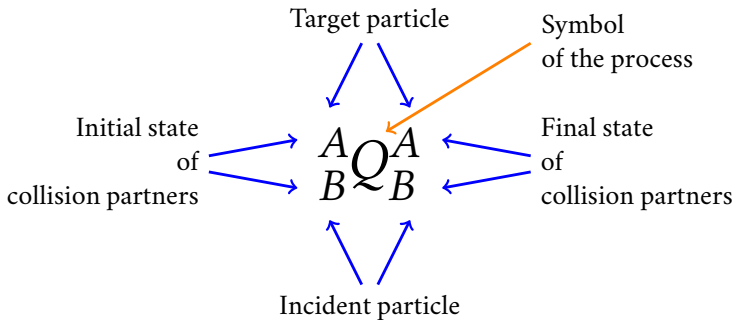
Figure 5.1: Adopted nomenclature for the description of the collision processes.

On the left hand side of cross section symbol Q, the initial states of collision partners are given. The left bottom index describes the initial state

of incident particle and the top left index that of the collision partner. On the right hand side, the indices of the final states of collision partners can be found. The absence of an index on the right hand side means, that the state of the given particle haven't changed after the collision.

Thereby, $^g_e Q^k (E)$ corresponds to the electron impact excitation cross section from ground state g into excited state k. The same nomenclature is extended also to the rate coefficients of generation and secondary processes.

5.2 Cross sections and rate coefficients

As can be seen from equation (5.1), the electron impact cross section of each process is needed to calculate the rate coefficient. Unfortunately, a comprehensive investigation was not undertaken for the materials selected as substitutes of mercury. No experimental cross sections for electron impact dissociation or ionization process of indium(I)iodide were found. Additionally, the excitation cross sections into the metastable states and ionization cross sections from metastable states were not found for atomic indium. Furthermore, the measured electron impact excitation cross sections of indium into optically accessible excited states can only be found in one reference [108]. Unfortunately, these cross sections show inconsistencies considering excitation energies and Einstein coefficients of the corresponding energy states. According to Heddle [109], the discrepancies can be explained with a stray light problem within the measurement setup of Shimon [108].

Therefore, a theoretical method has to be adopted to calculate the cross sections for generation processes. According to Bauer [110], the Gryziński method [107] delivers the most accurate cross sections compared to

the methods, introduced by Drawin and Thomson [111, 112]. The Gryziński method is derived from semiclassical mechanics.

5.2.1 Gryziński method

The Gryziński method considers the ionization and excitation process of an atom as the collision of a free incident electron with a bound orbital electron [107]. The cross section of this collision is given by

$$Q(E) = \xi_{\mathrm{j}} \cdot \frac{\varsigma_0}{E_{\mathrm{th}}^2} \cdot g_Q \left(\frac{\mathcal{E}}{E_{\mathrm{th}}}, \frac{E}{E_{\mathrm{th}}} \right), \tag{5.3}$$

where $\mathcal{E}$ is the kinetic energy of the orbital electron. For ionization, the binding energy E_{b} and for excitation, the energy difference between the initial j and final state k of excitation ΔE_{jk} should be used as the threshold energy E_{th}. For the bound electron in the utmost orbital of an atom, E_{b} is equal to the ionization energy E_{i}. An inelastic collision occurs, if only E exceeds the corresponding E_{th}. ξ_{j} is the number of the orbital electrons in the initial energy state j. ς_0 is a constant, calculated by

$$\varsigma_0 = 4\pi a_0^2 R_{\mathrm{H}}^2, \tag{5.4}$$

where R_{H} is the Rydberg constant and a_0 is the Bohr radius.

For light particles, e.g, electron and positrons, the function g_Q is calculated by

$$\begin{aligned}
g_Q \left(\frac{\mathcal{E}}{E_{\mathrm{th}}}, \frac{E}{E_{\mathrm{th}}} \right) &= f_{\overline{v}}(\mathcal{E}, E) \cdot \left(1 - \frac{E_{\mathrm{th}}}{E} \right)^{1 + \frac{\mathcal{E}}{\mathcal{E} + E_{\mathrm{th}}}} \\
&\times \left[\frac{E_{\mathrm{th}}}{\mathcal{E}} + \frac{2}{3} \left(1 - \frac{E_{\mathrm{th}}}{2E} \right) \ln \left(e_{\mathrm{Eu}} + \left(\frac{E - E_{\mathrm{th}}}{\mathcal{E}} \right)^{\frac{1}{2}} \right) \right],
\end{aligned} \tag{5.5}$$

with

$$f_{\bar{v}}(\mathcal{E}, E) = \frac{\mathcal{E}}{E} \cdot \left(\frac{E}{E + \mathcal{E}}\right)^{\frac{3}{2}},$$

where e_{Eu} is the Euler's number [113]. Equation (5.5) is cited from [113], since it is given incorrectly in [107].

5.2.2 Simplified Gryziński method

The kinetic energy of orbital electrons $\mathcal{E}$ is not available in the literature for the considered species except indium. Thus, the Gryziński method was simplified with the assumption that $\mathcal{E}$ is equal to E_{b} [107, p. A341].

Ionization

For the calculation of the electron impact ionization cross sections , the simplified Gryziński method [107], as given in equation (5.6) was used.

$$Q(E) = \xi_{\mathrm{j}} \cdot \frac{\varsigma_0}{E_{\mathrm{th}}^2} \cdot g_Q\left(\frac{E_{\mathrm{b}}}{E_{\mathrm{th}}}, \frac{E}{E_{\mathrm{th}}}\right). \tag{5.6}$$

For the sake of consistency, the simplified form of the Gryziński method was also adopted to calculate the ionization cross sections of indium, although $\mathcal{E}$ could be found for indium in the literature. The threshold energy E_{th} is replaced with the binding energy E_{b} and with the reduced kinetic energy $E_{\mathrm{rk}} = E/E_{\mathrm{b}}$, equation (5.6) is simplified to

$$_e^jQ_{2e}^i(E) = \xi_{\mathrm{j}} \cdot \frac{\varsigma_0}{E_{\mathrm{b}}^2} \cdot g_{Q_{\mathrm{i}}}(E_{\mathrm{rk}}), \tag{5.7}$$

with

$$g_{Q_{\mathrm{i}}}(E_{\mathrm{rk}}) = \frac{1}{E_{\mathrm{rk}}} \left(\frac{E_{\mathrm{rk}} - 1}{E_{\mathrm{rk}} + 1}\right)^{\frac{3}{2}} \cdot \left[1 + \frac{2}{3}\left(1 - \frac{1}{2E_{\mathrm{rk}}}\right) \ln\left(e_{\mathrm{Eu}} + \sqrt{E_{\mathrm{rk}} - 1}\right)\right].$$

The used binding energies of orbital electrons in relevant orbitals of argon, indium and iodine atom and averaged kinetic energies of orbital electrons of indium are listed in table 5.1.

Table 5.1: Binding energies of orbital electrons in relevant orbitals of argon, indium and iodine atoms ($<$ 200 eV) [114] and kinetic energies of orbital electrons of indium [115].

Ar	E_b / eV:	4.04	4.21	15.76	16.20	35.00
	Orbital conf.:	$4s_{1/2}$	$4s_{3/2}$	$3p_{3/2}$	$3p_{1/2}$	3s
In	E_b / eV:	5.52	5.79	10.79	27.13	28.09
	$\mathcal{E}$ / eV:	-	26.10	50.93	277.94	284.85
	Orbital conf.:	$5p_{3/2}$	$5p_{1/2}$	5s	$4d_{5/2}$	$4d_{3/2}$
In	E_b / eV:	95.17	102.13	144.46		
	$\mathcal{E}$ / eV:	426	454.83	516.24		
	Orbital conf.:	$4p_{3/2}$	$4p_{1/2}$	4s		
I	E_b / eV:	10.45	11.39	23.86	61.91	63.74
	Orbital conf.:	$5p_{1/2}$	$5p_{3/2}$	5s	$4d_{5/2}$	$4d_{3/2}$
I	E_b / eV:	148.33	159.72			
	Orbital conf.:	$4p_{3/2}$	$4p_{1/2}$			

Excitation

Gryziński [107] has proposed equation (5.8) to calculate the excitation cross section $_e^jQ^k$ from a lower state j into a higher state k. Equation (5.8) states that $_e^jQ^k$ decreases with increasing probability of an excitation into the next possible energy state k + 1 for incident electron energies $E \geq \Delta E_{j(k+1)}$.

$$\substack{j\\e}Q^{k}(E) = Q\left(\frac{E_b}{\Delta E_{jk}}, \frac{E}{\Delta E_{jk}}\right) - Q\left(\frac{E_b}{\Delta E_{j(k+1)}}, \frac{E}{\Delta E_{j(k+1)}}\right). \tag{5.8}$$

Furthermore, according to Gryziński, an electron exchange process should also be considered for low electron energies. The incident electron gains energy in the Coulomb field of the nucleus. It can cause a collision, at which the orbital electron gains a higher energy than the binding energy and is ejected from the atom, while the incident electron cannot escape the potential of the nucleus, thus an exchange of electrons takes place. If the incident electron has a higher energy than ΔE_{jk} after the collision, then the exchange process results in an excitation. The probability of an exchange process is given by the exchange cross section Q^{exch}:

$$
\begin{aligned}
Q^{\text{exch}}\left(\frac{E_b}{\Delta E_{jk}}, \frac{E_b}{\Delta E_{j(k+1)}}, \frac{E}{\Delta E_{jk}}\right) &= \frac{\varsigma_0}{\Delta E_{jk}^2}\frac{\Delta E_{j(k+1)} - \Delta E_{jk}}{\Delta E_{jk}} \\
&\times g_{Q_{\text{exch}}}\left(\frac{E_b}{\Delta E_{jk}}, \frac{E_b}{\Delta E_{j(k+1)}}, \frac{E}{\Delta E_{jk}}\right),
\end{aligned}
\tag{5.9}
$$

with

$$
g_{Q_{\text{exch}}}\left(\frac{E_b}{\Delta E_{jk}}, \frac{E_b}{\Delta E_{j(k+1)}}, \frac{E}{\Delta E_{jk}}\right) =
\begin{cases}
\dfrac{\Delta E_{jk}^2}{(E + E_b)(E + E_b - \Delta E_{jk})} & \text{for} \\
\times \dfrac{\Delta E_{jk}}{E_b}\dfrac{E - \Delta E_{jk}}{\Delta E_{j(k+1)} - \Delta E_{jk}} & E < \Delta E_{j(k+1)}, \\
\dfrac{\Delta E_{jk}^2}{(E + E_b)(E + E_b - \Delta E_{jk})} & \text{for} \\
\times \dfrac{\Delta E_{jk}}{E + E_b - \Delta E_{j(k+1)}} & E > \Delta E_{j(k+1)}.
\end{cases}
$$

Thus, the effective excitation cross section is given by equation (5.10)

$$
{}_e^j Q^k(E) = Q\left(\frac{E_b}{\Delta E_{jk}}, \frac{E}{\Delta E_{jk}}\right) - Q\left(\frac{E_b}{\Delta E_{j(k+1)}}, \frac{E}{\Delta E_{j(k+1)}}\right)
$$
$$
+ Q_{exch}\left(\frac{E_b}{\Delta E_{jk}}, \frac{E_b}{\Delta E_{j(k+1)}}, \frac{E}{\Delta E_{jk}}\right).
$$

(5.10)

By the calculation of the excitation cross sections, only the electrons in the utmost orbital are considered.

5.2.3 Extended Gryziński method for molecules

For this model, electron impact ionization and dissociation of indium(I)-iodide molecules should be considered. However, the Gryziński method can be applied only to atoms. For that reason, Bacri [30] and Teulet [31] have extended it to diatomic molecules, considering the potential energy curves of molecules and molecule ions.

Dissociation

The potential curves of indium(I)iodide molecule are displayed in figure 5.2 for different rotational states of the ground electronic and ground vibrational state. The needed molecular constants and atomic masses were taken from [24, 71, 116]. The rotational state J_L defines the lowest potential curve without a potential minimum. In this state, atoms experience only a repulsive force and the molecule dissociates.

This state was defined by Bacri [30] as the dissociation condition for molecules:

$$\frac{\partial U\left(T^{\text{el}}, v, J, r\right)}{\partial r} \overset{!}{<} 0 \quad \text{for all } r \geq 0. \tag{5.11}$$
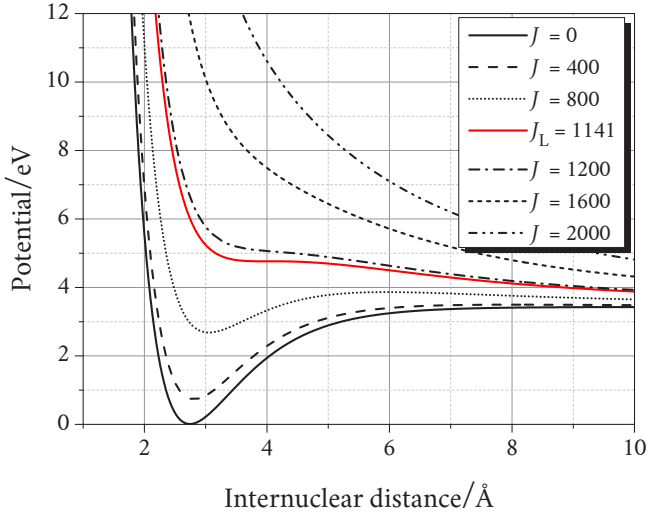
Figure 5.2: Potential curves of indium(I)iodide molecule in different rotational states of the ground electronic and ground vibrational state as a function of internuclear distance.

Thus, the energy threshold ΔE_{jk} for electron impact dissociation is defined by

$$\Delta E_{\text{jk}} = U\left(0, 0, J_{\text{L}}, r\right) - U\left(0, 0, 0, r\right). \tag{5.12}$$

The binding energy E_{b} can be determined in a similar way. Since this model neglects vibrational and rotational excitation, the ground state of the molecular ion is used to calculate E_{b}:

$$E_{\text{b}} = U_{\text{i}}\left(E_{\text{ad}}, 0, 0, r\right) - U\left(0, 0, 0, r\right), \tag{5.13}$$

where U_i is the potential curve of the molecular ion and E_{ad} is the adiabatic ionization energy of the molecule.

But it should be kept in mind that, according to Mishra [71], the valence electrons of indium(I)iodide form an $X^1\Sigma^+$-orbital, consisting of two suborbitals σ^4 and π^4. Mishra [71] stated that the indium(I)iodide ion takes the $A^2\Sigma^+$- or $X^2\Pi$-state, if an electron is removed from the σ- or π-suborbital, respectively. The potential curves of indium(I)iodide ground state and both ionized states are already given in figure 2.2.

With the reduced kinetic energy E_{rk} and the reduced binding energy $E_{rb} = E_b/\Delta E_{jk}$, the elementary cross section ${}_e^g q^{\text{diss.}}$ for dissociation can be calculated with equation (5.14) [113] as a function of r [31].

$$
{}_e^g q^{\text{diss.}}(E, r) = \xi_j \cdot 4\pi a_0^2 \left(\frac{R_H}{\Delta E_{jk}} \right)^2 \cdot g_{Q_{\text{diss.}}}(E_{rk}, E_{rb}), \tag{5.14}
$$

with

$$
g_{Q_{\text{diss.}}}(E_{rk}, E_{rb}) = \frac{1}{E_{rk}} \left(\frac{E_{rk} - 1}{E_{rk}} \right)^{1 + \frac{E_{rb}}{1 + E_{rb}}} \left(\frac{E_{rk}}{E_{rk} + E_{rb}} \right)^{\frac{3}{2}}
$$
$$
\times \left[1 + \frac{2E_{rb}}{3} \left(1 - \frac{1}{2E_{rk}} \right) \ln \left(e_{Eu} + \sqrt{\frac{E_{rk} - 1}{E_{rb}}} \right) \right].
$$

The elementary cross section should be then weighted with the probability function $P(r)$ of the given molecular state [30], in order to weaken the influence of the ranges $r \ll r_{eq}$ and $r \gg r_{eq}$, while strengthening the influence of the range $r \approx r_{eq}$. The probability function is calculated by equation (5.15) [26].

$$
P_v(r) = \frac{1}{2^v v!} \sqrt{\frac{\alpha}{\pi}} e^{-\alpha(r - r_{eq})^2} H_v^2(\chi), \tag{5.15}
$$

with

$$
\alpha = \frac{4\pi^2 \mu_{mol} \omega_{vib}}{h},
$$
$$
\chi = \sqrt{\alpha}(r - r_{eq}), \tag{5.16}
$$

where μ_{mol} is the reduced mass of the molecule, $H_v(\chi)$ is the Hermite polynomial, ω_{vib} is the angular frequency of the molecular vibration.

The electron impact dissociation cross section can then be calculated with [30, eq. 7] considering the contribution of excitation from all allowed electronic, vibrational and rotational states. Since the vibrational and rotational excitations caused by electron impact are not considered in this model, [30, eq. 7] can be simplified to equation (5.17).

$$\substack{g\\e}Q^{\text{diss.}}(E) = \int\limits_0^\infty P(r) \cdot \substack{g\\e}q^{\text{diss.}}(E,r)\,dr. \tag{5.17}$$

Ionization

The elementary ionization cross section of a molecule can be calculated by equations (5.7), (5.13) and (5.18).

$$\substack{g\\e}q^{i}_{2e}(E,r) = \xi_j \frac{\varsigma_0}{E_b^2} \cdot g_{Q_i}(E_{rk}). \tag{5.18}$$

Subsequently, $\substack{g\\e}q^{i}_{2e}(E,r)$ is weighted with the probability function from equation (5.15) and the ionization cross section $\substack{g\\e}Q^{i}_{2e}(E)$ is determined by

$$\substack{g\\e}Q^{i}_{2e}(E) = \int\limits_0^\infty P(r) \cdot \substack{g\\e}q^{i}_{2e}(E,r)\,dr. \tag{5.19}$$

5.3 Generation processes

5.3.1 Cross sections

Argon

For the argon atom, the electron impact excitation from the ground into the metastable states 4^2P_2 and 4^2P_0, from the metastable state 4^2P_2 into the state 4^2P_0 and also the ionization from all three states were considered as generation process. Spectroscopic measurements on indium(I)iodide plasmas in the laboratory showed either very weak argon emission lines or no lines at all. Therefore, optically accessible lower excited states of argon are neglected. The calculated excitation cross sections for argon can be found in figure 5.3, while the calculated ionization cross sections are plotted in figure 5.4 together with measured ones from two different references [117, 118] for ground state argon to check the validity of the Gryzinsky method.

In the considered range, the calculated cross section does not deviate more than 26 % from the measurement results of [117] and not more than 18 % compared with [118].

Indium

The kinetic energy of orbital electrons of indium atoms from literature is used to calculate the ionization cross sections of indium from ground state with an alternative method, called the binary-encounter Bethe model (BEB) [119, 120], as given in equation (5.20).

$$^A_e Q^{A^+}_{2e}(E) = \frac{S}{E_{rk} + E_{rok} + 1}$$

$$\times \left[\frac{\ln E_{rk}}{2} \left(1 - \frac{1}{E^2_{rk}} \right) + 1 - \frac{1}{E_{rk}} - \frac{\ln E_{rk}}{E_{rk} + 1} \right], \quad (5.20)$$

where $E_{rok} = \mathcal{E}/E_b$ is the reduced orbital electron kinetic energy and $S = \frac{4\pi a_0^2 N R_H^2}{E_b^2}$.

Additionally, the measured cross sections from [121] are used to check the validty of both methods. The Gryziński method and the BEB model show a very good agreement with a deviation smaller than 10 %. The deviation of both models from the measured results remains under 50 % for the whole range considered.
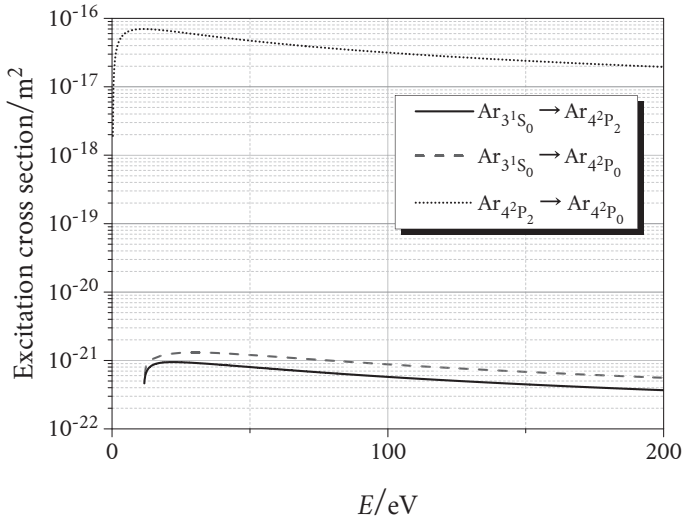
Figure 5.3: Excitation cross sections of argon atoms from ground state and metastable states as a function of incident electron energy.

All three ionization cross sections for ground state indium atoms as well as the calculated ionization cross sections for metastable indium are shown in figure 5.5.
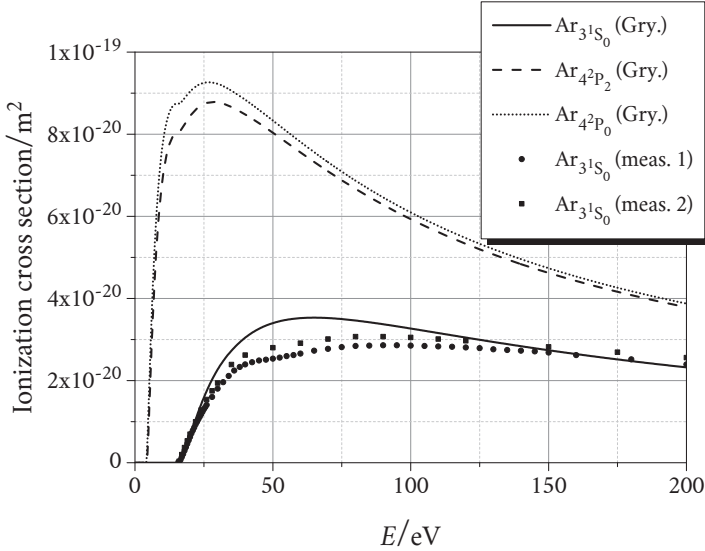
Figure 5.4: Ionization cross sections of argon atoms from ground state and metastable states as a function of incident electron energy. The calculated cross sections are marked with (Gry.), and the measured cross sections from [117] with (meas. 1) and from [118] with (meas. 2).

Since indium serves as the radiant component inside the lamp, the excitation cross sections from the ground state $5^2P_{1/2}$ and metastable state $5^2P_{3/2}$ into the optically accessible $6^2S_{1/2}$-, $5^2D_{3/2}$-, $7^2S_{1/2}$- and $6^2D_{3/2}$-states are calculated in addition to the ionization cross sections. The energy differences ΔE_{jk} between electronic states of indium are listed in table 5.2 with regard to the ground and metastable states.

Figure 5.6 displays the electron impact excitation cross sections of indium atom from $5^2P_{1/2}$- and $5^2P_{3/2}$-states into the aforementioned radiative states.
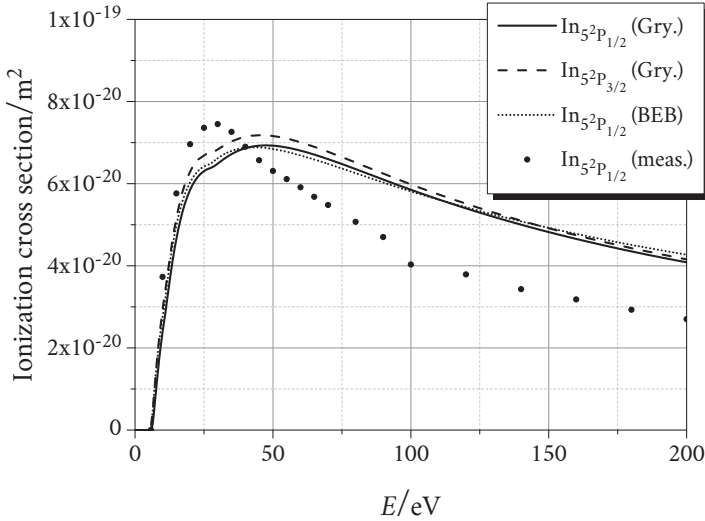
Figure 5.5: Ionization cross sections of indium atoms from ground and metastable states as a function of incident electron energy. The calculated cross sections are marked with (Gry.) for the Gryziński method, with (BEB) for the BEB model and with (meas.) for the measured cross sections from [121].

The main difference between the ionization cross sections in figure 5.5 and excitation cross sections in figure 5.6 is the location of the curves' maxima. The excitation cross section reaches its maximum very close to the threshold energy, while the ionization cross section has its maximum at an energy, which is about 4 times higher than the ionization threshold energy.

Table 5.2: Excitation energies into optically accessible states of indium with regard to ground state $5^2P_{1/2}$ and to metastable state $5^2P_{3/2}$ [24].

Ground state	ΔE_{jk} / eV:	0.27	3.02	4.08	
	Excited state:	$5^2P_{3/2}$	$6^2S_{1/2}$	$5^2D_{3/2}$	
Ground state	ΔE_{jk} / eV:	4.5	4.84		
	Excited state:	$7^2S_{1/2}$	$6^2D_{3/2}$		
Metastable state	ΔE_{jk} / eV:	2.75	3.81	4.23	4.51
	Excited state:	$6^2S_{1/2}$	$5^2D_{3/2}$	$7^2S_{1/2}$	$6^2D_{3/2}$

This can be explained with the electrostatic interaction between the three charged carriers after the ionization, whereas such an interaction is absent in the case of excitation [36].
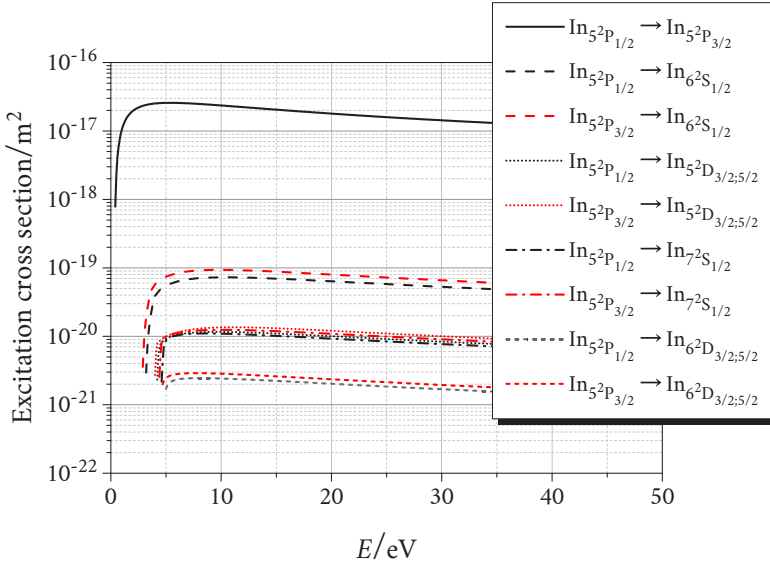
Figure 5.6: Excitation cross sections of indium atoms from ground and metastable states into higher states as a function of incident electron energy.

Iodine

For iodine atoms, only the electron impact ionization from ground state was considered. The calculated and measured cross sections from [122] are plotted in figure 5.7 with a deviation smaller than 20 % for the considered range.
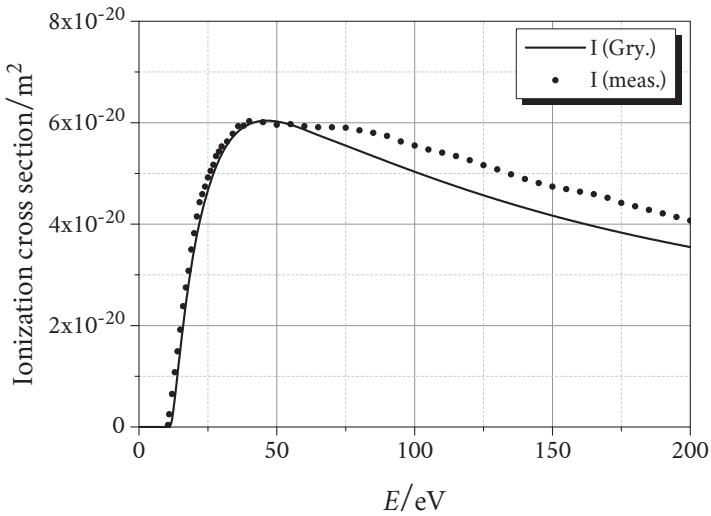
Figure 5.7: Ionization cross sections of iodine atoms from ground state as a function of incident electron energy. The calculated cross sections are marked with (Gry.), and the measured cross sections from [122] with (meas.).

Indium(I)iodide

The calculated ionization and dissociation cross sections of the indium(I)iodide molecule are presented in figure 5.8.
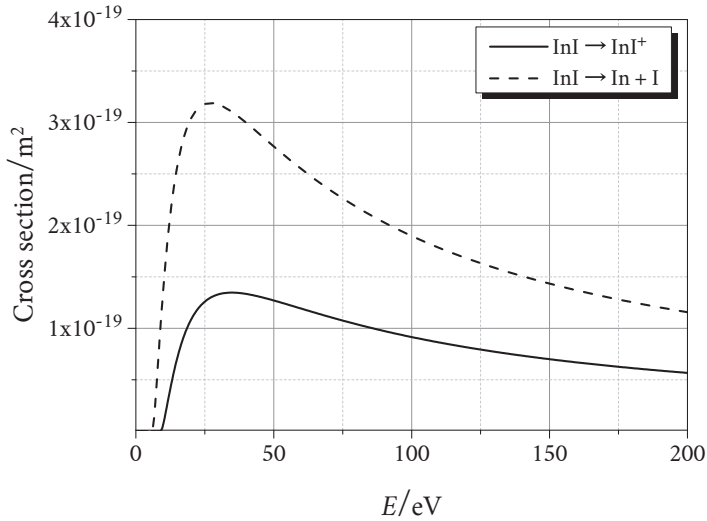
Figure 5.8: Electron impact ionization and dissociation cross sections for indium(I)iodide as a function of incident electron energy E.

Measurement data could not be found for dissociation and ionization of indium halides, but according to Teulet [31], the adopted method delivers satisfactory results for diatomic molecules.

5.3.2 Rate coefficient

The rate coefficients for all generation processes were calculated with the theoretical cross sections using equation (5.1) and are displayed in figure 5.9 for ionization and dissociation, in figure 5.10 for excitation of indium and in figure 5.11 for excitation of argon.
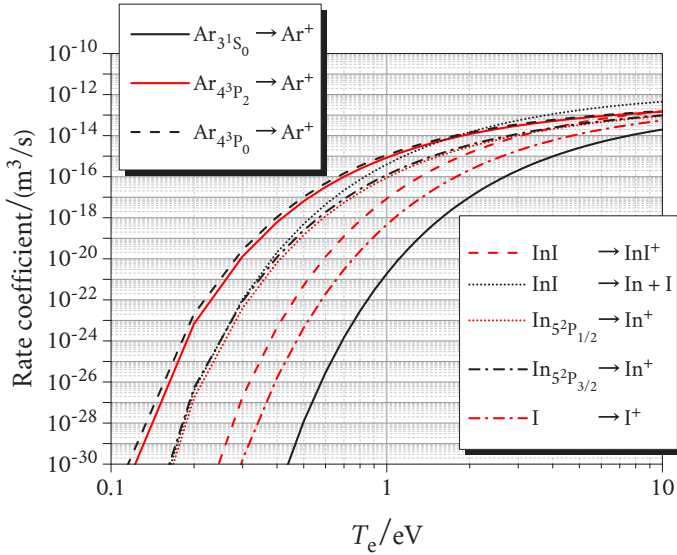
Figure 5.9: Rate coefficients for generation processes ionization and dissociation of all relevant species as a function of electron temperature T_e.
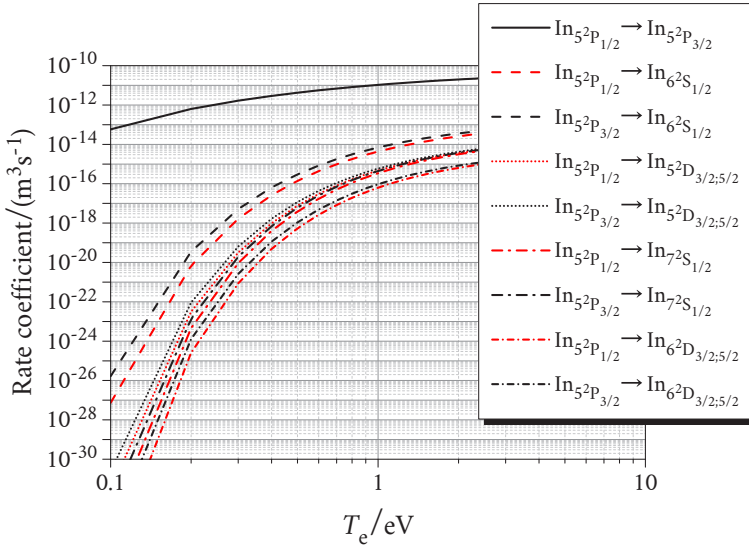
Figure 5.10: Rate coefficients for excitation of indium as a function of electron temperature T_e.

5.4 Secondary processes

5.4.1 Electron impact de-excitation

If the cross section for electron impact excitation ${}_e^j Q^k$ and the statistical weights $g_{j,k}$ of lower j and higher k energy states are known, the cross section for the inverse process ${}_e^k Q^j$ can be determined with the Klein-Rosseland formula [123], as given in equation (5.21).

$$ {}_e^k Q^j(E) = \frac{g_j}{g_k} \frac{E + \Delta E_{jk}}{E} {}_e^j Q^k(E + \Delta E_{jk}). \qquad (5.21) $$

According to Sobel'man [37], this formula is valid, as long as the electrons have a Maxwellian energy distribution. However, thermodynamic

equilibrium is not needed, even though the formula is based on the principle of detailed balance. The rate coefficients for electron impact de-excitation $^{A^*}_eC^A(T_e)$ for argon and indium atoms are shown in figure 5.12.
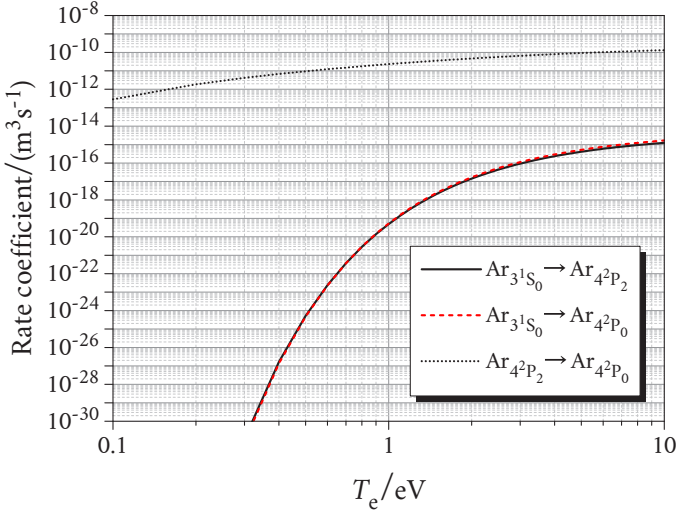
Figure 5.11: Rate coefficients for excitation of argon as a function of electron temperature T_e.

5.4.2 Three-body recombination

The three-body recombination rate coefficients $^{A^+}_{2e}\mathcal{B}^A_e(T_e)$ can be determined using the method of detailed balancing by

$$^{A^+}_{2e}\mathcal{B}^A_e = \frac{g_j}{2g_i}\left(\frac{h^2}{2\pi m_e T_e}\right)^{3/2}\exp\left(\frac{(E_b - E_j)}{E}\right)^A_e K^{A^+}_{2e},\qquad(5.22)$$

where g_i is the statistical weight of the ion, while g_j corresponds to the statistical weight of the final state j of the neutral atom after the recom-

bination [37]. The rate coefficients for argon, indium and iodine ions are plotted in figure 5.13.

The used statistical weights to calculate de-excitation and three-body recombination rate coefficients can be found in table 5.3.
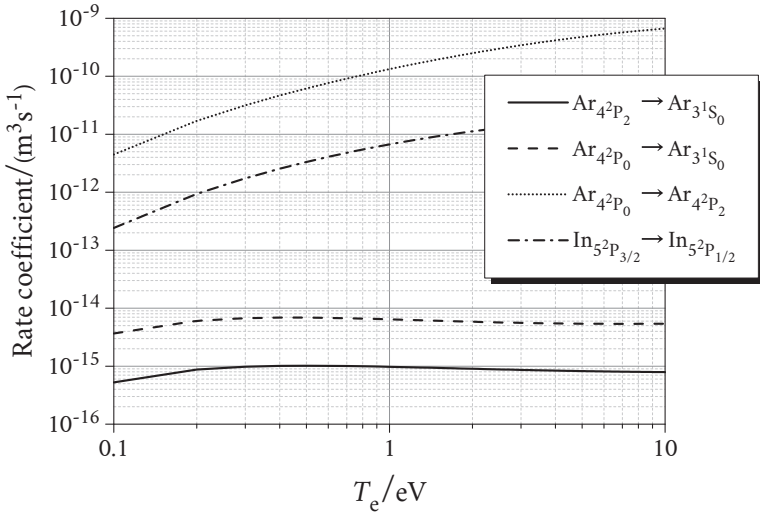
Figure 5.12: Rate coefficients for electron impact de-excitation of argon and indium as a function of electron temperature T_e.

5.4.3 Direct-dissociative recombination

In direct-dissociative recombination, the molecular ion captures an electron to form an excited state of a neutral molecule with a repulsive potential curve, which leads to the dissociation, if the electron is not emitted once again by auto-ionization.
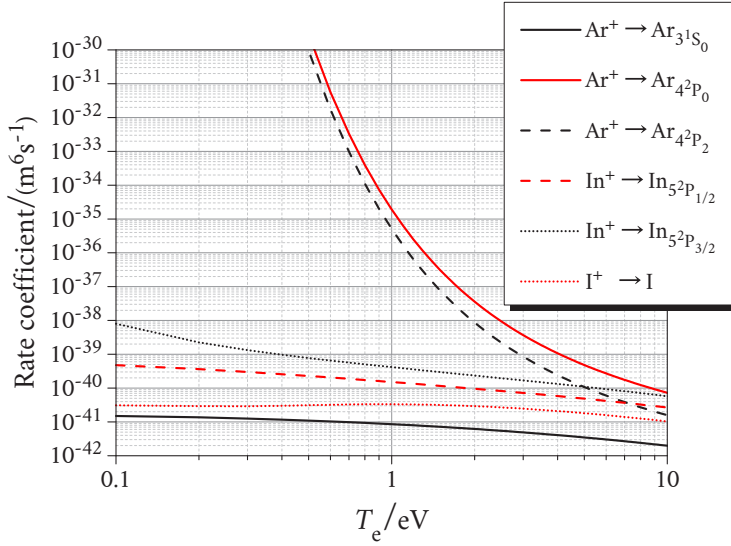
Figure 5.13: Rate coefficients for three-body recombination of argon, indium and iodine ions as a function of electron temperature T_e.

The direct-dissociative recombination rate coefficients $^{InI^+}_e\mathcal{R}^{In+I}_-(T_e)$ of indium(I)iodide ion are calculated with equation (5.23) by adopting a method introduced by Bardsley [124].

$$^{InI^+}_eQ^{In+I}_- = \frac{64\rho\Gamma_c}{a_{vib}U'_d(r_S)}\exp\left(-\frac{(r_S - r_{eqi})^2}{a^2_{vib}}\right)\left(\frac{T_e}{300}\right)^{-1/2},\qquad(5.23)$$

where a_{vib} is the vibrational amplitude, ρ is the ratio of multiplicities of the Rydberg state and molecular ion, r_{eqi} is the equilibrium internuclear distance of the ionic state, $U'_d(r_S)$ is the slope of the potential curve of dissociating neutral state U_d for indium(I)iodide at the intersection point r_S with the potential curve of the ionic state U_i and Γ_c is the capture width.

The capture width is determined by the interaction strength of two configurations, which are the resonance configuration of the excited state and the scattering of the electron by the ion.

Table 5.3: Statistical weights of electronic states of argon, indium and iodine atoms and ions [24].

	Argon			
State	3^1S_0	4^2P_2	4^2P_0	$3^2P_{3/2}$
g_n	1	5	1	4

	Indium		
State	$5^2P_{1/2}$	$5^2P_{3/2}$	5^1S_0
g_n	2	4	1

	Iodine	
State	$5^2P_{3/2}$	5^3P_2
g_n	4	5

The method of Bardsley [124] allows the use of spectroscopic data to estimate the capture width by replacing the electron scattering configuration with members of Rydberg series, as given by

$$\Gamma_c = 2\pi \frac{4\pi^2 m_e a_0^2}{h^2} n^{*3} \left| U_{Ryd}(r_{eqi}) \right|^2, \tag{5.24}$$

where U_{Ryd} is the potential curve of a Rydberg state with the effective quantum number n^*. Banerjee [116] stated that indium(I)iodide has three excited triplets $3^3\Sigma^+$, $3^3\Pi$ and $4^3\Pi$ with Rydberg character. However, the spectroscopic constants are only available for the first two states. Thus, the contribution of $4^3\Pi$-state could not be considered. Additionally, the quantum defect of Rydberg states to calculate the effective quantum number could not be found for indium(I)iodide. Therefore, the

quantum defects of Rydberg states of indium(I)chloride, as given by [71], were also used for indium(I)iodide as an estimation.

Furthermore, the vibrational amplitude a_vib is approximately calculated by equation (5.25) [125].

$$a_\text{vib} = \left(\frac{h}{8\pi^2} \frac{1}{\mu_\text{InI} f_\text{vib}} \coth \left(\frac{h v'_\text{i}}{2 k_\text{B} T_\text{g}} \right) \right)^{1/2},$$
(5.25)

where $f_\text{vib} = \frac{\omega_\text{vib}}{2\pi}$ and μ_InI are the vibration frequency and the reduced mass of the indium(I)iodide, respectively and T_g is the gas temperature.

The individual contribution of Rydberg states and the total direct-dissociative recombination rate coefficients for indium(I)iodide ion are shown in figure 5.14 at a gas temperature of 500 K.

5.5 Lifetimes

The diffusion of neutral particles and charge carriers to the wall of the discharge vessel is one of the most important loss mechanisms in low pressure plasmas. The lifetime τ of excited or ionized particles as well as of atoms with molecular feedstock can be calculated as

$$\tau = \frac{\Lambda^2}{D},$$
(5.26)

where D is the diffusion coefficient and Λ is the diffusion length [126].

For a cylindrical discharge vessel with the assumptions of azimuthal symmetry and a radial density distribution describable by a zero order Bessel function J_0 of the first kind, Mason [126] derived the diffusion length as

$$\frac{1}{\Lambda^2} = \left(\frac{\pi}{L} \right)^2 + \left(\frac{2.405}{R} \right)^2,$$
(5.27)

where L and R are the length and the inner radius of the discharge vessel, respectively, and the first zero of J_0 occurs at $r = 2.405$.
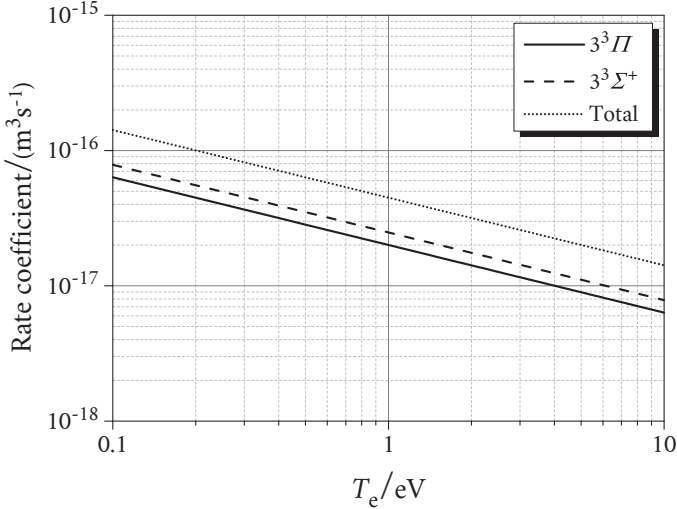
Figure 5.14: Total rate coefficients for direct-dissociative recombination of indium(I)iodide ions with individual contributions of the Rydberg states $3^3\Sigma^+$ and $3^3\Pi$ at $T_g = 500$ K as a function of electron temperature T_e.

For the calculation of the diffusion coefficient, the diffusion process must be divided into sub-processes: diffusion of neutral and charged particles.

5.5.1 Free diffusion

The wall loss of neutral particles is the result of the free diffusion process, in which indium and iodine atoms diffuse to the wall of the discharge vessel and recombine once again to indium(I)iodide. Hence, the lifetime of

indium $\tau_{\text{In}_{\text{g,m}}}$ and iodine τ_{I} after the dissociation is limited by the free diffusion. Additionally, the densities of metastable argon and indium atoms are strongly lowered due to free diffusion.

The interaction between a neutral particle of type 1 and a neutral particle of type 2 due to the van der Waal's forces are considered by means of the Lennard-Jones potential [32] as

$$\phi_{12}(r) = 4\epsilon_{12} \left[\left(\frac{\sigma_{12}}{r} \right)^{12} - \left(\frac{\sigma_{12}}{r} \right)^{6} \right]. \tag{5.28}$$

σ_{12} is the characteristic Lennard-Jones length, which denotes the equilibrium internuclear distance, where the interaction between the particles is zero. ϵ_{12} is the characteristic Lennard-Jones energy [32], which gives the depth of the potential well. The first and second terms of equation (5.28) describe the repulsive and attractive potentials, respectively. Lennard-Jones potentials between the relevant atoms are displayed in figure 5.15.

According to Poling [32], the free diffusion coefficients can then be calculated by equation (5.29), considering the diffusion of a gas particle of type 1 in a dominating buffer gas of type 2 , which has a higher density.

$$D_{12} = \frac{3}{8} \frac{1}{n_{12} \pi \sigma_{12}^2} \sqrt{\frac{\pi k_{\text{B}} T_{\text{g}}}{2\mu_{12}}} \cdot \frac{f_D}{\Omega_D}, \tag{5.29}$$

where n_{12} is the total particle density of both particle types, Ω_D is the collision integral for diffusion and f_D is a correction term. Neufeld [127] proposed equation (5.30) to calculate the collision integral for diffusion empirically.

$$\Omega_D = \frac{A}{(T^*)^B} + \frac{C}{\exp{(DT^*)}} + \frac{E}{\exp{(FT^*)}} + \frac{G}{\exp{(HT^*)}} \tag{5.30}$$

with

$$T^* = \frac{k_B T_g}{\epsilon_{12}}, \qquad A = 1.06036, \qquad B = 0.15610,$$

$$C = 0.19300, \qquad D = 0.47635, \qquad E = 1.03587,$$

$$F = 1.52996, \qquad G = 1.76474, \qquad H = 3.89411.$$

Equation (5.30) delivers precise results with an average deviation less than 0.08 %, for a reduced temperature $0.3 \leq T^* \leq 100$. For the investigated gas temperature range in this work ($453\,\text{K} \leq T \leq 513\,\text{K}$), this condition is always satisfied.
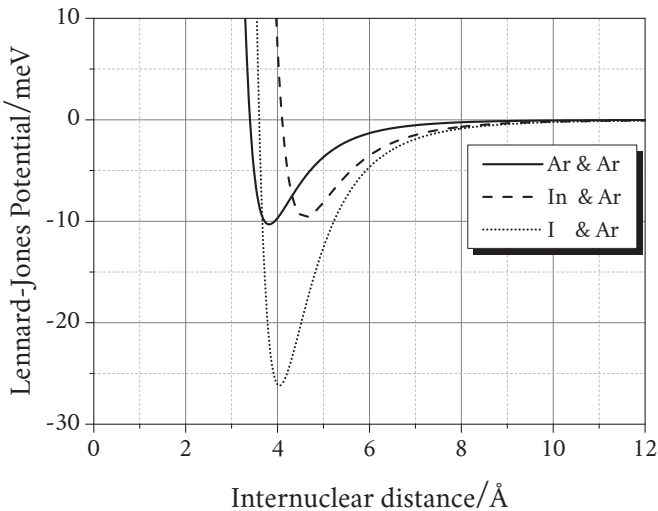
Figure 5.15: Lennard-Jones potentials caused by interatomic forces between two argon atoms, indium and argon atoms, and iodine and argon atoms.

The free diffusion coefficients of neutral particles can be calculated with the parameters in table 5.4 at any given p_{Ar} and T_{CS}. Since there is no available data about the Lennard-Jones potential for metastable argon and indium, the values of ground state atoms are used.

Table 5.4: Parameters used for the calculation of free diffusion coefficients of argon, indium and iodine atoms.

Atomic mass [80]		
m_{Ar} / u	m_{In} / u	m_I / u
39.95	114.82	126.90
Lennard Jones Parameter [128–130]		
ϵ_{ArAr} / meV	ϵ_{InAr} / meV	ϵ_{IAr} / meV
10.3	9.6	26.2
σ_{ArAr} / Å	σ_{InAr} / Å	σ_{IAr} / Å
3.4	4.1	3.6

5.5.2 Ambipolar diffusion

The ambipolar diffusion limits the lifetime of charged particles and can be described through the ambipolar diffusion coefficient, calculated by equation (2.43).

The mobility of ions can be calculated by equation (5.31) [131], which is derived from Chapman-Enskog theory.

$$\mu_i = \frac{3}{8} Z e \lambda_{\text{mfpi}} \sqrt{\frac{\pi}{\mu_{i2} k_B T_i}}, \quad (5.31)$$

with

$$\lambda_{\text{mfpi}} = \frac{1}{\sqrt{2} n_2 \pi \sigma_{i2}^2},$$

where Z and e are the charge number (valence) of the ion and the elementary charge, respectively, λ_{mfpi} is the mean free path length of the ion in a homogeneous gas following a Maxwellian temperature distribution, μ_{i2} is the reduced mass of the ion and the buffer gas atom and n_2 is the density of the buffer gas.

The internuclear forces cannot be considered for the calculation due to the lack of data. Instead, the ions are treated as hard spheres with a diameter ø. In addition, the diameter of indium(I)iodide cannot be found neither for neutral nor for ionic state. Hence, the principle illustrated in figure 5.16 is adopted to determine the diameter.
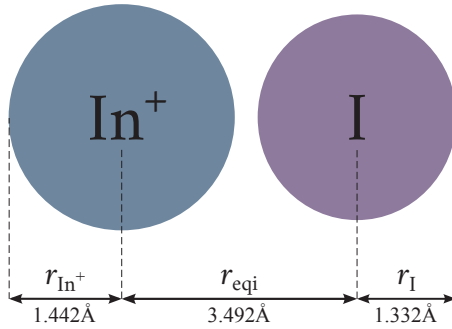
Figure 5.16: Illustration of the hard-sphere approximation to calculate the diameter of InI$^+$ as the sum of equilibrium internuclear distance r_{eqi} of the molecular ion [116], radii of indium ion r_{In^+} and iodine atom r_I [114].

According to Banerjee [116], the single ionization of the indium(I)iodide molecule results from an electron loss of the indium atom. Thus, the diameter can be calculated as the sum of the equilibrium internuclear distance r_{eqi} of the indium(I)iodide ion in $X^2\Pi$-state, the radius of indium ion and the radius of iodine atom. The radius of 5s-orbital of indium is used as the ion radius due to the lack of data. Finally, the mass of the

atoms are also used for the ions, given that the mass of the electron is negligibly small.

For the calculation of the electron mobility, the Chapman's correction factor $f_D = \frac{32}{9\pi}$ is employed, which considers the extremely disproportional masses of electrons and atoms. Furthermore, the electrons are assumed as dimensionless, since their diameter $\varnothing_e$ is far smaller than that of atoms $\varnothing_2$. Thus, the mean free path length of electrons λ_{mfpe} results in

$$\lambda_{mfpe} = \frac{1}{n_2 \pi \varnothing_{e2}^2} \approx \frac{4}{n_2 \pi \varnothing_2^2},$$

with

$$\varnothing_{e2} \approx \frac{\varnothing_2}{2}. \tag{5.32}$$

In due consideration of equation (5.32), of Chapman's correction factor, and that the reduced mass of an electron atom pair $\mu_{e2} = m_2$, the electron mobility is calculated by equation (5.33) [131].

$$\mu_e = \frac{3}{8} e \lambda_{mfpe} \sqrt{\frac{\pi}{2 m_2 k_B T_e}} \cdot f_D = \frac{8}{3} \frac{e}{n_2 \pi \varnothing_2^2} \sqrt{\frac{2}{\pi m_2 k_B T_e}}. \tag{5.33}$$

If the ion and electron mobilities are known, the free diffusion coefficients can be calculated by means of the Einstein relation [22] for ions by

$$D_i = \frac{k_B T_i}{e} \mu_i, \tag{5.34}$$

and for electrons by

$$D_e = \frac{k_B T_e}{e} \mu_e. \tag{5.35}$$

5.6 Model implementation

In this section, the rate equations are presented considering a steady-state discharge. The left hand side of the equations describes the generation processes and the right hand side the loss processes.

5.6.1 Rate equations

The partial vapor pressure of indium(I)iodide, source of the radiant component indium, is determined by the cold spot temperature. For this model, it is assumed that the discharge vessel is filled with enough indium(I)iodide to provide a saturated vapor pressure at any given cold spot temperature T_{CS}. On this basis, the neutral indium(I)iodide density n_{InI} in vapour phase is temperature dependent, but it is a constant for the given temperature, even after ionization and dissociation processes, and can be calculated by following equation (5.36) [69].

$$n_{InI} = \frac{p_{InI}}{k_B \cdot T_{CS}} = \frac{10^{\left(\frac{-6557}{T_{CS}} + 7.209\right) \cdot 101325}}{k_B T_{CS}}. \tag{5.36}$$

The indium(I)iodide ion density n_{InI^+} can be calculated as follows:

$$n_e n_{InI}{}^{InI}_e K^{InI^+}_{2e} = \frac{n_{InI^+}}{\tau_{InI^+}} + n_e n_{InI^+}{}^{InI^+}_e \mathcal{R}^{In+I}_-, \tag{5.37}$$

where τ_{InI^+} is the lifetime of indium(I)iodide ions due to the ambipolar diffusion.

On the other hand, it is assumed that the discharge vessel is filled with argon at standard ambient temperature of $298.15\,\text{K}$ ($25°\text{C}$) with a pressure of p_{Ar} and sealed. Thus, the total argon density is calculated with respect to that temperature and pressure, and limited to the calculated

value. Hence, all p_{Ar}-values in the following sections are given for a temperature of $298.15\,\mathrm{K}$ and the argon density is independent from T_{CS}.

This total argon density n_{Ar} corresponds to the sum of the argon densities in ground state n_{Ar_g}, metastable states $n_{Ar_{m1}}$ and $n_{Ar_{m2}}$, and ionic state n_{Ar^+}. The rate equation of n_{Ar^+} is given by

$$
\begin{aligned}
&n_e n_{Ar_g}\,{}_e^{Ar_g}K_{2e}^{Ar^+} + n_e n_{Ar_{m1}}\,{}_e^{Ar_{m1}}K_{2e}^{Ar^+} + n_e n_{Ar_{m2}}\,{}_e^{Ar_{m2}}K_{2e}^{Ar^+} = \\
&\frac{n_{Ar^+}}{\tau_{Ar^+}} + n_e^2 n_{Ar^+}({}_{2e}^{Ar^+}\mathcal{B}_e^{Ar_g} + {}_{2e}^{Ar^+}\mathcal{B}_e^{Ar_{m1}} + {}_{2e}^{Ar^+}\mathcal{B}_e^{Ar_{m2}}),
\end{aligned}
\tag{5.38}
$$

where τ_{Ar^+} is the lifetime of argon ions due to the ambipolar diffusion.

The density of argon atoms in metastable states 4^2P_2 and 4^2P_0 can be calculated with equations (5.39) and (5.40), respectively.

$$
\begin{aligned}
&n_e n_{Ar_g}\,{}_e^{Ar_g}K^{Ar_{m1}} + n_e n_{Ar_{m2}}\,{}_e^{Ar_{m2}}C^{Ar_{m1}} + n_e^2 n_{Ar^+}\,{}_{2e}^{Ar^+}\mathcal{B}_e^{Ar_{m1}} = \\
&\frac{n_{Ar_{m1}}}{\tau_{Ar_{m1}}} + n_e n_{Ar_{m1}}({}_e^{Ar_{m1}}K^{Ar_{m2}} + {}_e^{Ar_{m1}}K_{2e}^{Ar^+} + {}_e^{Ar_{m1}}C^{Ar_g}).
\end{aligned}
\tag{5.39}
$$

$$
\begin{aligned}
&n_e n_{Ar_g}\,{}_e^{Ar_g}K^{Ar_{m2}} + n_e n_{Ar_{m1}}\,{}_e^{Ar_{m1}}K^{Ar_{m2}} + n_e^2 n_{Ar^+}\,{}_{2e}^{Ar^+}\mathcal{B}_e^{Ar_{m2}} = \\
&\frac{n_{Ar_{m2}}}{\tau_{Ar_{m2}}} + n_e n_{Ar_{m2}}({}_e^{Ar_{m2}}C^{Ar_{m1}} + {}_e^{Ar_{m2}}C^{Ar_g} + {}_e^{Ar_{m2}}K_{2e}^{Ar^+}).
\end{aligned}
\tag{5.40}
$$

The ground state indium atom density n_{In_g} can be calculated with the rate equation (5.41).

$$
\begin{aligned}
&n_e n_{InI}\,{}_e^{InI}K^{diss.} + n_e n_{In_m}\,{}_e^{In_m}C^{In_g} + n_e^2 n_{In^+}\,{}_{2e}^{In^+}\mathcal{B}_e^{In_g} + n_e n_{InI^+}\,{}_e^{InI^+}\mathcal{R}_-^{In+I} = \\
&\frac{n_{In_g}}{\tau_{In_g}} + n_e n_{In_g}({}_e^{In_g}K^{In_m} + {}_e^{In_g}K_{2e}^{In^+}).
\end{aligned}
\tag{5.41}
$$

The indium density in metastable state n_{In_m} can be expressed as

$$
\begin{aligned}
&n_e n_{In_g}\,{}_e^{In_g}K^{In_m} + n_e^2 n_{In^+}\,{}_{2e}^{In^+}\mathcal{B}_e^{In_m} = \\
&\frac{n_{In_m}}{\tau_{In_m}} + n_e n_{In_m}({}_e^{In_m}C^{In_g} + {}_e^{In_m}K_{2e}^{In^+}),
\end{aligned}
\tag{5.42}
$$

while the indium ion density n_{In^+} is given by

$$n_e n_{\text{In}_g}\,{}^{\text{In}_g}_{\ e}K^{\text{In}^+}_{2e} + n_e n_{\text{In}_m}\,{}^{\text{In}_m}_{\ e}K^{\text{In}^+}_{2e} =$$
$$\frac{n_{\text{In}^+}}{\tau_{\text{In}^+}} + n_e^2 n_{\text{In}^+}({}^{\text{In}^+}_{2e}\mathcal{B}^{\text{In}_g}_e + {}^{\text{In}^+}_{2e}\mathcal{B}^{\text{In}_m}_e), \tag{5.43}$$

where τ_{In^+} is the lifetime of indium ions due to the ambipolar diffusion.

If the electron and indium densities in ground and metastable states are known, the density of optically accessible excited states $n_{\text{In}_{\text{Exc}}}$ can be calculated by equation (5.44) for the assumption of coronal equilibrium for radiative states.

$$n_e n_{\text{In}_g}\,{}^{\text{In}_g}_{\ e}K^{\text{In}_{\text{Exc}}} + n_e n_{\text{In}_m}\,{}^{\text{In}_m}_{\ e}K^{\text{In}_{\text{Exc}}} = n_{\text{In}_{\text{Exc}}}\left(A_{\text{In}_{\text{Exc}}\text{In}_g} + A_{\text{In}_{\text{Exc}}\text{In}_m}\right). \tag{5.44}$$

The line emission coefficient $\epsilon_{\lambda_{kj}}$ of the spontaneous emission from the higher state k into the lower state j can be calculated by using equation (5.45).

$$\epsilon_{\lambda_{kj}} = n_k \frac{hc}{\lambda_{kj} 4\pi} A_{kj}, \tag{5.45}$$

where λ_{kj} is the wavelength of the photon, emitted spontaneously, h is the Planck constant and c is the speed of light.

A summary of required Einstein coefficients A_{kj} for the relevant emission lines of indium found in the literature can be found in Appendix A. There are discrepancies between the given Einstein coefficients, which may lead to overestimation or underestimation of line emission coefficients. In this work, Einstein coefficients recommended by Kramida [24] are used for indium, since this reference represents the most actual review of available data.

The iodine density n_I is given by

$$n_e n_{\text{InI}}\,{}^{\text{InI}}_{\ e}K^{\text{diss.}} + n_e^2 n_{\text{I}^+}\,{}^{\text{I}^+}_{2e}\mathcal{B}^{\text{I}}_e + n_e n_{\text{InI}^+}\,{}^{\text{InI}^+}_{\ e}\mathcal{R}^{\text{In+I}}_- = \frac{n_I}{\tau_I} + n_e n_{\text{I}_e}\,{}^{\text{I}}_e K^{\text{I}^+}_{2e}, \tag{5.46}$$

considering the limited lifetime τ_I due to the free diffusion. The rate equation for iodine ion density n_{I^+} reads as

$$n_e n_I {}_e^I K_{2e}^{I^+} = \frac{n_{I^+}}{\tau_{I^+}} + n_e^2 n_{I^+} {}_{2e}^{I^+} \mathcal{B}_e^I. \tag{5.47}$$

τ_{I^+} corresponds to the lifetime of iodine ions due to the ambipolar diffusion.

Quasi-neutrality

The quasi-neutrality condition of plasma states that the electron density must be equal to the density of single ionized atoms and molecules, as given by equation (5.48), since multiple ionization is neglected in this model.

$$n_e = \sum_i n_{i^+} = n_{Ar^+} + n_{InI^+} + n_{In^+} + n_{I^+}. \tag{5.48}$$

MATLAB implementation

A series of MATLAB routines have been created to calculate the rate coefficients of all relevant processes, diffusion coefficients and lifetimes of individual particles for any given plasma conditions. The rate equations were coded as MATLAB symbolic functions and can be solved as a function of electron density, which is defined as a symbolic variable. The electron density, at which the ionization rate equations and the quasi-neutrality condition at the given electron temperature T_e and lamp parameters (L, R, p_{Ar} and T_{CS}) are fulfilled, represents the solution.

5.7 Results and discussions

In this section, the plasma kinetics of an indium(I)iodide-argon low pressure plasma inside a discharge vessel with a length of 60 mm, a diameter of 16 mm and a wall thickness of 1 mm obtained from the model will be presented and discussed. Lamp parameters from [132] are chosen as a starting point.

As mentioned above, the objective of this model is to determine the fundamental plasma parameters with the help of line emission coefficients obtained by means of SROES. Therefore, the line emission coefficients, as well as plasma parameters, e.g., electron n_e, ion n_i and excited atom densities n_{a^*}, should be calculated as a function of electron temperature T_e for a set of cold spot temperature T_{CS} and buffer gas pressure p_{Ar} pairs.

By comparing the measured ϵ_{meas} and simulated line emission coefficients $\epsilon_{sim}(T_e)$ of the given T_{CS}-p_{Ar} pair, the electron temperature of investigated lamps can be determined as $\epsilon_{meas} = \epsilon_{sim}(T_e) \implies T_e$. Subsequently, the corresponding plasma parameters are assigned to the electron temperature, as $T_e \implies n_e(T_e), n_i(T_e), n_{a^*}(T_e) \ldots$

5.7.1 Electron temperature and density

Figures 5.17 and 5.18 depict the calculated electron densities as a function of electron temperature at different T_{CS} and p_{Ar}, respectively. The ionization rate depends strongly on T_e, and n_e falls steeply with increasing electron temperature in the range studied.

In due consideration of the relationship between the electron temperature and the reduced electric field as $T_e \sim E/n$ [133], there are two pos-

sibilities to increase T_e without changing the lamp geometry or filling species.
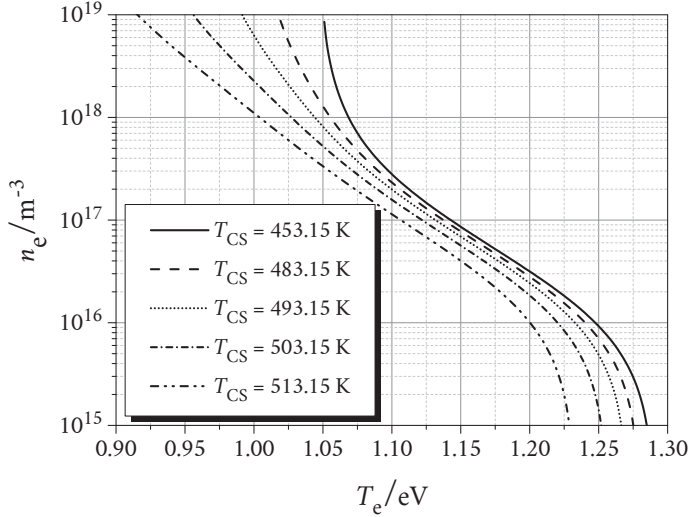
Figure 5.17: Electron density at different cold spot temperatures T_{CS} and at constant argon buffer gas pressure $p_{Ar} = 400\,\text{Pa}$ as a function of electron temperature T_e.

First, the indium(I)iodide density can be reduced, so that a longer mean free path is reached. As a result, the inelastic collision rate and thus n_e decreases. Secondly, the electric field strength can be increased. This way, more electrons have enough energy to ionize argon atoms and indium(I)iodide molecules directly. The energy dissipation in dissociative collisions with indium(I)iodide and in ionizing collisions with indium shrinks. It causes a decrease in n_e, since this two step ionization process is more energy efficient than direct ionization of argon and indium(I)iodine.

Furthermore, the increase of both the cold spot temperature and the argon buffer gas pressure reduces the mobility of electrons and ions due to the more frequent elastic collisions, which lead to lower ambipolar diffusion losses. Consequently, the electron density rises, which results in an increased rate of step-wise processes. As mentioned, step-wise processes are more energy efficient. But more importantly, the threshold energy for each step is smaller, which allows the electrons with lower kinetic energy also to participate in these processes. Thereby, a relatively larger part of electron kinetic energy is dissipated in inelastic processes and the electron temperature sinks [33]. As a result, higher electron densities can be reached at lower electron temperatures.
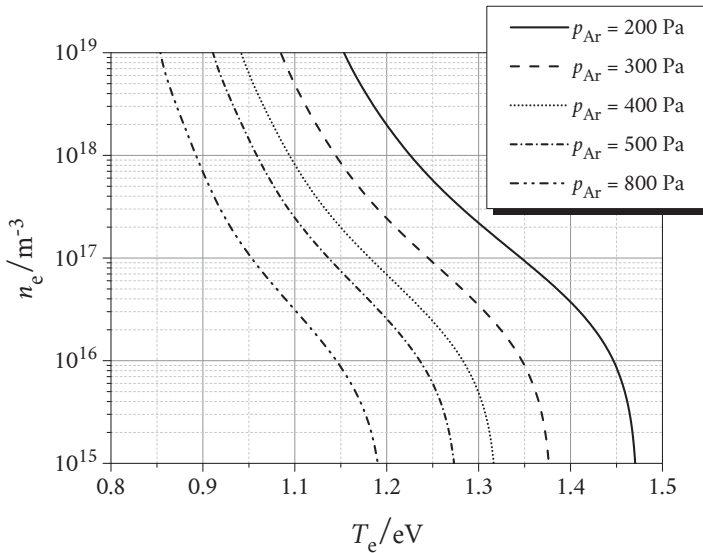
Figure 5.18: Electron density at different argon buffer gas pressures p_{Ar} and constant cold spot temperature $T_{CS} = 493.15\,\mathrm{K}$ as a function of electron temperature T_e.

The decreasing left-shift of the individual curves in figure 5.18 to lower electron temperatures is in good agreement with the resulting increase of argon density for each step of buffer gas variation. The increase of buffer gas pressure from 200 Pa to 300 Pa results in an argon density rise of 50 %, while the increase from 300 Pa to 400 Pa causes an argon density rise of only 33 %, etc. However, the indium(I)iodide vapor pressure is an exponential function of cold spot temperature, as demonstrated in figure 6.8. Therefore, the variation of cold spot temperature by 10 K steps leads to an increasing left-shift of the individual curves in figure 5.17.

5.7.2 Ion and atom densities

The calculated ion and neutral particle densities are plotted in figures 5.19 and 5.20 as a function of electron temperature at lamp parameters $T_{CS} = 493.15\,\text{K}$ and $p_{Ar} = 400\,\text{Pa}$.

The dissociation process of indium(I)iodide has the highest rate coefficients in the studied T_e-range compared to other generation processes except excitation of indium and ionization of argon metastables, as displayed in figure 5.9. In due consideration of constant indium(I)iodide density and high electron density at lower electron temperatures, the resulting dissociation rate of indium(I)iodide causes a high indium and iodine density. Furthermore, the direct dissociative recombination of indium(I)iodide ion is stronger at lower T_e, as can be seen in figure 5.14, which supports the generation of atomic indium and iodine.

Iodine features a longer lifetime than other species due to its small free diffusion coefficient, as given in table 5.5, and has the lowest ionization rate except ground state argon. Thus, the iodine atom density exceeds even the density of indium(I)iodide at low T_e, while the iodine ion has the

lowest density amongst all species. It should be noted that the electron attachment to iodine is neglected in this model.
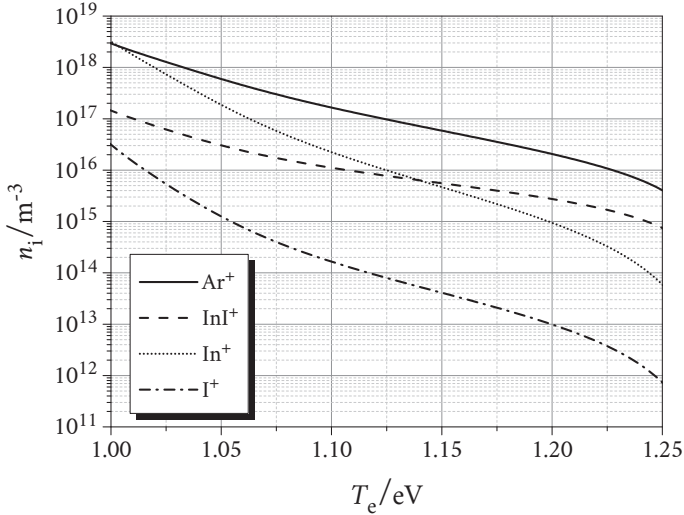
Figure 5.19: Ion density at $T_{CS} = 493.15\,\text{K}$ and $p_{Ar} = 400\,\text{Pa}$ as a function of electron temperature T_e.

Table 5.5: Free diffusion coefficients and lifetimes of neutral particles at $p_{Ar} = 400\,\text{Pa}$ and $T_{CS} = 493.15\,\text{K}$.

	$\text{Ar}_{4^2P_2,\,4^2P_0}$	$\text{In}_{5^2P_{1/2},\,5^2P_{3/2}}$	I
$D_{\text{free}} / \text{m}^2{\cdot}\text{s}^{-1}$	$6.8 \cdot 10^{-3}$	$4.1 \cdot 10^{-3}$	$3.8 \cdot 10^{-3}$
$\tau_{\text{free}} / \text{ms}$	1.2	2.0	2.2

On the contrary, indium has a high ionization rate coefficient and has also the contribution of its metastable state to the ionization. Therefore, at lower T_e, the total ion density is determined by argon and indium ions. Since the excitation rate of indium into the metastable state is nearly

twice as high as the de-excitation into the ground state, the indium metastable density is higher than the ground state indium density over the investigated T_e-range. It should also be kept in mind that the same free diffusion coefficient is assumed for both ground and metastable states of indium.
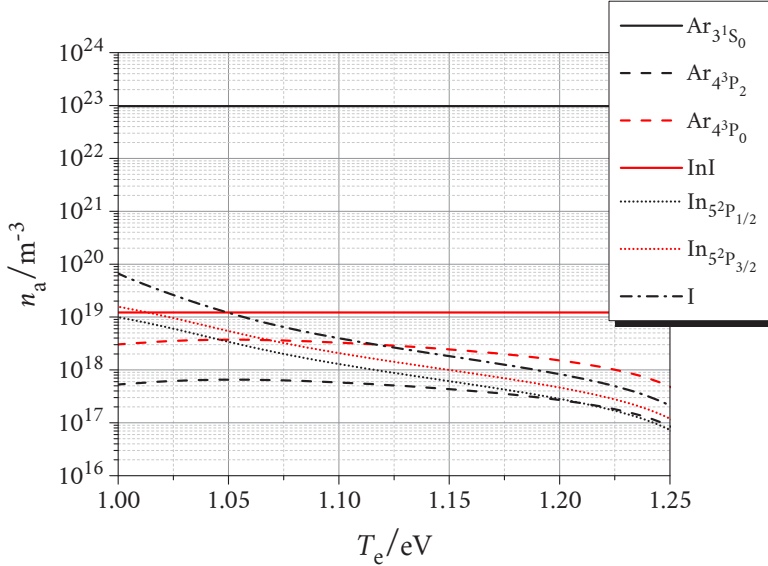
Figure 5.20: Particle densities of neutral argon, indium and iodine atoms as well as of neutral indium(I)iodide molecules at T_{CS} = 493.15 K and p_{Ar} = 400 Pa as a function of electron temperature T_e.

For higher T_e, the indium(I)iodide ion density exceeds the indium ion density due to the increasing inefficient direct ionization as explained in the section above. Although both the three body recombination rate coefficient of indium ion and the direct-dissociative recombination rate coefficient of indium(I)iodide ion fall with increasing T_e, the decrease of three body recombination rate is steeper. Additionally, the longer life-

time of indium(I)iodide ion due to the ambipolar diffusion, as demonstrated in table 5.6, supports the high ion density.

Table 5.6: Ambipolar diffusion coefficients and lifetimes of charged particles at $p_{Ar} = 400\,Pa$, $T_{CS} = 493.15\,K$ and $T_e = 1.15\,eV$.

	Ar^+	In^+	I^+	InI^+
$D_a\,/\,m^2{\cdot}s^{-1}$	$64.2 \cdot 10^{-3}$	$50.9 \cdot 10^{-3}$	$56.1 \cdot 10^{-3}$	$39.5 \cdot 10^{-3}$
$\tau_a\,/\,\mu s$	128.9	162.5	147.3	209.2

At $T_{CS} = 493.15\,K$ and $p_{Ar} = 400\,Pa$, n_{Ar} is about 3 orders of magnitude higher than n_{InI}. Additionally, the densities of argon metastable states are nearly in the same order of magnitude of indium(I)iodide molecule. Thus, the total ionization rate of argon from ground state and metastable states exceeds even the ionization rate of indium(I)iodide, although the ground state argon has the smallest the ionization rate coefficient amongst all species. This high ionization rate results in a higher argon ion density than the indium(I)iodide ion density over the investigated T_e-range. Nevertheless, the ground state argon density is nearly constant, since the argon ion density remains 4 to 8 orders of magnitude smaller than the neutral argon density due to strong three-body recombination into metastable states, de-excitation into the ground state and ambipolar diffusion. This shows the significant contribution of argon metastable states to the total plasma dynamics.

5.7.3 Line emission coefficients

Figures 5.21 and 5.22 show the calculated line emission coefficients ϵ_λ for the essential emission lines of indium as a function of T_e and n_e, respectively.

For the calculations of ϵ_{326}, the densities $n_{5^2D_{3/2}}$ and $n_{5^2D_{5/2}}$, and the Einstein coefficients $A_{5^2D_{3/2}\to5^2P_{3/2}}$ and $A_{5^2D_{5/2}\to5^2P_{3/2}}$ are added, since the emission lines are located within a distance of 0.25 nm and cannot be solved exactly with experimental setups available in the laboratory.
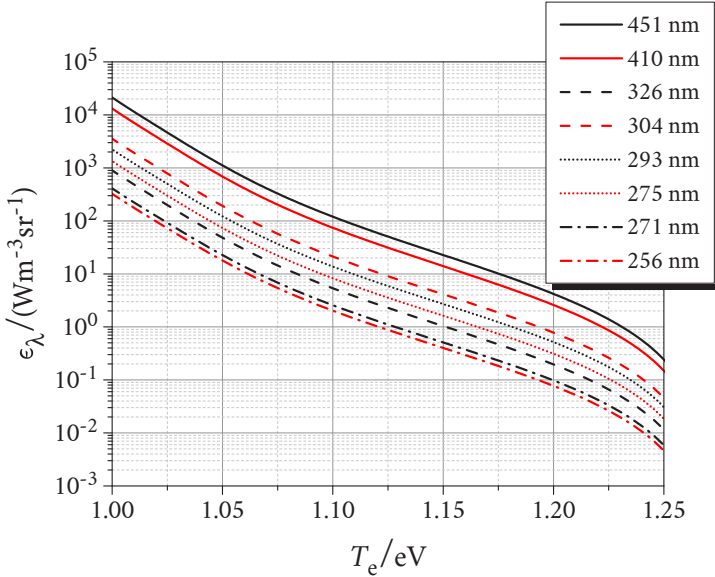
Figure 5.21: Line emission coefficients for relevant emission lines of indium at $T_{CS} = 493.15\,K$ and $p_{Ar} = 400\,Pa$ as a function of electron temperature T_e.

The calculated electron densities for different lamp configurations vary between $10^{15}\,m^{-3}$ and $10^{19}\,m^{-3}$ over the investigated T_e-range. The electron density of $10^{19}\,m^{-3}$ corresponds to a total radiant power density higher than $1\cdot10^6\,W\cdot m^{-3}$ for all emission lines accumulated. This value exceeds even the electrical power density of commercially available low pressure plasmas for general lighting applications. Therefore, the electron density range above $10^{19}\,m^{-3}$ is irrelevant for experimental pur-

poses in search of mercury substitutes. In the given range, the presented model can be applied to obtain the plasma parameters, if ϵ_λ is determined experimentally.
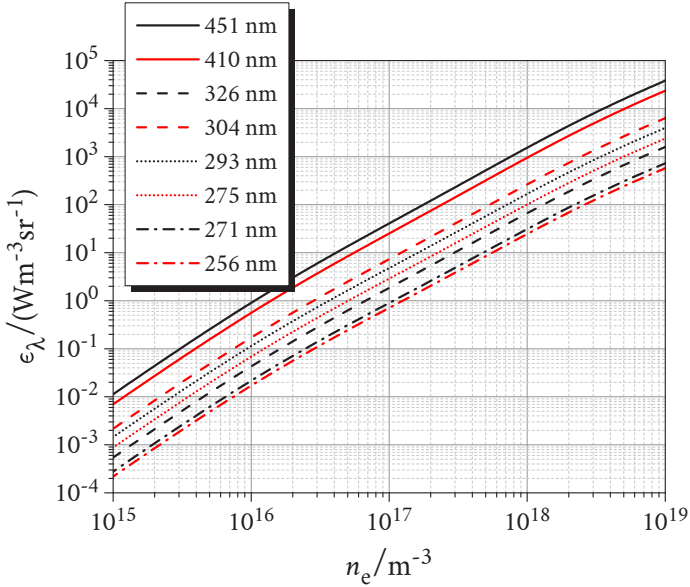
Figure 5.22: Line emission coefficients for relevant emission lines of indium at $T_{CS} = 493.15\,\mathrm{K}$ and $p_{Ar} = 400\,\mathrm{Pa}$ as a function of electron density n_e.

Chapter 6

Experimental setup

The mercury-free discharges based on the indium(I)iodide-argon system are driven by surface waves at a frequency of $f = 2.45\,\text{GHz}$ in a discharge vessel with cylindrical geometry. This chapter is dedicated to the description of the experimental setup, implemented to drive as well as to characterize the lamps radiometrically and electrically. In section 6.1, the equipment to generate and measure the microwave power is described. Section 6.2 presents the for this work developed microwave coupler "surfatron" and its characterization by means of electromagnetic simulations with the help of the simulation software CST Microwave Studio. The utilized lamp bodies and the production process of the lamps are explained in section 6.3, while section 6.4 details the optical measurement setup. The sketch of the experimental setup including the device names is shown in figure 6.1.

6.1 Microwave generation and measurement

Microwaves at the frequency of 2.45 GHz are generated by a signal generator (Rohde&Schwarz, SMT 03) and then amplified by a traveling wave tube microwave amplifier (Amplifier Research, 200T2G4). Forward and reflected power levels are measured with a directional power sensor (Ro-

hde&Schwarz, NRT-Z44) with an accuracy of 3.2 % of the reading. A circulator (Bonn Elektronik, BCI0120-200) and a dummy load (Bonn Elektronik, BT550) are inserted between the output of the microwave amplifier and the power sensor to prevent instabilities or any damage to the amplifier because of the reflected power. 50 Ω coaxial cables are used to match the output impedance of the amplifier.
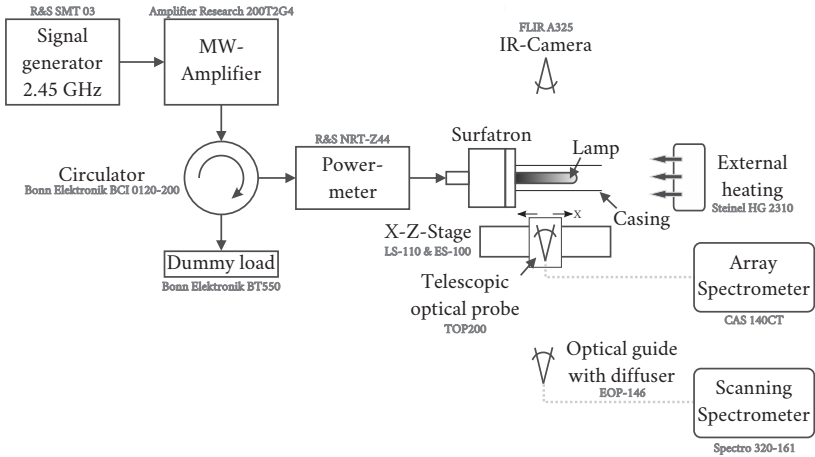
Figure 6.1: Sketch of the experimental setup, which consists of four parts, i.e., microwave generation and measurement, wave launcher, lamp and optical measurement.

6.2 Microwave coupler: SURFATRON

The microwaves are coupled into the lamp with a coaxial wave launcher known as "surfatron". The surfatron is an m = 0-mode surface wave launcher, which allows field shaping as well as impedance and frequency matching [134]. Both properties play an important role for the system efficiency.

The design of the surfatron is based on the works of Moisan [134], Selby [19] and Kaiser [89, 135, 136]. Figure 6.2 portrays the surfatron used in this work, whose main body is made of brass. It consists of two parts: the coupler and the wave forming structure. The former is an assembly of two joined parts, which are the input and the coupling capacitor. A standard 50 Ω PTFE-filled N-Type connector (Rosenberger, 53K506-500N5), made from brass with gold plated contacts, is used as input. The input transmission line of the N-type connector is threaded to allow a screw connection with a conical structure (dia. = 9.5 mm), which serves as the coupling capacitor.

N-type connector
Input line
Positioning glass rod
Adjustment screw
Coupling capacitor
Inner cylinder
Short circuit end
Cylindrical gap
Lamp
Front end
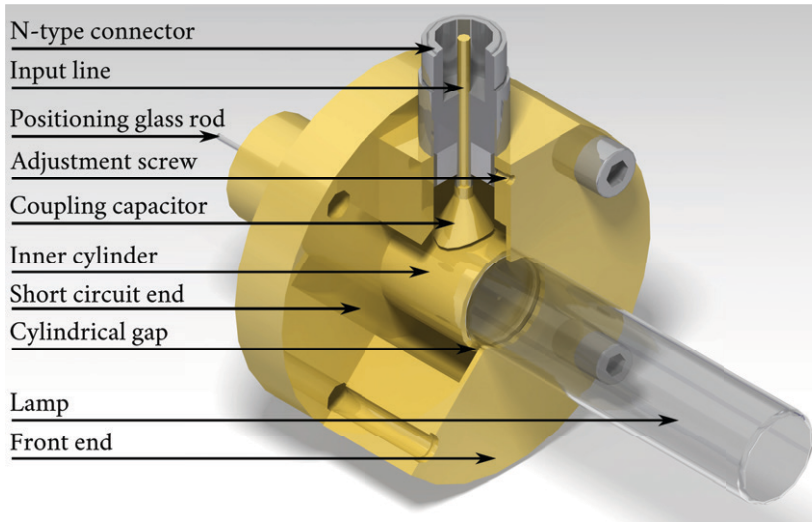
Figure 6.2: Wave launcher surfatron and its parts.

Figure 6.3 shows the true to scale cross section of the surfatron and the lamp. The dark grey areas identify conductive parts of the surfatron connected to the ground, while light grey designates the coupler itself. Finally, the dielectric parts of the system, i.e., lamp tube and PTFE of the N-type connector are indicated with diagonal stripes. The most impor-

tant difference between the presented surfatron and those from previous works is that the coupling capacitor is not a plate but has a conical geometry, which does not exhibit any 90° bends on the transmission line. In this way, parasitic capacitance effects between input line and plate are prevented. The entire coupler section can be moved radially and fixed with a screw. The wave forming structure consists of two metallic cylinders forming a section of an air filled coaxial line. This section is terminated by a short circuit at one end, while at the other end, a thin plate with a coaxial opening forms a circular gap with the inner cylinder. From this gap, azimuthally symmetric surface waves can be excited. The coaxial opening has a diameter of 17.5 mm, which results in a gap of 0.75 mm between the lamp surface and the surfatron. Thus, any heat loss due to thermal conduction at contact points is prevented, which would significantly complicate the accurate adjustment of the cold spot temperature.

The operation characteristics of the surfatron can be adjusted in three different ways [19, 137]: First, the distance l_1 between the short circuit end and the coupler can be varied, which results in a change of central operating frequency and the real part of the input impedance. The utilized surfatron has a fixed short circuit at the back side and it is not tunable, since the central operating frequency is predefined. In this way, a more compact design is achieved. Secondly, the insertion depth of the coupler x can be adjusted in order to alter the imaginary part of the input impedance. Thirdly, by varying the gap distance g, the impedance and the operating frequency can be altered. The presented surfatron has fixed dimensions, $l_1 = 9\,\text{mm}$, $l_2 = 9\,\text{mm}$, $D_1 = 16\,\text{mm}$ and $D_2 = 28.3\,\text{mm}$. Following the design guidelines from [137], the dimensions of the surfatron have been calculated with the help of the electromagnetic simulation software "CST MWS" (Computer Simulation Technology AG, Microwave Studio Module for high frequency components) in such a way that the central operating frequency of the surfatron is 2.45 GHz for $x = 1.14\,\text{mm}$ and $g = 0.6\,\text{mm}$.
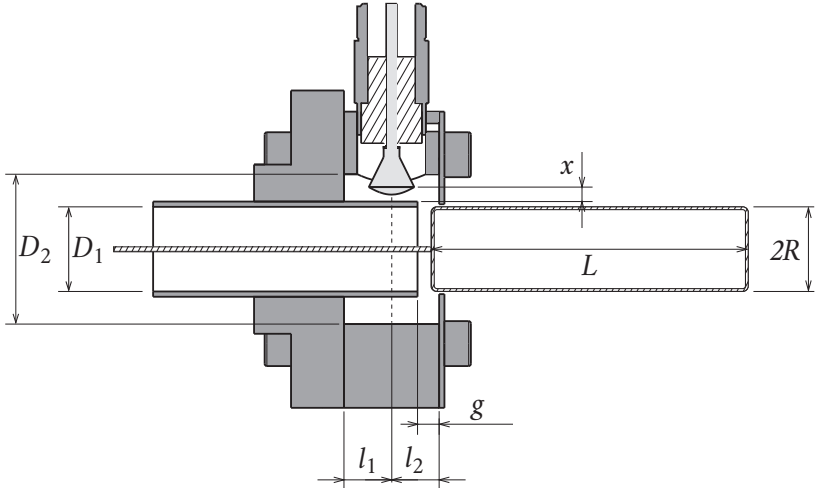
Figure 6.3: True to scale cross section of the utilized surfatron. Dark grey areas identify conductive parts of the surfatron connected to ground and light grey area designates the coupler, while the dielectric parts of the system, i.e., lamp tube and PTFE of the N-type connector are indicated with diagonal stripes.

For this configuration, the electromagnetic simulation results of the E-field distribution in open circuit operation are illustrated in figure 6.4 **a)** and **b)** for both field components, i.e., $\mathbf{E}_r$ and $\mathbf{E}_z$, respectively. A specific amplitude of $|\mathbf{E}_r|/P_{el} = 32\,\mathrm{kV{\cdot}m^{-1}{\cdot}W^{-1}}$ can be achieved between the coupling capacitor and the inner cylinder. Yet, the field strength in the cylindrical gap is of utmost importance for the plasma ignition and for the axial acceleration of electrons. A specific amplitude of $|\mathbf{E}_z|/P_{el} = 61\,\mathrm{kV{\cdot}m^{-1}{\cdot}W^{-1}}$ is achieved in the gap, which is one and a half times higher than that, achieved with the former design of Kaiser [136].

By neglecting the dielectric and ohmic power losses P_Ω within the surfatron, the power consumption in the system can be divided into three categories, i.e., the reflected power P_{ref} at the interface between the power supply line and the surfatron input, which results in the accepted power

P_{acc} from the surfatron, the radiated microwave power into the surrounding space P_{rad} and the absorbed power by the plasma P_{A}. The power balance is given by

$$
\begin{aligned}
P_{\mathrm{mw}} &= \eta_{\mathrm{ECG}} \cdot P_{\mathrm{el}}, \\
P_{\mathrm{acc}} &= P_{\mathrm{mw}} - P_{\mathrm{ref}}, \\
P_{\mathrm{A}} &= P_{\mathrm{acc}} - P_{\mathrm{rad}} - P_{\Omega}, \\
&\approx P_{\mathrm{acc}} - P_{\mathrm{rad}},
\end{aligned}
\tag{6.1}
$$

where P_{mw} is the generated microwave power by the microwave amplifier with the supply power P_{el} and the electronic control gear (ECG) efficiency η_{ECG}.
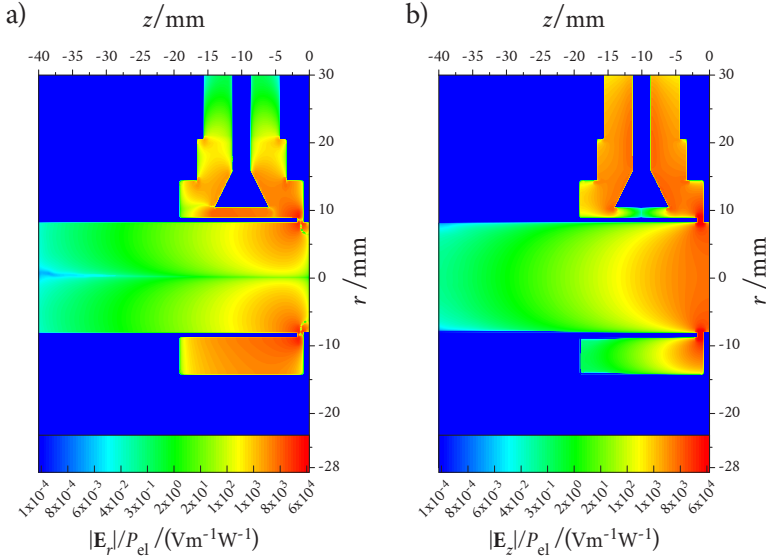
Figure 6.4: Simulated distributions of **a)** radial, E_r, and **b)** axial, E_z, electric field components inside the novel surfatron in open circuit operation.

By adjusting the impedance of the surfatron to the impedance of the supply line or of the plasma, one can either reduce the amount of reflected power at the interface between the supply line and the surfatron or maxi-

mize the absorbed power by the plasma, respectively. A low amount of reflected power does not always indicate a high P_A, unless P_{rad} also remains low. Moisan [134] stated that the undesirable radiation of non-guided waves can be minimized to a negligible level compared to the absorbed power by the plasma by means of impedance matching. In this work, the reflected power is neglected and only the accepted power P_{acc} and the total radiant flux of the plasma Φ_{total} are considered for the calculation of the plasma efficiency as $\eta_{Pl} = \Phi_{total}/P_{acc}$, while P_{rad} is monitored with a microwave leakage level detector (Robin, TX90).

The power balance is evaluated by parameter sweep simulations of gap distance and coupling capacitor insertion depth for $P_{mw} = 3\,\mathrm{W}$ at $f = 2.45\,\mathrm{GHz}$. The input port of the system is defined as the cross section of the N-type connector. The plasma is modeled as a composition of individual rings with a thickness of 1 mm and a width of 5.8 mm, whose attributes are calculated according to the Drude model. The plasma parameters, e.g., electron density and collision frequency are taken from measurement results in chapter 7 with respect to their radial and axial variation.

Figure 6.5 depicts the simulation results of the coupling factor of the surfatron, $\eta_{CF} = P_A/P_{mw}$. A maximum coupling factor of 0.81 is achieved at $g = 1\,\mathrm{mm}$ and $x = 0.8\,\mathrm{mm}$.

Furthermore, the reflection coefficient S 1,1, as well as P_{acc}, of this configuration is plotted in figure 6.6 **a)** and **b)**, respectively, as a function of excitation frequency. At $f = 2.45\,\mathrm{GHz}$, a reflection of $-13.03\,\mathrm{dB}$ is reached, which corresponds to 4.97 % of the input power. In due consideration of the coupling factor of 0.81, it can be concluded that only about 14 % of the input power is lost as dielectric and ohmic losses as well as radiation of non-guided waves. The simulation results on dielectric and ohmic losses correspond to $P_\Omega = 0.049\,\mathrm{W}$, while the microwave radiation into the surrounding reads as $P_{mw} = 0.37\,\mathrm{W}$, which can be blocked

by wrapping a metal mesh around the lamp as Faraday shield. However, a mesh with low direct transmission may result in a reduced radiant flux.
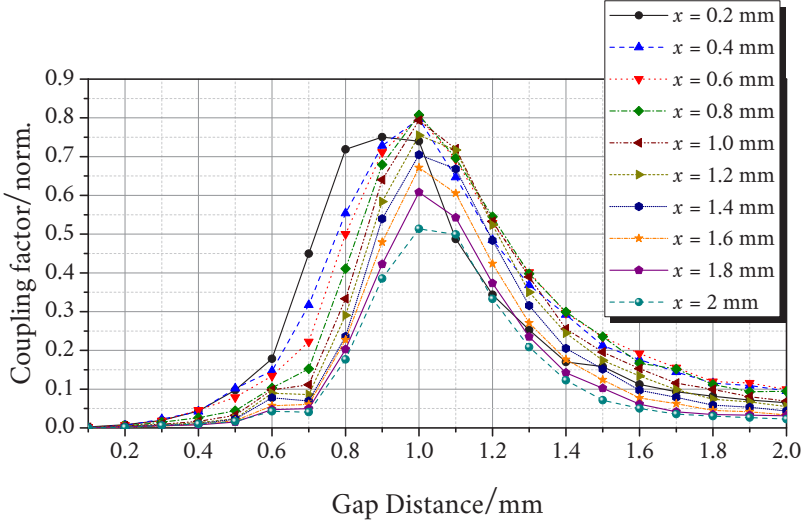
Figure 6.5: Simulation results of the surfatrons coupling factor at different coupling capacitor insertion depths for $P_{\text{mw}} = 3\,\text{W}$ at $f = 2.45\,\text{GHz}$ as a function of gap distance.

Additionally, the proper positioning of the lamp inside the surfatron is of utmost importance for achieving high efficiency. As stated in section 2.3.2, the surface waves, excited inside the cylindrical gap, propagate in both axial directions along the discharge vessel and sustain the plasma. However, the radiation, generated inside the discharge volume enclosed by the surfatron is blocked and counts as loss. Thus, the insertion depth of the lamp inside the surfatron should be minimized. Furthermore, the propagation of surface waves is interrupted, when a dielectric barrier, such as the end of the lamp, is encountered and the surface waves are reflected. If the lamp is inserted inside the surfatron

in such a way that one end of the lamp is located inside the cylindrical gap, then the reflection results in a constructive interference of both waves [136].
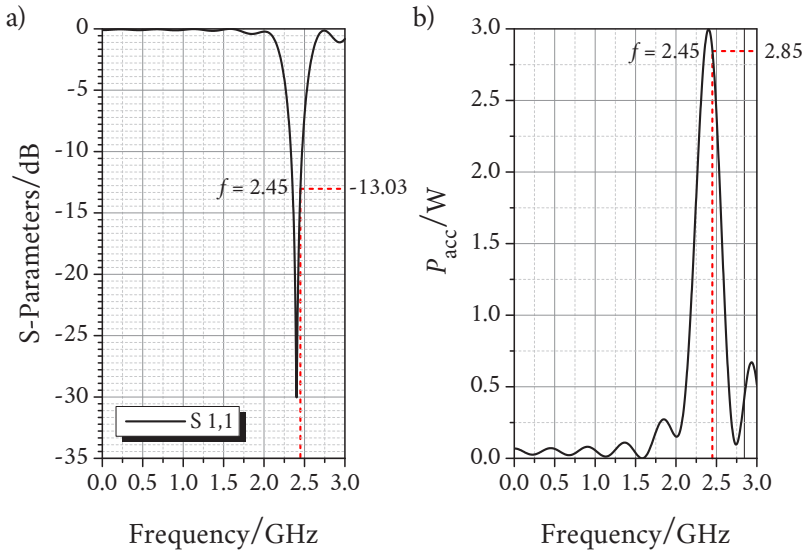
Figure 6.6: Simulation results of **a)** reflection coefficient S 1,1 and **b)** accepted power P_{acc} for $g = 1$ mm and $x = 0.8$ mm as a function of frequency.

6.3 Lamp geometry and filling

The lamps employed in this work have a length of $L = 60$ mm, a radius of $R = 8$ mm and a wall thickness of $d = 1$ mm. With increasing lamp diameter, the ratio of the surface area to the discharge volume decreases, which leads to lower ambipolar diffusion losses. However, a larger diameter results also in a stronger self-absorption, which has a negative effect on the efficiency. It should also be kept in mind that according

to Moisan [134], to launch and sustain a plasma using m = 0-mode waves is difficult, if the product of excitation frequency and lamp radius is > 20 GHz·mm. Hence, the upper limit for the discharge vessel radius at the chosen excitation frequency of 2.45 GHz is 8.2 mm.

The individual steps of the lamp production are demonstrated in figure 6.7. Fused silica glass tubes are sealed planar on one side, while narrowed and extended with a filling stem on the other side to simplify the filling of the lamp. A glass rod is fused axially to the planar surface to allow an easy positioning of the lamp inside the surfatron.

Figure 6.7: Individual steps of the lamp production. Fused silica tubes are fused planar on one side, while the other side is narrowed and extended with a filling stem. A glass rod is fused axially to the planar surface to simplify the accurate positioning of the lamp inside the surfatron. After the filling, the lamps are sealed by fusing the filling stem.

The lamp tubes are made of high purity electrically fused silica glass (Heraeus Quarzglas, HSQ 700) [138]. The manufacturer brands a glass type as "fused quartz glass", if natural quartz sand or quartz crystal is employed as the raw material of the fusion process [139]. The term "synthetic fused silica glass" is only used, if silicon tetrachloride $SiCl_4$ is oxidized in an oxyhydrogen flame to manufacture glass rods [139]. However, the commonly accepted nomenclature defines quartz glass as crystalline silica and fused silica as non-crystalline silica glass. To avoid any misunderstanding, the term "fused silica glass tubes" is used to describe the lamb bodies in this work.

The lamp bodies are cleaned with isopropyl alcohol and sealed with a valve (Swagelok, SS-6BG-MM with Ultra-Torr fittings), which remains connected to the lamp during the entire production process (except in the glovebox) to protect it from impurities. Then, the lamp bodies are baked in a self-made industrial oven at $1073.15\,\mathrm{K}$, while being evacuated with a vacuum system until the pressure inside the lamp body reaches $\leq\ 1\cdot 10^{-4}\,\mathrm{Pa}$, which takes typically 6 to 8 hours. In this way, the impurities like water or oxygen are removed from the lamp bodies. The vacuum system consists of a turbo molecular pump (Oerlikon Leybold Vacuum, Turbovac 50) and two rotary vane pumps (Oerlikon Leybold Vacuum, Trivac D 16 B), where one of them serves as a backing pump of the turbo molecular pump. Since the rotary vane pumps are oil-sealed, an adsorption trap (Vacom, KF Adsorption Trap including Heater) and oil mist eliminator (Vacom, OME) are used to prevent any oil contamination of the lamp.

The baked lamp bodies are cooled to room temperature and then filled with overpressure argon to prevent any impurity diffusion into the lamp during the transport into the glovebox. There, the lamp bodies are filled with 0.1 mg of indium(I)iodide in form of beads (Sigma-Aldrich, EC Number: 237-746-3) under nitrogen atmosphere. The beads are

weighed with a single-cell weighing system (Kern, ABT 120-5DM) inside the glovebox without any exposure to oxygen and moisture, whose concentrations are always kept below 0.1 ppm.

After the filling of indium(I)iodide, the lamp bodies are transported back to the vacuum system, where the nitrogen inside the lamp bodies is evacuated. Then, they are filled with high purity argon (Air Liquid, Argon N50) as buffer gas at different pressures, which are measured by a capacitive gauge (Pfeiffer Vacuum, CMR 363) with an accuracy of 0.2 % of the reading. Finally, the lamp bodies are sealed by fusing the filling stem.

Since the lamps are filled with buffer gas at the standard room temperature of 298.15 K, the specified p_{Ar}-values in this work are only valid at this temperature and the argon atom density must be calculated accordingly.

However, the amount of indium(I)iodide in gaseous phase is a function of cold spot temperature T_{CS} and not of the filled amount, as long as the filled amount is big enough to sustain a saturated vapor pressure for the given T_{CS}. Thus, the lamp bodies are encased with a cylinder made of fused silica with a diameter of 30 mm and heated externally by a hot air blower (Steinel, HG 2310) during the operation. On one side of the glass casing, a slit with a width of 1 mm was opened to allow the measurement of the temperature alongside the lamp body with an IR-camera (FLIR, A325). The slit is needed, since the IR-camera is sensitive in the spectral range between 7.5 μm and 13 μm, where fused silica glass is non-transparent [138]. The IR-cameras used in thermography application are calibrated with regard to an ideal black body radiator. The deviation of the emission properties of fused silica glass from an ideal black body radiator is taken into account with an emissivity of 0.88 [89]. In this way, the cold spot temperature can be adjusted and monitored for the systematic investigation with an accuracy of ±2 % of reading.

The density of indium(I)iodide molecules in gaseous phase is plotted in figure 6.8 as a function of T_{CS} together with the density of the entire indium(I)iodide filling.
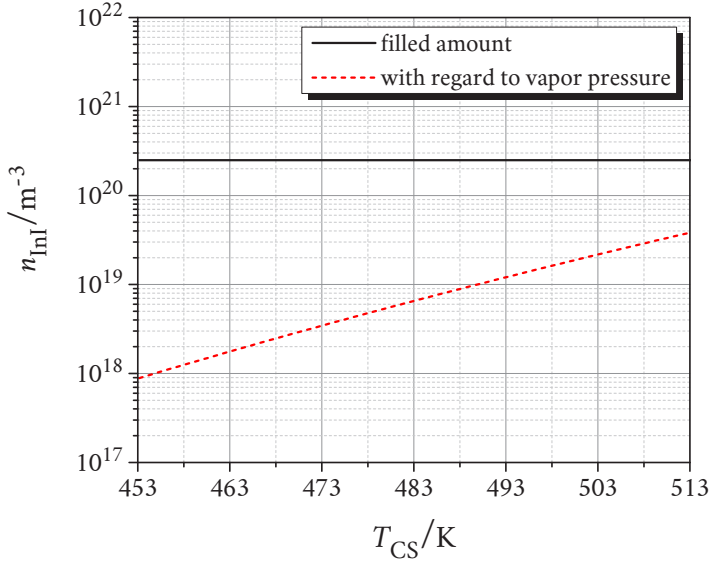
Figure 6.8: Density of indium(I)iodide molecules in gaseous phase as well as density of the entire indium(I)iodide filling as a function of T_{CS}.

According to the model in chapter 5, the filled amount is enough to ensure a saturated vapor pressure in the investigated T_{CS}-range and for the investigated lamp parameters, since the sum of the indium(I)iodide, indium and iodine densities (neutral and ionic) does not exceed the filling density.

After the fabrication of the lamps, the suitability of the chosen radius $R = 8$ mm is tested for the azimuthal symmetric operation mode with surface waves. For this purpose, the variation of the electric field strength

E_r is measured at different azimuthal positions $\phi = 0°, 90°, 180°$ and $270°$ of a lamp filled with 400 Pa argon and driven with $P_{acc} = 3$ W by a coaxial probe, whose axial distance from the end of the lamp and radial distance from lamp axis remain constant during the measurements. The signal from the coaxial probe, which is positioned perpendicular to the lamp surface, is read by an oscilloscope with a bandwidth of 4 GHz (Rohde&Schwarz, RTO 1044). Considering the oscilloscope input resistance of 50 Ω, the Fourier transformed measurement data are displayed in figure 6.9 as a function of frequency.
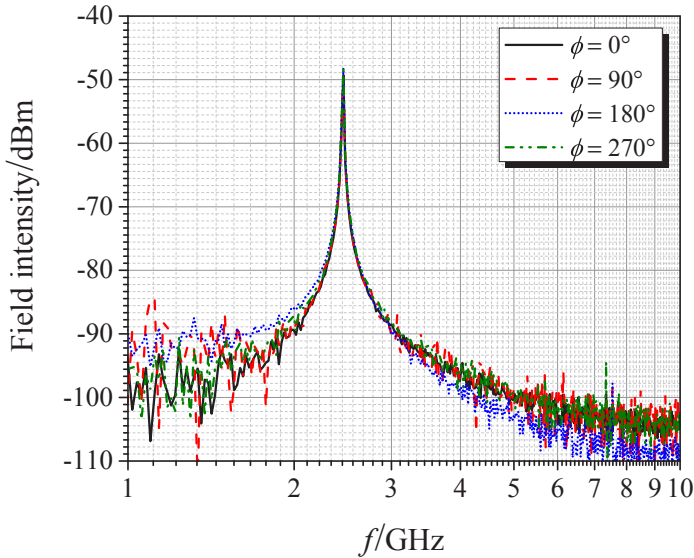
Figure 6.9: E-field strength of the lamp filled with 400 Pa and driven with $P_{acc} = 3$ W, measured by a coaxial probe at different azimuthal positions $\phi = 0°, 90°, 180°$ and $270°$, whose axial distance from the end of the lamp and radial distance from lamp axis remain constant.

An angular variation of the field strength could not be observed for $f = 2.45\,\text{GHz}$, which verifies the m = 0-mode operation of the surfatron.

6.4 Optical measurement

The schematic side view of the employed optical measurement setup including the lamp and the surfatron is shown in figure 6.10 for a better illustration of direction of movement of the telescopic optical probe mounted on the X-Z-stage relative to the lamp.
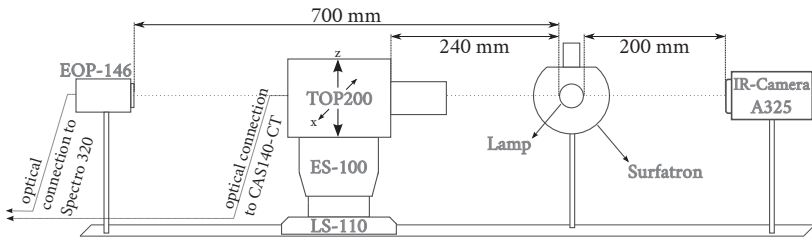
Figure 6.10: Schematic side view of the optical measurement setup including the surfatron and the lamp, as well as the direction of movement of the telescopic optical probe mounted on the X-Z-stage relative to the lamp. During the spectral irradiance measurements, the telescopic optical probe is removed from the setup.

Optical measurements to determine the spectral radiance of the lamps are carried out with an array spectrometer (Instrument Systems, CAS 140CT) in a crossed-Czerny-Turner monochromator setup and a telescopic optical probe (Instrument Systems, TOP200-102). The objective lens of the probe (Instrument Systems, TOP-100-311) features an aperture with a diameter of 125 μm and an objective with an f-number of $f/2.8$. At a distance of 240 mm, this optical system results in an active

measurement area of 0.068 mm^2 on the lamp surface. Since the lens is transparent down to 368 nm, only the emission lines of indium at 410.17 nm and 451.13 nm can be investigated. The calibration used for the measurements was established by the manufacturer with NIST-traceable (National Institute of Standards and Technology) standards. No data about the measurement uncertainty of the calibration standards is available. An instrumental accuracy of ±4 % is specified by the manufacturer.

The optical probe is assembled on a fully automated X-Z-stage (PI miCos, LS-110 & ES-100) with a digital controller (PI miCos, SMC corvus eco), which allows the scanning of the lamp vertically and horizontally with the maximum spatial resolution of 0.1 μm and a covered area of 360 × 26 mm^2. The stage is positioned in such a way that the telescopic optical probe is at a perpendicular distance of exactly 240 mm from the lamp surface. A self-developed Labview-program serves as a remote control unit for both the array spectrometer and the X-Z-stage, thus enabling their co-operation. With this combined system, a spatial lamp scan with a total of 9600 recorded spectra (160 radial × 60 axial) between the wavelengths 380 nm and 800 nm takes about 20 min.

The effect of the operating conditions of the lamp, e.g., electrical input power and cold spot temperature, on the plasma efficiency is investigated by means of irradiance measurements. Spectral irradiance is measured with the help of a scanning spectrometer (Instrument Systems, Spectro 320-164) in a double Czerny-Turner monochromator setup, a cosine-corrected optical probe with diffuser (Instrument Systems, EOP-146) and a UV-transparent fiber bundle (Instrument Systems, OFG-465). Two detectors, i.e., a photomultiplier tube and an InGaAs-photodiode cover a spectral sensitivity range between 190 nm and 1700 nm, while two holographic gratings with 1200 grooves/mm and two ruled gratings

with 600 grooves/mm are responsible for the diffraction in UV-VIS and IR region, respectively.

The optical probe is positioned in a distance of 700 mm from the lamp to allow the point source approximation according to the inverse-square-law with a systematic error of 0.74 %. The wavelength calibration of the spectrometer was established using a mercury-argon line source (Lot-Oriel, Pen-Ray LSP035). Two lamps, i.e., a deuterium lamp (Cathodeon Lt., UK, V03) and a halogen lamp (Osram Sylvania, FEL 1000 W 120 V) serve as transfer standards for irradiance calibration in UV and VIS-IR-region, respectively. Both lamps are PTB-certified (Physikalisch-Technische Bundesanstalt) with a measurement uncertainty of 7 % and ±1.6 % for UV- and VIS-IR-region, respectively, while the spectrometer exhibits an irradiance measurement uncertainty of ±3.5 % for the entire spectral range.

Chapter 7

Investigation of indium(I)iodide-argon plasmas

Electrodeless, surface wave driven mercury-free low pressure lamps based on the indium(I)iodide-argon system are investigated systematically for a broad range of operating parameters. The spatially resolved optical emission spectroscopy (SROES) assisted by spectral irradiance measurements is chosen as the diagnostic method to identify the plasma parameters and to determine the plasma efficiency. Thus, relevant insights can be gained into the relationship between plasma efficiency, plasma parameters and operating parameters. Section 7.1 is devoted to the validation of applicability of SROES for the investigated lamps, while the results of the investigations are presented and discussed in section 7.2.

7.1 Validation of the diagnostic method

In section 4.1, the SROES method is simplified under the assumption of specific conditions, such as cylindrical symmetry, optically thin plasma

and a radial emission profile suitable for the Abel transformation. For a low pressure plasma in cylindrical geometry, cylindrical symmetry of radiation is a safe assumption as long as the applied surface waves exhibit the m = 0-mode, which is already demonstrated in section 6.3. However, the optical thinness of the plasma should be proved theoretically. The sections 7.1.1 and 7.1.2 are dedicated to the verification of optical thinness. Furthermore, in section 7.1.3, the applicability of Abel's inversion method for the radial emission profile of the investigated lamps is discussed. Finally, the emission spectrum of the indium(I)iodide-argon system is presented and analysed in section 7.1.4.

7.1.1 Broadening of emission lines and self-absorption

The Ladenburg relation to calculate the line absorption coefficient α_λ is already given in equation (4.5). Figure 7.1 depicts the calculated α_λ for both emission lines of indium at 410.17 nm and 451.13 nm at different T_{CS} and $p_{Ar} = 400\,\text{Pa}$ as well as at $T_{CS} = 493.15\,\text{K}$ and $p_{Ar} = 200\,\text{Pa}$ as a function of T_e. The needed lower state densities n_j depend strongly on T_e and are taken from the collisional-radiative model (CRM) presented in chapter 5, while the used constants can be found in table 7.1.

Table 7.1: Needed constants to calculate α_λ via Ladenburg relation for both emission lines of indium [24].

λ_0 / nm	k - j	g_k - g_j	A_{kj} / s^{-1}
410.17	$6^2S_{1/2}$ - $5^2P_{1/2}$	2 - 2	$5 \cdot 10^7$
451.13	$6^2S_{1/2}$ - $5^2P_{3/2}$	2 - 4	$8.9 \cdot 10^7$
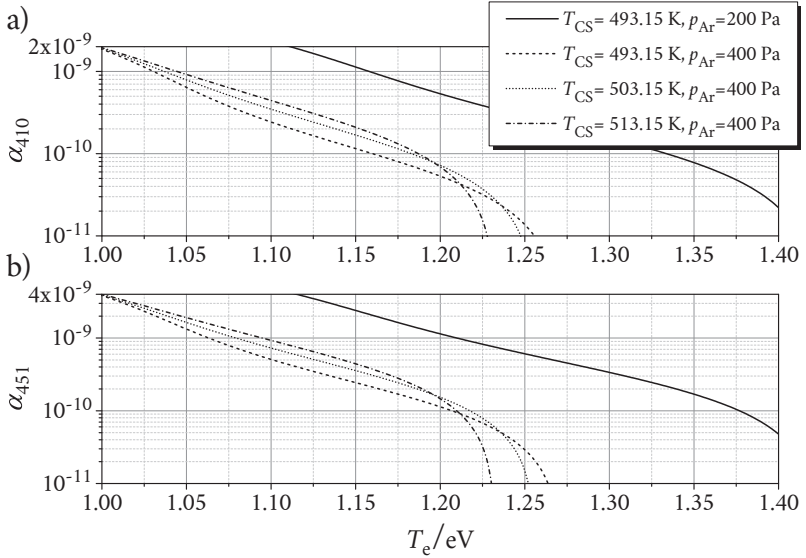
Figure 7.1: Calculated line absorption coefficients α_λ for different T_{CS} and p_{Ar} as a function of T_e.

In addition to α_λ, the broadening profiles of emission and absorption lines should be determined, beginning with the calculation of their FWHMs. Equation (4.6) gives the FWHM $\Delta\lambda_{Natural}$ of a line experiencing natural broadening. $\Delta\lambda_{Natural}$ depends on the lifetimes of the higher and lower energy states of the optical transition resulting in the investigated line. The lower state of the transition at 410.17 nm is the ground state of indium, while that at 451.13 nm is the first metastable state. Since the lifetime of a ground state is infinite and the lifetime of a metastable state is orders of magnitude longer than that of an optically accessible state, the last term in equation (4.6) can be neglected for both emission lines. Furthermore, the energy distribution function of gas particles is assumed as Maxwellian. Thus, equation (4.10) can be used to calculate the FWHM of Doppler broadening $\Delta\lambda_{Doppler}$.

The Voigt profile is given in equation (4.11) as the convolution of Doppler and natural broadening profiles. In due consideration of equations (4.8) and (4.9), it can be concluded that the Voigt profile depends only on the gas temperature T_g. In a low pressure plasma, the spatial distribution of the gas temperature does not vary strongly. Thus, for the following calculations, the gas temperature is approximated as $T_g = T_{CS}$ and $\Psi_\lambda(\lambda)$ is assumed as spatially constant. Furthermore, the kinetic energy of indium atoms in higher and lower energy states does not differ strongly. Therefore, the same profile $\Psi_\lambda(\lambda) = \Psi_\epsilon(\lambda) = \Psi_\alpha(\lambda)$ is used for both emission and absorption. The FWHMs of natural and Doppler broadening are displayed in table 7.2 for $T_{CS} = 493.15\,\mathrm{K}$, with the constants needed to calculate equations (4.6) and (4.10).

Table 7.2: Calculated FWHMs of natural and Doppler broadening for the relevant emission lines of indium at 493.15 K and the needed constants to solve equation (4.6) and equation (4.10).

	FWHM		Constants	
	410.17 nm	451.13 nm	Mass [80]	Lifetime [24]
$\Delta\lambda_{\text{Natural}}$ / pm	0.012	0.015	m_{In} / u	$\tau_{6^2\text{S}_{1/2}}$ / ns
$\Delta\lambda_{\text{Doppler}}$ / pm	0.609	0.669	39.95	7.19

7.1.2 Calculation of the escape factor

The mathematical approach proposed by Summers [92] to evaluate the escape factor Θ for a given line of sight is already presented in section 4.1.2. For the further simplification of equation (4.3), Summers made some assumption such as a spatially constant $\alpha(\lambda, r)$. However, $\alpha(\lambda, r)$ depends on the absorber density n_j, i.e., indium density in ground and metastable

state. Indium atoms are formed in the plasma by dissociating indium(I)-iodide molecules. The dissociation rate is a function of electrical field strength, which is non-uniform in surface-wave driven plasmas [105]. Thus, the radial variation of n_j cannot be neglected in a lamp with molecular filling, which does not serve directly as the radiating species. Since the radial profile of E-field or electron density n_e is not known a priori, an approximation is needed. Irons [93] states that an absolute upper limit to Θ is in the case of uniform emission, while the lower limit is in the case of a Dirac delta emission function in the center of the lamp surrounded by absorbers. Both cases are not plausible for a low pressure plasma. Thus, the electron density profile is approximated by equation (7.1), as predicted by Moisan [58].

$$n_e(r) = n_{e0} J_0(\kappa r/R),\tag{7.1}$$

where n_{e0} is the electron density on the central axis of the lamp and $J_0(\kappa r/R)$ is the zero order Bessel function of the first kind. Since Ferreira [60] showed that the profile for surface wave driven plasmas must be flatter than the Bessel function with $\kappa = 2.405$, $\kappa = 2$ is chosen to calculate n_e-distribution. The n_j and ϵ_λ-values are assigned to corresponding n_e-values with the help of the CRM. The escape factor Θ_λ is then calculated by equation (4.3).

The effective escape factor $\Theta_\lambda^{\text{eff}}$ is determined by equation (4.4) considering the removal factor ϵ_{rem}. Different methods are proposed by Kastner [94] and Athay [140] to calculate the removal factor. In this work, an extended version of the Athay's method is adopted by

$$\epsilon_{\text{rem}} = \frac{\epsilon_{\text{deg}}}{1 + \epsilon_{\text{deg}}},\tag{7.2}$$

where ϵ_{deg} is the degradation rate, which considers both the collisional de-excitation of the absorber from the excited state k into a lower energy state j but also its excitation into a higher energy state l as well as its direct ionization.

The degradation rate is the ratio of non-radiative decay rate of the excited state k to its radiative decay rate. It can be calculated by

$$
\begin{aligned}
\epsilon_{\text{deg}} &= \frac{n_e n_k \sum_{l>k} {}_e^k K^l(T_e) + n_e n_k \sum_{j<k} {}_e^k C^j(T_e) + n_e n_k {}_e^k K_{2e}^i(T_e)}{n_k A_{kj}} \\
&= \frac{n_e \left(\sum_{l>k} {}_e^k K^l(T_e) + \sum_{j<k} {}_e^k C^j(T_e) + {}_e^k K_{2e}^i(T_e) \right)}{A_{kj}},
\end{aligned}
\tag{7.3}
$$

where ${}_e^k K^l(T_e)$, ${}_e^k C^j(T_e)$ and ${}_e^k K_{2e}^i(T_e)$ are the electron impact excitation, de-excitation and ionization rate coefficients, respectively. The degradation rate and consequently the removal factor depend only on the electron temperature and density. The density of the emitting particles does not affect the rate.

The needed cross sections and the rate coefficients for the energy state $6^2S_{1/2}$ are calculated with the help of the CRM and plotted in figures 7.2 and 7.3, respectively. The de-excitation due to collisions with heavy particles are neglected both in the model and in the calculation of the degradation rate.

Figure 7.4 displays the calculated Θ_λ and $\Theta_\lambda^{\text{eff}}$ for both emission lines of indium at different T_{CS} and $p_{\text{Ar}} = 400\,\text{Pa}$ as well as at $T_{\text{CS}} = 493.15\,\text{K}$ and $p_{\text{Ar}} = 200\,\text{Pa}$ as a function of α_λ. In the considered T_e-range of figure 7.1, the effective escape factor for the emission line at 451.13 nm is over 90 %, while a self-absorption up to 50 % should be anticipated for the emission line at 410.17 nm. Thus, the former is chosen for further investigations, since it fulfills the applicability condition of SROES for optically thin plasma.
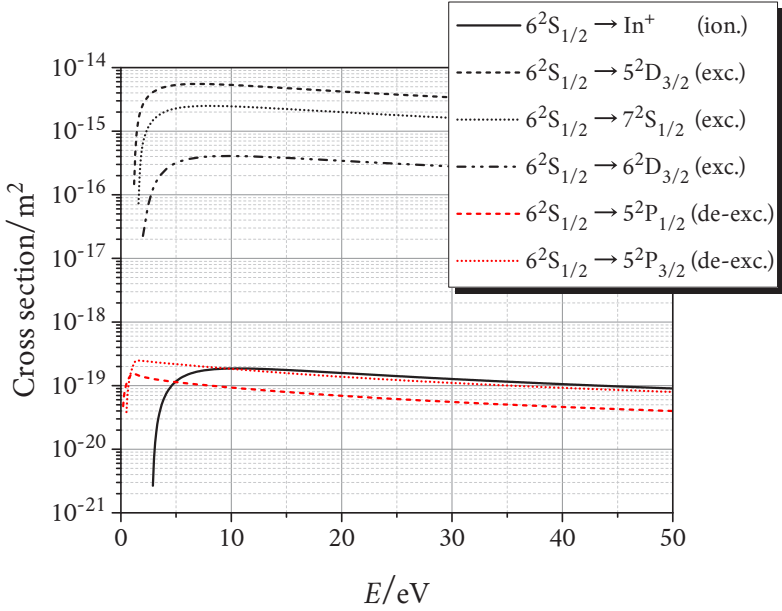
Figure 7.2: Calculated cross sections for electron impact excitation (exc.), de-excitation (de-exc.) and ionization (ion.) of the indium state $6^2S_{1/2}$ as a function of incident electron energy E.

7.1.3 Validation of Abel's inversion method

The final condition for SROES is the suitability of the radial emission profile of the investigated lamps for the inverse Abel transformation. Figure 7.5 **a)** shows the spatially resolved radiance data measured on a lamp filled with $p_{Ar} = 400\,\text{Pa}$, while driven with $P_{acc} = 3\,\text{W}$ at $T_{CS} = 493.15\,\text{K}$.

The x-axis represents the perpendicular distance y from lamp axis in **a)**, but the radial position r in **b)**, **c)** and **d)**, where $r = 0$ is the axis of the lamp. Figure 4.1 serves as a better illustration of y and r. The y-axis gives

the axial position l along the lamp, where $l = 0$ is the coupling position between surfatron and the lamp.
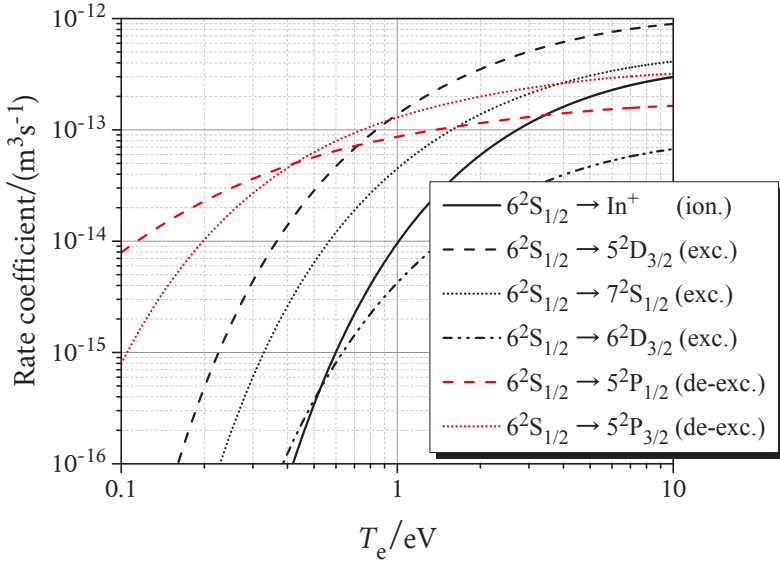
Figure 7.3: Calculated rate coefficients for electron impact excitation (exc.), de-excitation (de-exc.) and ionization (ion.) of the indium state $6^2S_{1/2}$ as a function of electron temperature T_e.

The radiance data were converted to line emission coefficients by means of curve fitting and cosine-expansion methods, as shown in figure 7.5 **b)** and **c)**, respectively. In figure 7.5 **d)**, the deviation of both methods is given. The deviation of the derived emission coefficients is smaller than 10 % in the central part of the lamp for -5.5 mm $\leq r \leq 5.5$ mm. Although a maximum deviation of 48 % is reached near the boundary between the lamp wall and the plasma, the overall deviation of total radiant fluxes calculated by volume integration of emission coefficients is only 3.95 %.
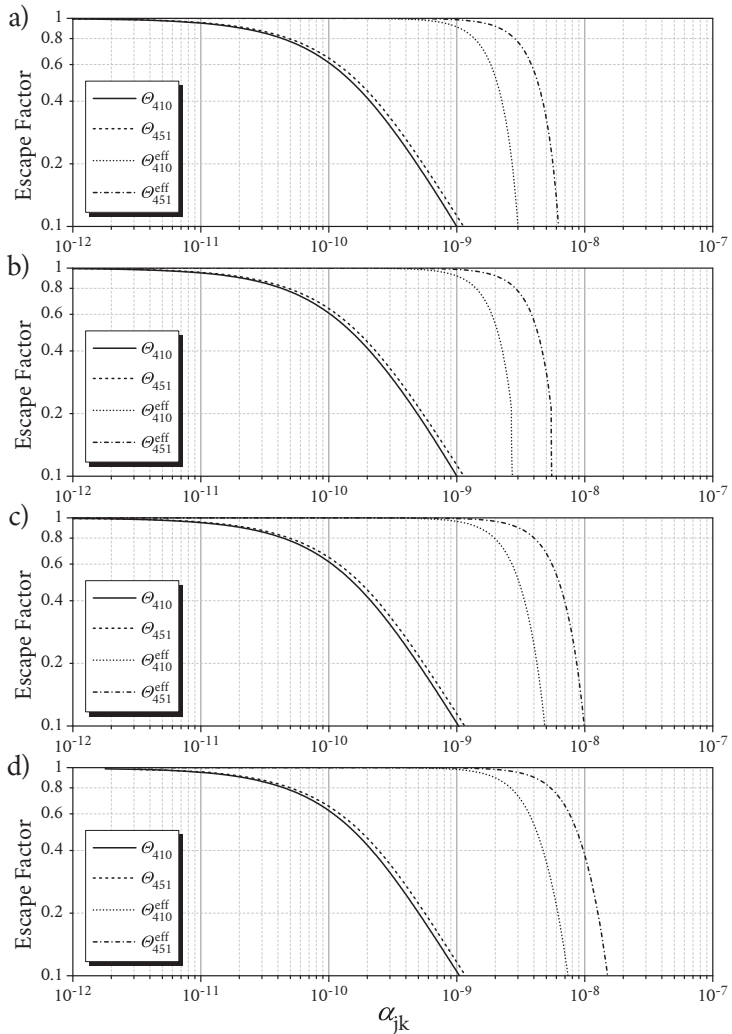
Figure 7.4: Calculated Θ_λ and $\Theta_\lambda^{\text{eff}}$ for the indium emission lines at 410.17 nm and 451.13 nm as a function of α_λ at **a)** $p_{\text{Ar}} = 200\,\text{Pa}$ and $T_{\text{CS}} = 493.15\,\text{K}$; **b)** $p_{\text{Ar}} = 400\,\text{Pa}$ and $T_{\text{CS}} = 493.15\,\text{K}$; **c)** $p_{\text{Ar}} = 400\,\text{Pa}$ and $T_{\text{CS}} = 503.15\,\text{K}$, and **d)** $p_{\text{Ar}} = 400\,\text{Pa}$ and $T_{\text{CS}} = 513.15\,\text{K}$.
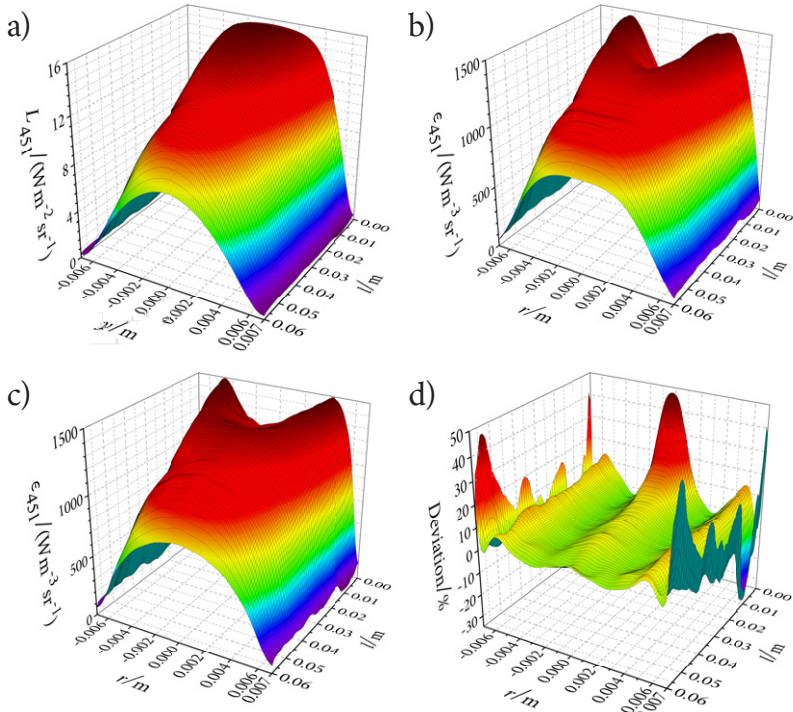
Figure 7.5: a) Radiance at 451.13 nm measured on the lamp filled with p_{Ar} = 400 Pa, while driven with P_{acc} = 3 W at T_{CS} = 493.15 K; **b)** Line emission coefficients calculated with curve fitting method; **c)** Line emission coefficients calculated with cosine-expansion method; **d)** Deviation of both methods.

Furthermore, a photographic image was taken from the face of the lamp with a 12.2-megapixel digital single-lens reflex camera (Canon, 450D), while filtering the incident radiation with a bandpass filter (Edmund optics, Techspec 65140) at 450 nm. The image is analyzed with the technical computing software Matlab by importing the image's blue channel as 8-bit integers and then by normalizing the intensity distribution,

as shown in figure 7.6 **a)**. The radial intensity distribution is displayed in figure 7.6 **b)** together with the corresponding curve fitting. Additionally, the spatial ϵ_{451}-distribution from figure 7.5 **b)** is axially integrated, normalized and plotted for comparison. The external heating should be moved sidewards for the frontal photo shoot, which results in an inhomogeneous heating. Consequently, the off-axis peak on the left-hand side is taller than the one on the right hand side. Apart from such small deviations, the radial emission profiles from the Abel's inversion technique and from the photographic image are in very good agreement.
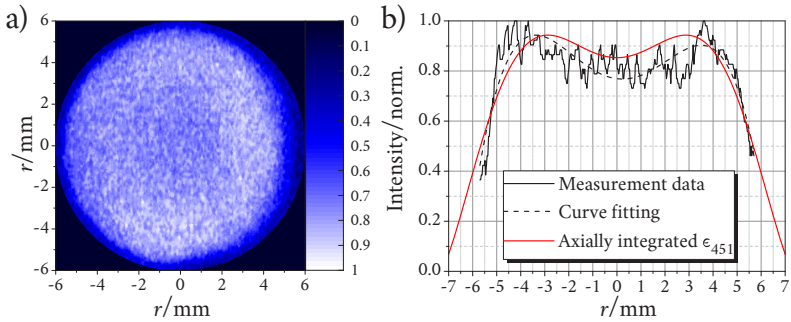
Figure 7.6: a) Photographic image taken from the face of the lamp with a single-lens reflex camera and a bandpass filter at 450 nm. The blue channel of the image is imported and the intensity of the emission is normalized. **b)** Radial emission profile of the lamp taken from the image, the corresponding curve fitting and the axial integration of ϵ_{451}-distribution from figure 7.5 **b)** as comparison.

Thus, the applicability of the inverse Abel transformation on the radial emission profiles of the surface-wave driven lamps is proved. Furthermore, it is shown that both Abel's inversion methods deliver very similar results, although the curve fitting method is easier to adopt and faster to perform. Thus, the curve fitting method is adopted for further investigations. Subsequently, the conversion factor between radiant flux and irradiance is calculated as $\xi_{con} = 5.119 \, \text{m}^2$ for the given geometry.

7.1.4 Spectral analysis of indium(I)iodide-argon filling

Figure 7.7 shows the spectral irradiance measured with the lamp filled with $p_{Ar} = 800$ Pa, while operating at the peak efficiency configuration $T_{CS} = 493.15$ K and $P_{acc} = 3$ W.
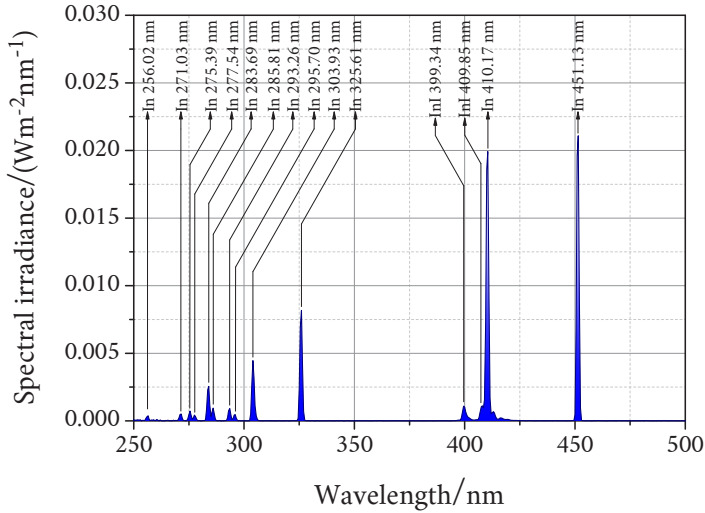
Figure 7.7: Spectral irradiance measured with a lamp filled with $p_{Ar} = 800$ Pa, while driven with $P_{acc} = 3$ W at $T_{CS} = 493.15$ K.

The spectrum is dominated by the atomic emission lines of neutral indium, whose transitions are illustrated in figure 2.1. Yet, the resonance line at 410.17 nm is overlapped with weak molecular radiation. According to Wehrli [141, 142], indium(I)iodide exhibits molecular radiation with two maxima at 399.34 nm and 409.85 nm. Since the given wavelengths of the maxima are in complete agreement with the measured spectrum, molecular radiation is related to indium(I)iodide. Nonetheless, the two atomic lines at 410.17 nm and 451.13 nm account for about

67 % of the total emission, while the contribution of molecular radiation remains below 5 %. The contribution of argon emission is negligible in the investigated T_{CS}-range, while neutral iodine does not feature any strong emission lines in the relevant wavelength range between 200 nm and 800 nm [24]. Therefore, only the emission of indium between 256 nm and 451 nm is considered to determine the efficiency.

The emission line at 410.18 nm was already ruled out for the investigations via SROES due to the strong self-absorption at this wavelength, as shown in section 7.1.2. In addition to that, the overlapped molecular radiation may result in the overestimation of line emission coefficients and consequently of the plasma parameters.

7.2 Parameter study and investigation of plasma properties

The plasma is characterized with regard to plasma efficiency as a function of operating parameters, i.e, field strength, cold spot temperature T_{CS}, buffer gas pressure p_{Ar} and accepted MW-power P_{acc}. Thereby, the relation between operating configurations, plasma parameters and plasma efficiency could be identified, as presented and discussed in the following sections.

7.2.1 Variation of field strength

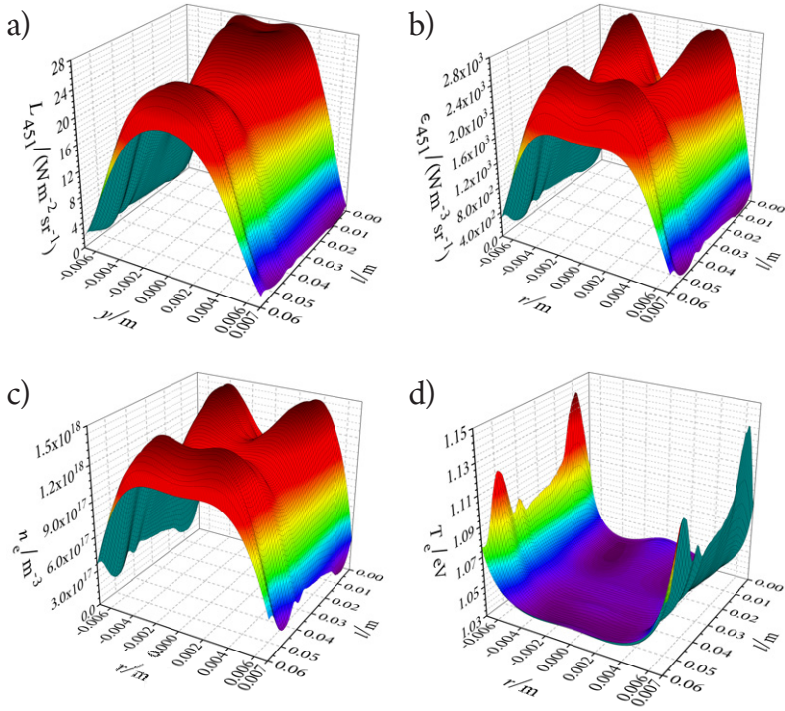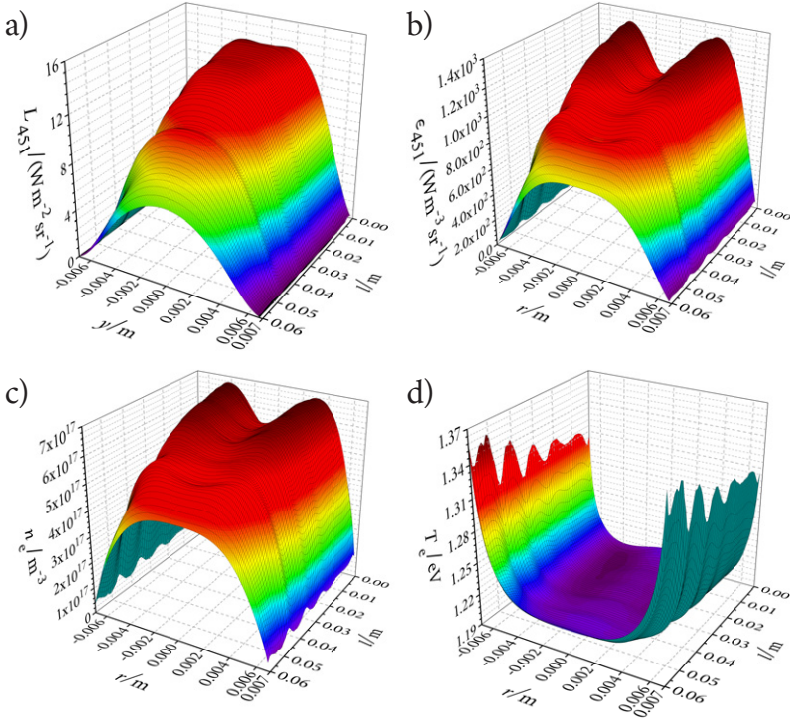The radiance data measured at 451.13 nm on a lamp filled with $p_{Ar} = 400$ Pa, while driven at $P_{acc} = 3$ W and $T_{CS} = 493.15$ K is plotted in figure 7.5 **a)**, while the spatial distribution of line emission coefficients

can be found in figure 7.5 **b)**. The plasma parameters, e.g., electron density n_e and electron temperature T_e can then be derived from the line emission coefficients with the help of the CRM, as shown in figure 7.8 **a)** and **b)**, respectively. Near the surfatron-lamp interface for $l \leq 10$ mm, a relative minimum of ϵ_λ as well as of n_e occurs on the axis, while twin maxima are located near the lamp walls, as can be seen in figure 7.5 **b)** and in figure 7.8 **a)**, respectively.
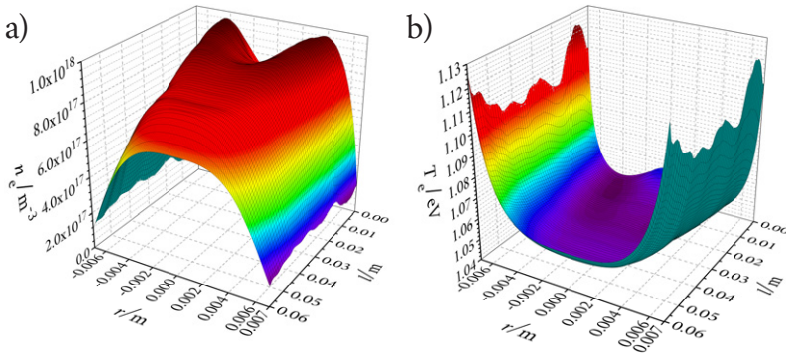
Figure 7.8: a) Spatial distribution of the calculated electron densities of the lamp filled with $p_{Ar} = 400$ Pa, while driven with $P_{acc} = 3$ W at $T_{CS} = 493.15$ K; **b)** Spatial distribution of the corresponding electron temperatures.

Moisan [58] and Margot [143] stated that the so-called *off-axis peaks* occur at higher frequencies, where the electric field strength rises significantly from lamp axis to the lamp wall, while for lower frequencies $f < 800$ MHz, a nearly uniform radial field strength with a Bessel-like electron density distribution can be observed. According to Besner [144], at the end of the plasma column, the radial maximum is located on the axis regardless of the frequency and pressure. It should be kept in mind that Besner used open ended fused silica tubing, where the length of the plasma column can be varied by changing the input power. Yet, the

electrical field strength drops always under a critical value at the end of the plasma column [38].

In summary, the off-axis peaks of ϵ_λ may be attributed to the skin effect. The alternating microwave field cannot penetrate into the plasma at higher frequencies and for higher electrical conductivities, which is mostly the case near the surfatron, where the electron density is maximum.

To verify this assumption, the radiance measurements were undertaken for different buffer gas pressures and operating configurations: Figure 7.9 **a)** shows the radiance data measured on the lamp filled with 400 Pa argon, while driven with $P_{acc} = 6$ W at $T_{CS} = 493.15$ K, while the spatial distributions of line emission coefficients, of the electron density and of the electron temperature can be found in subfigures **b)**, **c)** and **d)**, respectively. The results for the lamp filled with 400 Pa argon, while driven with $P_{acc} = 9$ W at $T_{CS} = 493.15$ K can be found in figure 7.10. Similarly, the measured and derived data of the lamp filled with 200 Pa argon, while driven with $P_{acc} = 3$ W at $T_{CS} = 493.15$ K are given in figure 7.11.

With increasing input power, the length of the plasma column also increases, until it reaches the end of the discharge vessel and the surface waves are reflected. Hence, standing wave patterns arise along the plasma column, causing a modulation of the axial radiation and electron density profiles, as can be seen in subfigures 7.9 **b)** and **c)**. Multiple axial maxima homogenize the axial radiation profile [145]. Additionally, the strong electrical field due to the constructive interference leads to the formation of the off-axis peaks also at the end of the discharge vessel, as demonstrated in figure 7.10 **b)**.

Another possibility to increase the electrical conductivity and subsequently to intensify the skin effect, is to reduce the buffer gas pres-

sure. It results in an increase of the reduced electrical field [133, 146] and of the mobility of the charged particles, which leads to a higher electrical conductivity and to the formation of the off-axis peaks, outspread farther from the surfatron at the same input power, as can be seen in figure 7.11 **b)**.
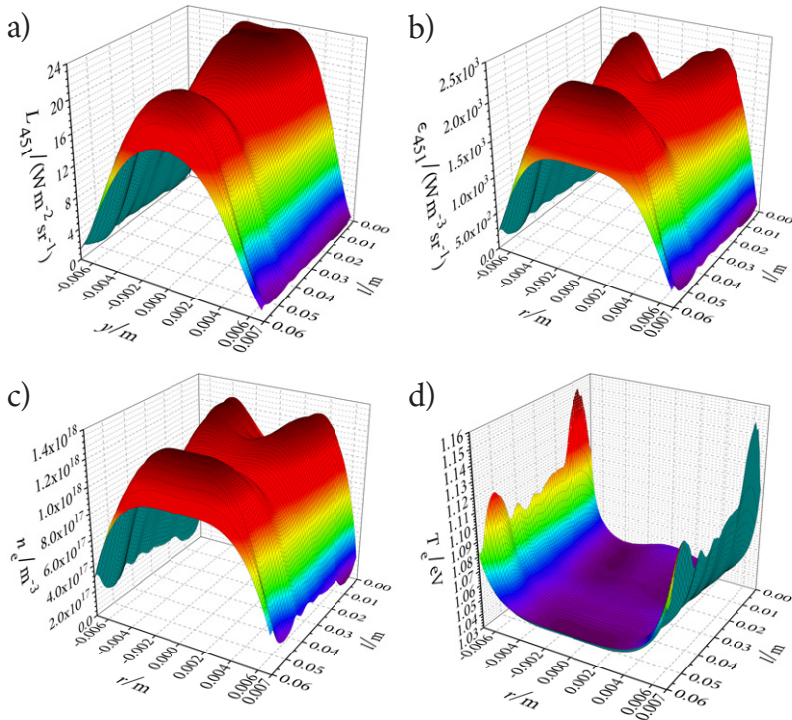
Figure 7.9: a) Radiance data measured at 451.13 nm on a lamp filled with $p_{Ar} = 400$ Pa, while driven with $P_{acc} = 6$ W at $T_{CS} = 493.15$ K; **b)** Spatial distribution of the calculated line emission coefficients at 451.13 nm; **c)** Spatial distribution of the calculated electron densities; **d)** Spatial distribution of the calculated electron temperatures.

Figure 7.10: a) Radiance data measured at 451.13 nm on a lamp filled with $p_{Ar} = 400$ Pa, while driven with $P_{acc} = 9$ W at $T_{CS} = 493.15$ K; **b)** Spatial distribution of the calculated line emission coefficients at 451.13 nm; **c)** Spatial distribution of the calculated electron densities; **d)** Spatial distribution of the calculated electron temperatures.

7.2.2 Variation of cold spot temperature

Indium(I)iodide is filled into the lamp in the form of condensed pellets. In the closed volume of the discharge vessel, the cold spot temperature determines saturated vapor pressure of the indium(I)iodide. Hence, the plasma parameters depend strongly on the T_{CS}. The efficiency, as well the radiant flux, of the lamps filled with $p_{Ar} = 100, 200, 400$ and 800 Pa

is plotted as a function of T_{CS} for $P_{acc} = 3$ and 6 W in figure 7.12 **a)**, **b)**, **c)** and **d)**, respectively.

Figure 7.11: a) Radiance data measured at 451.13 nm on a lamp filled with $p_{Ar} = 200$ Pa, while driven with $P_{acc} = 3$ W at $T_{CS} = 493.15$ K; **b)** Spatial distribution of the calculated line emission coefficients at 451.13 nm; **c)** Spatial distribution of the calculated electron densities; **d)** Spatial distribution of the calculated electron temperatures.

The lower limit of T_{CS} is chosen as 451.15 K for this investigation, since the indium(I)iodide density is too low for a significant contribution to the emission below this temperature and the spectrum of the lamp becomes that of a pure argon plasma.

The saturated vapor pressure of indium(I)iodide, whose density can be calculated by [69, p. 129] and the ideal gas law, is an exponential function of the cold spot temperature. With increasing T_{CS}, an increase in radiant flux as well in plasma efficiency can be observed, whereas the maximum efficiency is located at $483.15\,\mathrm{K} \leq T_{CS} \leq 503.15\,\mathrm{K}$ for different buffer gas pressures. For higher T_{CS} than the optimum, the efficiency declines once again, although the spectrum does not change significantly. The thermal development of the emission spectrum can be found in figure 7.13 for the lamp filled with $p_{Ar} = 400\,\mathrm{Pa}$ and driven at $P_{acc} = 3\,\mathrm{W}$. The resonance emission line at 410.17 nm shrinks for $T_{CS} > 493.15\,K$, while the rise of emission line at 451.13 nm continues up to $T_{CS} = 503.15\,K$.

This effect can be explained as follows: In figure 7.14, the densities of indium atoms in ground, metastable and $6^2S_{1/2}$ states, calculated with the CRM, are shown for $p_{Ar} = 400\,\mathrm{Pa}$ and different T_{CS} as a function of T_e.

The density of ground and metastable state indium atoms increases monotonically with the cold spot temperature. However, the density of excited indium atoms at $6^2S_{1/2}$-state saturates for $T_{CS} > 493.15\,\mathrm{K}$. Thus, the self-absorption of emitted radiation increases with cold spot temperature, while the number of emitted photons remains constant above the optimum T_{CS}, which results in the decrease of the radiant flux and the efficiency.

The relevant T_e-range for the lamp filled with $p_{Ar} = 400\,\mathrm{Pa}$ is between 1.04 eV and 1.13 eV, as can be seen in figure 7.8 **b)**. In this range, an increasing cold spot temperature leads to a higher α_λ, as given in figure 7.1. Additionally, figure 7.4 demonstrates that $\Theta_{451}^{\mathrm{eff}}$ exceeds $\Theta_{410}^{\mathrm{eff}}$, although α_{410} is lower than α_{451} in the T_e-range of interest. Thus, the diminution of the emission line at 451.18 nm starts at higher cold spot temperatures than at 410.17 nm.
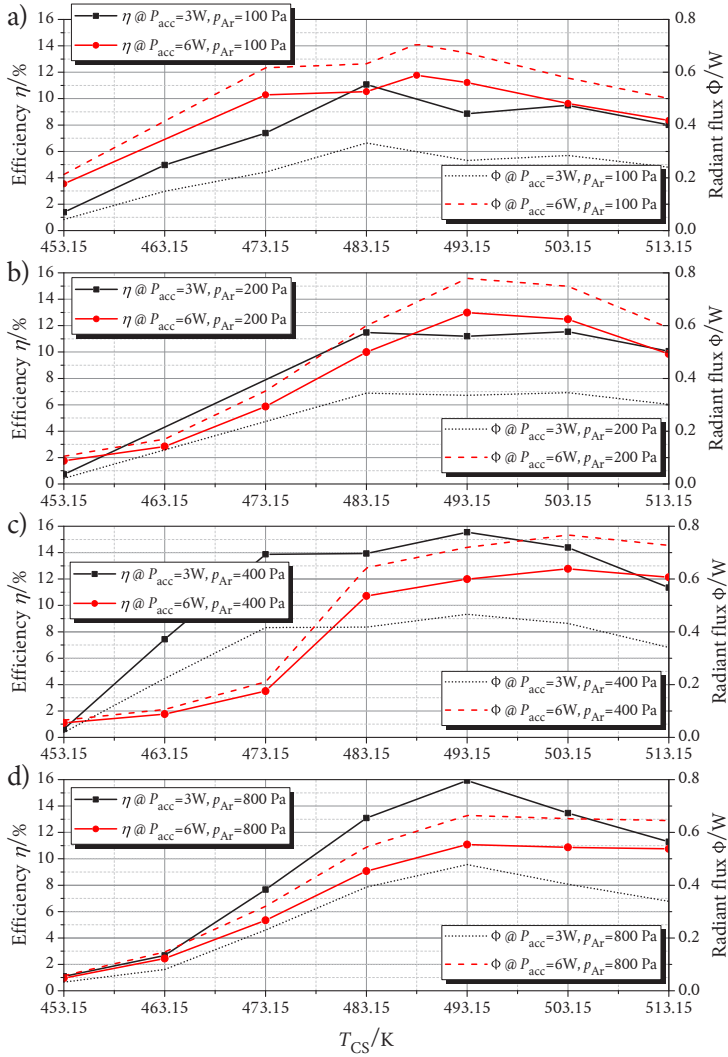
Figure 7.12: Efficiency and radiant flux of the lamps filled with $p_{Ar} = 100, 200, 400$ and 800 Pa, driven with $P_{acc} = 3$ W and 6 W as a function of T_{CS}.
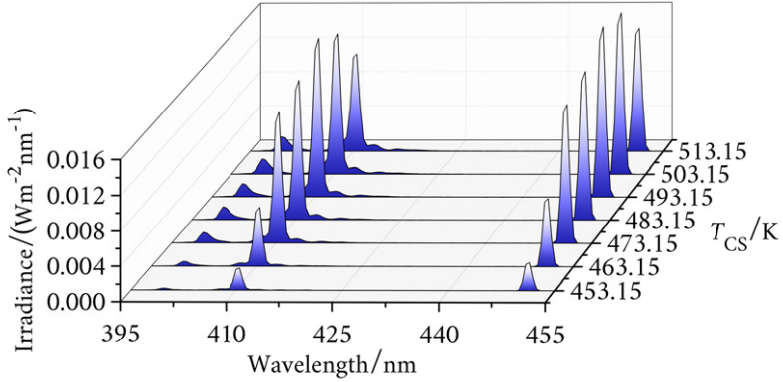
Figure 7.13: Spectral irradiance measured with a lamp filled with $p_{Ar} = 400\,\text{Pa}$, while driven with $P_{acc} = 3\,\text{W}$ at different cold spot temperatures $453.15\,\text{K} < T_{CS} < 513.15\,\text{K}$.

Figures 7.15 and 7.16 depict the measured radiance data and the spatial distributions of the line emission coefficients, the electron densities and the electron temperatures for the lamps filled with $p_{Ar} = 400\,\text{Pa}$, while driven with $P_{acc} = 3\,\text{W}$ at $T_{CS} = 503.15$ and $513.15\,\text{K}$, respectively. The subfigure **d)** has in both figures a reversed y-axis for a better illustration. Thus, the effect of cold spot temperature on the spatial distribution of T_e can be analyzed by comparing the corresponding subfigures from figures 7.8, 7.15 and 7.16.

Two important observations can be made from this analysis: First, T_e depends very weakly on T_{CS}. Secondly, the plasma column shrinks with increasing T_{CS}.

The former can be explained with the weak momentum transfer between electrons and indium(I)iodide molecule and also its atomic byproducts indium and iodine. The indium(I)iodide density in the investigated T_{CS}-range is 3 to 5 orders of magnitude lower than the argon density. Therefore, the frequency of elastic collisions between electrons and indium(I)-

iodide molecules is negligible with respect to that of collisions between electrons and argon atoms.

Additionally, the kinetic energy transfer during an elastic collision is proportional to the ratio between the masses of the collision partners. Since the indium(I)iodide, indium and iodine are much heavier than argon, the kinetic energy transfer from electrons is also negligible for these species.

Similar to the electron temperature, the electron density also drops with increasing T_{CS} above the optimum. As shown in figure 7.14, the percentage of electrical power dissipated in the dissociation of indium(I)iodide rises with T_{CS} (since neutral indium density increases) for the investigated T_e-range, while power dissipated in the excitation of indium atoms remains nearly constant, which results in a smaller power investment in the ionization for a constant P_{acc}. Consequently, the electron density decreases, as demonstrated in subfigure **c)** of figures 7.15 and 7.16.

Figure 7.17 **a)**, **b)** and **c)** depict the calculated ion densities of argon, indium and indium(I)iodide, respectively. Below the optimum T_{CS}, the contribution of indium to the electron density grows with increasing T_{CS}, while that of argon declines. Since the ionization of indium is more efficient than that of argon, an increase in the efficiency can be observed in figure 7.12 with increasing T_{CS}. However, the indium ion density saturates above the optimum T_{CS} for electron temperatures $T_e > 1.06$. Nevertheless, the decrease of argon ion density continues, which results in a lower overall electron density. Furthermore, the direct ionization of indium(I)iodide molecules becomes more frequent despite its higher energy cost compared to the step-wise ionization of indium atom, which leads to an decreased efficiency and to an increased power absorption from the wave field per unit length of the plasma column. Since the length of the plasma column depends on the input power and its axial attenuation rate [38], the plasma column shortens for increasing T_{CS} at a constant P_{acc}, as shown in subfigure **b)** of figures 7.15 and 7.16.
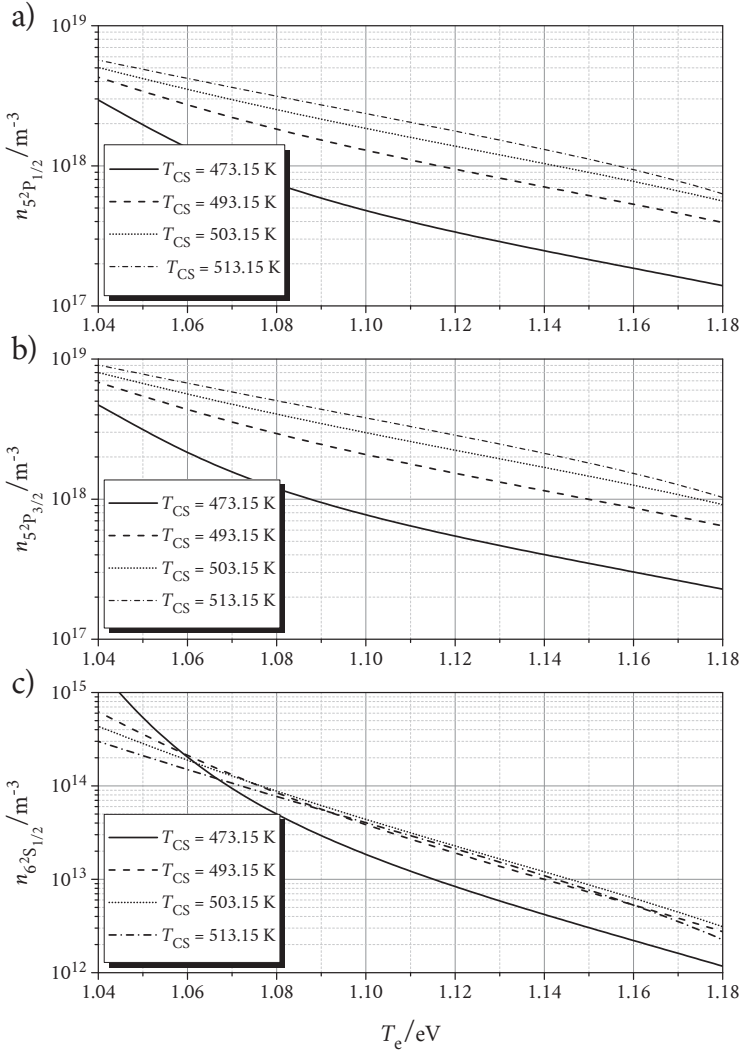
Figure 7.14: Calculated densities of indium atoms in energy states **a)** $5^2P_{1/2}$, **b)** $5^2P_{3/2}$ and **c)** $6^2S_{1/2}$ at different T_{CS} for $p_{Ar} = 400\,\text{Pa}$ as a function of electron temperature T_e.
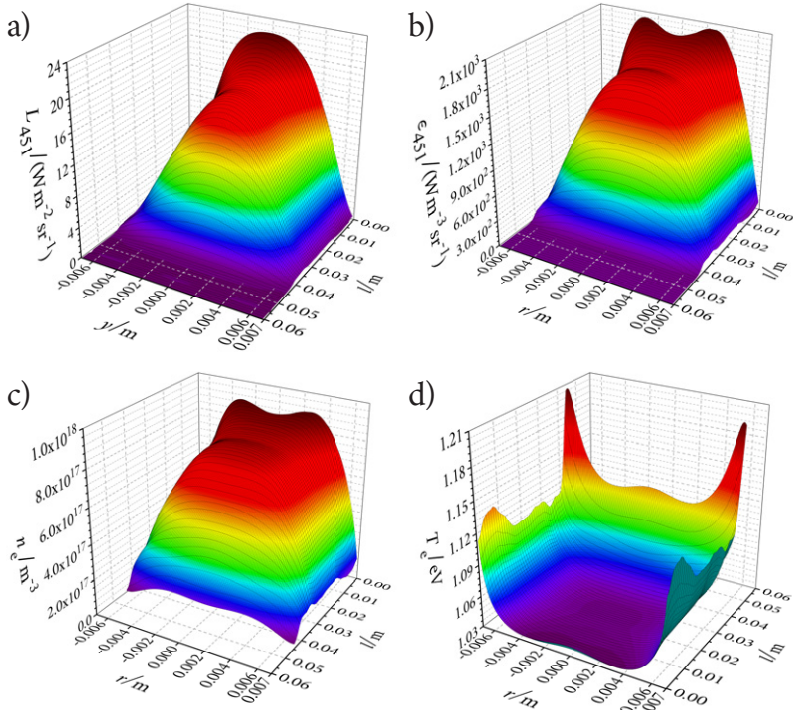
Figure 7.15: a) Radiance data measured at 451.13 nm on a lamp filled with $p_{Ar} = 400\,Pa$, while driven with $P_{acc} = 3\,W$ at $T_{CS} = 503.15\,K$; **b)** Spatial distribution of the calculated line emission coefficients at 451.13 nm; **c)** Spatial distribution of the calculated electron densities; **d)** Spatial distribution of the calculated electron temperatures.

7.2.3 Variation of buffer gas pressure

In low pressure plasmas, the dominating loss mechanism is the diffusion of neutral and charged particles to the wall due to the free and ambipolar diffusion, respectively, where they recombine. The mobilities and diffusion coefficients of electrons as well as of heavy particles decrease with increasing buffer gas pressure [32, 131], which lead to lower diffusion

losses and consequently to higher particle densities. As a result, the step-wise processes, e.g., step-wise ionization of argon or ionization of indium after the dissociation of indium(I)iodide, become more frequent.
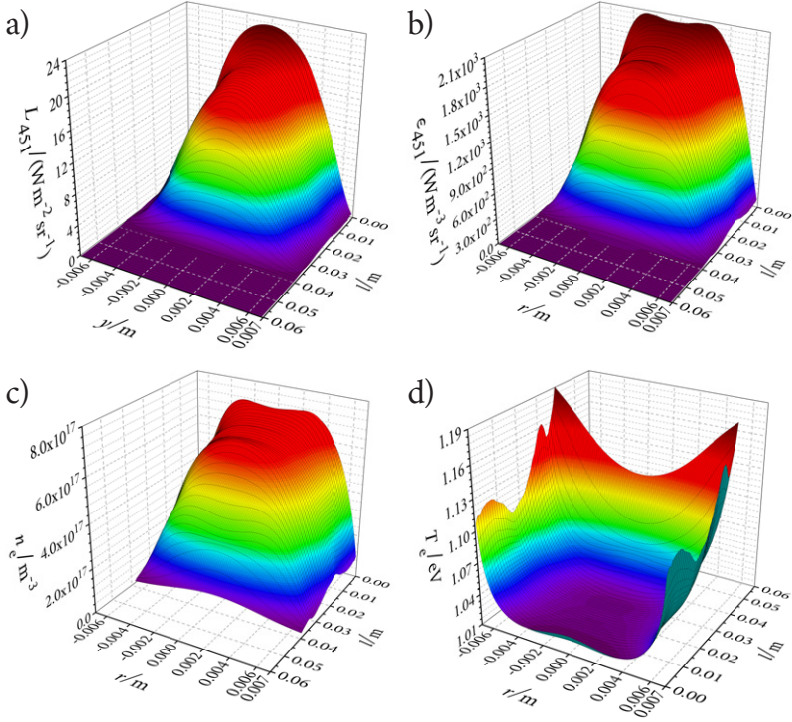
Figure 7.16: a) Radiance data measured at 451.13 nm on a lamp filled with p_{Ar} = 400 Pa, while driven with P_{acc} = 3 W at T_{CS} = 513.15 K; **b)** Spatial distribution of the calculated line emission coefficients at 451.13 nm; **c)** Spatial distribution of the calculated electron densities; **d)** Spatial distribution of the calculated electron temperatures.

Since the needed kinetic energy for each step is smaller than the energy required for the direct processes, the electrons with lower kinetic energies can also participate in inelastic collisions, which results in a higher

kinetic energy dissipation in inelastic processes. Consequently, the average energy of electrons, or in another words, the electron temperature drops [33]. In summary, for lower diffusion losses, lower electron temperatures are needed to achieve the same electron densities. In figures 7.8 and 7.11, the electron temperature distribution of the lamps filled with p_{Ar} = 200 and 400 Pa is plotted for T_{CS} = 493.15 K and P_{acc} = 3 W, respectively.

Low electron temperatures reduce the rates of inefficient inelastic collisions with high threshold energies, e.g., direct ionization of argon atom or indium(I)iodide molecule, and the input power is dissipated in more energy efficient processes, as explained in section 5.7.1. Therefore, the higher the buffer gas pressure, the higher the maximum efficiency of the lamp, as demonstrated in figure 7.12. However, the increase of the efficiency is limited due to two counteractions: First, the frequency of elastic collisions rises with buffer gas pressure, which results in a more excessive momentum transfer from electrons to heavy particles, while the amount of energy dissipated in the excitation of indium atoms decreases. Secondly, with increasing particle densities, secondary processes, e.g., volume recombination of electrons and ions, and collisional de-excitation of excited indium atoms, become more effective. Thus, an optimum buffer gas pressure exists, at which the efficiency of the plasma is maximum. In the investigated p_{Ar}-range, a decline in the maximum achievable efficiency due to the increased gas pressure could not be observed for P_{acc} = 3 W, as can be seen in figure 7.12. However, the rise of the maximum efficiency, achieved by doubling the pressure from p_{Ar} = 400 to 800 Pa, is marginal. Hence, it is assumed that the optimum buffer gas pressure is around 800 Pa for the given lamp configuration.

According to Smith [10], the maximum efficiency is achieved at p_{Ar} = 67 Pa for mercury and at p_{Ar} = 667 Pa for gallium(III)iodide discharges inside a lamp with a diameter of 25 mm.
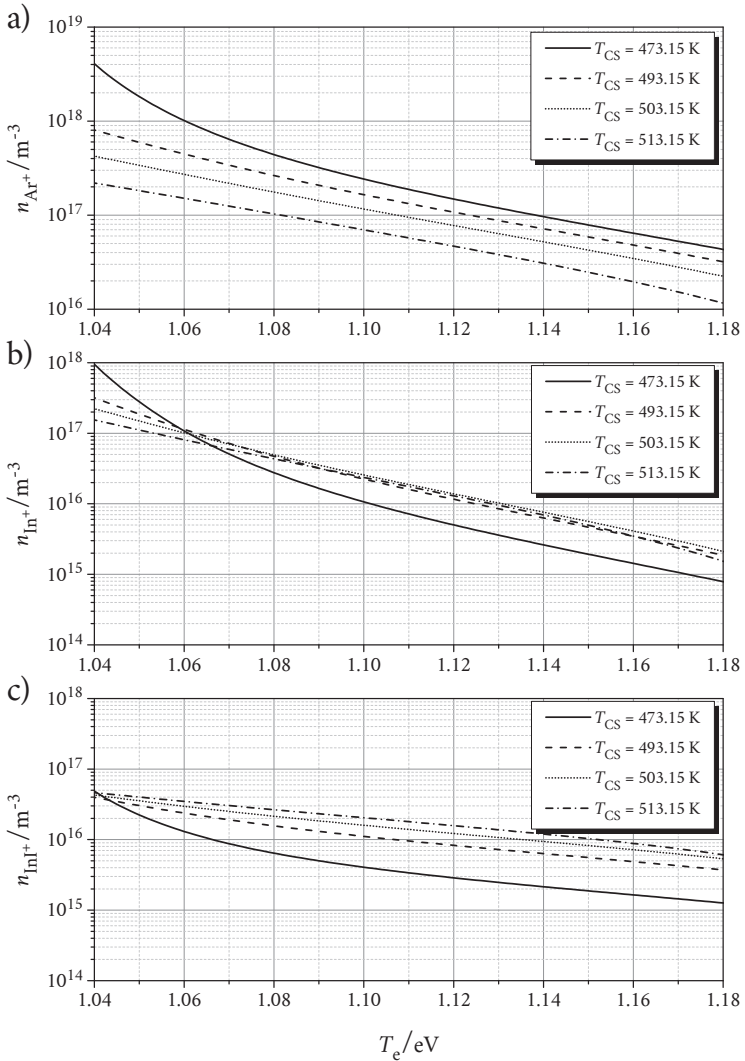
Figure 7.17: Calculated densities of **a)** argon ions, **b)** indium ions and **c)** indium(I)iodide ions as a function of electron temperature at different T_{CS} for $p_{Ar} = 400\,\text{Pa}$.

Smith[10] stated that the difference between mercury and gallium(III)iodide arises from the high energy investment in the dissociation of the molecular filling, while mercury atoms do not cause such electron energy losses. Thus, the compromise between diffusion and gas heating losses should be shifted in favor of diffusion. The same reasoning can be applied also on indium(I)-

iodide discharge. Since the dissociation energy of indium(I)iodide is lower than that of gallium(III)iodide, the optimum buffer gas pressure can be estimated as $p_{Ar} < 667\,Pa$ instead of $p_{Ar} \approx 800\,Pa$. However, the diameter of the lamps used in this work is only half as large than that of Smith, resulting in higher ambipolar diffusion losses.

On the other hand, the maximum achievable efficiency declines at $P_{acc} = 6\,W$ for $p_{Ar} > 200\,Pa$. The impact of accepted MW-power on the plasma efficiency is explained in the next section.

7.2.4 Variation of power density

Figures 7.18 and 7.19 depict the efficiency and the radiant flux of the lamps filled with $p_{Ar} =$100, 200, 400 and 800 Pa for $T_{CS} =$453.15, 483.15 and 513.15 K as a function of P_{acc}, respectively. In due consideration of the lamp geometry, input power densities between 330-1680 mW·cm^{-3} are investigated.

The highest plasma efficiency is achieved, when the plasma column fills the whole discharge volume without any power reflection and standing wave pattern. At lower p_{Ar}, strong diffusion losses lead to a shrunken plasma column for a constant P_{acc}. Thus, the input power must be increased to reach the optimum operating configuration, as can be seen in figure 7.18 **a)**.
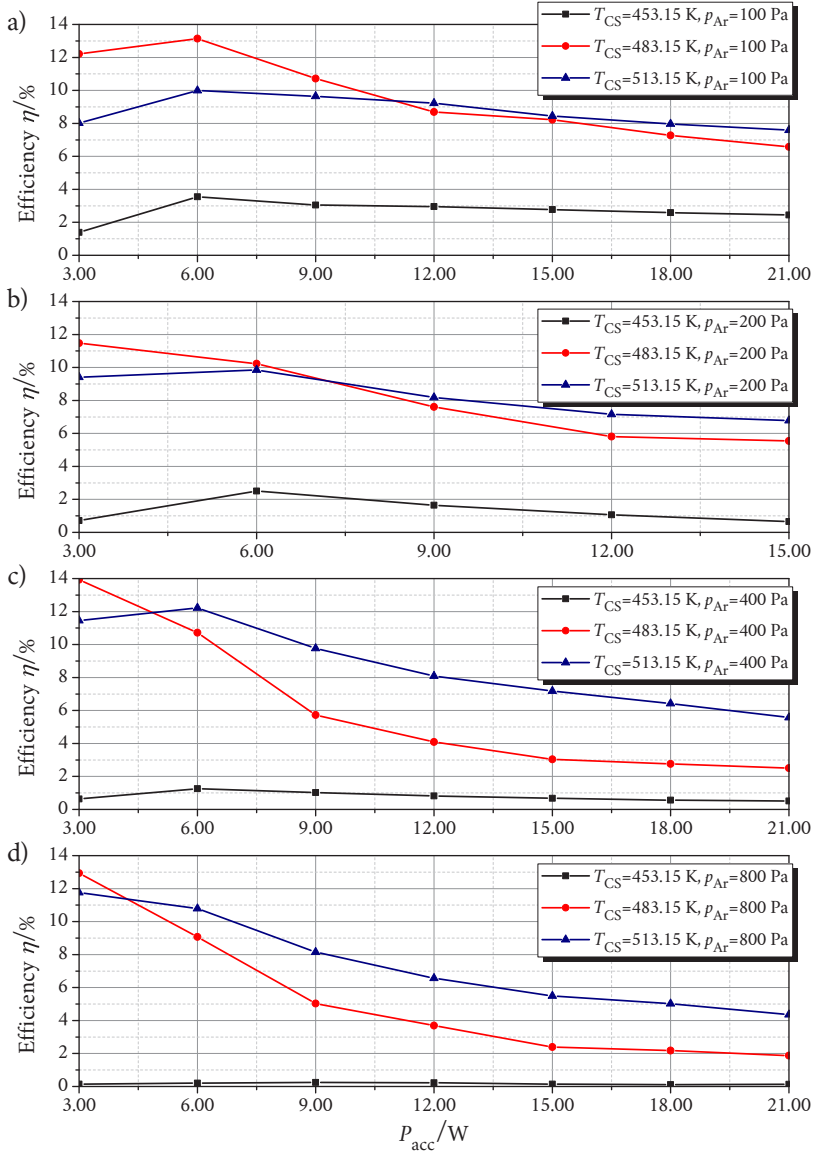
Figure 7.18: Efficiency of the lamps filled with different p_{Ar} at T_{CS} =453.15, 483.15 and 513.15 K as a function of P_{acc}.
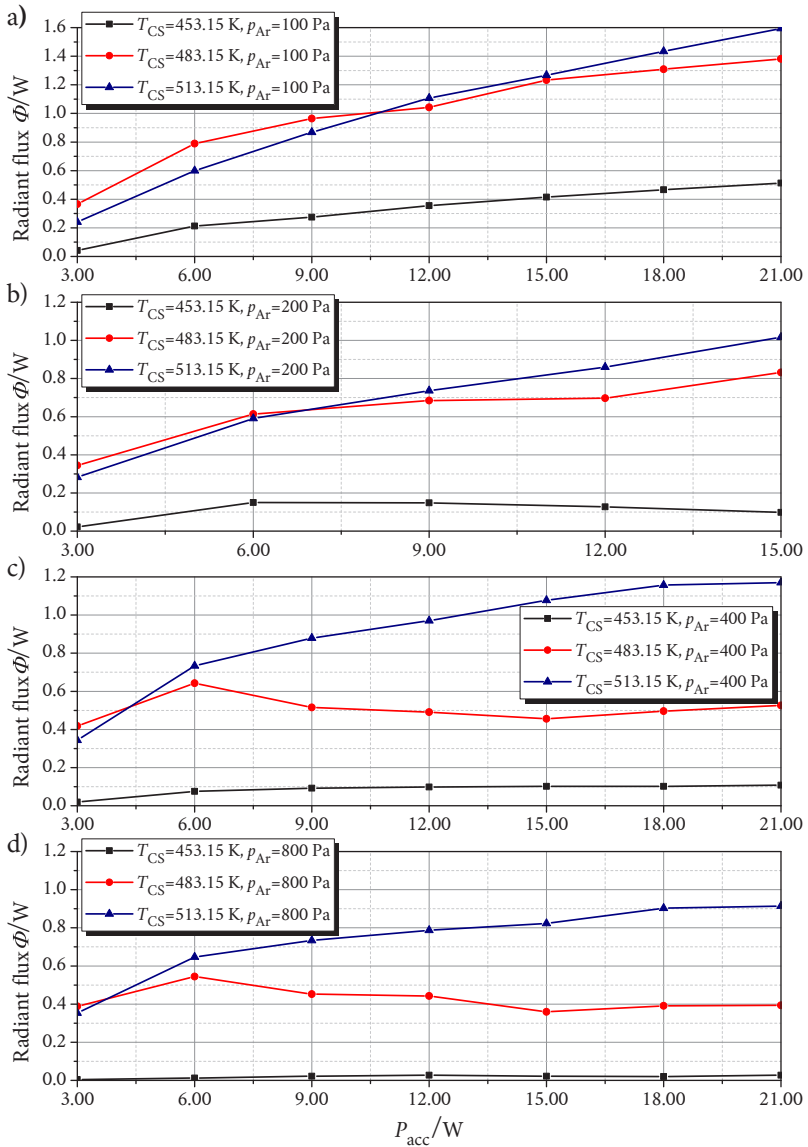
Figure 7.19: Radiant flux of the lamps filled with different p_{Ar} at T_{CS} =453.15, 483.15 and 513.15 K as a function of P_{acc}.

A cold spot temperature higher than the optimum also causes the shortening of the plasma column due to stronger attenuation rate of the wave power, as mentioned in section 7.2.2. Hence, even at higher p_{Ar}, the input power must be increased to reach the highest efficiency for $T_{CS} = 513.15\,\text{K}$, as demonstrated in figure 7.18 **b)** and **c)**. The same approach is also valid for $T_{CS} = 453.15\,\text{K}$. As displayed in figure 7.17, argon is the main electron supplier of the plasma for low T_{CS} despite its high energy cost. Therefore, a higher power is needed to fill the discharge vessel with plasma. For the optimized T_{CS} and p_{Ar}, the lower the power density the higher the efficiency, until the input power drops below the necessary level to sustain a plasma with a length equal to that of the discharge volume.

The indium density in energy state $6^2S_{1/2}$ rises with increasing P_{acc} until saturation, since the total density of indium atoms is limited by T_{CS}. Thus, the radiant flux of the lamps increases sub-linearly towards higher input powers, as can be observed in figure 7.19. Additionally, self-absorption becomes stronger with decreasing T_e, as shown in figures 7.1 and 7.4. As mentioned in section 7.2.3, T_e depends strongly on p_{Ar}.

Hence, the increase rate of the radiant flux as a function of P_{acc} decreases with increasing p_{Ar}. For $p_{Ar} = 400$ and $800\,\text{Pa}$, where T_e is relatively low, the gradient becomes even negative at $T_{CS} = 483.15\,\text{K}$. The saturation of emission lines as well as the growing effect of self-absorption can also be observed in mercury-argon discharges, regardless of the excitation frequency [145, 147].

7.3 Evaluation of the results

The surface wave driven lamps with indium(I)iodide-argon filling have been investigated as a possible mercury substitute with regard to the plasma efficiency for varying operating configurations, e.g., electrical input power, cold spot temperature and buffer gas pressure. The lamps were characterized by means of spatially resolved optical emission spectroscopy assisted by spectral irradiance measurements and plasma parameters were determined with the help of a collisional-radiative model.

A strong analogy between the investigated filling and the mercury-argon discharge could be observed concerning the plasma behavior and operating configurations:

- The spectra of the lamps feature strong atomic radiation, although the molecular filling of indium(I)iodide is employed.

- The plasma efficiency increases with increasing buffer gas pressure, until energy loss by elastic collisions, and secondary processes balance the gain obtained by reduced diffusion losses. The optimum buffer gas pressure is higher than that of a mercury-argon discharge in a lamp with same geometry.

- A similar behavior is also observed with the cold spot temperature. At lower temperatures, the lamps feature the spectrum of a pure argon discharge. With increasing temperature, the contribution of indium emission grows. The highest efficiency is reached at $488.15\,\text{K} \leq T_{CS} \leq 503.15\,\text{K}$ for different buffer gas pressures, which is a higher value than the optimum cold spot temperature of $313.15\,\text{K}$ for mercury. Above the optimum temperature, the efficiency drops again.

- The radiant flux of the lamp increases sub-linearly with increasing electrical power. It results from the saturation of emission lines and growing effect of self-absorption, which are also observable with mercury-argon discharges, regardless of the excitation frequency.

The highest plasma efficiency is achieved, when the plasma column fills the whole discharge volume without any power reflection. In due consideration of the chosen lamp geometry and the axial attenuation rate of the coupled MW-power, the optimum P_{acc} lies between 3 W and 6 W depending on the used filling and the cold spot temperature. A global maximum plasma efficiency of $\eta_{Pl} = 15.93\,\%$ was achieved at $p_{Ar} = 800\,Pa$ and $T_{CS} = 493.15\,K$ with an input power of $P_{acc} = 3\,W$.

Nevertheless, some important differences and limitations should be noted between a surface wave driven indium(I)idodie-argon plasma and a conventional mercury-argon glow discharge due to their *modi operandi*:

- The power coupling with surfatron is only one-sided, which results in an inhomogeneous field distribution. Both the axial E_z and the radial field component E_r vary along the lamp. Thus, the optimum field strength, at which the optimum electron temperature and consequently the maximum efficiency are achieved, can only be realized at one axial position along the lamp. The accepted power P_{acc} can be adjusted in order to achieve the lowest mean deviation of the field strength along the lamp from the optimum.

  In contrast to surface wave driven plasmas, the most important part of a conventional glow discharge driven with electrodes is the positive column, where the electric field strength remains constant independent of the distance from the electrodes. Most of the UV-radiation is generated by the positive column in low pressure fluorescent lamps. The geometry of the lamp and the applied voltage

is adjusted to achieve the optimum field strength in the positive column by considering the cathode and anode falls [67].

• The wall recombination of free indium and iodine atoms, which are generated by dissociating indium(I)iodide molecules, constitutes another source of losses in addition to the ambipolar diffusion losses of charge carriers. Such a source of losses does not exist for mercury-argon plasmas. Thus, the buffer gas pressure should be increased further to reduce the wall losses, although it leads to excessive gas heating due to increased elastic collision rate.

• Highly electronegative atoms, e.g., free iodine atoms, may also lead to the limitation of electron density by forming iodide ions (I^-) via electron capture. Particularly at low electron temperatures, at which the free iodine density, as well as the capture rate, is high, attachment of I and e may result in an excessive loss of invested ionization energy and in a decrease of plasma efficiency. However, the negative ion formation is neglected in the collisional-radiative model.

• The low pressure fluorescent lamps deliver their highest efficiency for diameters 25~50 mm [67]. Smaller diameters lead to higher ambipolar diffusion losses, while larger diameters result in a stronger self-absorption of the generated radiation. As mentioned above, low diffusion losses are of utmost importance for a high efficiency. Hence, a relatively high optimum buffer gas pressure of 800 Pa is required to achieve the maximum efficiency. However, for surface wave driven plasmas, the upper limit for lamp diameter is defined by electromagnetic properties of surface waves and not by plasma properties. As mentioned in section 6.3, the lamp diameter should not exceed 16.4 mm for an excitation frequency of 2.45 GHz, if m = 0-mode is desired.

The mentioned limitations, e.g., inhomogeneous field distribution, additional wall diffusion losses, formation of negative ions and a relatively small lamp diameter, prevent achieving a higher efficiency than 16 % in the investigated geometry and for the investigated operating parameters.

Chapter 8

Implementation
of the new lamp technology

The mercury-free low pressure plasma technology based on indium(I)iodide-argon system has been investigated with regard to plasma efficiency. However, the implementation of the investigated technology into a product requires solutions to application-specific problems, which are not considered during experimental investigations in the laboratory. The comparison between conventional lamp technologies and the investigated indium(I)iodide lamp is not straightforward. For general lighting applications, a phosphor coating is required to convert the line emission of indium into white light. Furthermore, the adjustment and stability of the cold-spot temperature is of utmost importance for the implementation. Thus, sections 8.1 and 8.2 are devoted to the assessment of heat and conversion losses, respectively. In section 8.3, the energy balance of a MW-driven, mercury-free lamp system is presented and future development steps are discussed.

8.1 Heat management

During the investigation of plasma parameters, T_{CS} is adjusted with the help of an external heat source, while being monitored with an IR-camera. However, the employment of an external heat source is not feasible for a commercial low pressure lamp. Thus, some measures should be taken to achieve the optimum T_{CS} intrinsically, as is the case with the low pressure sodium lamp, which requires a cold spot temperature of $T_{CS} = 533.15\,\text{K}$ for the optimal operation [148]. However, the level of heat losses is not known a priori, which prevents a sound assessment. Therefore, the heat losses due to thermal radiation and convection are determined on a theoretical basis.

8.1.1 Thermal radiation

Each material emits electromagnetic radiation for body temperatures $T_B > 0\,\text{K}$. The spectral radiance $L_{\Omega,\,\lambda,\,BB}\,[\text{W·m}^{-2}\text{·nm}^{-1}\text{·sr}^{-1}]$ of an ideal body, or a so-called black body, can be calculated with the help of Planck's law, as given by equation (2.26) in section 2.1.3. The emission properties of real bodies deviate from that of a black body, in which the deviation can be described mathematically by the spectral emissivity $\varepsilon(\lambda)$. By following Lambert's cosine law, and by integrating the product of spectral radiance and spectral emissivity over the wavelength, the radiant exitance $M_e\,[\text{W·m}^{-2}]$ of a real body can be calculated, which reads as the power radiated by a surface per unit area.

$$M_e = \pi \int_{\lambda} \varepsilon(\lambda) L_{\Omega,\,\lambda,\,BB}\,\text{d}\lambda. \tag{8.1}$$

Assuming that T_B is spatially constant, the total thermal radiation power $\Phi_{TR} = M_e A$ is determined by multiplying the radiant exitance with the surface area A of the body.

Spectral emissivity of a material depends usually on T_B. The spectral emissivity of fused silica glass $\varepsilon_{FSG}(\lambda)$ for low temperatures is taken from the publication of Petrov [149], where the spectral emissivity is given for $T_B = 295\,\text{K}$ and $673\,\text{K}$. Since the optimum cold spot temperature is $493.15\,\text{K}$, $\varepsilon_{FSG}(\lambda)$ at $T_B = 673\,\text{K}$ and for a wall thickness of 1 mm is chosen for further calculations as an approximation. Figure 8.1 displays the spectral radiance calculated for a black body at $T_B = 493.15\,\text{K}$, $\varepsilon_{FSG}(\lambda)$ and their convolution.
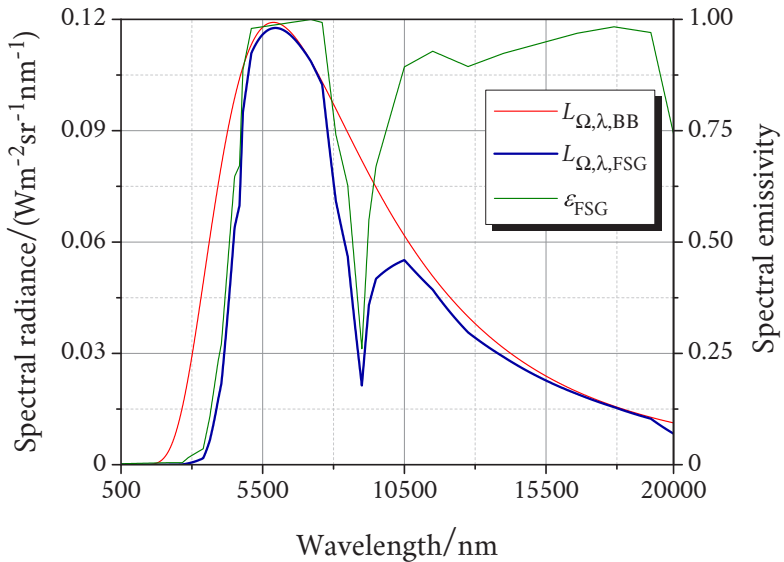
Figure 8.1: Spectral radiance of a black body (BB) and a real body made of fused silica glass (FSG) at a body temperature of 493.15 K as well as the spectral emissivity of fused silica glass at 673 K.

The total thermal radiation is demonstrated in figure 8.2 as a function of T_{CS}, assuming that $T_{CS} = T_B$ and the surface temperature of the lamp does not vary spatially. Since the surface area of the lamp is calculated as $A = 0.0032\,\mathrm{m}^2$, a thermal radiation power of 8.33 W should be considered for $T_{CS} = 493.15\,\mathrm{K}$.
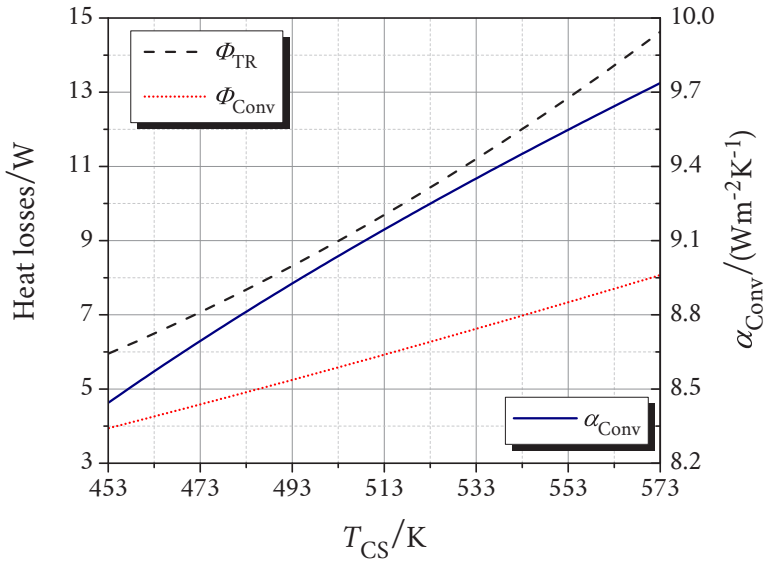
Figure 8.2: Thermal radiation power Φ_{TR} as well as heat transfer rate Φ_{Conv} and heat transfer coefficient α_{Conv} due to the natural convection calculated for an air temperature of $T_{SM} = 298.15\,\mathrm{K}$ as a function of cold spot temperature T_{CS}.

8.1.2 Convective heat transfer

The second thermal loss mechanism is the heat transfer through convection into the surrounding medium. Since a higher temperature compared to low pressure mercury lamps is needed for the optimal operation of indium(I)iodide-argon lamps, any external cooling mechanisms, such as pumps and fans, should be avoided. Thus, only the natural convection is considered to calculate the heat transfer rate Φ_{Conv} by

$$\Phi_{\text{Conv}} = 2\pi R L \alpha_{\text{Conv}} \left(T_{\text{SM}} - T_{\text{B}}\right), \tag{8.2}$$

where α_{Conv} is the heat transfer coefficient, T_{SM} is the temperature of the surrounding medium, and R and L are the radius and the length of the lamp, respectively. The determination of α_{Conv} is a complex problem, whose theoretical background is beyond the scope of this work. Lambrecht [150] proposed a calculation method for bodies in cylindrical geometry. Additionally, he listed the needed coefficients considering a body made of fused silica glass and air as the surrounding medium.

By adopting the proposed method, the heat transfer coefficient α_{Conv} and subsequently the heat transfer rate Φ_{Conv} are calculated for an air temperature of $T_{\text{SM}} = 298.15\,\text{K}$ and are plotted in figure 8.2 as a function of the cold spot temperature T_{CS} with the assumption that $T_{\text{CS}} = T_{\text{B}}$. With $R = 0.008\,$m and $L = 0.06\,$m, a heat loss of 5.25 W should be considered for $T_{\text{CS}} = 493.15\,\text{K}$ due to natural convection.

8.1.3 Design considerations

As demonstrated in sections 8.1.1 and 8.1.2, a total heat loss of 13.58 W should be considered for the lamp design. The high magnitude of losses necessitates measures against both thermal radiation and convection.

Without preventing the excessive heat losses, the thermal power has to be supplied continuously through surface waves into the lamp, which prevents to achieve a high efficiency with the indium(I)iodide-argon low pressure lamp at low power densities. Four practical measures can be implemented:

First, an extra glass bulb with an IR-reflecting coating can be placed around the lamp body. In this way, the thermal radiation is reflected, which reduces the thermal radiation losses significantly. For commercial sodium low pressure lamps, an indium oxide coating is the state of the art, which reflects about 90 % of thermal radiation, while transmitting > 91 % of the sodium resonance radiation [151]. Since the transmission of indium oxide layer drops below 80 % for the emission wavelengths of indium [148], it is not beneficial to employ the same coating for indium(I)iodide-argon low pressure lamp. Nevertheless, an adequate coating with the same reflection properties can reduce the heat losses due to the thermal radiation down to 0.83 W.

Secondly, the extra glass bulb placed around the lamp body can be hermetically sealed after the volume between the glass bulb and lamp body is evacuated. In the absence of gas particles or at least with a very low density of gas particles, the natural convection as well as conduction losses are widely suppressed. It is also very common to use gas getter, which ensures long term stability of the vacuum. With a pressure below 1 Pa, the convection and conduction losses can be suppressed nearly completely [148].

Thirdly, the microwave amplifiers (MWA) feature relatively low efficiencies with regard to control gears at lower frequencies, which leads to a stronger heating. This heat power can also be employed to increase the temperature of the lamp body. The microwave coupler itself, which is made of brass, can be utilized to transfer the heat from the MWA to the lamp system.

And finally, there is also non-guided microwave radiation into the surroundings, as demonstrated in section 6.2. For a microwave power of $P_{mw} = 3\,\text{W}$, a radiation power of $P_{rad} = 0.37\,\text{W}$ is estimated. This radiation can be employed to generate heat by wrapping a metal mesh around the lamp as Faraday shield. However, the metal mesh may feature a low direct transmission and lead to a lower radiant flux. Instead of a metal mesh, a conductive coating can be applied on the lamp body, which is also transparent in VIS-range. Indium tin oxide (ITO) coatings may come to mind. However, the inadequacy of indium oxide based coatings due to the low transmission in the 400 nm range was already mentioned.

In conclusion, the heat losses at cold spot temperatures > 493.15 K are high enough to prevent a high system efficiency. However, appropriate measures, e.g., IR-reflective coating, heat insulation and Faraday shielding, can help to suppress them extensively. In this way, the relative high temperatures needed for an optimal operation can be reached without efficiency loss. A short warm-up time and a robust operation nearly independent of the environmental temperature are further advantages of good thermal isolation.

A Faraday shield may be also needed due to safety regulations. According to the IEEE [152], the maximum permissible exposure value of general public to the electromagnetic fields at the frequency of 2.45 GHz corresponds an incident power density of $10\,\text{W}\cdot\text{m}^{-2}$. As mentioned in section 2.3, the excitation of surface waves and bulk waves are associated, which takes place in the gap of the surfatron. A radiation power of 0.37 W corresponds a power density of $8.2\,\text{W}\cdot\text{m}^{-2}$ at the end of the lamp with a length of 0.06 m. Although the given limit is not exceeded, a Faraday shield may help to reduce the EMI further.

The acceleration of ions inside the electric field may lead to a severe ion bombardment of the inner surface of the lamp, which results with the depletion of radiant component, sputtering of the fluorescent coating and

even the sputtering of the glass envelope [15]. The threshold for sputtering corresponds an ion energy of 20~30 eV [15]. In a surface wave driven, low pressure plasma at a frequency of 2.45 GHz, it can be assumed that the ion density is low and ions do not response to the alternating electric field [33]. The ions are accelerated to the glass walls only due to the ambipolar diffusion, which is not strong enough to generate fast ions with energies > 20 eV. Therefore, the sputtering of the glass walls by ions can be neglected. This assumption can be supported with the fact that low pressure electrodeless lamps driven with 915 MHz achieved lifetimes over 20 years [15]. Nevertheless, a protective coating based on fumed alumina (Al_2O_3) can be applied on the inner surface of the lamp to reduce the diffusion of the radiant component into the glass and to increase the lifetime of the lamp [153, 154].

8.2 Fluorescent coating

The fluorescent coating, also known as the phosphor coating, of an ordinary mercury-argon compact fluorescent lamp features a down-conversion efficiency of about η_{DC} = 45 %, corresponding to a lumen equivalent of 145 lm·W^{-1} for white light [155], with a near unity quantum efficiency and an absorption efficiency higher than 90 % [156]. The down-conversion of the UV emission lines in the phosphor coating constitutes the primary energy loss mechanism of the whole lamp system. The conversion efficiency can be substantially improved by employing indium as the radiant component together with an appropriate phosphor coating.

A virtual trichromatic phosphor coating is modeled to compare the conversion losses with mercury and indium. The emission function $\phi_{\lambda,\text{pc}}$ of the virtual phosphor consists of three Dirac delta functions at

λ = 455 nm, 555 nm, and 600 nm with differing heights. Figure 8.3 shows the fluorescence spectrum of the virtual phosphor together with the color matching functions $\overline{x}(\lambda)$, $\overline{y}(\lambda)$ and $\overline{z}(\lambda)$ according to CIE 1931 standard colorimetric observer [157].
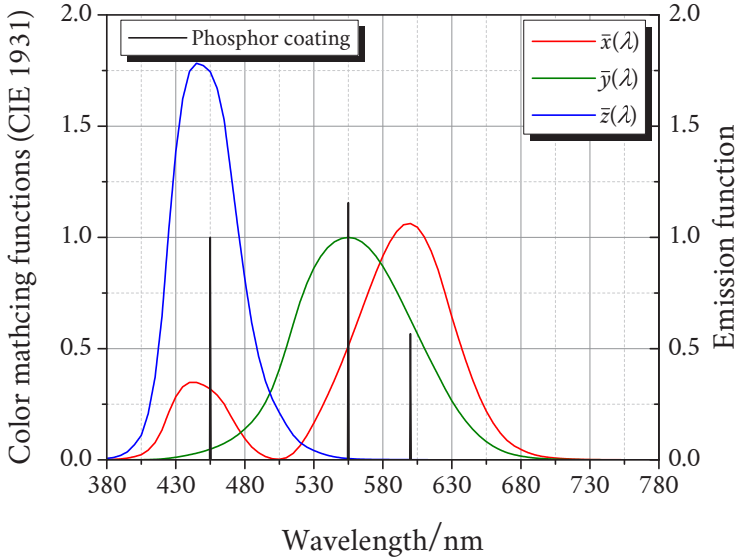
Figure 8.3: Color matching functions according to CIE 1931 and emission function of the virtual trichromatic phosphor coating with three Dirac delta functions at λ = 455 nm, 555 nm, and 600 nm. The heights of individual Dirac delta functions are adjusted to simulate the daylight illuminant [157].

With the help of the color matching functions, the tristimulus values X_{ts}, Y_{ts} and Z_{ts} of color stimuli can be calculated, as given in equation (8.3) [157].

$$X_{ts} = \int_\lambda \phi_{\lambda,pc}(\lambda)\overline{x}(\lambda)\,d\lambda,$$

$$Y_{ts} = \int_\lambda \phi_{\lambda,pc}(\lambda)\overline{y}(\lambda)\,d\lambda, \qquad (8.3)$$

$$Z_{ts} = \int_\lambda \phi_{\lambda,pc}(\lambda)\overline{z}(\lambda)\,d\lambda.$$

With known tristimulus values, the chromaticity coordinates x_{cc}, y_{cc}, z_{cc} of the generated radiation in color space can be determined by

$$x_{cc} = \frac{X_{ts}}{X_{ts} + Y_{ts} + Z_{ts}},$$

$$y_{cc} = \frac{Y_{ts}}{X_{ts} + Y_{ts} + Z_{ts}}, \qquad (8.4)$$

$$z_{cc} = 1 - x_{cc} - y_{cc}.$$

The heights of individual Delta dirac functions are chosen in such a way that the fluorescent radiation features chromaticity coordinates of $x_{cc} = 0.3135$ and $y_{cc} = 0.3236$ in the CIE 1931 color space using the standard observer [157], as shown in figure 8.4. Thus, the position of the phosphor emission in the color space can be approximated with CIE standard illuminant D65, which corresponds to a black body radiator with a correlated temperature of 6503.6 K, also referred to as the daylight illuminant [157].

It is also assumed that the absorption of the fluorescent powder, as well as the quantum efficiency, is ideal between the wavelengths 180 nm and 455 nm, which means that every incident photon with a wavelength below 455 nm is absorbed by the coating and for every absorbed photon, a new photon is created in the coating at one of the three emission wavelengths. The probability of individual wavelengths is given by the height of the Dirac delta functions.
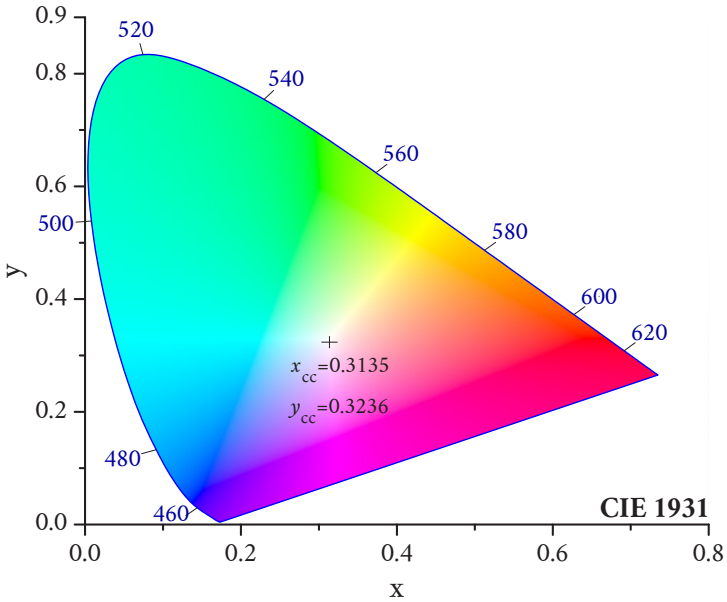
Figure 8.4: CIE 1931 color space using the standard observer and chromaticity coordinates of the emission of the virtual trichromatic phosphor, which can be approximated with CIE standard illuminant D65.

Hence, the Stokes' losses are calculated and plotted in figure 8.5 as a function of wavelength. The down-conversion of the mercury emission lines at 184.95 nm and 253.65 nm results in the loss of 64.5 % and 51.3 % of the radiation energy, while the Stokes' losses are reduced down to 21.3 % and 13.5 % for the indium emission lines at 410.17 nm and 451.13 nm, respectively. Under optimum operating conditions, the radiation at 184.95 nm amounts to 9 % of the input power and that at 253.65 nm to 55 % [158]. Thus, a mean Stokes' loss of 53.2 % can be estimated with the help of the virtual coating, which is in very good agreement with the conversion efficiency of real phosphor coatings [159]. Analogously, a mean conversion loss of 17.4 % can be anticipated for both lines of indium,

since they exhibit nearly the same strength. By considering all emission lines of indium between 250 nm and 451 nm and assuming a maximum achievable lumen equivalent of $330 \, \text{lm·W}^{-1}$ for white light [155], a down-conversion efficiency of 75.8 % can be achieved, which corresponds to an efficacy of $250 \, \text{lm·W}^{-1}$.
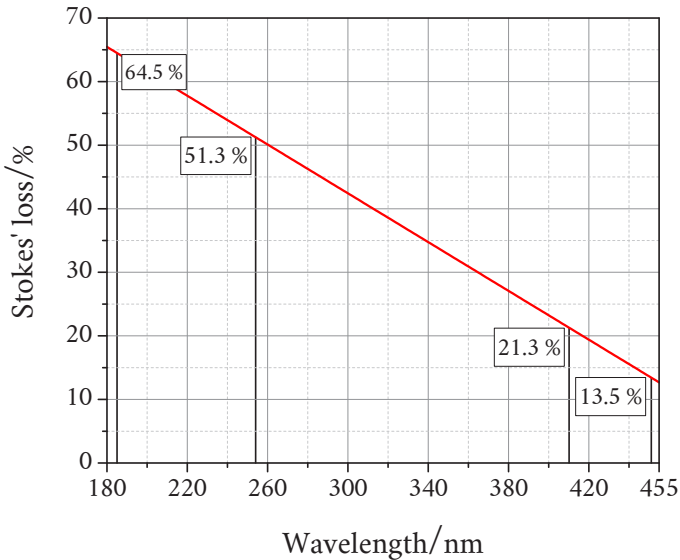
Figure 8.5: Stokes' losses in the virtual trichromatic phosphor coating for the emission lines of mercury at 184.95 nm and 253.65 nm as well as the emission lines of indium at 410.17 nm and 451.13 nm.

Therefore, a comparable luminous efficacy may be achieved with the indium(I)iodide-argon filling as with mercury-argon filling by employing an appropriate phosphor coating such as the state-of-the-art blue LED phosphor, even if the plasma efficiency using indium(I)iodide is nearly half as high as when using mercury.

8.3 Energy balance and efficiency

8.3.1 Energy balance

Electronic control gears (ECG) of commercial compact fluorescent lamps (CFL) exhibit an average efficiency of about $\eta_{\mathrm{ECG}} = 90\,\%$ [160], while the highest efficiency in GHz-range is achieved with solid-state power amplifiers based on Gallium-Nitride (GaN) technology and is about $\eta_{\mathrm{ECG}} = 84\,\%$ [161]. Although, the efficiency of microwave amplifiers is still low compared to that of conventional ECGs, an upward trend exists, since the same semiconductor-technology is essential for radar and telecommunication applications as well and thus studied intensively.

The generated microwave power is coupled into the lamp via the MW-coupler surfatron with a coupling efficiency of $\eta_{\mathrm{CF}} = 81\,\%$. The reflected power P_{ref} can be reduced by more than $-30\,\mathrm{dB}$ by means of frequency matching, as shown in figure 6.6, since GaN-technology is suitable for broadband operation. Therefore, the coupling efficiency should be considered as the ratio of the absorbed power P_{A} by the plasma and the accepted power P_{acc} by the surfatron and not the generated microwave power P_{mw} by the ECG. Bearing the ohmic losses and the radiated microwave power into the surrounding in mind, which can be re-used to balance the heat losses, an effective coupling factor of $\eta_{\mathrm{CFeff}} = P_{\mathrm{A}}/P_{\mathrm{acc}} = 94\,\%$ can be achieved. Analogously, the conventional lamps suffer electrode losses due to the voltage drops at cathode and anode. The percentage of electrode losses to total input power depends on the lamp length [67]. An average electrode loss of 27.5 % can be estimated for CFLs [148].

The absorbed electrical power from the plasma is converted into utilizable radiation, i.e., UV- and VIS-radiation, with an efficiency of

$\eta_{Pl} = 60\%$ and 16% for mercury-argon and indium(I)iodide-argon system, respectively [148]. Furthermore, a down-conversion efficiency of $\eta_{DC} = 45\%$ and 76% should be considered for the line emission of mercury and indium, respectively.

Table 8.1 summarizes the energy balances of both a conventional CFL and a MW-driven mercury-free low pressure lamp for comparison.

Table 8.1: Energy balance comparison of conventional CFL and MW-driven indium(I)iodide-argon low pressure lamp.

η	Description	CFL	MW-driven In(I)I
η_{ECG} / %	Efficiency of the electronic control gear or the microwave amplifier	90	84
η_{CFeff} / %	Coupling efficiency with electrodes	72.5	-
	Effective coupling efficiency of the surfatron	-	94
η_{Pl} / %	Plasma efficiency	60	16
η_{DC} / %	Down conversion efficiency of the phosphor coating	45	76
η_{total} / %	Total lamp efficiency	17.6	9.6
Lumen equivalent for white light $= 330 \, \text{lm·W}^{-1}$			
η_{lum} / lm·W^{-1}	Luminous efficacy of the lamp system	58	32

Summarizing, an overall luminous efficacy of 32 lm·W^{-1} can be reached with the mercury-free technology. It is simply obvious that the low plasma efficiency is the limiting factor for the implementation of the MW-driven low pressure lamps as a product. In the following section, possible development steps to increase the plasma efficiency are listed.

8.3.2 Possible future developments

For the lamp geometry investigated in this work, the optimum input power is determined as $P_{\mathrm{acc}} = 3$ W. Considering the luminous efficacy of the lamp, the wattage of the lamp should be scaled up to achieve a higher lumen package. For this purpose, two approaches can be adopted:

In the first approach, the geometry of the lamp remains unaltered. It is already demonstrated in section 7.2.4 that higher powers than the optimum accepted power result in plasma overload, thus the plasma efficiency decreases. Yet, a compromise can be made between the rates of increased power and decreased efficiency. In figure 7.18, the variation of the plasma efficiency is displayed as a function of accepted power. The lamp filled with 100 Pa argon, and driven at $T_{\mathrm{CS}} = 513.15$ K and $P_{\mathrm{acc}} = 21$ W exhibits a plasma efficiency of 8 %, which is only half as high as the maximum achievable efficiency. Nevertheless, the accepted power is increased sevenfold, resulting in a net rise of 250 % of the lamps radiant flux.

In the second approach, the plasma efficiency should remain constant, while the lamp geometry is modified. In section 7.2.4, it is ascertained that the highest plasma efficiency is achieved, when the plasma column fills the discharge vessel completely without forming standing wave patterns due to the reflected power at the end of the discharge vessel. Thus,

the input power, the attenuation rate of wave power and the length of the lamp must be in agreement. The attenuation rate can be increased by increasing the cross section of the lamp body. Hence, a higher input power is required to fill the lamp with plasma, as long as the operating and lamp parameters, e.g., cold spot temperature and buffer gas pressure remain constant. However, a larger radius prevents the launching of m = 0-waves from the surfatron, as explained in section 6.3. Furthermore, the self-absorption of generated emission grows with increasing radius. The optimum attenuation rate is already identified for the given cross section by varying the cold spot temperature and buffer gas pressure. Therefore, the only feasible method to increase the input power without efficiency loss is to make the lamp body longer without changing the remaining parameters. Surely, a longer lamp body has a larger surface area, which increases the heat losses due to convection and thermal radiation. However, the heat losses are considered to be widely compensated with the help of appropriate measures and neglected for the power balance. A similar method is also adopted for high wattage sodium low pressure lamps.

Moreover, the wave coupler has to be able to deliver the increased microwave power into the lamp. Surfatron exhibits no upper limit for power handling capacity except the limitation due to the increasing temperature with increasing ohmic losses P_Ω [62], which can lead to the deformation of the surfatron (melting point of brass $\approx$ 650 K). Since the ohmic losses account for about 1.6 % of P_{mw}, as demonstrated in section 6.2, the heating of the surfatron causes no practical problems, when dealing with low pressure plasmas.

Furthermore, the following approaches can be used to increase the luminous efficacy of the lamp:

- The mixing ratio of the individual isotopes of indium in the indium(I)iodide filling can be optimized to reduce the self-

absorption. This method is already investigated for mercury with good results, as presented in section 3.1.5.

- The long wave UV-region and the VIS can be populated with the help of additive materials, e.g., thallium. A detailed assessment of thallium mono-halides as additives can be found in section 3.1. Figure 8.6 shows the spectral irradiance measured with a lamp filled with both indium(I)iodide and thallium(I)iodide as well as argon as buffer gas with a pressure of $p_{Ar} = 200$ Pa, while driven at $P_{acc} = 3$ W and $T_{CS} = 513.15$ K.
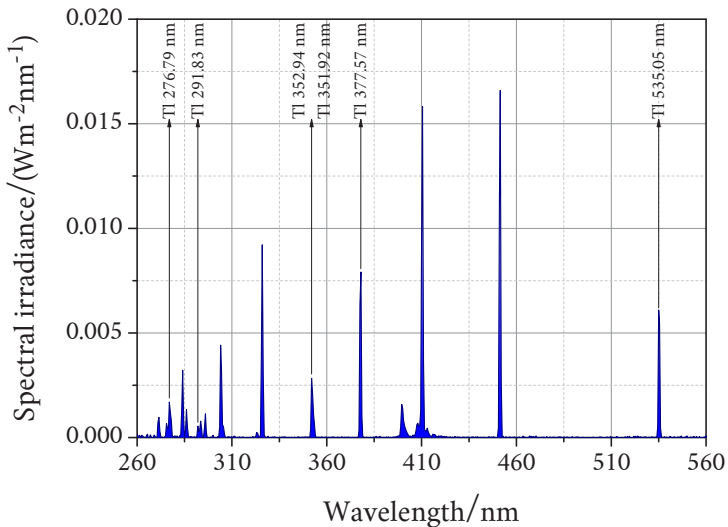
Figure 8.6: Spectral irradiance measured with a lamp filled with indium(I)iodide and thallium(I)iodide as well as argon with $p_{Ar} = 200$ Pa, while driven with $P_{acc} = 3$ W at $T_{CS} = 513.15$ K.

The emission lines of neutral thallium atom are labeled accordingly, whereas the emission lines of neutral indium were already

given in figure 7.7. This cold spot temperature is chosen, since the vapor pressure and consequently the emission of thallium is negligible below 513.15 K. In contrast to indium(I)iodide, thallium(I)-iodide is one of the molecular species, which exhibit pure line emission in low pressure gas discharge [9].

Although the lamp and operating parameters were not optimized for this filling system, a plasma efficiency of $\eta_{Pl} = 13.61\,\%$ could be achieved, which is not as high as that achieved with pure indium(I)-iodide-argon system. Even though, the additional emission lines may help to achieve a higher luminous efficacy. The emission line at 535.05 nm is located very closely to the maximum of the spectral sensitivity of the human eye at 555 nm. Furthermore, the strong emission line at 377.57 nm is situated at the boundary between UV and VIS, which reduces the Stokes' losses in the phosphor coating significantly. The ratio of the emission line strength at 535.05 nm to that at 377.57 nm can be adjusted nearly linearly with the cold spot temperature [9]. In this way, the color temperature of the lamp can be optimized as well.

- One of the advantages of electrodeless power coupling is that the plasma ignition occurs without any delay due to the warming-up of the electrodes. Furthermore, the re-strike (re-ignition) of the lamp even at the optimum cold-spot temperature of 493.15 K succeeds without any problems. Hence, the low pressure lamp can be driven in pulsed mode, which offer some advantages: First, depending on the duty-cycle, which gives the percentage of pulse width to period, the peak power coupled into the lamp can be increased, while the mean accepted power remains constant. Thus, a higher radiant flux can be achieved by the same radiant energy. The first investigations showed that for a duty cycle of 50 % and with a double so high peak power than the mean power, ir-

radiance values about 2.3-times higher than those measured in continuous operation could be achieved [162]. However, high peak powers result in the thermalization of the electrons, as well as in the saturation of excited levels in pulsed operation. As a result, the high irradiance, achieved during the plasma formation in the first instants of the pulse, declines after the final stationary electron density is reached [163, 164]. Thus, a radiant exposure equal to only 91 % of what was measured in continuous operation could be achieved [162]. Yet, the pulse width and the time between two pulses can be adjusted in such a way that the power overload and thermalization of the plasma are widely eliminated. In this way, the product of irradiance and duty cycle can be increased without any loss in radiant exposure, resulting in a higher plasma efficiency.

- As mentioned in section 7.3, the inhomogeneous field distribution along the lamp results in a deviation from the optimum field strength. The excitation frequency of 2.45 GHz corresponds to a wavelength of about 122.36 mm in vacuum. With the assumption of spatially constant electron density of $1 \cdot 10^{18}\,\mathrm{m}^{-3}$ and with weak collisional plasma approximation, the relative permittivity of the plasma can be calculated as $|\varepsilon_\mathrm{p}| = 12.43$, which results in a wavelength of about 34.71 mm inside the plasma. Therefore, standing wave inside the lamp with the length of 60 mm extends to nearly two periods. With an adequate amplifier, the excitation frequency can be reduced down to 1 GHz, which is the lower limit of the microwave range. Thus, the wavelength increases and consequently the field distribution along the lamp becomes more homogenous, which allows a more precise adjustment of the field strength. In this way, the mean deviation of the field strength from the optimum may be reduced along the lamp, which leads to a higher efficiency.

Chapter 9

Summary

The technological transition from inefficient incandescent and halogen lamps to high efficient light sources is now the global trend driving the general lighting market. Traditional energy efficient light sources based on gas discharges have still the lion's share of the market, although LEDs penetrate the market faster than expected due to its rapidly decreasing price. Another important reason for rapid abandoning of low pressure plasma light sources, e.g., CFLs and LFLs, is the environmental and health problems associated with their radiant component, i.e., mercury. A non-hazardous and environmentally friendly substitute of mercury as the radiant component of low pressure lamps may once again promote the use of CFLs, at least for higher wattage applications, where LEDs suffer from heat management issues. Furthermore, the relatively short lifetime of some CFLs compared to LEDs is an issue to be solved to make the CFL competitive.

This work presents the research activities to develop an electrodeless, mercury-free, molecular low pressure lamp driven with surface waves. Two important technological transitions were carried out at once: First, a molecular filling, i.e., indium(I)iodide, was employed as the feedstock of neutral indium, i.e., radiant component of the lamp. Spectral analysis of the lamps exhibited also weak molecular radiation of neutral indium(I)iodide itself. Secondly, the electrodes, which are the main fail-

ure mechanism of the gas discharge lamps, were removed from the lamp. The power coupling into the lamp was realized by means of guided microwaves, namely, surface waves.

The substitute of mercury was theoretically selected by applying a set of criteria, which evaluate suitability of materials based on their chemical and radiometric properties. Indium was selected as the radiant component due to its strong emission lines at 410.17 nm and 451.13 nm, its low ionization energy of 5.79 eV and its electronic structure with a metastable state, situated only 0.27 eV higher than the ground state and thus constitutes nearly a second ground state. Compared to mercury, which exhibits an ionization energy of 10.44 eV and two strong resonance lines at 184.95 nm and 253.65 nm, indium proves to be a good candidate.

However, indium exhibits a relatively low vapor pressure compared to mercury. A cold spot temperature of 314.92 K is needed to achieve a vapor pressure of 0.93 Pa with mercury, which is the optimum mercury vapor pressure inside a fluorescent lamp with a diameter of 30~40 mm, while indium requires a cold spot temperature of 1179 K to achieve the same vapor pressure. Therefore, the use of metallic indium is not feasible in a low pressure lamp. This limitation is removed by employing indium mono-iodide (indium(I)iodide) as the feedstock of indium inside the lamp. Although other indium halides feature higher vapor pressures at the same temperature, indium(I)iodide exhibits the lowest dissociation energy of 3.43 eV among others. Furthermore, fluorine and chlorine are volatile and aggressive, which reduce the lifetime of the lamp significantly. As the buffer component, argon was chosen in due consideration of its moderate breakdown voltage, moderate mass and low price compared to other noble gases.

A surface wave launcher, i.e., surfatron was chosen to couple the microwave power into the lamp. Surfatrons are easy to manufacture,

can operate in a broad range of lamp parameters, e.g., length of the discharge vessel and buffer gas pressure, as well as operating parameters, e.g., microwave input power and excitation frequency. Furthermore, surfatrons allow mechanical impedance and frequency matching without any additional matching network. The design of the surfatron was improved with the help of the electromagnetic simulation software "CST MWS" (Computer Simulation Technology AG) to achieve relatively high electric field strengths inside of its coupling gap, which allows the ignition of the plasma without external support. Additionally, the new design prevents any parasitic capacitance effects inside the surfatron. The power balance of the surfatron was compiled by simulating the individual sources of power consumption.

The main focus of this work lies in the characterization of the molecular low pressure plasma by means of radiometric measurements assisted by a collisional-radiative model to identify and understand the relations between operating configurations, plasma parameters and plasma efficiency.

Spatially resolved optical emission spectroscopy (SROES) is based on the measurement of the spectral radiance of the lamp. Due to the spectral limitations of the optical measurement setup, only the two emission lines of indium in VIS could be recorded with SROES. Thus, spectral irradiance measurements were performed as a complementary measure to investigate the emission spectra of the lamps from 200 nm up to 800 nm.

The adopted diagnostic method is applicable, only if the plasma is optically thin for the investigated wavelengths. Thus, the emission lines of indium at 410.17 nm and 451.13 nm were evaluated with regard to self-absorption, which was estimated by means of the escape factor concept. The escape factor gives the probability that a photon propagates to the wall of the lamp in a single flight without absorption. However, the energy of an absorbed photon can be re-emitted or can be dissipated in

non-radiative processes in the plasma, thus removing the photon completely. Therefore, the effective escape factor was calculated for the relevant emission lines of indium, which gives the probability that a photon leaves the lamp independently of the number of re-absorptions and re-emissions. The emission line at 451.13 nm was chosen for further investigations due to its relatively lower self-absorption compared to the emission line at 410.17 nm.

The radiance data at 451.13 nm were converted into line emission coefficients by means of Abel's inversion. The applicability of Abel's inversion on the emission profile of a surface wave driven low pressure plasma was verified optically and electromagnetically. Furthermore, the m = 0-mode of the applied surface waves was verified.

Two mathematical methods based on curve fitting and cosine-expansion to solve the inverse Abel's integral equation were compared. The curve fitting method, by which the measured data is fitted with an 8th order polynomial function and then integrated analytically, was chosen for further calculations due to its simplicity and speed. By integrating the line emission coefficients over the whole volume of the lamp and 4π-solid angle, the radiant flux generated by the plasma at the wavelength of 451.13 nm could be calculated.

By measuring the irradiance of the same lamp at the same operating configurations and at the same wavelength, a conversion factor between radiant flux and irradiance could be calculated. Then, this conversion factor was used to transform the irradiances of all relevant emission lines of indium into the total radiant flux of the lamp. In this way, the plasma efficiency could be determined by means of simple and fast spectral irradiance measurements without any complex measurement setups such as Ulbricht-sphere or goniometer. A maximum plasma efficiency of about 16 % could be achieved.

Nevertheless, the measured radiance data or derived line emission coefficients do not deliver the desired plasma parameters, e.g, electron density, electron temperature and ion density. Thus, the experimentally obtained data must be interpreted, which requires information about the state of the plasma. Since low pressure plasmas do not exhibit thermal equilibrium not even on a local level, relevant plasma processes should be considered individually. Rate equations were formed by balancing the generation processes and their counterpart inverse processes. Furthermore, free and ambipolar diffusions were included into the rate equations to consider the wall losses of neutral and charged particles. However, rate coefficients of individual processes can only be calculated with known cross sections. They are not available in the literature for molecular processes, e.g., dissociation of neutral indium(I)iodide molecule and direct-dissociative recombination of indium(I)iodide ion, or for atomic secondary processes such as de-excitation and three-body recombination. In addition to that, the available cross sections for the excitation of neutral indium into higher energy states proved to be incorrect. Therefore, cross sections of all relevant processes that are caused by electron impact, were calculated by means of the simplified Gryziński method, extended Gryziński method for molecules, Klein-Rosseland formula, method of detailed balancing and Bardsley method. Additionally, the free and ambipolar diffusion coefficients were determined. The plasma parameters, as well as line emission coefficients, were calculated by solving the rate equations for varying cold spot temperatures and buffer gas pressures as a function of electron temperature.

The line emission coefficients obtained experimentally were compared with the simulated ones, which were calculated as a function of electron temperature. In this way, the electron temperatures could be determined. Then, the remaining plasma parameters were assigned to the electron temperature. In this way, radial and axial profiles of plasma parameters could be obtained at varying lamp and operating configurations.

The relations between plasma parameters, e.g, electron temperature and density, and lamp and operating configurations, e.g., accepted microwave power by the coupler, cold spot temperature of the lamp and buffer gas pressure, as well as the relations between plasma parameters and plasma efficiency, were identified. The behavior of the plasma parameters for varying operating configurations could be predicted by the collisional-radiative model in very good qualitative and quantitative agreement with the measurement results.

Strong analogies between indium(I)iodide-argon plasma and mercury-argon plasma could be found. Both plasmas feature an optimum cold spot temperature with regard to plasma efficiency. Below the optimum, the plasma exhibits the emission spectrum of an argon plasma with very small contribution of the radiant component, while above the optimum, the efficiency of the plasma sinks, although the spectrum is dominated by the emission lines of radiant component. A similar behavior could be also observed for the buffer gas pressure. Below the optimum, the strong ambipolar diffusion results in lower electron densities, while above the optimum, the elastic collisions between electrons and buffer gas atoms lead to an excessive gas heating. Additionally, saturation of atomic emission lines could be observed with increasing input power.

Furthermore, the differences and limitations of the employed filling and the adopted power coupling method were evaluated. One sided power coupling of the surfatron leads to an inhomogeneous field distribution along the lamp, which results in a lower maximum achievable plasma efficiency compared to a glow discharge, where the field strength remains constant along the positive column. The wall recombination of indium and iodine atoms constitutes a source of loss for the invested dissociation energy. In addition to that, the attachment of highly electronegative iodine atoms and free electrons leads to the loss of the invested ionization energy and may limit the maximum achievable electron density.

Finally, a feasibility study on the implementation of surface wave driven indium(I)iodide-argon low pressure plasma as a CFL was performed. Heat losses due to thermal radiation and natural convection were modeled and adequate measures to solve the heat management issues were introduced. Furthermore, a suitable fluorescent coating to convert the emission lines of indium into the white light was modeled and Stokes' losses were calculated. An energy balance of this novel CFL was compiled and compared with conventional mercury-argon CFL. A luminous efficacy of $32\,\mathrm{lm\cdot W^{-1}}$ could be anticipated. The shortcomings of this technology were identified and further development steps were recommended as outlook.

Chapter A

Appendix

A.1 Einstein coefficients

Einstein coefficients A_{kj} [s^{-1}] for the relevant emission lines of indium found in the literature are summarized below. The marking "T." indicates that the given values are theoretically determined, while the entries without any marking present measurement values. The Einstein coefficient for a given transition from a higher energy state k into a lower energy state j can be calculated by equation (2.20) using the absorption oscillator strength f_{jk}. The statistical weights g_k and g_j are calculated by $g = 2j_{taq} + 1$ considering the total angular quantum number j_{taq} of the corresponding energy state.

451.13 nm: $6^2S_{1/2} \rightarrow 5^2P_{3/2}$

A_{kj} / $10^7 \cdot s^{-1}$	Ref.	A_{kj} / $10^7 \cdot s^{-1}$	Ref.
8,9	[24]	10,0	[165]
10,3	[166]	13,9	[167]
7,28	[168]	8,91	[169]
10,0	T. [170]	9,05	T. [171]

410.17 nm: $6^2S_{1/2} \rightarrow 5^2P_{1/2}$

$A_{kj} / 10^7 \cdot s^{-1}$	Ref.	$A_{kj} / 10^7 \cdot s^{-1}$	Ref.
5,0	[24]	5,59	[165]
6,82	[172]	13,9	[167]
5,71	[166]	4,95	[169]
4,76	[168]	5,15	T. [171]
6,07	T. [170]		

325.86 nm: $5^2D_{3/2} \rightarrow 5^2P_{3/2}$

$A_{kj} / 10^7 \cdot s^{-1}$	Ref.	$A_{kj} / 10^7 \cdot s^{-1}$	Ref.
3,0	[24]	14,5	[167]
3,77	[166]	13,2	[173]
1,63	[168]	3,52	T. [170]
2,49	T. [171]		

325.61 nm: $5^2D_{5/2} \rightarrow 5^2P_{3/2}$

$A_{kj} / 10^7 \cdot s^{-1}$	Ref.	$A_{kj} / 10^7 \cdot s^{-1}$	Ref.
13,0	[24]	13,0	[174]
15,5	[166]	12,8	[167]
10,1	[168]	12,8	[173]
13,2	[175]	12,99	[169]
20,6	T. [170]	14,7	T. [171]

303.93 nm: $5^2D_{3/2} \rightarrow 5^2P_{1/2}$

A_{kj} / $10^7 \cdot s^{-1}$	Ref.	A_{kj} / $10^7 \cdot s^{-1}$	Ref.
11,1	[24]	14,3	[176]
12,2	[172]	15,9	[175]
13,0	[166]	14,5	[174]
10,1	[168]	13,9	[167]
11,2	[169]	18,4	T. [170]
13,0	T. [171]		

293.26 nm: $7^2S_{1/2} \rightarrow 5^2P_{3/2}$

A_{kj} / $10^7 \cdot s^{-1}$	Ref.	A_{kj} / $10^7 \cdot s^{-1}$	Ref.
2,3	[24]	2,5	T. [170]
2,64	[166]	2,31	T. [171]

275.39 nm: $7^2S_{1/2} \rightarrow 5^2P_{1/2}$

A_{kj} / $10^7 \cdot s^{-1}$	Ref.	A_{kj} / $10^7 \cdot s^{-1}$	Ref.
1,3	[24]	1,39	T. [170]
1,50	[166]	1,37	T. [171]

271.03 nm: $6^2D_{3/2} \rightarrow 5^2P_{3/2}$

A_{kj} / $10^7 \cdot s^{-1}$	Ref.	A_{kj} / $10^7 \cdot s^{-1}$	Ref.
2,7	[24]	5,4	[177]
3,15	[166]	4,35	[173]
4,24	[174]	6,06	T. [170]
4,05	T. [171]		

256.03 nm: $6^2D_{3/2} \rightarrow 5^2P_{1/2}$

A_{kj} / $10^7 \cdot s^{-1}$	Ref.	A_{kj} / $10^7 \cdot s^{-1}$	Ref.
2,0	[24]	4,7	[175]
2,29	[166]	4,1	[174]
3,9	[176]	3,85	[173]
5,6	T. [170]	3,63	T. [171]

List of figures

List of tables

List of symbols

$\alpha(\lambda)$	Spectral absorption coefficient
α_λ	Line absorption coefficient
α_{Conv}	Heat transfer coefficient for natural convection
α_{e}	Correction factor for the interaction between rotor and oscillator
β_0	Molecule specific quantity for Morse potential
β_{Dtr}	Contribution of the Doppler broadening to β_{tr}
β_{e}	Correction factor for the interaction between rotor and oscillator
β_{Rtr}	Contribution of the resonance broadening to β_{tr}
β_{tr}	Ratio of the fundamental mode trapped decay rate to the vacuum decay rate
δ_c	Characteristic penetration depth
$\varnothing$	Diameter
$\epsilon(\lambda)$	Spectral emission coefficients
ϵ_{deg}	Degradation rate
ϵ_{rem}	Removal factor
ϵ_λ	Line emission coefficient
η_{CFeff}	Effective coupling factor of the surfatron
η_{CF}	Coupling factor of the surfatron
η_{DC}	Down-conversion efficiency of a phosphor coating
η_{ECG}	Efficiency of the electronic control gear
η_{lum}	Luminous efficacy of a lamp system
η_{Pl}	Plasma efficiency
η_{total}	Total efficiency of a lamp system

Γ_{a}	Ambipolar flux of charge carriers
Γ_{c}	Capture width
Γ_{e}	Net electron flux
Γ_{H}	Net flux of heavy particles
Γ_{i}	Net ion flux
Λ	Total orbital angular momentum along the internuclear axis of a molecule
λ	Wavelength
λ_{De}	Debye length for electrons
λ_{Di}	Debye length for ions
λ_{D}	Debye length
λ_{mfpe}	Mean free path length of electrons
λ_{mfpi}	Mean free path length of ions
λ_{mfpp}	Mean free path of a photon between re-emission and re-absorption
λ_{mfp}	Mean free path
$\mathcal{A}$	Auxiliary function to solve the dispersion relation of surface waves
$\mathcal{B}$	Rate coefficient for three-body recombination
C	Rate coefficient for electron impact de-excitation
$\mathcal{E}$	Kinetic energy of the orbital electron
$\mathcal{R}$	Rate coefficient for direct-dissociative recombination
μ_0	Vacuum permeability
μ_{e}	Electron mobility
μ_{i}	Ion mobility
ν	Frequency
ν_0	Center frequency of an emission line
Ω	Solid angle
ω	Angular excitation frequency
ω_{e}	Harmonic wavenumber
Ω_{mol}	Total projection quantum number of a molecule

ω_{pe}	Angular electron plasma frequency
ω_{vib}	Vibrational angular frequency of the oscillator
Ω_D	Collision integral for diffusion
$\overline{\nu}_{12}$	Average collision frequency for momentum transfer between particles of types 1 and 2
$\overline{\nu}_1$	Total collision frequency for momentum transfer for particles of type 1
$\overline{\nu}_e$	Total electron collision frequency for momentum transfer
$\overline{C}_1$	Mean speed of incident particles of type 1 relative to the local mean mass velocity of the gas
$\overline{E}_{kin}$	Mean kinetic energy
$\overline{n}_e$	Cross section average electron density
$\overline{Q}_{12}$	Average momentum transfer cross section between particles of types 1 and 2
$\overline{v}_T$	Mean speed of a Maxwellian particle with the temperature T
$\overline{x}(\lambda)$	Color matching function according to CIE 1931
$\overline{y}(\lambda)$	Color matching function according to CIE 1931
$\overline{z}(\lambda)$	Color matching function according to CIE 1931
ϕ	Electrostatic potential
Φ_λ	Radiant flux at a given wavelength λ
$\phi_{12}(r)$	Lennard-Jones potential between the neutral particles of types 1 and 2
Φ_{Conv}	Heat transfer rate due to natural convection
ϕ_D	Debye-Hückel potential
Φ_{total}	Total radiant flux
Φ_{TR}	Thermal radiation power
$\phi_{\lambda,pc}$	Emission function of the virtual phosphor coating
Ψ	Spectral line profile
Ψ_α	Spectral line absorption profile
Ψ_ϵ	Spectral line emission profile

Ψ_{Doppler}	Line profile due to Doppler broadening
Ψ_{Natural}	Line profile due to natural broadening
Ψ_{Voigt}	Voigt line profile
ρ	Ratio of multiplicities of the Rydberg state and molecular ion
σ	Total electrical conductivity
σ_0	DC electrical conductivity
σ_{e}	Electrical conductivity of electrons
σ_{i}	Electrical conductivity of ion
τ	Lifetime of particles due to diffusion losses
τ_{k}	Life time of the state k
τ_{pe}	Electron response time
q	Elementary cross section
$\mathbf{E}$	Electric field strength
$\mathbf{E}_0$	Amplitude of the electric field
$\mathbf{E}_{\text{rms}}$	Root mean square of the total electric field strength
$\mathbf{H}$	Magnetic field strength
$\mathbf{H}_0$	Amplitude of the magnetic field
J	Total angular momentum
L	Total orbital angular momentum
S	Total spin angular momentum
C_{W}	Equivalent circuit element for the stored energy during wave excitation
g	Label for ground state
i	Label for ionic state
j	Label for a lower excited state
k	Label for a higher excited state
m	Label for metastable state
R_{W}	Equivalent circuit element for the power carried by surface waves

Z_E	Equivalent circuit element for the stored energy by the EM-field in the gap
Z_P	Equivalent circuit element for the absorbed power by the plasma in the gap
θ	Azimuth
Θ_λ	Escape factor at a given wavelength λ
$\Theta_\lambda^{\text{eff}}$	Effective escape factor at a given wavelength λ
θ_A	Mean power absorbed per electron
θ_L	Mean power lost per electron
α	Attenuation coefficient
β	Phase coefficient
ΔE_{jk}	Energy difference between the initial j and final state k of excitation
ΔE_{jk}	Energy difference between the initial j and final state k
$\Delta\lambda_{\text{Doppler}}$	FWHM of Doppler broadening
$\Delta\lambda_{\text{Natural}}$	FWHM of natural broadening
ϵ_{12}	The characteristic Lennard-Jones energy between the particles of types 1 and 2
γ	Propagation coefficient
Λ	Diffusion length
μ_{12}	Reduced mass of two particles of types 1 and 2
ν	Vibrational quantum number
σ_{12}	Characteristic Lennard-Jones length between the particles of types 1 and 2
ξ_{con}	Conversion factor between radiant flux and irradiance
$\varepsilon(\lambda)$	Spectral emissivity
ε_0	Permittivity of vacuum
ε_a	Relative permittivity of air
$\varepsilon_{\text{FSG}}(\lambda)$	Spectral emissivity of fused silica glass
ε_g	Permittivity of fused silica glass
ε_p	Plasma permittivity

ε_r	Relative permittivity of medium
ς_0	Constant for Gryziński method
ξ_j	Number of the orbital electrons at the energy state n
A	Surface area of a body
a	Radius of plasma column
a_0	Bohr radius
A_{kj}	Einstein coefficient for spontaneous emission (Decay rate of radiative transition)
a_{vib}	Vibrational amplitude
a_n	Orbital radius of an electron with the principal quantum number n
B	Magnetic field
b	Radius of plasma column with wall thickness of dielectric tube
B_{jk}	Einstein coefficient for absorption
B_{kj}	Einstein coefficient for induced emission
B_{rc}	Rotational constant
B_v	Average rotational constant over the vibrational motion
c	Speed of light
D	Diffusion coefficient
D_a	Ambipolar diffusion coefficient
D_{dc}	Centrifugal distortion constant
D_e	Diffusion coefficient of electrons
D_i	Diffusion coefficient of ions
D_v	Average centrifugal constant over the vibrational motion
E	Energy
e	Elementary charge
E^{mol}	Total energy of a molecule
E_λ	Irradiance at a given wavelength λ
E_{ad}	Adiabatic ionization energy of the molecule
E_b	Binding energy

$E_{\text{diss.}}$	Dissociation energy of a molecule
E_{el}	Energy of the electronic state of a molecule
e_{Eu}	Euler's number
E_{i}	Ionization energy
E_{Photon}	Energy of a photon
E_{rb}	Reduced binding energy
E_{rk}	Reduced kinetic energy
E_{rok}	Reduced orbital electron kinetic energy
E_{rot}	Energy of the rotational state of a molecule
E_{vib}	Energy of the vibrational state of a molecule
f_{α}	Radial profile of α_{λ} inside the discharge vessel
f_{jk}	Absorption oscillator strength for the transition from the state j into k
$f_{\text{M}}(E, T_{\text{e}})$	Maxwellian electron energy distribution function
f_{pe}	Electron plasma frequency
f_{vib}	Vibration frequency
f_{D}	Correction term for diffusion
f_{ϵ}	Radial profile of ϵ_{λ} inside the discharge vessel
$F_{\text{v}}(J)$	Term value for the rotational state energy of a molecule
g	Gap distance of the surfatron
$G(v)$	Term value for the vibrational state energy of a molecule
g_{i}	Statistical weight of the ion
g_{n}	Statistical weight of an energy state n
g_Q	Gryziński function for the calculation of cross section Q
$g_{Q_{\text{diss.}}}$	Gryziński function for the calculation of dissociation cross section
$g_{Q_{\text{exch}}}$	Gryziński function for the calculation of electron exchange cross section
$g_{Q_{\text{i}}}$	Gryziński function for the calculation of ionization cross section
h	Planck constant

H_ν	Hermite polynomial
I_o	Modified Bessel's function of first kind of order o
J	Rotational quantum number
j	Total current density
J_0	Zero order Bessel function of the first kind
j_e	Current density of electrons
j_i	Current density of ions
j_{taq}	Total angular quantum number
K	Rate coefficient of an excitation or ionization process
k_B	Boltzmann constant
K_o	Modified Bessel's function of second kind of order o
L	Length
l	Orbital angular momentum number
L_λ	Spectral radiance at the wavelength λ
m	Mass of the given particle
m_{Ab}	Mass of the absorber
M_e	Radiant exitance
m_e	Electron mass
m_H	Mass of heavy particles
m_l	Direction of orbital angular momentum
m_s	Direction of electron spin
n	Particle density
n^*	Effective quantum number
n_Λ	Number of the total angular momentum along the internuclear axis of a molecule
n_J	Total angular momentum number
n_L	Total orbital angular momentum number
n_S	Total spin angular momentum number
n_{Ab}	Absorber density
n_{e0}	Electron density on the central axis of the lamp
n_{ec}	Critical electron density

n_e	Electron density
n_H	Density of heavy particles
n_i	Ion density
n_p	Principal quantum number
N_{red}	Reduced number of the absorbing atoms in cubic wavelength
n_{res}	Resonance electron density
o	Order of a Bessel's or Hankel's function
$P(r)$	Probability function of the given molecular state
P_{acc}	Accepted power by the surfatron from power supply line
P_A	Absorbed power by plasma
P_{drc}	Probability of a dephasing resonance collision during a radiative life time
P_{el}	Power consumption of the ECG
P_L	Power lost by the electrons in the plasma
P_{mw}	Microwave power generated by the ECG
P_{rad}	Radiated microwave power into the surrounding by the surfatron
P_{ref}	Reflected power at the interface between power supply line and surfatron input
P_{SW}	Surface wave power flux
P_{Ω}	Dielectric and ohmic power losses within the surfatron
R	Radius
r	Radial distance
r_{eqi}	Equilibrium internuclear distance of the ionic state of a molecule
r_{eq}	Equilibrium internuclear distance
R_H	Rydberg constant
R_{red}	Reduced radius
r_S	Intersection point of U_d and U_i
S	Energy state specific constant for BEB model

T	Temperature
t	Time
T^{el}	Term value for the electronic state energy of a molecule
T^{mol}	Term value for the total energy of a molecule
T_{B}	Temperature of a body
T_{CS}	Cold spot temperature of the lamp
T_{eV}	Equivalent temperature of a particle given in eV
T_{e}	Electron temperature
T_{g}	Temperature of neutral particles
T_{i}	Temperature of ions
T_{SM}	Temperature of the surrounding medium
U_{d}	Potential curve of dissociating neutral state of a molecule
$U_{\text{d}}'(r_{\text{S}})$	Slope of the potential curve of dissociating neutral state at the intersection point r_{S}
U_{i}	Potential curve of the molecular ion
U_{Ryd}	Potential curve of a Rydberg state
v	Translational velocity
v_{12}	Mean relative speed of the incident particle of type 1 with regard to the field particle of type 2
v_{d}	Drift velocity
v_{e}	Velocity of the electrons
$v_{T\text{max}}$	Most probable speed of a Maxwellian particle with the temperature T
x	Insertion depth of the coupler capacitor of the surfatron
x_{cc}	Chromaticity coordinate
x_{e}	Anharmonicity constant
X_{ts}	Tristimulus value of color stimuli according to CIE 1931
y	Perpendicular distance from the lamp axis
y_{cc}	Chromaticity coordinate
Y_{ts}	Tristimulus value of color stimuli according to CIE 1931

Z	Number of charge carriers or charge number (valence) of an ion
z	Axial coordinate in the direction of propagation
z_{cc}	Chromaticity coordinate
Z_p	Complex plasma impedance
Z_{ts}	Tristimulus value of color stimuli according to CIE 1931

Bibliography

[1] European Commission, *Green Paper: Lighting the future, Accelerating the deployment of innovative lighting technologies*, Brussels, Dec. 15, 2011.

[2] McKinsey & Company, Inc., *Lighting the way, Perspectives on the global lighting market*, edited by T. Baumgartner, F. Wunderlich, A. Jaunich, T. Sato, G. Bundy, N. Grießmann, J. Kowalski, S. Burghardt, and J. Hanebrink, version 2, 2012.

[3] P. Bertoldi, N. Labanca, and B. Hirl, *Energy efficiency status report 2012, Electricity consumption and efficiency trends in the EU-27*, Vol. 25405 (Publications Office of the European Union, Luxembourg, 2012), 142 pp.

[4] The European Parliament and the Council of the European Union, *Directive 2005/32/EC on ecodesign for energy-using appliances*, July 22, 2005.

[5] IEA, *Light's labour's lost, Policies for energy-efficient lighting*, Energy Efficiency Policy Profiles (OECD Publishing, Paris, 2006), 561 pp.

[6] J. Schleich, B. Mills, and E. Dütschke, "A brighter future? Quantifying the rebound effect in energy efficient lighting", Energy Policy **72**, 35–42 (2014).

[7] The European Parliament and the Council of the European Union, *Directive 2011/65/EU on the restriction of the use of certain hazardous substances in electrical and electronic equipment*, ROHS 2011/65/EU, 2011.

[8]   D. Uhrlandt, R. Bussiahn, S. Gorchakov, H. Lange, D. Loffhagen, and D. Nötzold, "Low-pressure mercury-free plasma light sources: Experimental and theoretical perspectives", Journal of Physics D: Applied Physics **38**, 3318–3325 (2005).

[9]   R. Scholl, "A new generation of highly efficient light sources", Forschungsspitzen und Spitzenforschung, 175–187 (2009).

[10] D. J. Smith, J. D. Michael, V. Midha, G. M. Cotzas, and T. J. Sommerer, "Efficient radiation production in a weakly ionized, low-pressure, nonequilibrium gallium-iodide positive column discharge plasma", Journal of Physics D: Applied Physics **40**, 3842–3856 (2007).

[11] R. Friedl and U. Fantz, "Spectral intensity of the N_2 emission in argon low-pressure arc discharges for lighting purposes", New Journal of Physics **14**, 043016 (2012).

[12] S. Briefi and U. Fantz, "Diagnostics of low-pressure discharges containing InBr studied for lighting applications", Plasma Sources Science and Technology **22**, 055003 (2013).

[13] N. Masoud and D. Murnick, "High efficiency, fluorescent excimer lamps, an alternative to CFLs and white light LEDs", Journal of Light & Visual Environment **37**, 171–175 (2013).

[14] S. Kitsinelis, G. Zissis, and E. Fokitis, "A strategy towards the next generation of low pressure discharge lamps: Lighting after mercury", Journal of Physics D: Applied Physics **42**, 045209 (2009).

[15] V. Godyak, "Bright idea: Radio-frequency light sources", IEEE Industry Applications Magazine **8**, 42–49 (2002).

[16] N. Tesla, *Experiments with alternate currents of very high frequency and their application to methods of artificial illumination*, 1st ed (Wilder Publications, Radford, Va., 2007), 48 pp.

[17] M. Shinomiya, K. Kobayashi, M. Higashikawa, S. Ukegawa, J. Matsuura, and K. Tanigawa, "Development of the electrodeless fluorescent lamp", Journal of the Illuminating Engineering Society **20**, 44–49 (1991).

[18] M. Chaker, M. Moisan, and Z. Zakrzewski, "Microwave and RF surface wave sustained discharges as plasma sources for plasma chemistry and plasma processing", Plasma Chemistry and Plasma Processing **6**, 79–96 (1986).

[19] M. Selby and G. M. Hieftje, "Taming the surfatron", Spectrochimica Acta Part B: Atomic Spectroscopy **42**, 285–298 (1987).

[20] W. Lochte-Holtgreven, ed., *Plasma diagnostics* (North-Holland Pub. Co., Amsterdam, 1968), xvi, 928.

[21] U. S. Inan and M. Gołkowski, *Principles of plasma physics for engineers and scientists* (Cambridge University Press, Cambridge and New York, 2011), xiv, 270.

[22] M. A. Lieberman and A. J. Lichtenberg, *Principles of plasma discharges and materials processing*, 2nd ed (Wiley-Interscience, Hoboken, N.J, 2005), xxxv, 757.

[23] W. Demtröder, *Atoms, molecules and photons, An introduction to atomic-, molecular-, and quantum-physics*, 2nd ed, Graduate Texts in Physics (Springer, Heidelberg and London, 2010), xvii, 589.

[24] A. Kramida, Y. Ralchenko, J. Reader, and NIST ASD Team, *NIST atomic spectra database (version 3.1.5)*, Gaithersburg, MD.: National Institute of Standards and Technology, Gaithersburg, MD, 2013.

[25] K.-P. Huber, *Constants of diatomic molecules*, Vol. 4, Molecular Spectra and Molecular Structure (Van Nostrand Reinhold, New York, 1979), xiii, 716.

[26] G. Herzberg, *Spectra of diatomic molecules*, 2nd ed, Vol. 1, Molecular Spectra and Molecular Structure (Van Nostrand, New York, 1950), xv, 658.

[27] G. Herzberg, *Electronic spectra and electronic structure of polyatomic molecules*, 1st ed, Vol. 3, Molecular Spectra and Molecular Structure (Van Nostrand, New York, 1966), vi, 745.

[28] H. Haken and H. C. Wolf, *Molekülphysik und Quantenchemie, Einführung in die experimentellen und theoretischen Grundlagen*, 5th ed, Springer-Lehrbuch (Springer, Berlin [u.a.], 2006), xxii, 530.

[29] H. Haken and H. C. Wolf, *The physics of atoms and quanta, Introduction to experiments and theory*, 7th rev. and enl. ed, Advanced Texts in Physics (Springer, Berlin and New York, 2005), xx, 517.

[30] J. Bacri and A. Medani, "Electron diatomic molecule weighted total cross section calculation", Physica B+C **101**, 399–409 (1980).

[31] P. Teulet, J. P. Sarrette, and A. M. Gomes, "Calculation of electron impact inelastic cross sections and rate coefficients for diatomic molecules. Application to air molecules", Journal of Quantitative Spectroscopy and Radiative Transfer **62**, 549–569 (1999).

[32] B. E. Poling, J. M. Prausnitz, and J. P. O'Connell, *The properties of gases and liquids*, 5th ed (McGraw-Hill, New York, 2001), 768 pp.

[33] M. Moisan and J. Pelletier, *Physics of collisional plasmas, Introduction to high-frequency discharges* (Springer, Dordrecht and New York, 2012), xxiv, 480.

[34] M. Mitchner and C. H. Kruger, *Partially ionized gases*, Wiley Series in Plasma Physics (Wiley, New York, 1973), 518 pp.

[35] A. Piel, *Plasma physics, An introduction to laboratory, space, and fusion plasmas* (Springer, Berlin and London, 2010), xviii, 398.

[36] G. Franz, *Low pressure plasmas and microstructuring technology* (Springer, Berlin and London, 2009), 732 pp.

[37] I. I. Sobel'man, E. A. Ukov, and L. A. Vaĭnshteĭn, *Excitation of atoms and broadening of spectral lines*, 2nd ed, Vol. 15, Springer Series on Atoms + Plasmas (Springer, Berlin and New York, 1995), x, 309.

[38] M. Moisan and J. Pelletier, *Microwave excited plasmas*, Vol. 4, Plasma Technology (Elsevier, Amsterdam and New York, 1992), xviii, 519.

[39] G. Janzen, *Plasmatechnik, Grundlagen, Anwendungen, Diagnostik* (Hüthig Buch Verlag, Heidelberg, 1992), 334 pp.

[40] H. Conrads and M. Schmidt, "Plasma generation and plasma sources", Plasma Sources Science and Technology **9**, 441–454 (2000).

[41] A. Bogaerts, E. Neyts, R. Gijbels, and J. van der Mullen, "Gas discharge plasmas and their applications", Spectrochimica Acta Part B: Atomic Spectroscopy **57**, 609–658 (2002).

[42] R. B. Piejak, V. A. Godyak, and B. M. Alexandrovich, "A simple analysis of an inductive RF discharge", Plasma Sources Science and Technology **1**, 179–186 (1992).

[43] J. Hopwood, "Review of inductively coupled plasmas for plasma processing", Plasma Sources Science and Technology **1**, 109–116 (1992).

[44] G. Lister, J. Lawler, W. Lapatovich, and V. Godyak, "The physics of discharge lamps", Reviews of Modern Physics **76**, 541–598 (2004).

[45] M. Kando, T. Fukaya, Y. Ohishi, T. Mizojiri, Y. Morimoto, M. Shido, and T. Serita, "Application of an antenna excited high pressure microwave discharge to compact discharge lamps", Journal of Physics D: Applied Physics **41**, 144026 (2008).

[46] M. Moisan, A. Shivarova, and A. W. Trivelpiece, "Experimental investigations of the propagation of surface waves along a plasma column", Plasma Physics **24**, 1331–1400 (1982).

[47] H. M. Barlow and J. Brown, *Radio surface waves* (Clarendon Press, Oxford, 1962), 200 pp.

[48] H. M. Barlow and A. L. Cullen, "Surface waves", Proceedings of the IEE - Part III: Radio and Communication Engineering **100**, 329–341 (1953).

[49] A. Sommerfeld, "Über die Fortpflanzung elektrodynamischer Wellen längs eines Drahtes", Annalen der Physik und Chemie **303**, 233–290 (1899).

[50] G. Goubau, "Surface waves and their application to transmission lines", Journal of Applied Physics **21**, 1119–1128 (1950).

[51] R. E. Collin, *Field theory of guided waves*, 2nd ed (IEEE Press, New York, 1991), xii, 851.

[52] G. Goubau, "On the excitation of surface waves", Proceedings of the IRE **40**, 865–868 (1952).

[53] F. Harms, "Elektromagnetische Wellen an einem Draht mit isolierender zylindrischer Hülle", Annalen der Physik **328**, 44–60 (1907).

[54] N. H. Frank, "Die Fortpflanzung elektrischer Wellen in Kabeln mit zwei Isolationsschichten", Annalen der Physik **391**, 422–434 (1928).

[55] I. Zhelyazkov and V. Atanassov, "Axial structure of low-pressure high-frequency discharges sustained by travelling electromagnetic surface waves", Physics Reports **255**, 79–201 (1995).

[56] I. Zhelyazkov and E. Benova, "Modeling of a plasma column produced and sustained by a traveling electromagnetic surface wave", Journal of Applied Physics **66**, 1641–1650 (1989).

[57] J. Margot and M. Moisan, "Characteristics of surface-wave propagation in dissipative cylindrical plasma columns", Journal of Plasma Physics **49**, 357–374 (1993).

[58] M. Moisan, C. M. Ferreira, Y. Hajlaoui, D. Henry, J. Hubert, R. Pantel, A. Ricard, and Z. Zakrzewski, "Properties and applications of surface wave produced plasmas", Revue de Physique Appliquée **17**, 707–727 (1982).

[59] R. Darchicourt, S. Pasquiers, C. Boisse-Laporte, P. Leprince, and J. Marec, "Influence of the radial electron density profile on the determination of the characteristics of surface-wave-produced discharges", Journal of Physics D: Applied Physics **21**, 293–300 (1988).

[60] C. M. Ferreira, "Theory of a plasma column sustained by a surface wave", Journal of Physics D: Applied Physics **14**, 1811–1830 (1981).

[61] N. A. Azarenkov, I. B. Denysenko, A. V. Gapon, and T. W. Johnston, "The radial structure of a plasma column sustained by a surface wave", Physics of Plasmas **8**, 1467–1481 (2001).

[62] M. Moisan and Z. Zakrzewski, "Plasma sources based on the propagation of electromagnetic surface waves", Journal of Physics D: Applied Physics **24**, 1025–1048 (1991).

[63] G. G. Lister and T. R. Robinson, "Strongly damped surface waves in plasmas. I. The WKB approximation", Journal of Physics D: Applied Physics **24**, 1993–1999 (1991).

[64] C. M. Ferreira and M. Moisan, *Microwave discharges, Fundamentals and applications*, Vol. 302, NATO ASI series. Series B, Physics (Plenum Press, New York, 1993), ix, 564.

[65] C. M. Ferreira, "Modelling of a low-pressure plasma column sustained by a surface wave", Journal of Physics D: Applied Physics **16**, 1673–1685 (1983).

[66]   Z. Zakrzewski, "Conditions of existence and axial structure of long microwave discharges sustained by travelling waves", Journal of Physics D: Applied Physics **16**, 171–180 (1983).

[67]   W. Elenbaas, *Fluorescent lamps;* 2nd ed, Philips Technical Library (Macmillan, London, 1971), [8], 266.

[68]   K. Trampert, *Ladungstransportmodell dielektrisch behinderter Entladungen* (Universitätsverlag, Karlsruhe, 2009), 163 pp.

[69]   S. C. Hansen, J. Getchius, R. Steward, and T. R. Brumleve, *Vapor pressure of metal bromides and iodides, With selected metal chlorides and metals*, 2nd ed. (APL Engineered Materials, Inc., Urbana, Illinois, USA, 2006), xvi, 205.

[70]   S. Briefi, "Spectroscopic investigation of indium halides as substitutes of mercury in low pressure discharges for lighting applications", Mathematisch-Naturwissenschaftliche Fakultät, Dissertation (Universität Augsburg, 2012).

[71]   Mishra, S. K., "Spectroscopic studies of diatomic indium halides", Journal of Physical and Chemical Reference Data **33**, 453–470 (2004).

[72]   J. E. Lawler and J. J. Curry, "Analytical formula for radiation trapping with partial frequency redistribution", Journal of Physics D: Applied Physics **31**, 3235–3242 (1998).

[73]   J. E. Lawler, J. J. Curry, and G. G. Lister, "Analytic formula for radiation trapping with partial frequency redistribution and foreign gas broadening", Journal of Physics D: Applied Physics **33**, 252–256 (2000).

[74]   J. E. Lawler and J. J. Curry, "Resonance radiation transport in glow discharge plasmas", in *Electron Kinetics and Applications of Glow Discharges*, Vol. 367, edited by U. Kortshagen and L. D. Tsendin,

NATO Science Series: B (Kluwer Academic Publishers, Boston, 2002), pp. 471–487.

[75] M. T. Herd, J. E. Lawler, and K. L. Menningen, "Radiation trapping of the Hg 254 nm resonance line", Journal of Physics D: Applied Physics **38**, 3304–3311 (2005).

[76] T. Holstein, "Imprisonment of resonance radiation in gases", Physical Review **72**, 1212–1233 (1947).

[77] H. Anderson, S. Bergeson, D. Doughty, and J. Lawler, "Xenon 147-nm resonance f value and trapped decay rates", Physical Review A **51**, 211–217 (1995).

[78] C. van Tright, "Analytically solvable problems in radiative transfer. IV", Physical Review A **13**, 726–733 (1976).

[79] P. Bicchi, C. Marinelli, E. Mariotti, M. Meucci, and L. Moi, "Radiation trapping and vapor density of indium confined in quartz cells", Optics Communications **106**, 197–201 (1994).

[80] M. E. Wieser, N. Holden, T. B. Coplen, J. K. Böhlke, M. Berglund, W. A. Brand, P. d. Bièvre, M. Gröning, R. D. Loss, J. Meija, T. Hirata, T. Prohaska, R. Schoenberg, G. O'Connor, T. Walczyk, S. Yoneda, and X.-K. Zhu, "Atomic weights of the elements 2011 (IUPAC Technical Report)", Pure and Applied Chemistry **85**, 1047–1078 (2013).

[81] M. Berglund and M. E. Wieser, "Isotopic compositions of the elements 2009 (IUPAC Technical Report)", Pure and Applied Chemistry **83**, 397–410 (2011).

[82] P. Walsh, "Effect of simultaneous doppler and collision broadening and of hyperfine structure on the imprisonment of resonance radiation", Physical Review **116**, 511–515 (1959).

[83]   J. E. Lawler and M. G. Raizen, "Enhanced escape rate for Hg 254 nm resonance radiation in fluorescent lamps", Journal of Physics D: Applied Physics **46**, 415204 (2013).

[84]   D. A. Jackson, "Hyperfine structures of the resonance lines of indium 115", Proceedings of the Royal Society of London. Series A, Mathematical and Physical Sciences **241**, 283–298 (1957).

[85]   D. A. Jackson, "Isotope shift in the spectrum of indium I", Physical Review **105**, 1925 (1957).

[86]   J. Eberz, G. Huber, T. Kuhl, and G. Ulm, "Pressure broadening and pressure shift of the 410 nm indium line perturbed by foreign gases", Journal of Physics B: Atomic and Molecular Physics **17**, 3075–3082 (1984).

[87]   S. Briefi, C. Wimmer, and U. Fantz, "Correction factors for saturation effects in white light and laser absorption spectroscopy for application to low pressure plasmas", Physics of Plasmas **19**, 053501 (2012).

[88]   M. Schonhuber, "Breakdown of gases below Paschen minimum: Basic design data of high-voltage equipment", IEEE Transactions on Power Apparatus and Systems **PAS-88**, 100–107 (1969).

[89]   C. Kaiser, *Mikrowellenangeregte quecksilberfreie Hochdruckgasentladungslampen*, Vol. 3, Spektrum der Lichttechnik (KIT Scientific Publishing, Karlsruhe, 2013), xi, 255.

[90]   R. H. Huddlestone and S. L. Leonard, eds., *Plasma diagnostic techniques*, Vol. 21, Pure and Applied Physics (Academic Press, New York, 1965), xii, 627.

[91]   H. R. Griem, *Principles of plasma spectroscopy*, Vol. 2, Cambridge Monographs on Plasma Physics (Cambridge University Press, Cambridge and New York, 1997), xix, 366.

[92] H. P. Summers, *The ADAS User Manual 2.6, Escape factors for line emission and population calculations*, (2006) `http://www.adas.ac.uk` (visited on 10/02/2015).

[93] F. E. Irons, "The escape factor in plasma spectroscopy—I. The escape factor defined and evaluated", Journal of Quantitative Spectroscopy and Radiative Transfer **22**, 1–20 (1979).

[94] S. O. Kastner, "Photon escape probabilities; Concepts and clarifications", Space Science Reviews **65**, 317–362 (1993).

[95] R. Ladenburg, "Die quantentheoretische Deutung der Zahl der Dispersionselektronen", Zeitschrift für Physik **4**, 451–468 (1921).

[96] A. P. Thorne, *Spectrophysics, Principles and applications*, 2nd ed (Chapman and Hall, London and New York, 1988), xvi, 390.

[97] A. W. Ali and H. R. Griem, "Theory of resonance broadening of spectral lines by atom-atom impacts", Physical Review **140**, A1044–A1049 (1965).

[98] A. F. Molisch and B. P. Oehry, *Radiation trapping in atomic vapours* (Clarendon Press, New York, 1998), xxvi, 510.

[99] S. J. Young, "Iterative Abel inversion of optically thick, cylindrically symmetric radiation sources", Journal of Quantitative Spectroscopy and Radiative Transfer **25**, 479–481 (1981).

[100] P. Ding, Y. Mu, and Y. Wang, "An improved block-bi-quadric interpolation of the abel transformation for use in optically-thick, cylindrically-symmetric plasmas", Journal of Quantitative Spectroscopy and Radiative Transfer **57**, 291–294 (1997).

[101] M. Buie, J. Pender, J. Holloway, T. Vincent, P. Ventzek, and M. Brake, "Abel's inversion applied to experimental spectroscopic data with off axis peaks", Journal of Quantitative Spectroscopy and Radiative Transfer **55**, 231–243 (1996).

[102] G. Pretzier, H. Jäger, T. Neger, H. Philipp, and J. Woisetschläger, "Comparison of different methods of Abel inversion using computer simulated and experimental side-on data", Zeitschrift für Naturforschung A **47**, 955–970 (1992).

[103] G. Pretzier, "A new method for numerical Abel-inversion", Zeitschrift für Naturforschung A **46**, 639–641 (1991).

[104] R. F. Boivin, J. L. Kline, and E. E. Scime, "Electron temperature measurement by a helium line intensity ratio method in helicon plasmas", Physics of Plasmas **8**, 5303–5314 (2001).

[105] V. Godyak, "Nonequilibrium EEDF in gas discharge plasmas", IEEE Transactions on Plasma Science **34**, 755–766 (2006).

[106] J. Cotrino, A. Palmero, V. Rico, A. Barranco, J. P. Espinós, and A. R. González-Elipe, "Electron temperature measurement in a slot antenna 2.45 GHz microwave plasma source", Journal of Vacuum Science & Technology B: Microelectronics and Nanometer Structures **19**, 410–414 (2001).

[107] M. Gryziński, "Classical theory of atomic collisions. I. Theory of inelastic collisions", Physical Review **138**, A336–A358 (1965).

[108] L. L. Shimon and E. I. Nepiypov, "Effective cross-sections of indium excitation by electron impact", Ukrainian Journal of Physics **19**, 627–631 (1974).

[109] D. Heddle and J. Gallagher, "Measurements of electron impact optical excitation functions", Reviews of Modern Physics **61**, 221–278 (1989).

[110] E. Bauer and C. D. Bartky, "Calculation of inelastic electron-molecule collision cross sections by classical methods", The Journal of Chemical Physics **43**, 2466–2476 (1965).

[111] H.-W. Drawin, "Zur formelmäßigen Darstellung der Ionisierungs-querschnitte gegenüber Elektronenstoß", Zeitschrift für Physik **164**, 513–521 (1961).

[112] J. J. Thomson, "XLII. Ionization by moving electrified particles", Philosophical Magazine Series 6 **23**, 449–457 (1912).

[113] M. Gryziński, "Two-particle collisions. II. Coulomb collisions in the laboratory system of coordinates", Physical Review **138**, A322–A335 (1965).

[114] L. Visscher and K. G. Dyall, "Dirac–Fock atomic electronic structure calculations using different nuclear charge distributions", Atomic Data and Nuclear Data Tables **67**, 207–224 (1997).

[115] Y.-K. Kim and P. Stone, "Ionization of boron, aluminum, gallium, and indium by electron impact", Physical Review A **64**, 052707 (2001).

[116] A. Banerjee and K. K. Das, "Theoretical spectroscopic studies of InI and InI$^+$", International Journal of Quantum Chemistry **112**, 453–469 (2010).

[117] D. Rapp and P. Englander-Golden, "Total cross sections for ionization and attachment in gases by electron impact. I. Positive ionization", The Journal of Chemical Physics **43**, 1464–1479 (1965).

[118] J. Fletcher and I. R. Cowling, "Electron impact ionization of neon and argon", Journal of Physics B: Atomic and Molecular Physics **6**, L258–L261 (1973).

[119] W. Hwang, Y.-K. Kim, and M. E. Rudd, "New model for electron-impact ionization cross sections of molecules", The Journal of Chemical Physics **104**, 2956–2966 (1996).

[120] Y.-K. Kim, "Electron-impact ionization cross sections for polyatomic molecules, radicals, and ions", AIP Conference Proceedings, 220–241 (2000).

[121]   L. A. Vaĭnshteĭn, D. G. Golovach, V. I. Ochkur, V. I. Rakhovskiĭ, N. M. Rumyantsev, and V. M. Shustryakov, "Cross sections for ionization of gallium and indium by electrons", Zhurnal Ehksperimental'noj i Teoreticheskoj Fiziki **93**, 65–70 (1987).

[122]   T. Hayes, R. Wetzel, and R. Freund, "Absolute electron-impact-ionization cross-section measurements of the halogen atoms", Physical Review A **35**, 578–584 (1987).

[123]   O. Klein and S. Rosseland, "Über Zusammenstöße zwischen Atomen und freien Elektronen", Zeitschrift für Physik **4**, 46–51 (1921).

[124]   J. N. Bardsley, "The theory of dissociative recombination", Journal of Physics B: Atomic and Molecular Physics **1**, 365–380 (1968).

[125]   M. Wolfsberg and E. A. Peter, "The calculation of vibrational mean square amplitudes of molecular internal coordinates by a perturbation theory technique", The Journal of Chemical Physics **70**, 5722–5725 (1979).

[126]   E. A. Mason and E. W. McDaniel, *Transport properties of ions in gases* (Wiley and Wiley-VCH Verlag GmbH & Co. KGaA, New York, 1988), xvi, 560.

[127]   P. D. Neufeld, "Empirical equations to calculate 16 of the transport collision integrals $\Omega^{(l,s)*}$ for the Lennard-Jones (12-6) potential", The Journal of Chemical Physics **57**, 1100–1102 (1972).

[128]   J. O. Hirschfelder, *Molecular theory of gases and liquids*, Corr. print. with notes added, Structure of matter series (Wiley, London, 1964), xxvi, 1249.

[129]   N. Hishinuma and O. Sueoka, "Measurements of the anisotropic interaction potential for Ga-Ar, Ga-Kr, Ga-Xe, In-Ar, and In-Kr systems", Chemical Physics Letters **121**, 293–296 (1985).

[130] M. Krauss and P. S. Julienne, "Collision-induced I(^{2}P$_{1/2}$) emission in argon and xenon", The Journal of Chemical Physics **67**, 669–673 (1977).

[131] E. H. Kennard, *The kinetic theory of gases. With an introduction to statistical mechanics*, 1st ed. (McGraw-Hill Publishing Co, Ltd., London, 1938), xiv, 483.

[132] Ögün, C. M., C. Kaiser, and R. Kling, *Sequentially emission line addressing by microwave driven mercury free low pressure lamps*, Salt Lake City, Utah, USA: 64th Annual Gaseous Electronics Conference, 2011.

[133] A. A. Fridman and L. A. Kennedy, *Plasma physics and engineering* (Taylor & Francis, New York, 2004), 853 pp.

[134] M. Moisan, "Radio frequency or microwave plasma reactors? Factors determining the optimum frequency of operation", Journal of Vacuum Science & Technology B: Microelectronics and Nanometer Structures **9**, 8–25 (1991).

[135] C. Kaiser, C. M. Ögün, R. Kling, and W. Heering, "Electrodeless mercury-free microwave-driven indium-iodide-based high-intensity discharges with high color rendering index", IEEE Transactions on Plasma Science **41**, 77–81 (2013).

[136] C. Kaiser, M. Katona, C. M. Ögün, R. Kling, and W. Heering, "High-intensity discharge lamps with high color rendering indices based on molecular radiation of indium iodide", IEEE Transactions on Plasma Science **42**, 20–28 (2014).

[137] M. Moisan, Z. Zakrzewski, and R. Pantel, "The theory and characteristics of an efficient surface wave launcher (surfatron) producing long plasma columns", Journal of Physics D: Applied Physics **12**, 219–237 (1979).

[138] Heraeus Quarzglas, *CFQ 099 / HSQ 100 / HSQ 300 / HSQ 700, Electrically fused quartz glass*, Brochure, 2001.

[139] Heraeus Quarzglas, *Base materials*, Brochure, 2013.

[140] R. G. Athay, *Radiation transport in spectral lines*, Vol. 1, Geophysics and Astrophysics Monographs (Reidel, Dordrecht, 1972).

[141] M. Wehrli and E. Miescher, "Spektroskopische Untersuchung dampfförmiger Indiumhalogenide", Helvetica Physica Acta 7, 298–330 (1934).

[142] R. W. B. Pearse and A. G. Gaydon, *Identification of molecular spectra* (Chapman & Hall, 1950), 276 pp.

[143] J. Margot, M. Moisan, and A. Ricard, "Optical radiation efficiency of surface-wave-produced plasmas as compared to DC positive columns", Applied Spectroscopy **45**, 260–271 (1991).

[144] A. Besner, J. Margot, S. Bordeleau, and J. Hubert, "Spatially resolved distribution of excited species in an argon surface-wave produced plasma at intermediate pressures (10–600 torr) obtained by tomography", Spectrochimica Acta Part B: Atomic Spectroscopy **48**, 985–1001 (1993).

[145] C. Beneking and P. Anderer, "Radiation efficiency of Hg-Ar surface wave discharges", Journal of Physics D: Applied Physics **25**, 1470–1482 (1992).

[146] S. Adamson, V. Astapenko, I. Chernysheva, V. Chorkov, M. Deminsky, G. Demchenko, A. Demura, A. Demyanov, N. Dyatko, A. Eletzkii, A. Knizhnik, I. Kochetov, A. Napartovich, E. Rykova, L. Sukhanov, S. Umanskii, A. Vetchinkin, A. Zaitsevskii, and B. Potapkin, "Multiscale multiphysics nonempirical approach to calculation of light emission properties of chemically active nonequilibrium plasma: Application to Ar–GaI$_3$ system", Journal of Physics D: Applied Physics **40**, 3857–3881 (2007).

[147] J. F. Waymouth and F. Bitter, "Analysis of the plasma of fluorescent lamps", Journal of Applied Physics **27**, 122–131 (1956).

[148] C. Meyer and H. Nienhuis, *Discharge lamps* (Philips Technical Library, Kluwer Technische Boeken, Deventer, 1988), 312 pp.

[149] V. A. Petrov and S. V. Stephanov, "Radiation characteristics of quartz glasses: Spectral radiating power (in Russian)", Teplofizika Vysokikh Temperatur (High-temperature Thermal Physics) **13**, 335–345 (1975).

[150] M. Lambrecht, *Untersuchungen an Quecksilberhochdrucklampen zur effizienten Erzeugung ultravioletter Strahlung*, Berichte aus der Elektrotechnik (Shaker, Aachen, 1999), ii, 208.

[151] I. Hamberg and C. G. Granqvist, "Transparent and infrared-reflecting indium-tin-oxide films: Quantitative modeling of the optical properties", Applied Optics **24**, 1815–1819 (1985).

[152] *IEEE standard for safety levels with respect to human exposure to radio frequency electromagnetic fields, 3 kHz to 300 GHz* (Institute of Electrical and Electronics Engineers, New York, N.Y., 2006), x, 238.

[153] A. Santos Abreu, *Einfluss von Metalloxidschutzschichten auf die Quecksilberaufzehrung in Leuchtstofflampen, Messung und Modellierung* (Mensch & Buch Verl., Berlin, 2012), 139 pp.

[154] J. M. Mayer, *Analyse und Modellierung der Quecksilberaufzehrung in Leuchtstofflampen*, physics (Mensch & Buch Verl., Berlin, 2013), vi, 122.

[155] C. R. Ronda, "Recent achievements in research on phosphors for lamps and displays", Journal of Luminescence **72-74**, 49–54 (1997).

[156] C. R. Ronda, "Phosphors for lamps and displays: An applicational view", Journal of Alloys and Compounds **225**, 534–538 (1995).

[157]   Commission Internationale de l'Eclairage (CIE), *Colorimetry*, Vienna, 2004.

[158]   J. M. Proud and L. H. Luessen, *Radiative processes in discharge plasmas*, Vol. 149, NATO ASI series. Series B, Physics (Plenum Press, New York, 1987), viii, 592.

[159]   S. Samukawa, M. Hori, S. Rauf, K. Tachibana, P. Bruggeman, G. Kroesen, J. C. Whitehead, A. B. Murphy, A. F. Gutsol, S. Starikovskaia, U. Kortshagen, J.-P. Boeuf, T. J. Sommerer, M. J. Kushner, U. Czarnetzki, and N. Mason, "The 2012 plasma roadmap", Journal of Physics D: Applied Physics **45**, 253001 (2012).

[160]   W. J. van den Hoek, G. M. J. F. Luijks, and C. G. H. Hoelen, "Lamps", in *Ullmann's Encyclopedia of Industrial Chemistry* (Wiley-VCH Verlag GmbH & Co. KGaA, Weinheim, Germany, 2000).

[161]   M. Roberg, J. Hoversten, and Z. Popović, "GaN HEMT PA with over 84% power added efficiency", Electronics Letters **46**, 1553 (2010).

[162]   B. Grübel, "Untersuchung gepulster quecksilberfreier Indium(I) iodide-Niederdruckplasmen", Light Technology Institute, Bachelor's thesis (Karlsruher Institute of Technology, Karlsruhe, 2014).

[163]   A. Gamero, A. Sola, J. Cotrino, and V. Colomer, "Experimental study of the ionization front in pulsed-surface-wave-produced plasmas", Journal of Applied Physics **65**, 2199–2204 (1989).

[164]   A. Gamero, A. Sola, J. Cotrino, and V. Colomer, "Temporal evolution of the electric field intensity in pulsed surface-wave-produced plasmas", Journal of Physics D: Applied Physics **22**, 1482–1486 (1989).

[165] N. P. Penkin and L. N. Shabanova, "Oscillator strengths and effective cross sections of the resonance lines of gallium and indium atoms for line-broadening collisions", Optics and Spectroscopy **23**, 11–13 (1967).

[166] N. P. Penkin and L. N. Shabanova, "Oscillator strengths of spectral lines of the aluminum, gallium and indium atoms", Optics and Spectroscopy **14**, 5–8 (1963).

[167] N. M. Erdevdi and L. L. Shimon, "Lifetimes of excited states of indium, strontium, and barium", Optics and Spectroscopy **40**, 443–444 (1976).

[168] G. M. Lawrence, J. K. Link, and R. B. King, "The absolute oscillator strengths of lines in the spectra of ten elements", The Astrophysical Journal **141**, 293–307 (1965).

[169] P. S. Doidge, "A compendium and critical review of neutral atom resonance line oscillator strengths for atomic absorption analysis", Spectrochimica Acta Part B: Atomic Spectroscopy **50**, 209–263 (1995).

[170] J. Migdałek, "Theoretical relativistic oscillator strengths I. Transitions in principal, sharp, and diffuse series of Al I, Ga I, In I, and Tl I spectra", Canadian Journal of Physics **54**, 118–129 (1976).

[171] U. Safronova, M. Safronova, and M. Kozlov, "Relativistic all-order calculations of In I and Sn II atomic properties", Physical Review A **76**, 022501 (2007).

[172] N. L. Moise, "A study of absolute atomic transition probabilities; the correlation of oscillator strengths and vapor pressure", Dissertation (California Institute of Technology, 1963).

[173] K. B. Blagoev, Y. F. Verolainen, V. N. Gorshkov, and V. A. Komarivskii, "Experimental investigation of lifetimes of In I and In II excited states", Optika i spektroskopiya (USSR) **59**, 937–940 (1985).

[174] T. Andersen, "Beam-foil spectroscopy with low-energy accelerators", Nuclear Instruments and Methods **110**, 35–42 (1973).

[175] T. Andersen and G. Sørensen, "Systematic study of atomic lifetimes in gallium, indium, and thallium measured by the beam-foil technique", Physical Review A **5**, 2447–2451 (1972).

[176] M. Brieger, H. Bucka, A. Reichelt, and P. Zimmermann, "Untersuchung der Hyperfeinstruktur des $5s^2 5d^2 D_{3/2}$- und $5s^2 6d^2 D_{3/2}$-Terms im In I-Spektrum durch Resonanzstreuung von Licht im äußeren Magnetfeld", Zeitschrift für Naturforschung A **24**, 903–908 (1969).

[177] M. A. Z. Ewiss and C. Snoek, "Lifetime measurements of low-lying S and D levels in indium", Journal of Physics B: Atomic and Molecular Physics **16**, L153–L157 (1983).

Publications by the author

Journal papers

1. **C. M. Ögün**, C. Kaiser, R. Kling und W. Heering
   Diagnostics of surface wave driven low pressure plasmas based on indium monoiodide-argon system
   J. Phys. D: Appl. Phys, vol. 48, p. 255201 (2015)

2. **C. M. Ögün**, W. Truong, C. Kaiser, R. Kling und W. Heering
   Modelling of indium(I)iodide-argon low pressure plasma
   J. Phys. D: Appl. Phys, vol. 47, p. 285202 (2014)

3. C. Kaiser, M. Katona, **C. M. Ögün**, R. Kling und W. Heering
   High-Intensity discharge lamps with high color rendering indices based on molecular radiation of indium iodide
   IEEE Transactions on Plasma Science, vol. 42, 20-28 (2014)

4. C. Kaiser, **C. M. Ögün**, R. Kling und W. Heering
   Electrodeless mercury-free microwave-driven indium-iodide-based high-intensity discharges with high color rendering index
   IEEE Transactions on Plasma Science, vol. 41, 77-81 (2013)

5. S. Valouch, **C. M. Ögün**, S. W. Kettlitz, S. Züfle, N. Christ und U. Lemmer
   Printed circuit board encapsulation and integration of high-speed polymer photodiodes
   Sensor Lett., vol. 8, 392 (2010)

Some passages of this work have been quoted verbatim from the publications listed above as 1. and 2.

Patent applications

1. **C. M. Ögün**, C. Kaiser, R. Kling, *Flash lamp and method for generating a flash with high power density in the UV region*, EP 2879159 A1, published on 03.06.2015

2. **C. M. Ögün**, K. Hähre, R. Kling, *Light generating unit and electrodeless discharge lamp*, EP 2866249 A1, published on 29.04.2015

3. **C. M. Ögün**, C. Kaiser, R. Kling, *Electrodeless general service lamp operated by means of HF power*, WO2015025010, published on 26.02.2015

4. **C. M. Ögün**, C. Kaiser, R. Kling, *Electrodeless HF lamp*, WO2014170296, published on 23.10.2014

Conference contributions

1. **C. M. Ögün**, R. Kling, W. Heering, *Gepulste UV-Strahlungsquellen für photobiologische Applikationen*, 20. DAfP-Symposium "Alternative Strahlungs quellen – LED vs. Plasmastrahler", Aachen, Germany (2015)

2. **C. M. Ögün**, T. Doll, R. Kling, *Modelling and characterization of a microwave driven low pressure lamp based on indium(I)iodide argon system*, DPG Frühjahrstagung, Bochum, Germany (2015)

3. R. Kling, **C. M. Ögün**, *Strahlungsquellen im Gesundheitsbereich*, 8. Symposium Licht u. Gesundheit, Symposiums Schrift, 155-166, Berlin (2014)

4. **C. M. Ögün**, R. Kling, H. Heuermann, C. Schopp, *Elektrodenlose quecksilberfreie Niederdrucklampen betrieben mit Mikrowellen*, LICHT 2014, 21. Gemeinschaftstagung , Den Haag, NL (2014)

5. **C. M. Ögün**, K. Hähre, R. Kling, *Modeling and Characterization of an Indium(I)Iodide-Argon Low Pressure Lamp*, The 41st IEEE International Conference on Plasma Science and the 20th International Conference on High-Power Particle Beams (ICOPS/BEAMS), Washington DC, USA (2014)

6. K. Hähre, **C. M. Ögün**, R. Kling, *Radiometric and Electrical Characterization of Medium-Power Inductively Coupled UV-Radiation Source*, The 41st IEEE International Conference on Plasma Science and the 20th International Conference on High-Power Particle Beams (ICOPS/BEAMS), Washington DC, USA (2014)

7. **C. M. Ögün**, C. Kaiser, R. Kling, *Untersuchung der transienten Prozesse bei der Erzeugung von elektrodenlosen mikrowellenangeregten Niederdruckentladungen*, DPG Frühjahrstagung der Sektion AMOP (SAMOP), Jena, Germany (2013)

8. C. Kaiser, **C. M. Ögün**, R. Kling, W. Heering, *Molekulare Strahlung mikrowellenangeregter Hochdruckentladungslampen auf Indiumiodid*, DPG Frühjahrstagung der Sektion AMOP (SAMOP), Jena, Germany (2013)

9. C. Kaiser, **C. M. Ögün**, R. Kling, *Electrodeless Mercury Free High Intensity Discharge Lamps with high Color Rendering Indices driven by Guided Microwaves*, Proceedings of the International Symposium on the Science and Technology of Lighting (LS 13), 139-140, New York, USA (2012)

10. C. Kaiser, **C. M. Ögün**, R. Kling, *The Influence of Iodine Buffer in Indium(I)Iodide Based Electrodeless Mercury Free High Intensity Discharge Lamps Driven by Guided Microwaves*, Proceedings of the International Symposium on the Science and Technology of Lighting (LS 13), 143-144, New York, USA (2012)

11. **C. M. Ögün**, C. Kaiser, R. Kling, *Characterization of dual metal halide emission system by microwave driven mercury free low pressure lamps*, Proceedings of the International Symposium on the Science and Technology of Lighting (LS 13), 97-98, New York, USA (2012)

12. **C. M. Ögün**, C. Kaiser, R. Kling, *Characterization of transient processes inside an electrodeless low pressure mercury lamp driven with pulsed mode surface waves*, Proceedings of the International Symposium on the

Science and Technology of Lighting (LS 13), 95-97, New York, USA (2012)

13. C. Kaiser, **C. M. Ögün**, R. Kling, *Operating of electrodeless, indium iodide based high intensity discharge lamps within the use of plasma guided microwaves*, 39th IEEE International Conference on Plasma Science (ICOPS 2012), Edinburgh, Great Britain (2012)

14. **C. M. Ögün**, C. Kaiser, R. Kling, *Characterization of the Starting and Stabilization Processes Inside an Electrodeless Low Pressure Mercury Lamp Driven with Pulsed Mode Surface Waves*, 39th IEEE International Conference on Plasma Science (ICOPS 2012), Edinburgh, Great Britain (2012)

15. C. Kaiser, **C. M. Ögün**, R. Kling, *Betrieb von elektrodenlosen HID-Lampen durch plasmageführte Mikrowellen*, DPG Frühjahrstagung der Sektion AMOP (SAMOP), Stuttgart, Germany (2012)

16. C. Kaiser, **C. M. Ögün**, R. Kling, *Guided Microwave High Pressure Plasmas for General Lighting Applications with High Color Rendering Index*, Gaseous Electronics Conference, Salt Lake City, USA (2011)

17. **C. M. Ögün**, C. Kaiser, R. Kling, *Sequentially emission line addressing by microwave driven mercury free low pressure lamps*, Gaseous Electronics Conference, Salt Lake City, USA (2011)

18. S. Valouch, **C. M. Ögün**, S. W. Kettlitz, S. Züfle, U. Lemmer, *Printed Circuit Board Integration and Encapsulation of High-Speed Polymer Photodiodes*, E-MRS Spring Meeting 2009, Strasbourg, Frankreich (2009)

Supervised theses

1. Alexandra Pera, *Charakterisierung von koaxialen Xenon Excimer DBE Lampen im bipolaren Pulsbetrieb*, Bachelor's thesis (2013)

2. Felix Manger, *Tomographische Untersuchung von mikrowellenangeregten Niederdruckplasmen*, Bachelor's thesis (2013)

3. William Truong, *Modellierung einer quecksilberfreien Niederdrucklampe*, Master's thesis (2013)

4. Benjamin Grübel, *Untersuchung gepulster quecksilberfreier Indium(I)-iodide-Niederdruckplasmen*, Bachelor's thesis (2014)

5. Sabrina Felicitas Kost, *Charakterisierung technischer UV-Strahlung im VUV-Bereich*, Bachelor's thesis (2015)

Acknowledgment

Band 1   Christian Jebas
          Physiologische Bewertung aktiver und passiver
          Lichtsysteme im Automobil. 2012
          ISBN 978-3-86644-937-4

Band 2   Jan Bauer
          Effiziente und optimierte Darstellungen von
          Informationen auf Grafikanzeigen im Fahrzeug. 2013
          ISBN 978-3-86644-961-9

Band 3   Christoph Kaiser
          Mikrowellenangeregte quecksilberfreie
          Hochdruckgasentladungslampen. 2013
          ISBN 978-3-7315-0039-1

Band 4   Manfred Scholdt
          Temperaturbasierte Methoden zur Bestimmung der
          Lebensdauer und Stabilisierung von LEDs im System. 2013
          ISBN 978-3-7315-0044-5

Band 5   André Domhardt
          Analytisches Design von Freiformoptiken
          für Punktlichtquellen. 2013
          ISBN 978-3-7315-0054-4

Band 6   Franziska Herrmann
          Farbmessung an LED-Systemen. 2014
          ISBN 978-3-7315-0173-2

Band 7   Simon Wendel
          Freiform-Optiken im Nahfeld von LEDs. 2014
          ISBN 978-3-7315-0251-7

Band 8   Carmen Kettwich
          Ablenkung im Straßenverkehr und deren
          Einfluss auf das Fahrverhalten. 2014
          ISBN 978-3-7315-0288-3

Die Bände sind unter www.ksp.kit.edu als PDF frei verfügbar oder als Druckausgabe bestellbar.

Band 9   Steffen Michenfelder
           Konzeption, Realisierung und Verifikation eines automobilen
           Forschungsscheinwerfers auf Basis von Digitalprojektoren. 2015
           ISBN 978-3-7315-0301-9

Band 10   Celal Mohan Ögün
           Surface wave driven molecular low pressure plasmas
           for general lighting. 2016
           ISBN 978-3-7315-0464-1

LEPT

Lichttechnisches Institut
Karlsruher Institut für Technologie (KIT)

SPEKTRUM DER LICHTTECHNIK

Nowadays, compact fluorescent lamps (CFL) are widely-used in general lighting applications. However, they still struggle with acceptance problems due to the hazardous mercury, which serves as the radiant component inside the lamp. The removal of the mercury from the lamp presents a challenge, which still remains unsolved. The presented work deals with the development of a mercury-free, electrodeless, low pressure plasma based on a molecular filling and driven by microwaves, which may represent a viable alternative to the conventional CFLs.